Universidad
del País Vasco
Euskal Herriko
Unibertsitatea

Study of the structural behaviour and analytical characterization of wire-race slewing bearings

Presented by:

Iñigo Martín Lorenzo

Thesis Advisors:

Dr. Josu Aguirrebeitia Celaya
Dr. Iker Heras Miguel

Bilbao, March 2022

A Marcelino Lorenzo

Agradecimientos

Ich danke Matthias Stammler und dem gesamten Team des Fraunhofer IWES dafür, dass sie meinen Forschungsaufenthalt in Hamburg trotz der schwierigen Situation ermöglicht haben. Es war mir eine Freude mit Ihnen zusammenzuarbeiten, vielen Dank für Ihre Gastfreundschaft.

No podría terminar este apartado sin mencionar a las personas que más cerca han estado de mí durante estos años. A mis padres, Carmen y Tomás, sin vuestro apoyo y confianza nunca hubiera llegado hasta aquí. A mi hermana Elena y a mi tío Iñaki, quienes son un ejemplo de esfuerzo y dedicación. Por último, a mi abuelo Marcelino, gracias a tu trabajo y sacrificio he podido aprovechar las oportunidades que tu no tuviste. Espero que estés orgulloso.

Iñigo

Abstract

   Slewing bearings are large bearings mainly used for heavy structure orientation. Given the nature of this purpose, they have to support a combination of axial, radial and tilting moment loads. To cite some application examples, these bearings are used to rotate the nacelle and blades of wind turbines, heavy machinery, cranes, radio telescopes or tunnelling machines. Regarding the rolling elements, there are different configurations depending on the application. The most common configurations consist of balls or rollers in one or various rows, crossed rollers or even a combination of both. It is true that they are not the most used type of bearing in the industry. Nevertheless, the research interest of these kind of components has increased in recent years, mainly motivated by the rise of the wind energy.

   Wire-race slewing bearings are a special type of slewing bearings. In this case, the raceways are not machined over the rings, but over cylindrical section wires. These wires, in turn, are embedded on the rings. This layout increases the complexity of the component, and also provides several unique characteristics. For example, the wires and the rolling elements must be manufactured in hardened steel, since they have to support high contact pressures and must be resistant to wear. However, the rings can be manufactured in any other material. Aluminium is typically the material used for the rings, but bronze, plastic, carbon fibre or 3D printing are also possible alternatives. As a result, the weight of the component decreases significantly, which is the main advantage of this layout. Besides, its performance supporting shock loads is better and it also has more travelling vibrations absorption capacity. Because of this, wire-race bearings can be found in high added value applications such as the medical industry, robotics, astronomy, aeronautics, renewable energy or defence.

   Despite the fact that the market for wire-race bearings is growing, only a few specialized manufacturers or big corporations include these bearings in their product catalogues. Therefore, almost no research work has been published in

this area, in contrast with the conventional slewing bearings. In order to make this technology available to more modest manufacturers, a research line to study and characterize the structural behaviour of wire-race slewing bearings was established. The resulting work will lay the foundations for the technology and will be used as reference for future research work. In the first chapter of this Doctoral Thesis, all the aforementioned information is included and developed. Besides, it also includes a technical background necessary to understand the following chapters, a review of the state-of-the-art and a general overview of the document.

Among the different rolling element configurations, four-point contact slewing bearings is one of the most common. Because of that, the first part of the research work is focused on these. As a first approach to the component, a study of the structural behaviour is carried out and its performance compared with an equivalent conventional slewing bearing. To this end, several FE (Finite Element) simulations are performed, where the bearings are subjected to axial load. After studying the results, several physical phenomena are identified, with the wire twisting phenomenon being the most relevant. The influence of several design parameters is also evaluated. Because of the important implications of the wire twisting phenomenon, two analytical formulae for the calculation of the wire twisting stiffness are developed. One formula can be used for non-machined wires and another one for race-shaped wires. Once the structural behaviour of the component is known, an analytical model to perform static structural calculations under axial or tilting moment loads is conceived. The first step consists of defining a system of equations that represent the structural response of one bearing sector with one rolling element under axial load. Then, each bearing sector can be solved independently and the response of the whole bearing obtained by the summation of all of them. Of course, results obtained with the analytical model are compared with FE reference results. It was determined that the analytical model is accurate after observing good correlation in terms of stiffness, wire twist, contact force and angle.

Crossed roller wire-race slewing bearings are another common bearing configuration, where the rolling elements are oriented in two directions and alternatively disposed. In this case, a more ambitious objective is established, which consists in developing an analytical calculation tool to obtain the bearing response under any load combination. As a first step, the structural behaviour of the bearing must be studied in order to identify the physical phenomena and define the necessary simplifications for the conception of the analytical model.

The development of the analytical model is similar to the previous one, where all the bearing sectors were solved independently to obtain the response of the bearing. Nonetheless, to obtain the analytical calculation tool, an algorithm must be developed based on the analytical model. This algorithm does not only obtain the static load capacity and stiffness curves under pure loads, but also performs an iterative process to solve the load distribution problem under combined load cases. Finally, the analytical calculation tool is validated via a comparison with FE results.

The use of FE models is intensive throughout the Doctoral Thesis, since they are used to study the structural behaviour of the bearings and to validate the analytical models. Because of this, it is essential to carry out any kind of experimental validation. To this end, an experimental test campaign is performed on a tension-compression test bench. The test specimens are four crossed roller wire-race bearings of two different bearing designs. Experimental tests are processed and compared with FE results, obtaining good correlation. Finally, it can be said that all the FE models developed in this Thesis are accurate, since the modelling strategy is the same for all of them. In addition, some relevant conclusions related with the behaviour of the bearings are obtained.

It is true that FE calculations are accurate, but they have a high computational cost and usually present convergence problems. To address these problems, several efficient FE modelling strategies are proposed. Regarding four-point contact wire-race slewing bearings, a simplification that is already used for conventional slewing bearings is implemented. After some modifications, it is proved to be an efficient and accurate FE modelling strategy. Two other efficient FE modelling strategies are also proposed for crossed roller wire-race slewing bearings. The first one consists of implementing the analytical formulation developed for these kind of bearings into an FE model. This is made by means of a matrix element, which represents the structural behaviour of one roller with its corresponding wire sections. The second alternative also consists in the replacement of the latter elements with a non-linear spring, which represents the stiffness of the contacts. Both FE modelling strategies are accurate and efficient, being the first one more tedious to implement but also obtaining slightly better results.

In order to finish the research work of the Thesis, the procedure to obtain some design guidelines for four-point contact and crossed roller wire-race slewing bearings is explained. To this end, an FE analysis campaign based on a

DoE (Design of Experiments) is performed. The variables of the DoE are the ones that define the bearing contact geometry. After studying the influence of these parameters on several performance indicators, several conclusions about the bearing design criteria are obtained.

Resumen

Los rodamientos de vuelco son rodamientos de gran tamaño utilizados principalmente con fines de orientación de grandes estructuras. Debido a la naturaleza de este propósito, han de soportar una combinación de cargas axial, radial y de momento de vuelco. Por citar algunas áreas de aplicación, este tipo de componentes se emplean en orientación de la góndola y palas de turbinas eólicas, en maquinaria pesada, grúas, radiotelescopios o tuneladoras. Dependiendo de la aplicación, se pueden encontrar configuraciones cuyos elementos rodantes son bolas en una o varias hileras, dos o tres hileras de rodillos, rodillos cruzados o incluso mixtos. Si bien no son el tipo de rodamiento más empleado en la industria, el auge de la energía eólica durante los últimos años ha hecho que se inviertan recursos en investigar y desarrollar este tipo de componente.

Un tipo especial de rodamiento de vuelco son los rodamientos con pista de rodadura alámbrica (o wire-race bearings). En este caso, las pistas de rodadura no están mecanizadas sobre los anillos, sino sobre unos alambres de sección cilíndrica. Estos alambres, a su vez, van embebidos en los anillos. Si bien esta innovación aporta complejidad al componente, también proporciona una serie de características únicas. En lo relativo a la selección de materiales, cabe destacar que los elementos rodantes y los alambres han de ser fabricados en acero endurecido, debido que han de soportar grandes presiones de contacto y resistir el desgaste. Sin embargo, los anillos pueden ser fabricados en cualquier otro material. Lo más habitual es encontrar rodamientos de alambre con anillos de aluminio, pero también se pueden fabricar en bronce, plástico, fibra de carbono o por impresión 3D. Como resultado, el peso del componente disminuye de forma considerable, siendo esta su principal ventaja. Además, su comportamiento es mejor frente a cargas de impacto y tienen mayor capacidad de absorber vibraciones. Por esto, los rodamientos de alambre se pueden encontrar en aplicaciones de alto valor añadido como la industria de

dispositivos médicos, robótica, astronomía, aeronáutica, energías renovables o aplicaciones militares.

A pesar de que el mercado de los rodamientos con pista de rodadura alámbrica está creciendo en los últimos años, sólo unos pocos fabricantes especializados o grandes corporaciones disponen de estos componentes en sus catálogos. Debido a esto, y a diferencia de los rodamientos de vuelco convencionales, apenas existen trabajos de investigación publicados en este área. Por este motivo, y con el fin de hacer esta tecnología accesible a empresas más modestas del sector, se planteó como objetivo abrir una línea de investigación para estudiar y caracterizar el comportamiento estructural de rodamientos con pista de rodadura alámbrica. El trabajo resultante sentará las bases de esta línea de investigación y servirá como referencia para futuras investigaciones. En el primer capítulo de la tesis doctoral se incluye y desarrolla toda la información mencionada hasta ahora junto con los antecedentes necesarios para el desarrollo de los capítulos posteriores, una revisión del estado del arte y una vista general del trabajo desarrollado.

Si bien existen diferentes configuraciones, una de las más comunes son los rodamientos de bolas de cuatro puntos de contacto. Por ello, en ella se centran los primeros capítulos del presente documento. Como primera labor de investigación, se lleva a cabo un estudio del comportamiento estructural de dicho componente y se compara con su equivalente convencional. Para ello se realizan varias simulaciones por EF (Elementos Finitos) sometiendo a los rodamientos a carga axial. Tras observar los resultados se identifican varios fenómenos físicos relevantes, como es el giro del alambre bajo carga. Además, se estudia la influencia de algunos parámetros de diseño y se lleva a cabo la comparativa en términos de varios indicadores. Debido a la relevancia del giro del alambre, se desarrollan dos fórmulas analíticas para la obtención de su rigidez torsional. Una fórmula sirve para alambres sin mecanizar y la otra para alambres con pista de rodadura mecanizada. Una vez el comportamiento del componente es conocido, se desarrolla un modelo analítico para realizar cálculos estructurales estáticos bajo cargas axiales y de momento de vuelco. Para ello, se define un sistema de ecuaciones que representa el comportamiento bajo carga de un sector de rodamiento con un elemento rodante. Tras resolver todos los sectores de forma independiente se obtiene la respuesta del rodamiento completo. Por supuesto, los resultados del modelo analítico se comparan con resultados de modelos de EF de referencia. Tras observar una buena

correlación en términos de rigidez, giro del alambre y fuerzas y ángulos de contacto, se determinó que el modelo analítico es satisfactoriamente preciso.

Otra configuración común son los rodamientos de rodillos cruzados con pista de rodadura alámbrica, donde los elementos rodantes son rodillos orientados en dos direcciones y dispuestos de forma alternativa. En este caso, se planteó un objetivo más ambicioso, que consiste en el desarrollo de una herramienta de cálculo analítica, capaz de hacer frente a cualquier caso de carga. Para ello, se estudia de la respuesta estructural del componente. De este modo se entiende su comportamiento y se pueden definir las simplificaciones necesarias para la concepción del modelo analítico. El desarrollo del modelo analítico es análogo al anterior, donde se resuelven todos los sectores independientemente para obtener la respuesta del rodamiento completo. Sin embargo, para obtener una herramienta de cálculo es necesario desarrollar un algoritmo basado en dicho modelo analítico. Este algoritmo no solo obtiene las curvas de rigidez y capacidad estática bajo cargas puras, sino que también lleva a cabo un proceso iterativo para resolver el problema de distribución de carga cuando se aplican cargas combinadas. Finalmente, la herramienta de cálculo se valida mediante una comparativa con resultados de EF.

A lo largo de la tesis se utilizan modelos de EF de forma extensiva, ya que por medio de ellos se estudia el comportamiento de los rodamientos y se validan los modelos analíticos. Por ese motivo, se hace indispensable algún tipo de validación experimental. Para ello, se lleva a cabo una campaña de ensayos experimentales en una máquina de tracción-compresión. Los especímenes de ensayo son cuatro rodamientos de rodillos cruzados con pista de rodadura alámbrica correspondientes a dos diseños diferentes. Los resultados experimentales se procesan y comparan con resultados de EF. Como la correlación obtenida es buena, se puede afirmar que los modelos de EF son precisos, ya que todos se han desarrollado siguiendo la misma estrategia de modelado. Adicionalmente, de los resultados también se obtienen conclusiones relevantes en cuanto al comportamiento del componente.

Si bien se demuestra la validez de los modelos de EF, estos son computacionalmente costosos y, a menudo, presentan problemas de convergencia. Para paliar esto, se proponen varias estrategias para el modelado eficiente mediante EF. En primer lugar, una simplificación ya utilizada en rodamientos de vuelco convencionales se implementa en rodamientos de bolas con pista de rodadura alámbrica. Tras algunas modificaciones, se comprueba que también tiene validez en estos componentes. Por otra parte, se proponen

dos alternativas para rodamientos de rodillos cruzados con pista de rodadura alámbrica. La primera consiste en implementar en EF la formulación analítica propuesta en capítulos anteriores. Esto se lleva a cabo de forma que un elemento matriz representa el comportamiento de un rodillo con sus respectivas secciones de alambre. La segunda alternativa consiste en sustituir esto último en vez de por una matriz, por un elemento muelle que simula la rigidez de los contactos. Ambas alternativas resultaron ser precisas y muy eficientes, siendo la primera alternativa algo más tediosa de implementar pero con ligeramente mejores resultados.

Para cerrar el ámbito de investigación de la tesis, se expone el procedimiento llevado a cabo para la obtención de una serie de directrices de diseño para rodamientos con pista de rodadura alámbrica de bolas y de rodillos cruzados. Para ello, se realiza una campaña de simulaciones de EF basada en un DoE (Diseño de Experimentos), donde las variables son los parámetros geométricos que definen la geometría interior del rodamiento. Tras estudiar la influencia de estos parámetros sobre varios indicadores, se obtuvieron conclusiones sobre cómo tomar decisiones a la hora de diseñar estos componentes.

Contents

List of Figures

List of Tables

Nomenclature

$A_{eq.}$	Equivalent bolt stress area.
a	Major contact ellipse semi-axis.
a^*	Dimensionless tabulated parameter.
b	Minor contact ellipse semi-axis.
b^*	Dimensionless tabulated parameter.
C	Constant determined via FE.
C_s	Coefficient for the bearing stiffness calculation iterative process.
C_0	Static load capacity.
C_{0a}	Axial static load capacity.
C_{0r}	Radial static load capacity.
C_{0m}	Tilting moment static load capacity.
$Cte1$	Tabulated constants for the contact calculations.
$Cte2$	Tabulated constants for the contact calculations.
c	Coefficient for the calculation of k_1, k_2 and k_3.
c_{Dw}	Coefficient for the calculation of k_1, k_2 and k_3.
c_λ	Coefficient for the calculation of k_1, k_2 and k_3.
c_{Rf}	Coefficient for the calculation of k_1, k_2 and k_3.
$c_{Dw\lambda}$	Coefficient for the calculation of k_1, k_2 and k_3.
c_{DwRf}	Coefficient for the calculation of k_1, k_2 and k_3.
d	Projection of the ball-wire contact spring.
d_0	Depth of reference.
d_n	Nominal bolt diameter.
D_{cw}	Diameter between wire centres.
D_w	Rolling element diameter.
D_{wn}	Normalized rolling element diameter.
D_{pw}	Bearing mean diameter.
E'	Elastic modulus.
E	Equivalent elastic modulus.
e^i	Total contact interference of sector i.
e_A^i	Contact interference generated by axial load in sector i.
e_R^i	Contact interference generated by radial load in sector i.
e_t^i	Contact interference generated by tilting load in sector i.
$\Sigma\rho$	Curvature sum.
f_0	ISO-76 tabulated value.

F_a	Axial force.
F_A^{input}	Input axial force.
F_A^{opt}	Axial force resulting from the optimization process.
F_B	Ball-wire normal contact force.
F_{eqw}	Force of the equivalent spring (k_1, k_2).
F_N^i	Normal contact force of the sector i.
F_r	Radial force.
F_R^{input}	Input radial force.
F_R^{opt}	Radial force resulting from the optimization process.
F_{Tg}^i	Tangential contact force of the sector i.
$F_{Tot.}^i$	Total contact force of the sector i.
F_x	Bearing force in the x direction.
F_y	Bearing force in the y direction.
F_z	Bearing force in the z direction.
H	Bearing housing.
H_g	Standard ring geometry parameter.
i	Bearing sector number.
j	Number of iteration.
k	Ratio of equivalent radius.
K	Wire twisting stiffness constant.
k_B	Ball-wire stiffness constant.
$\boldsymbol{k_{cbn}}$	Combin39 equivalent spring stiffness.
k_{eqw}	Stiffness of the equivalent spring (k_1, k_2).
k_1	Contact 1 normal stiffness constant.
k_2	Contact 2 normal stiffness constant.
k_3	Contact 3 normal stiffness constant.
k_{tw}	Wire twisting stiffness constant.
K_s	Stiffness of the spring.
K^{Origin}	First load step wire twisting stiffness constant.
$K^{An.}$	Analytical wire twisting stiffness constant.
K_f	Coefficient of friction of the bolt.
L	Length of the line contact.
L_{ns}	Length of the no-separation contact.
L_{RC}	Distance between wire and raceway centres.
$L_{\rho\theta}$	Undeformed wire arc.
$L_{\rho\theta,\varphi}$	Deformed wire arc.
M_B	Twisting moment generated by the contact force.
M_f	Friction torque.
M_{f0}	Idling friction torque.
M_t	Tilting moment.
M_t^{input}	Input tilting moment.
M_t^{opt}	Tilting moment resulting from the optimization process.

M_w	Wire twisting moment.
N_1^i	Normal contact force in the contact 1 of the sector i.
N_2^i	Normal contact force in the contact 2 of the sector i.
N_{1A}^i	Normal contact force in the contact 1 of the sector i type A roller
N_{1B}^i	Normal contact force in the contact 2 of the sector i type B roller
N_{2A}^i	Normal contact force in the contact 1 of the sector i type A roller.
N_{2B}^i	Normal contact force in the contact 2 of the sector i type B roller.
N_B	Number of balls.
N_R	Number of rollers.
n	Number of springs.
P_{max}	Maximum contact pressure.
Q	Normal contact force.
Q_{max}	Maximum normal contact force.
R	Wire mean radius.
R_{wh}	Wire housing radius.
R_c	Raceway radius.
Rf	Raceway factor.
Rf_n	Normalized raceway factor.
R_x	Equivalent radius perpendicular to the rolling direction.
R_y	Equivalent radius in the rolling direction.
R_H	Standard ring geometry parameter.
R_L	Standard ring geometry parameter.
R_{Lg}	Standard ring geometry parameter.
R_1	Contact force in the contact 1.
R_2	Contact force in the contact 2.
R_3	Contact force in the contact 3.
s	Osculation ratio.
T	Wire twisting moment.
t	Thickness of the outer race section.
T_2	Wire-ring tangential contact force.
T_b	Bolt preload.
$T_{max.}$	Bolt maximum allowable torque.
W_{PC}	Dimensionless load.
W_{ns}	Width of the no-separation contact.
x_{RC}	Raceway centre horizontal displacement.
x_w	Wire centre horizontal displacement.
y_{RC}	Raceway centre vertical displacement.
y_w	Wire centre vertical displacement.
y_B	Axial displacement input.
α	Contact angle.
α_0	Initial contact angle.
α_b	Bolt thread angle.
$\alpha_{Tot.}^i$	Angle of the total contact force of the sector i.
β	Span angle.

γ_0	Half-included roller centre line angle.
γ	Wire-raceway position angle.
δ	Normal contact deformation.
δ^*	Dimensionless tabulated parameter.
δ_{eqw}	Deformation of the equivalent spring (k_1, k_2).
δ_p	Diametrical rolling element preload.
δ_{x1}	Node 1 DoF in the x direction.
δ_{x2}	Node 2 DoF in the x direction.
δ_{y1}	Node 1 DoF in the y direction.
δ_{y2}	Node 2 DoF in the y direction.
δ_{z1}	Node 1 DoF in the z direction.
δ_{z2}	Node 2 DoF in the z direction.
Δ_A	Axial displacement imposed to the bearing.
Δ_{A0}	Initial axial displacement imposed to the bearing.
Δ_α	Contact angle variation.
Δ_R	Radial displacement imposed to the bearing.
Δ_{R0}	Initial radial displacement imposed to the bearing.
Δ_1^i	Contact interference in the contact 1 of the sector i.
Δ_2^i	Contact interference in the contact 2 of the sector i.
Δ_3^i	Contact interference in the contact 3 of the sector i.
Δ_A^i	Axial displacement imposed to sector i.
Δ_R^i	Radial displacement imposed to sector i.
ε	Coefficient for the load distribution problem optimization process.
η	Constant determined via FE.
θ_i	Angular position of sector i.
θ_R	Orientation of the radial load.
θ_R^{input}	Input orientation of the radial load.
θ_t	Orientation of the tilting load.
θ_t^{input}	Input orientation of the tilting load.
θ_w	Wire centre twisting angle.
λ	Wire diameter.
λ_n	Normalized wire diameter.
λ_r	Normalized wire diameter with respect to D_w.
μ	Coefficient of friction.
μ'	Coefficient of friction between the bolt head and the surface.
ν	Poisson's ratio.
σ	Contact pressure.
σ_{yp}	Yield stress.
φ	Twisting angle.
φ_t	Tilting angle imposed to the bearing.
φ_{t0}	Initial tilting angle imposed to the bearing.
ω	Angle related with the wire twist.

1 Introduction

1.1 Context and motivation

Slewing bearings are a kind of bearing whose diameter is far greater than the rolling element diameter. These bearings are widely used for orientation purposes, so they are designed to rotate at slow speeds and under an oscillatory regime. The nature of the applications where they are used usually makes them subject to large tilting moments and axial and radial loads. They can be found in a wide variety of applications, such as cranes, heavy-duty machinery, renewable energy and defence among others. However, the wind energy sector has been the main research driving force in this field, since these components are key and this is a pushing technology sector. Figure 1.1a shows a four-point contact slewing bearing and the loads they have to withstand.

Wire race bearings are a different concept of slewing bearing as can be seen in Figure 1.1b, since the rolling element runs over race-shaped wires embedded within the rings. Rolling elements and wires support large loads and high contact pressures, so they must be manufactured in hardened steel, or less frequently, in ceramic. Moreover, this design offers a concept that opens a wide range of materials for the rings, such as aluminium, bronze, carbon fibre, plastic or even 3D printed rings, reducing a considerable amount of weight. Figure 1.2 shows the weight comparison between bearings with the same cross-section and different ring materials performed by the manufacturer Franke [1]. Other manufacturers such as SKF or Rothe Erde agree that weight reductions of up to around 60% can be achieved with an equivalent bearing if the rings are made of aluminium [2,3]. Another advantage of the race shaped wires is that they can be placed anywhere, even embedded in the design of the machine. This helps to reduce the mounting space and increases compactness. This layout also provides maintenance and reparation advantages with the possibility of replacing wires when they suffer race damage instead of replacing the whole bearing.

(a)

(b)
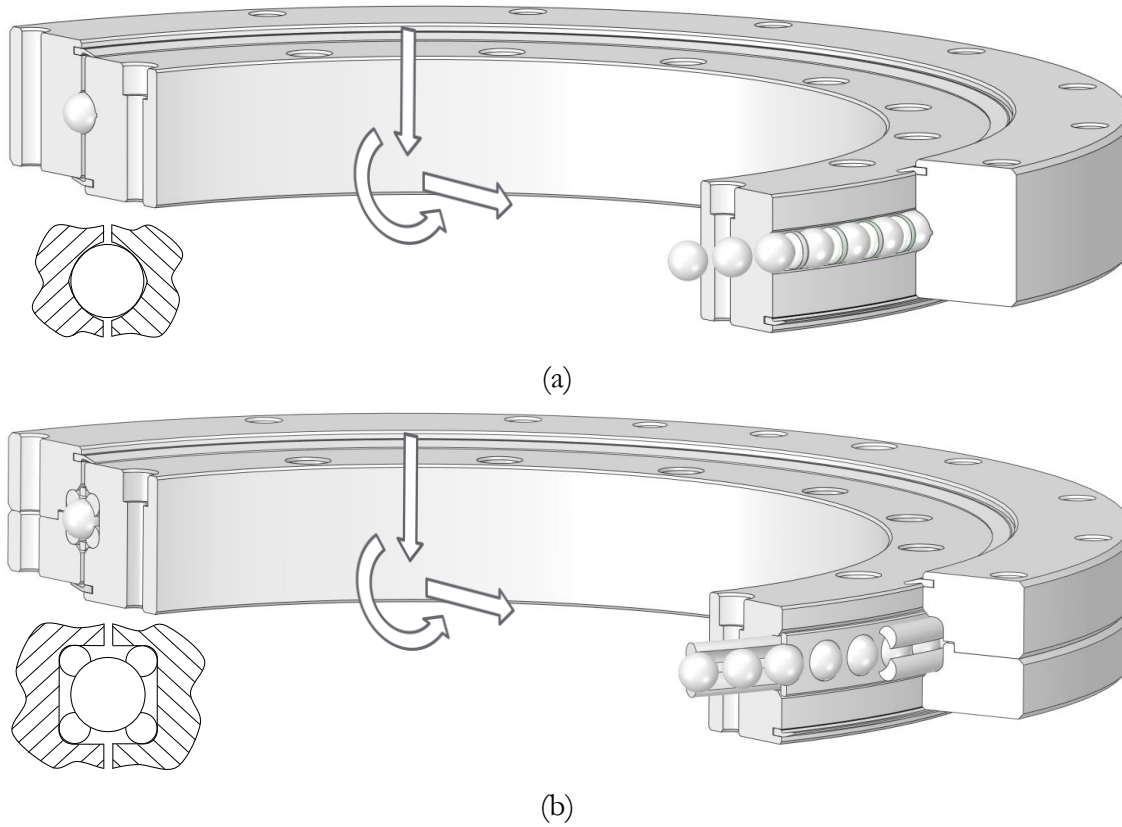
Figure 1.1 Four-point contact slewing bearing: (a) Conventional; (b) Wire-race.
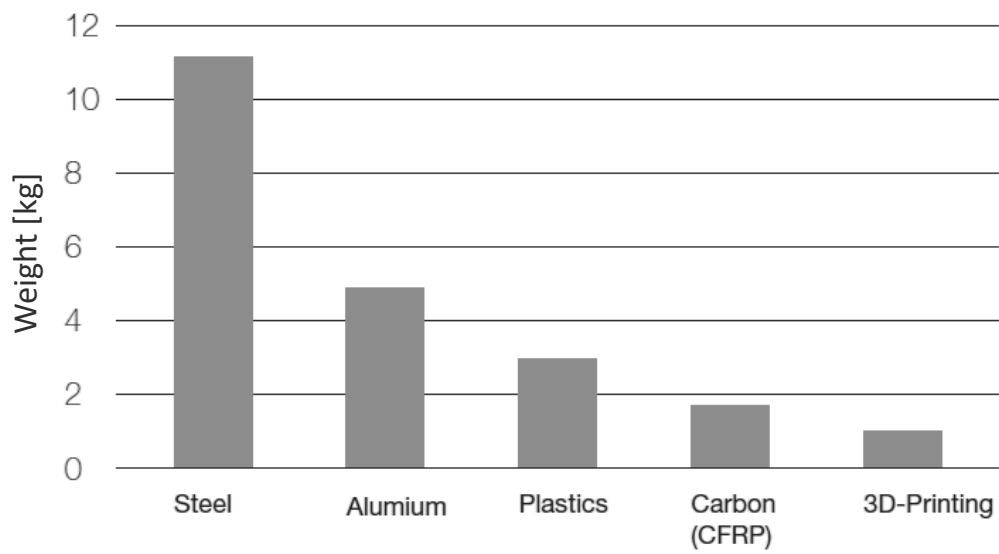
Figure 1.2 Wire-race bearings weight comparison with different ring materials (300 mm diameter and identical load characteristics) [1].

These kind of bearings are not as popular as conventional slewing bearings, but their presence in specific applications is increasing [4] and more manufacturers are including them into their catalogues. There are many areas where these bearings provide substantial advantages that are not so evident at first glance; these are shown in Figure 1.3 and are going to be enumerated together with the advantages these bearings provide in each application. In robotics there is a constant pursuit to achieve higher accelerations and decelerations; for this reason, wire bearings are a good choice since they can provide a more integrated design and weight reductions. This property is also welcomed in a sector aware of weight reductions, such as aeronautics. Besides, the fluctuation of the temperature with the height creates contractions and expansions of the bearing rings, resulting in a non-constant torque. Wire bearings also provide constant torque in a range of temperatures, since the wires are open and the existing gap absorbs the length variations [2]. For those reasons, new camera systems placed in helicopters and drones implements this technology. Another sector that is committed to wire bearings is the medical industry, where noise and travelling vibrations are a common issue. Wire bearings are implemented in X-Ray and Computer Tomography machines with an innovative vibration damper made of elastomer placed between the wires and the rings [5]. Moreover, the low elastic modulus and the higher damping provided by the additional contacts, make these bearings excellent to use, absorbing the eventual shock loads that could damage the races. For that reason, wire race bearings are also employed in the defence industry, rotating turrets and guns. Furthermore, building the component with non-corrosive materials is a huge differentiating factor in the shipping industry. Besides this fact, shock loads generated by waves hitting ships' hulls can be better absorbed by wire-race bearings. For those reasons, wire-race bearings are an interesting alternative for on-board equipment such as radars and antennas.

(a)   (b)

(c)   (d)

(e)   (f)
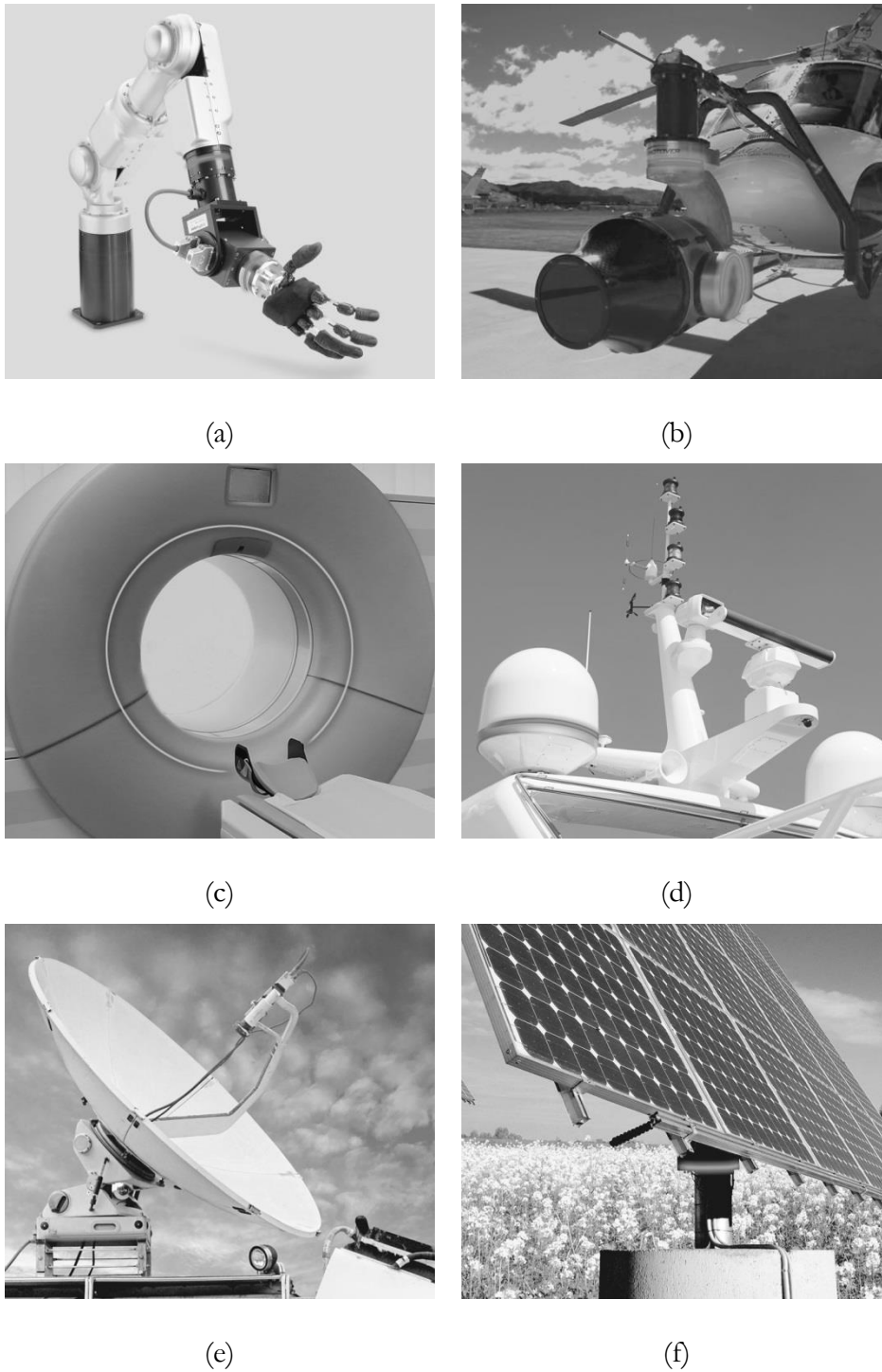
Figure 1.3 Applications of wire-race bearings [6]: (a) robotics; (b) aeronautics; (c) medical devices; (d) shipping industry; (e) radars and antennae; (f) renewable energy.

The performance of wire race bearings is therefore different from that of conventional slewing bearings. Nevertheless, little literature can be found that addresses this topic. This fact makes it difficult to characterize these components or foresee their mechanical response. Moreover, the manufacturing process of wire race bearings is complex because of the inherent difficulty of producing ring-shaped hardened wires. For that reason, there are

not so many manufacturers, and only the most powerful bearing manufacturers like SKF and Rothe Erde, or specialized labels like Franke, can afford to include this product in their catalogues. These bearings are usually custom made (95% according to Franke [6]) rather than mass-produced, and for that reason it is difficult to find technical data sheets. Another possible reason regarding the lack of information can be related to occultism among manufacturers, who save their technology for themselves. There are also smaller companies interested in commercializing wire-race bearings, but they have to face an unknown world. In terms of product development, wire race bearings are currently being applied in high tech applications as well as in renewable energy sources. For these reasons, wire-race bearings manufacturers are making efforts towards developing new solutions to adapt these components to the future. The path to follow is through sustainability, where energy efficient machines which weigh less and optimized designs are a major concern. There is also a trend in the reuse philosophy, where remanufacturing and reuse instead of manufacturing new components is a rising reality. This attitude not only reduces the waste, saves resources and energy, but is also a much cheaper solution. The aim of this work is to provide knowledge in this area and lead the way in this technology, making the know-how accessible for the industry, promoting the competitiveness and the continuous improvement of these components.

The ADM Mechanical Design research group [7] of the University of the Basque Country started a research line in the scope of slewing bearings several years ago meeting the demand for research in the field. Many research articles have been published since then; mainly analytical approaches for the static characterization of slewing bearings [8–15] and friction torque [16–18] in addition to Finite Element modelling techniques [19]. The research group also has a close relationship with Iraundi S.A., participating in research projects and providing mutual technical support. This relationship states that the research group is aware of the current interests of the industry and that the developed work is also valuable for the industry. The research presented in this Doctoral Thesis gathers the results of the research work carried out in the field of wire race bearings under the guidance of the ADM Mechanical Design group.

1.2 Wire-race and conventional slewing bearing description

Wire race slewing bearings are the topic of this thesis, so they must be described in great detail. As they are slewing bearings, they share many similarities with conventional slewing bearings. In this section, the components of a conventional and wire race slewing bearing shown in Figure 1.4 will be described first, and the bearing types afterwards.

Rings: The main parameter that defines the rings is the mean diameter (D_{pw}), which happens to be much larger than the rolling element diameter (D_w) in slewing bearings. This layout makes the bearings more slender, in relative terms, in comparison with standard bearings. Wire-race bearings rings can be produced in many types of materials, but they are usually manufactured using anodized aluminium; carbon fibre or plastic rings are also produced, but they are less common. In conventional slewing bearings, rings are usually manufactured with medium carbon steel forging and induction hardened raceways. Wire-race bearing rings consist of a one-piece ring, and a two-piece ring, this arrangement allows for the mounting process. This strategy can be also employed with conventional slewing bearings, but in this latter case it is more common to have both solid rings.

Wires: These are the characteristic elements of wire bearings. Basically, they are steel wires with a machined race where the rolling elements run. To avoid wear and to support high loads, they are subjected to a hardening process. A wire does not form a closed ring, they have a cut with a clearance that allows for the mounting process and keeps the friction torque absorbing the thermal expansions constant.

Rolling Elements: Balls or rollers typically manufactured with hardened chrome alloy steel can be used for this purpose. The ball-raceway contact shown in Figure 1.5 is a point contact (the contact takes place in a point) at a certain angle (α_0), where the osculation ratio is the ratio between the ball and raceway curvatures $(s = D_w/(2 \cdot R_c) < 1)$. The roller-raceway contact is a line contact (the contact take place along a line) perpendicular to a certain angle (α_0). Besides, there are different roller profiles (crowned, partially crowned logarithmic…) that improve the contact pressure distribution and the bearing performance. More information about this topic is introduced in Section 0. On another note, a typical practice in slewing bearings that involves the rolling

elements is preloading, which consists in introducing oversized rolling elements. This practice avoids clearances between the rolling elements and the raceways, so undesirable vibrations are eliminated [20]. In addition, the stiffness of the bearing increases, which also improves accuracy. Preloading does not have a relevant effect on the static load capacity [21], but it increases the friction torque and consequently the wear rates.

Spacers and cages: These parts, typically made of plastic materials, are used to separate the rolling elements and prevent them from coming into contact, banging or rubbing each other. Besides, they assess an evenly rolling element position within the races. A spacer is a piece of plastic or metal that is placed between two consecutive rolling elements. As shown in Figure 1.4a, spacers are specifically designed to accommodate both rolling elements preventing undesirable gaps. Another alternative consists of a cage like the one shown in Figure 1.4b. This cage consists of a continuous crown made of metal or plastic, which contains the rolling elements.

Mounting holes: Slewing bearings are linked to the surrounding structure by means of bolted joints. The holes are equally spaced along the inner and outer rings and can be through holes or tapped holes.

Assembly joints: When a ring is divided into two parts, it becomes necessary to fix them by means of a minimum number of bolts. The objective of these joints is to maintain the assembly and, once the bearing is mounted, they lose their purpose.

Gear: This makes the relative movement of one ring with respect to the other possible when an electric motor transmits movement on the gear. Depending on the application, the gear can be placed on the inner or outer ring or there is not one if the gear is manufactured in the surrounding structures or another actuation system is employed.

Load plug: if both rings are solid, the only solution for inserting the rolling elements into the raceways is by means of a radial drilled hole. Once all the rolling elements are in position, the hole is filled with a plug, which is carefully placed in order to provide continuity to the races. In 1986 INA-Schaeffler patented a technology to apply this methodology to wire-race bearings [22], but it is not used currently.

Grease fitting: lubrication of the raceways is a key aspect in bearing operation; for this reason, lubricant or grease is introduced through these

radially drilled holes. There are also automated lubrication systems that perform this task automatically.

Seals: seals are an important part in terms of the durability of the bearing. They prevent grease leakages and keeps moisture and undesired particles outside the bearing. Seals become more relevant when the bearing is subjected to extreme conditions such as marine water or desert conditions, among others.
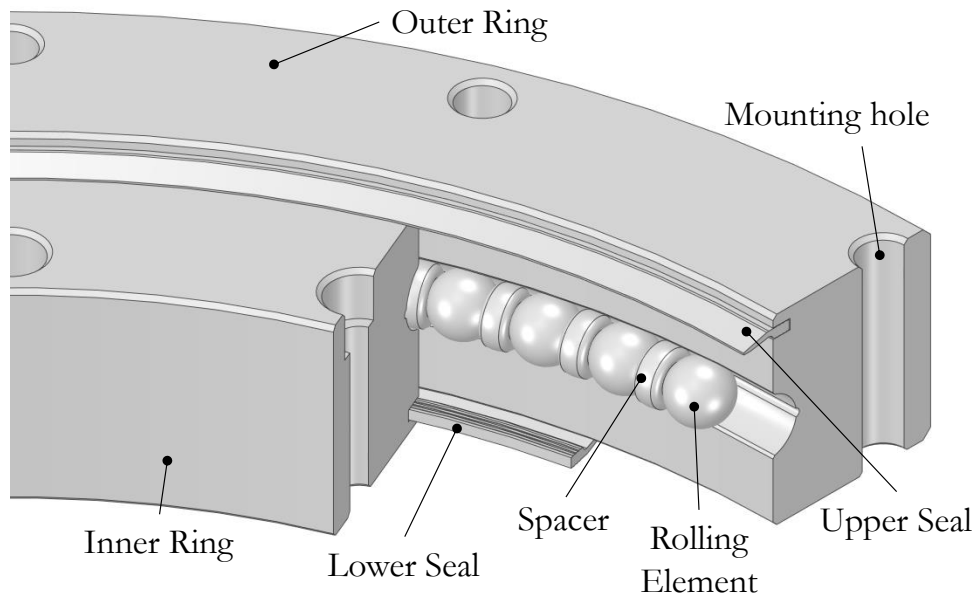
(a)
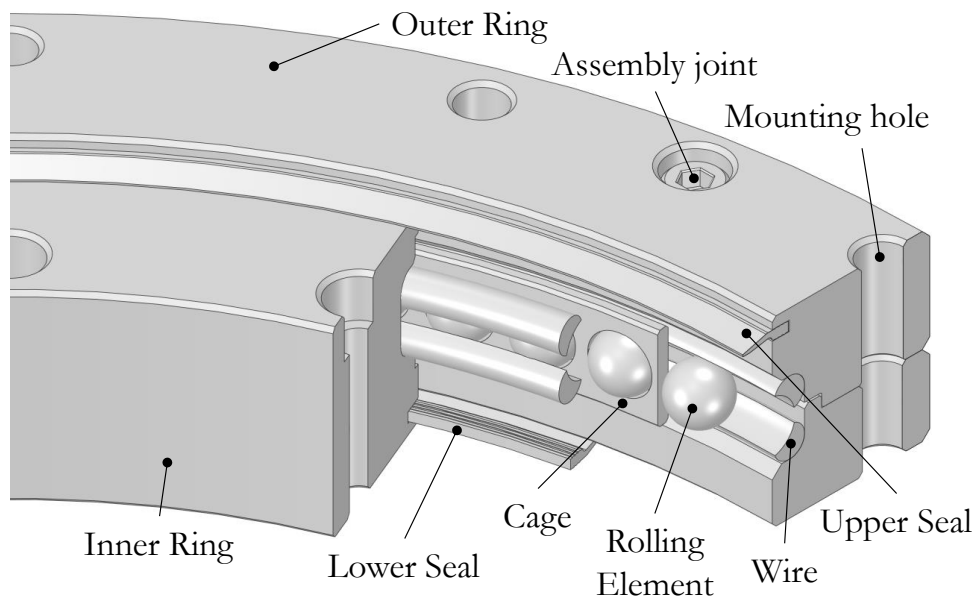
(b)

Figure 1.4 Four-point contact bearing components: (a) Conventional slewing; (b) Wire-race slewing.
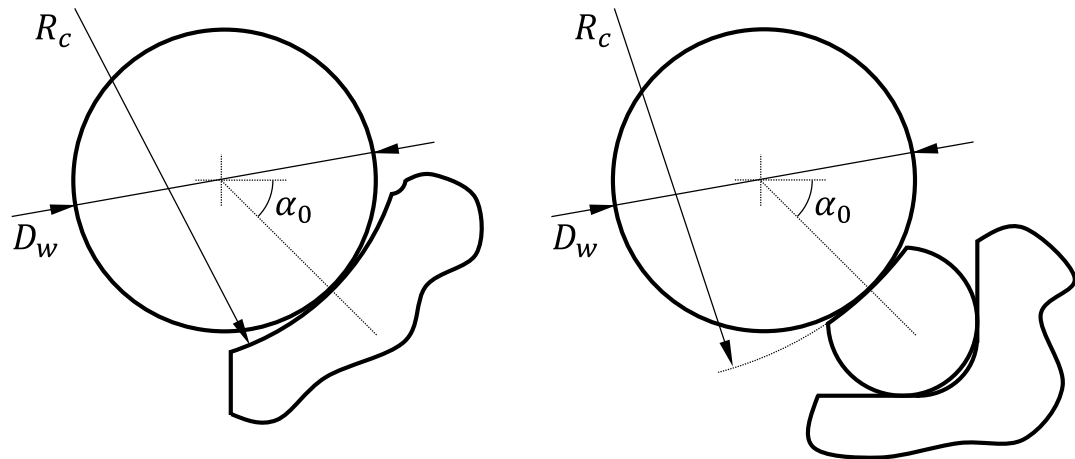
Figure 1.5 Ball-raceway contact geometry parameters.

Once the bearing components have been introduced, it would be convenient to classify the slewing bearings according to the employed rolling element. The proposed classification falls very short considering the number of existing slewing bearing designs. Nevertheless, some of the most popular bearing types are going to be mentioned.

Generally, the most popular are the four-point contact slewing bearings and the crossed roller slewing bearings, both represented in Figure 1.6. Four-point contact slewing bearings are widely used because of their versatility, low friction torque and reduced cost in comparison with other bearing types. Crossed roller slewing bearings offer greater stiffness and static load capacity, but involve larger friction torques and manufacturing costs.

The number of rows is another key aspect to take into account. More than one row of rolling elements can be considered in order to increase the capacity of the bearing. Regarding ball bearings, two rows can be arranged with two or four contacts on each ball. In the case of roller bearings, two or even three rows can be used to deal with particularly high loads. These configurations are shown in Figure 1.7.

When the design specifications are restrictive in terms of weight and the application does not demand high stiffness values, light series (also known as profile bearings) or custom made rings are more suitable (Figure 1.8).
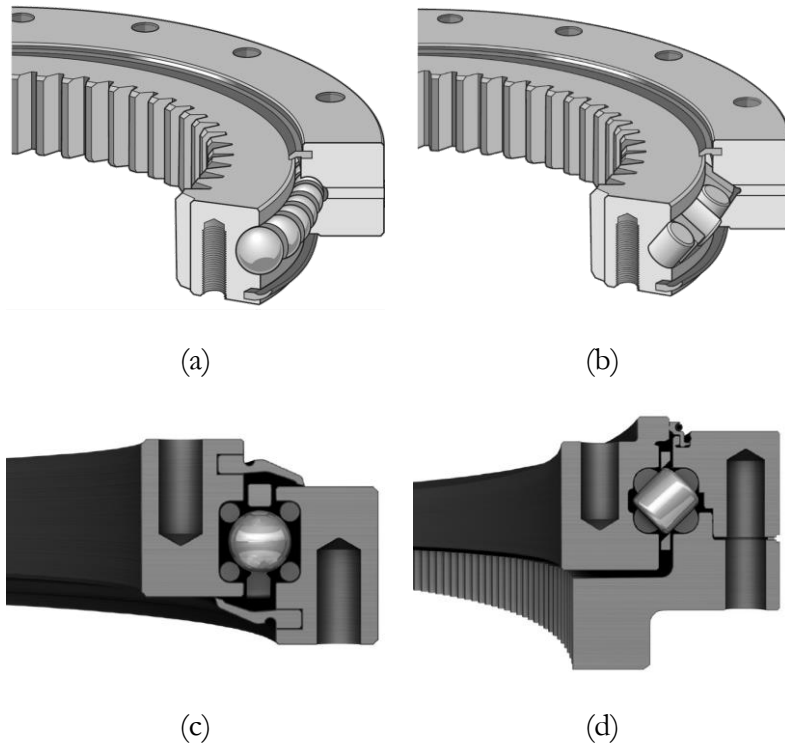
Figure 1.6 Slewing bearing types: (a) Four-point contact [23]; (b) Crossed roller [23]; (c) Four-point contact wire-race [2]; (d) Crossed roller wire-race [2].
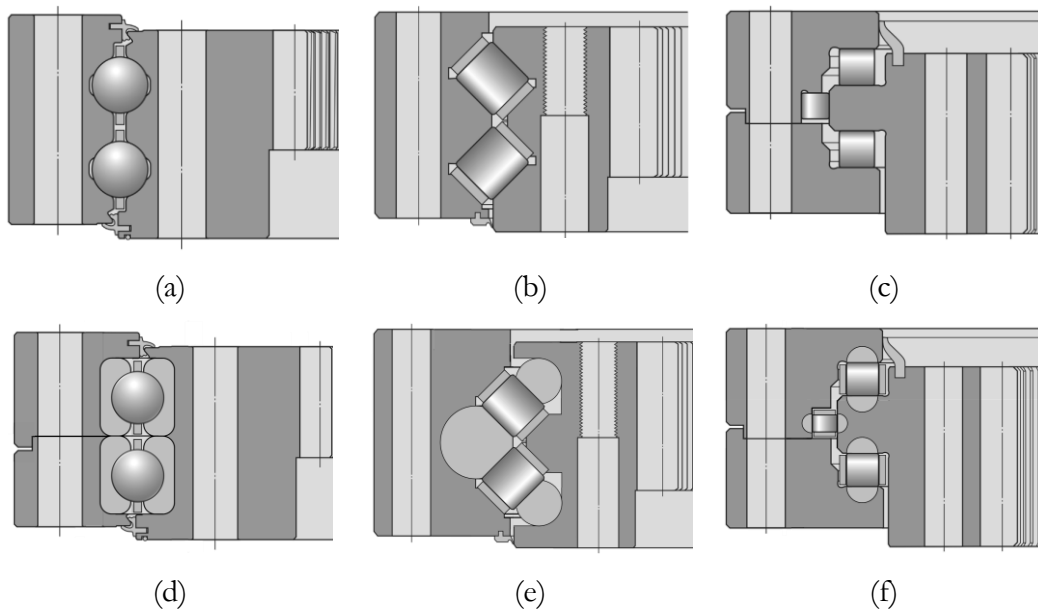
Figure 1.7 Slewing bearing types: (a) Eight-point contact double row ball [23]; (b) Double row roller [23]; (c) Three row roller [23]; (d) Four-point contact double row ball wire-race; (e) Double row roller wire-race; (f) Three row roller wire-race.
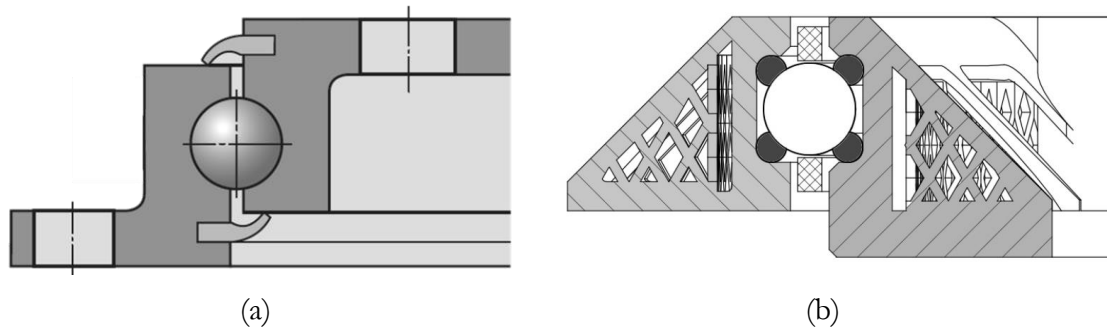
Figure 1.8 (a) Light series slewing bearing [23]; (b) 3D printed rings wire-race bearing [1].

1.3 Slewing bearing selection criteria

There are several parameters based on the operating performance that measure the capabilities of a bearing. These aspects are the base of the design or selection criteria of a slewing bearing for a specific application, and they are explained in detail in this section.

1.3.1 Static load carrying capacity

Static load carrying capacity is closely related with permanent contact deformations. Permanent deformation in raceways and rolling elements occurs even under light loads, but experience has shown that it has little effect in bearing operation under a certain limit. This limit of permanent deformation is proposed in the ISO-76 [24,25] standard and universally accepted in literature as 0.0001 of the rolling element diameter in the contact centre of the most loaded element. This degree of permanent deformation can be tolerated in almost all bearing applications, but beyond that value, noise and vibrations increases and under poor lubrication surface fatigue can appear. Nonetheless, contact permanent deformations are difficult to measure or calculate; for that reason, it has been stated in the ISO-76 standard that this limit of permanent deformation happens when the contact stresses obtained from a linear elastic calculation reach a certain value for each bearing type in a linear elastic calculation, which are shown in Table 1.1.

Table 1.1 Contact stress that causes 0.0001 rolling element diameter permanent deformation.

Bearing Type	Contact Stress
Self-aligning ball bearing	4600 [MPa]
Other ball bearings	4200 [MPa]
Roller bearings	4000 [MPa]

However, maximum contact pressure is not a practical indicator when it comes to the calculation of the static load capacity. For that reason the ISO standard also proposes two simplified formulas to obtain the axial and radial static load capacity (C_{0a}, C_{0r}), but none for the tilting moment. Moreover, these formulas were developed under certain simplifications, assuming for example, that the contact angle does not vary with the applied load and that the flexibility provided by rings or the surrounding structures has no effect. As an example, Equation (1.1) and Equation (1.2) are proposed to calculate the axial static load capacity of thrust ball and roller bearings respectively. Where N_B and N_R are the number of rolling elements, f_0 is a tabulated value and L is the contact length.

$$C_{0a} = f_0 \cdot N_B \cdot D_w^2 \cdot sin(\alpha_0) \tag{1.1}$$

$$C_{0a} = 220 \cdot \left(1 - \frac{D_w \cdot cos(\alpha_0)}{D_{pw}}\right) \cdot N_R \cdot L \cdot D_w \cdot sin(\alpha_0) \tag{1.2}$$

The standard was conceived for conventional bearings, which have reduced dimensions and completely hardened rings. Because of their dimensions, conventional slewing bearing raceways can only be induction hardened, leaving the remaining ring material soft. This difference in the material properties can lead to a failure mode called core crushing, which consists in sub-surface crack nucleation. This phenomenon was studied by Lai et al. for the ball-raceway contact [26] and Göncz et al. for the case of roller-raceway contact [27]. Core-crushing is not a problem in wire bearings, since the whole wire is hardened [2,4,28,29] and the ring does not receive thermal treatment. Nevertheless, the standards have even more limitations when it comes to application to wire-race slewing bearings.

Another phenomenon related with the static failure of the bearing that affects both ball conventional and wire-race slewing bearings is the contact ellipse

truncation. It is known that the contact angle tends to increase or decrease depending on the applied load. If the applied load is too high, the rings are too flexible or the surrounding structures are not stiff enough, the ball can climb over the raceway in such a way that the contact ellipse reaches the limits of the raceway. This situation leads to a free edge effect that generates a stress concentration near the edge far greater than the admissible one, as seen in Figure 1.9. Besides, the pressure at the centre of the contact also rises due to the contact area reduction. In order to avoid this phenomenon in the design stage, FE analysis or analytical tools can retrieve the evolution of the contact along the most demanding loading process. There is no standard measure to assess when this phenomenon happens exactly, but it can be established that truncation occurs when the contact ellipse reaches the raceway edge.
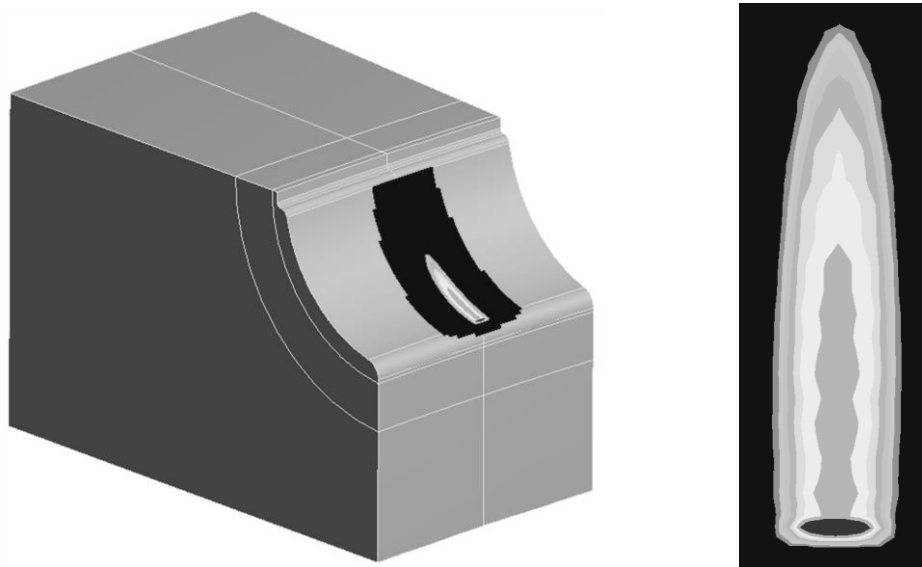
Figure 1.9 Truncation of the contact ellipse.

From the roller bearings point of view, truncation as it has been described does not occur. However, the nature of the roller-raceway contact may generate stress concentrations in the vicinity of the cylinder edges. These stress concentrations are called free edge effects, which generate an abrupt local stress rising that transforms the ideal contact area into a "dogbone" shaped one (see Figure 1.10a). In order to prevent this behaviour, it has been proven that the best practice consists on applying a geometry correction to the roller profile. Four different roller profile examples are presented in Figure 1.10, where the contact patch and the pressure distribution along the major axis are compared. The "dogbone" contact area and relevant edge effects only appear for the straight profile roller, while the corrected roller profiles present smoother pressure distributions. Figure 1.11 represents a more realistic case, where FE

results for a heavy loaded crowned roller are shown. It can be observed that the edge effects and the "dogbone" contact area can also appear in a corrected roller profile under heavy load circumstances. For this reason, the roller profile design is crucial for preventing or delaying early edge effects, but they may arise under eventual high loads.

The election of the proper roller profile has a significant effect not only on the static load capacity but also on the wear damage and the fatigue life. For that reason, ISO/TS 16281: 2008 standard [30] provides a logarithmic roller profile equation (Figure 1.10c).
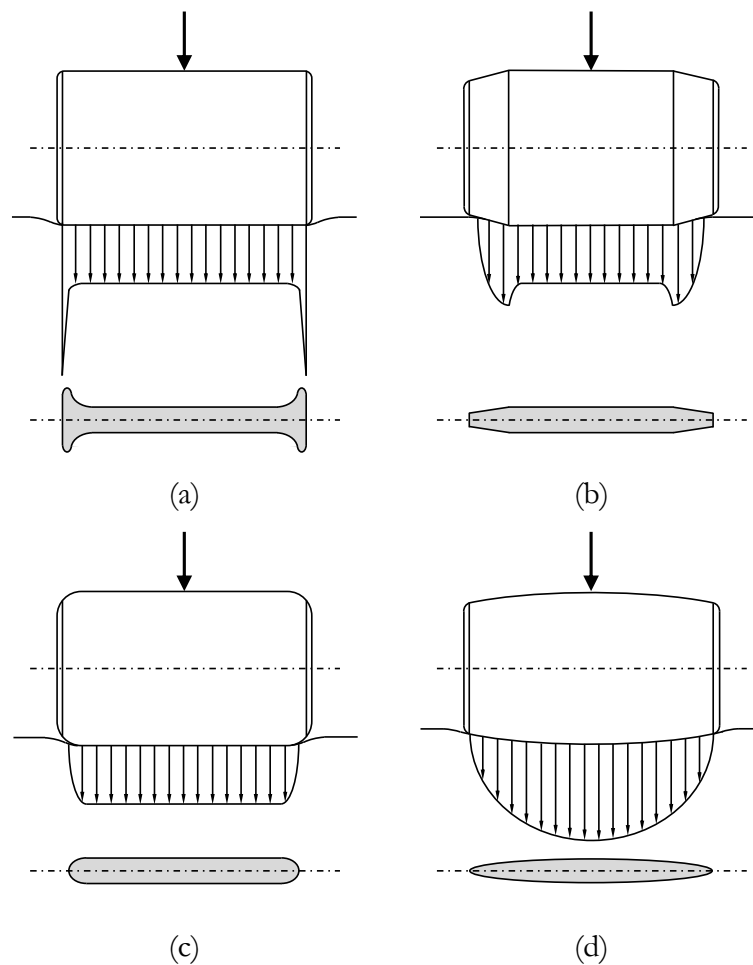
Figure 1.10 Contact pressure patch and distribution along the major axis for different roller profiles: (a) Straight; (b) Partially crowned; (c) Logarithmic profile; (d) Fully crowned.
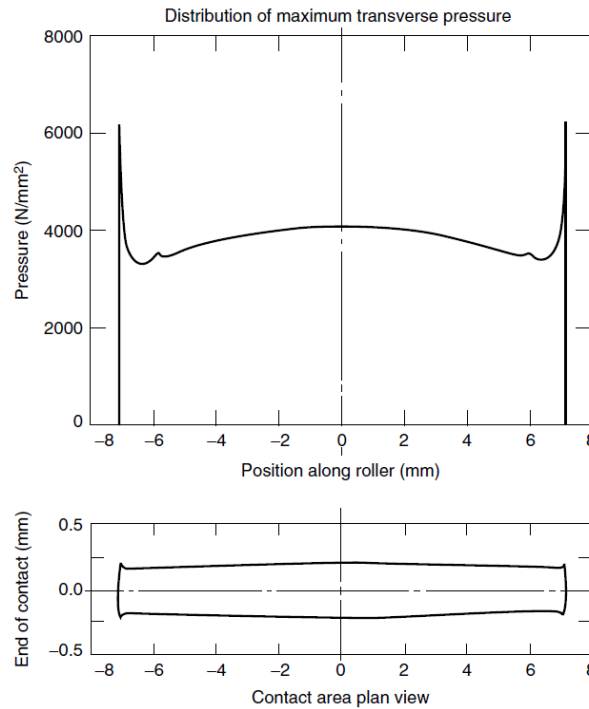
Figure 1.11 Heavy loaded crowned roller bearing contact [31].

1.3.2 Stiffness

Stiffness can be defined as the relationship between the applied force and the consequent deformation in that direction. There are no specific design criteria regarding bearing stiffness, but stiff components are usually preferred since they stay in position under high loads and minimize the possibility of interfering with other structures. This is valuable data for manufacturers and customers in the design stage in order to know how the bearing is going to behave under certain loads and how it affects the performance of the whole structure or machine assembly.

Providing a reliable stiffness data is not easy because it depends on the surrounding structures [32]. It is highly recommended to be very careful with the stiffness data and take into consideration the boundary conditions and assumptions made for its calculation. An overestimated bearing stiffness can lead to unsafe designs and potential failures. Nevertheless, bearing stiffness can be obtained by means of Finite Element analysis or analytical model calculations within their limitations.

1.3.3 Friction torque

Friction on lubricated or non-lubricated rolling contacts is considerably lower than on sliding contacts; for that reason, rolling bearings retrieve much less

friction in comparison with most fluid film or journal bearings. Friction of any magnitude slows the motion and results in energy loss that causes an increase in the temperature and in rolling bearings can be measured as a friction torque. Friction torque is the required applied moment in the hoop direction that makes the relative movement between rings possible. Depending on the bearing type, the friction source can be different, but the principal causes under load are the sliding motions in the deformed rolling contacts [31].

A low friction torque is desirable for many reasons, such as cheaper actuation systems and more durability due to the lower loads in the kinematic chain. However, despite the beneficial structural properties that retrieves the preload, the friction torque is also increased. For that reason, it is important to reach an equilibrium between preload values and friction torque.

Correct estimation of the friction torque of the bearing is crucial to design the actuation system and have better control over the rotation. For that reason, the estimation of the friction torque is a research field in itself. On the one hand, manufacturers usually provide simple formulas with many limitations to obtain this parameter. On the other hand, a lot of research work has been published with regard to this topic proposing analytical formulations.

1.3.4 Dynamic load carrying capacity and fatigue

The working principle of a rolling bearing is closely related with its fatigue life. The rotational movement of the rolling elements generates pulsating loads over the raceways, so even a stationary load applied to a running bearing will generate a fatigue failure. In real operating conditions, a bearing has to withstand varying load magnitudes in different directions while rotating at fluctuating speeds. These changing conditions can result in a longer or shorter bearing life because of wear or fatigue. It is impossible to predict all the loads the bearing will be subject to during its life cycle; for that reason, simplified procedures are provided by manufacturers [33–36] and standard organizations [30,37–39] to estimate the bearing life. These procedures consider several bearing constructive parameters, such as the geometry or the surface finish, structural parameters, such as the static load capacity, and operational parameters, such as the loads, the lubrication and the environmental conditions. These procedures were developed for conventional bearings, at continuous running speeds and under hydrodynamic lubrication assumption. Therefore, they present limitations when it comes to its application to slewing bearings, where the rotation is oscillatory and not continuous, thus affecting not only the

way the stresses vary in loaded areas but also the lubrication regime. Needless to say, more limitations arise when applying these procedures to wire-race slewing bearings. Nevertheless, research is being carried out in this area to obtain new estimation procedures according to the slewing bearings characteristics, as explained in the following section.

1.4 Slewing bearings literature review

In this section, a brief literature review of the fundamentals and state of the art research in the scope of conventional slewing bearings is presented. As the research carried out for these kind of bearings is more extensive, it was considered appropriate to place this section prior to the wire race bearing literature review, which can be found afterwards.

As it has been previously introduced, there are standard procedures for the calculation of bearings such as ISO-76 [24,25] and ISO-281[37–39], but they are only suitable for conventional bearings. Other well accepted and referenced work are the books published by Harris and Kotzalas [31,40], which are the most extensive guidelines in bearing design, taking into account many aspects that do not appear in the standards. Nevertheless, many of the contents are also only suitable for conventional bearings and not for slewing bearings. To try to solve these limitations, Harris et al. developed a guideline for the design of wind turbine jaw and pitch bearings for the National Renewable Energy Laboratory of the U.S. Department of Energy (NREL) [41]. Despite this work was specifically conceived for slewing bearings and deals with many of the limitations other works, it can only be applied for wind turbine bearings or other ones that operate under similar conditions. There are some other limitations, with the following being the most relevant:

- Ring flexibility: the deformation of the rings is not taken into account or even mentioned in the document.
- Tilting moment: the consideration of this load is a clear improvement with respect to the standards. Nevertheless, its representation in a simpler way leads to some limitations for the static load capacity and friction torque calculation.
- Contact preload and clearance: rolling element preload or eventual contact clearances generated by manufacturing errors are not considered. These parameters have a significant effect on the structural behaviour of bearings and are commonly used in the design of slewing bearings.

Regarding manufacturers, they have their own guidelines and methodologies to design and calculate bearings. This knowledge is part of their own know-how and they are quite wary of sharing details of these procedures. They only provide some characteristics and properties of their own products in catalogues.

Due to the limitations of the current standards, the confidentiality of the manufacturers and the lack of specialized literature, slewing bearings are a growing and interesting topic for the research community. Some of the most relevant and latest research works in this area related to the scope of this thesis are presented in this section.

1.4.1 Normal contact problem

The study of the tribology and contact mechanics is probably the most important area in the field of bearings. In this regard, the normal contact problem is usually the first issue to deal with.

The most relevant contacts in the scope of bearings are the ball-raceway and the roller-raceway contacts. These contacts are represented in Figure 1.12 and because of the shape of the contact pressure distribution, they are commonly called point contact and line contact respectively. For the sake of clarity, this section is divided in two parts, one for the literature review of each contact type.
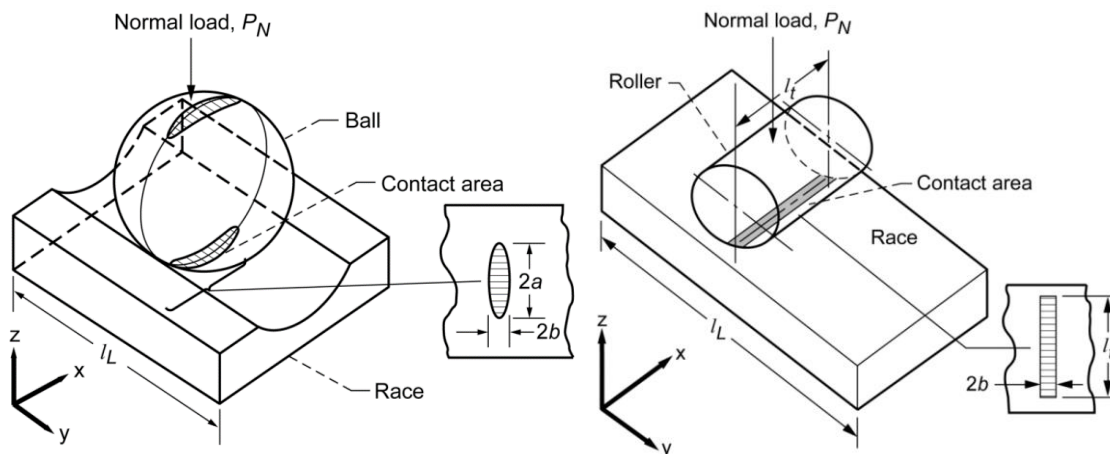
Figure 1.12 Ball and cylindrical roller raceway contacts [42].

Point contact

The most remarkable contribution regarding the point contact was developed by Heinrich Hertz in 1896 [43,44], where he proposed a contact theory for non-conformal elastic solids. For this theory, Hertz considered the following assumptions:

- The deformations are within the elastic limit and small in comparison with the curvature radii of contacting surfaces.
- The dimensions of the contact area are very small in comparison with the dimensions of contacting bodies or the curvature radii of the surfaces.
- Contacting surfaces are non-conformal and smooth (with no roughness).
- There is no friction, so only normal forces are present in the contact.
- The materials of both contacting bodies must be isotropic.

In the case of ball bearings, the ball-raceway contact does not comply with all of the aforementioned assumptions. As it can be seen in Figure 1.12, the contact is conformal in the radial plane (the xz plane) but non-conformal in the circumferential direction (y axis). This leads to a small contact area in the circumferential direction but to a large one in the radial direction that can be the order of the curvature radii. Besides, friction exists on this contact. Nevertheless, Pandiyarajan demonstrated via FE simulations that Hertz's theory can be applied to large ball bearings since it obtains good results [45]. Hertz contact theory is not simple and includes calculations that require solving elliptic integrals. In an attempt to provide an engineering approach, Brewe and Hamrock [46] applied a linear regression by the least squares method on the geometric variables of Hertz's equation. They proposed simplified equations to calculate the major and minor contact ellipse semi-axes (a, b) and the normal contact deformation (δ). Equations (1.3) to (1.5) are the proposed expressions for the calculation of these results assuming both steel contact bodies, where Q is the normal contact force, $\Sigma\rho$ is the sum of the curvatures and a^*, b^* and δ^* are dimensionless parameters that are tabulated.

$$a = 0.0236 \cdot a^* \cdot \left(\frac{Q}{\Sigma\rho}\right)^{1/3} \tag{1.3}$$

$$b = 0.0236 \cdot b^* \cdot \left(\frac{Q}{\Sigma\rho}\right)^{1/3} \tag{1.4}$$

$$\delta = 2.79 \cdot 10^{-4} \cdot \delta^* \cdot Q^{2/3} \cdot \Sigma\rho^{1/3} \tag{1.5}$$

Houpert also developed an engineering approach avoiding the elliptical integrals for ball-raceway contacts [47]. In this work, it was stated that the ratios a/R_y, b/R_y, δ/R_y and P_{max}/E can be approached for the point contact case with the same functional form; with R_y being the equivalent radius in the rolling direction, P_{max} the maximum contact pressure and E' the equivalent elastic modulus. This functional form is represented in Equation (1.6), where Y

represents the aforementioned relationships, $Cte1$ and $Cte2$ are tabulated constants, k is the ratio of equivalent radius and W_{PC} the dimensionless load. In this case, $Cte1$ and $Cte2$ values depend on the type of the bearing (ball, spherical roller or tapered roller) and on k and Y. In comparison with the work proposed by Brewe and Hamrock [46], this alternative is more efficient, since the tabulated constants are less and application is less tedious. In the case of the point contact, $Cte1$ and $Cte2$ can have two different values for each ratio depending on the value of the osculation ratio (low or high).

$$Y \approx Cte1 \cdot k^{Cte2} \cdot W_{PC}^{2/3} \qquad (1.6)$$

$$\frac{1}{E'} = \frac{1}{2} \cdot \left(\frac{1-v_1^2}{E_1} + \frac{1-v_2^2}{E_2} \right) \qquad (1.7)$$

$$k = \frac{R_y}{R_x} \qquad (1.8)$$

$$W_{PC} = \frac{Q}{E' \cdot R_x^2} \qquad (1.9)$$

These formulations applied to the ball-raceway normal contact provide good results and its application is commonly accepted in literature. In another work, Houpert proposed a similar approach for non-hertzian contacts, although it has no application to slewing bearings [48].

Line contact

The contact involving cylindrical bodies is a special case of hertzian contact called line contact. It is considered as a line contact, the contact between two parallel-axis cylinders of infinite length and the contact between a cylinder of infinite length and an elastic half-space. If the bodies of each case are compressed, each infinitesimal cross-section of the bodies behaves the same (plain strain assumption). Besides, the resulting contact patch is a rectangle with an infinite side. Because of the length difference between its dimensions, this kind of contact is commonly called line contact. The transformation from point contact to line contact can be made considering that one of the two curvature radii on each contacting body is infinite for two contacting parallel cylinders, and the two curvature radii of one body in the case of cylinder-elastic half-space contact. Doing so implies singularities according to Hertz's formulation, so he did not derive the formulation to the cylinder-elastic half-space case. The

contact deformation (δ), relative to a point on the z-axis at a depth of d_0, is given by Equation (1.10)[49]. Where L is the length of the contact.

$$\delta = \frac{Q}{L} \cdot \left[\frac{(1 - \nu^2)}{\pi \cdot E} \right] \cdot \left[2 \cdot ln\left(\frac{d_0}{b} \right) - \frac{\nu}{(1 - \nu)} \right] \tag{1.10}$$

It can be noted that if d_0 increases without a limit, so does δ. This means that the line contact between a cylinder and an elastic half-space requires the definition of an appropriate depth of reference (d_0) at which the local deformation is assumed null, which varies depending on the author. Various approximations to these problem have been developed over the years, with the Prescott [50], Thomas and Hoersch [51] and Lundberg et al. [52] works being the early studies on the cylinder to cylinder contact.

Some of the first strategies followed to represent the behaviour of the line contact consisted in obtaining empirical formulas based on experimental results. Good examples are those developed by Lundberg [53], Eschmann [54] and Palmgren [55] (Equations (1.11), (1.12) and (1.13) respectively, where L is the length of the contact). The first two formulae are valid for the cylinder-plane contact and the one proposed by Palmgren for crowned roller-raceway contact. These expressions are simple but not so versatile, since both contacting bodies were assumed to be made of steel.

$$\delta = 3.95 \cdot 10^{-5} \cdot \frac{Q^{0.9}}{L^{0.8}} \tag{1.11}$$

$$\delta = 4.05 \cdot 10^{-5} \cdot \frac{Q^{0.925}}{L^{0.85}} \tag{1.12}$$

$$\delta = 3.84 \cdot 10^{-5} \cdot \frac{Q^{0.9}}{L^{0.8}} \tag{1.13}$$

Years later, the formulae that can be found in the reports provided by Puttock [56] and Norden [57] are still widely used today. These formulae are based on the pressure distribution for elliptical contact, assuming that one axis of the ellipse is infinitely large ($R_x = \infty$) and the contact area is a rectangle whose length is much larger that its width. Puttock defined the line contact case between a cylinder and a plane of different materials represented in Figure 1.13 with Equation (1.14).
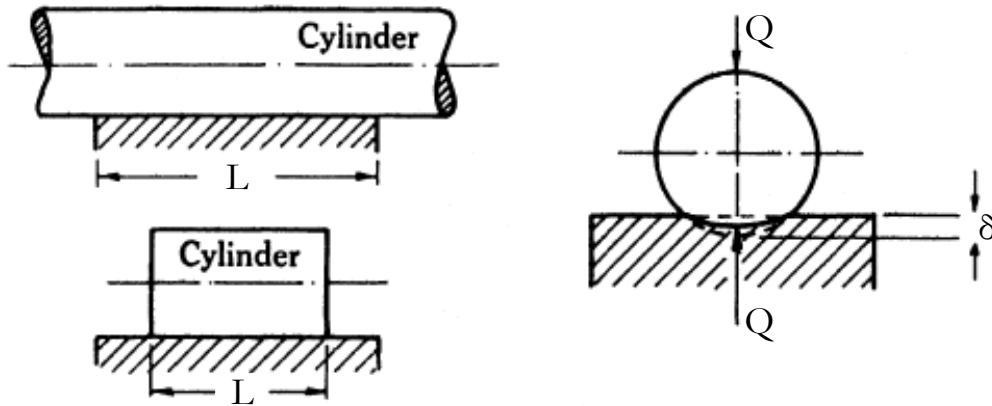
Figure 1.13 Cylinder-plane contact defined by Puttock [56].

$$\delta = \frac{Q}{L} \cdot (V_1 + V_2) \cdot \left[1 + \ln\left(\frac{L^3}{(V_1 + V_2) \cdot Q \cdot R_y}\right)\right] \qquad (1.14)$$

$$V = \frac{(1 - \nu^2)}{\pi \cdot E} \qquad (1.15)$$

Tripp [58] gathered the more frequent contact expressions based on Hertz theory, with Equations (1.16) and (1.17) being the deformations of the elastic half-space and the cylinder respectively. The reference depth d_0 is assumed to be constant and fixed as $2 \cdot R_x$.

$$\delta_1 = \frac{2 \cdot (1 - \nu_1^2) \cdot Q}{\pi \cdot E_1 \cdot L} \cdot \left[\ln\left(\frac{2 \cdot d_0}{b}\right) - \frac{\nu_1}{2 \cdot (1 - \nu_1^2)}\right] \qquad (1.16)$$

$$\delta_2 = \frac{2 \cdot (1 - \nu_2^2) \cdot Q}{\pi \cdot E_2 \cdot L} \cdot \left[\ln\left(\frac{4 \cdot R_x}{b}\right) - \frac{1}{2}\right] \qquad (1.17)$$

$$b = 2 \cdot \left(\frac{R_x \cdot Q}{\pi \cdot E' \cdot L}\right)^{1/2} \qquad (1.18)$$

Johnson [59] and Hamrock [60] provided another form of force-deformation relationship for the cylinder-plane contact, where there is a constant term that these authors determined to be equal to 1. The proposed relationship to obtain the contact deformation is defined in Equation (1.19), where W_{PC} is the "dimensionless load" of Equation (1.20) and E' the equivalent elastic modulus of Equation (1.7).

$$\delta = \frac{2 \cdot W_{PC} \cdot R_x}{\pi} \cdot \left[ln \left(\frac{2 \cdot \pi}{W_{PC}} \right) - 1 \right] \tag{1.19}$$

$$W_{PC} = \frac{Q}{L \cdot E' \cdot R_x} \tag{1.20}$$

In the previously mentioned work [47], Houpert developed the formulation proposed by Tripp [58] to create specific force-deformation relationships for raceway-roller contact. Once again, the curve fitting strategy allowed for simpler formulae. These force-deformation relationships are represented in Equations (1.21) and (1.22) for the outer raceway-roller and inner raceway-roller contacts, respectively. Where β and γ_0 are coefficients obtained with geometrical parameters and t is the thickness of the outer race section.

$$Q \approx 0.2723 \cdot E \cdot L \cdot \left(\frac{cos(\beta)}{D_{pw}} \right) \cdot \delta^{1.074} \tag{1.21}$$

$$Q \approx 0.27835 \cdot E \cdot L \cdot \left(\frac{1 + \gamma_0}{t} \right) \cdot \delta^{1.078} \tag{1.22}$$

Harris and Kotzalas [31] suggested Equation (1.23) to obtain the steel-steel contact pressure (σ) at any point of the contact patch width (y).

$$\sigma = \frac{2 \cdot Q}{\pi \cdot L \cdot b} \cdot \left[1 - \left(\frac{y}{b} \right)^2 \right]^{1/2} \tag{1.23}$$

$$b = 3.35 \cdot 10^{-3} \left(\frac{Q}{L \cdot \sum \rho} \right)^{1/2} \tag{1.24}$$

In all the works presented until this point, it was assumed that the line contact was infinite. Consequently, free edge effects were not considered. Because of the significant rise in the contact pressure that can lead to the static failure, Najjari and Guibault [61] proposed a semi-analytical method to estimate the stress distribution on the surface and subsurface. Qiang and Popov [62] also developed an analytical equation that solves the normal contact problem by approximating numerical results from Boundary Element Method (BEM) analyses. All these endeavours are valuable contributions to get to know this phenomenon; however, it has been proved that the best practice to avoid free edge effects consists in applying a geometry correction to the roller profile.

To this regard, the logarithmic roller profile proposed in the ISO/TS 16281: 2008 standard [30] is quite similar to the expression developed by Lundberg in [63]. Some researchers such as Johns and Gohar[64] proposed improvements to Lundberg's logarithmic profile. Based on that work, Fujiwara et al.[65] offered a new approach that prevents the eventual edge loading caused by misalignment. Recently, Tudose [66] presented a procedure to find the optimal roller profile. However, sometimes it is not feasible to apply the optimal solution, so a simpler partially crowned profile was also proposed.

1.4.2 Load distribution

When external loads are applied to one bearing ring, reaction forces appear in the other as a result of load transmission through the rolling elements. The purpose of a load distribution model is to calculate how the external applied loads, as shown in Figure 1.14, are distributed among the rolling elements. The load distribution is the initial step for further calculations such as the static load capacity or the friction torque under a combined load case. Because of the amount of research works carried out regarding this topic, this section is divided into two parts. Literature review is firstly introduced for ball bearings and secondly for roller bearings.
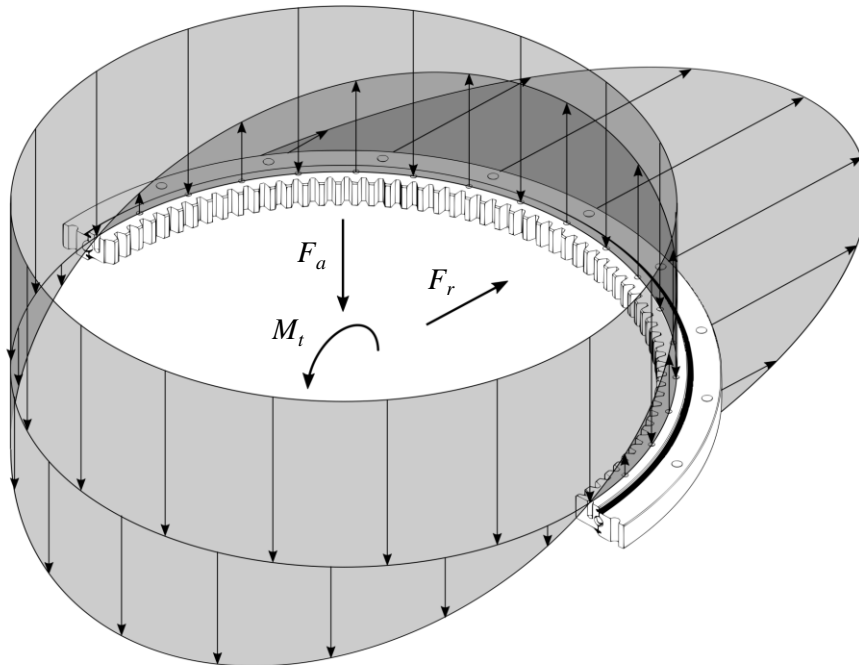
Figure 1.14 Combined external loads applied on a slewing bearing [18].

Ball bearings

An early approach to solve this problem for conventional ball bearings was provided by Stribeck in [67–69]. Later, Sjoväll [70] presented a group of load-distribution integrals to obtain the load among the balls when a combination of axial and radial loads is applied to the bearing. Jones [71,72] proposed a model for radial bearings that considered any kind of external load, but consisted of a highly significantly non-linear equation system that required numerical methods to find a solution. Soon after, Rumbarger [73] introduced another method for thrust bearings that considered a combination of axial load and a tilting moment generated by an eccentric load. Many years later, Houpert [74] proposed a novel analytical approach to solve the load distribution problem considering 5 race relative displacements (3 translations and 2 tilting angles). Zupan and Prebil [75] applied the formulation proposed by Jones to four-point contact slewing bearings and studied the effect of some geometrical parameters and the stiffness of the surrounding structures in the static load capacity. To take into consideration ring deformations, an FE model was used to obtain the equivalent stiffness values in axial and radial directions, which were implemented in the analytical model. Later, Jones' approach was also adapted by Amasorrain et al. [76] for four-point contact bearings and a procedure was proposed by Olave et al. [77] to implement ring deformations. It is worth mentioning that the cited models did not consider any initial preload or clearance. Aguirrebeitia et al. [8] proposed a procedure for four-point contact slewing bearings that calculates the load combinations that result in static failure. Later, some improvements such as the variation of the ball-raceway contact [11] and ball preload [13] were added to the four-point contact slewing bearing model.

In recent years, the influence on the performance of manufacturing errors has been a subject of research. Starvin and Manisekar [78] and Aithal et al. [79] performed FE simulations of large diameter angular bearings with manufacturing errors. It was proven that manufacturing errors can significantly affect the load distribution among the rolling elements. In this sense, Potočnik et al. [80] presented a calculation approach to obtain the contact load distribution and static load capacity of ball bearings with irregular geometry, clearances or ring deformations. Heras et al. [16,18] also proposed a methodology for the calculation of the load distribution problem on four-point contact slewing bearings, where ball preload, manufacturing errors and ring flexibility can be considered for the calculations.

Roller bearings

Regarding the load distribution problem in roller bearings, the previously mentioned methodology proposed by Sjoväll [70] was also valid for roller bearings. Later, Lundberg [81] used the integrals proposed by Sjoväll to evaluate the maximum rolling element load. Jones [72] and Houpert [74] also considered roller bearings in their analytical models. In a more recent study, Oswald et al. [82] evaluated the influence of negative and positive clearance on bearing life, developing a procedure for the calculation of the roller load distribution based on Sjoväll's equations. Aguirrebeitia et al. [9] presented a unified approach to solve the load distribution problem for ball and crossed roller bearings. A similar approach was also proposed for three-row roller bearings [12].

All the aforementioned load distribution models for roller bearings did not consider the effect of manufacturing errors. Chen et al. [83] studied the influence on the load distribution of the difference in the roller diameters within the manufacturing tolerance. Yu et al. [84] presented an analytical method to solve the load distribution problem in radial roller bearings with uneven roller sizes due to manufacturing errors. Later, Xiaoli et al. [85] developed a mathematical model for the calculation of the load distribution on ball and roller bearings under radial load considering positive, negative and zero clearance. Recently, Aschenbrenner et al. [86] developed a method for single row cylindrical roller bearings to determine the load distribution for the radial case considering geometrical deviations.

1.4.3 Stiffness

As it has been stated in the previous section, stiffness is an important performance indicator for the selection of the adequate bearing for a particular application. However, no procedures or methodologies for its calculation can be found in the standards or in the NREL guidelines [41]. Manufacturers generally provide stiffness curves, which are usually not included in catalogues, but the problem is that they do not specify the calculation procedure. This secrecy from manufacturers and the lack of standardized procedures to obtain stiffness curves makes it unfeasible to make direct comparisons between data provided by different manufacturers.

Early works were developed by Jones and Harris [87] and Harris and Broschard [88] for planetary gear-transmission bearings. Many years later, and based on the previous works, Mignot et al. [89] proposed a new approach. The

development of these approaches was possible because these bearings are always subjected to the same loads and boundary conditions. Besides this, the flexibility of the surrounding structures was also considered. It is a fact that each slewing bearing application has its own loads and conditions; for this reason, it is not so straightforward to develop a robust analytical approach.

Several works studied the matter of the stiffness for two-point angular contact bearings, but assuming rigid rings, that is to say, only considering ball-raceway contact deformations. Lim and Singh [90], Houpert [74], Hernot et al. [91], Liew and Lim [92] and Noel [93] are good examples. Later, Guo and Parker [94] proposed a numerical method to compute the stiffness matrix of any rolling element bearing considering ring deformations through FE analysis.

Some of the load distribution models presented in the previous section can be used to obtain the stiffness curves in four-point contact slewing bearings, such as the analytical model in [76] for rigid rings, or the semi-analytical methodology in [77] to consider global deformations. Another example can be found in the work presented by Aguirrebeitia et al. [13], where their analytical model was used to study the effect of the preload on the stiffness. The analytical tool proposed by Heras et al. [18] was also capable of performing the calculation of the structural stiffness of four-point contact slewing bearings considering not only ring flexibility but also manufacturing errors. The mentioned models are hard to implement and require numerical methods to calculate a solution. Besides, it is necessary to perform FE analyses to consider ring flexibility. Considering the difficulty of this task, a simple engineering formulation for the calculation of stiffness in four-point contact slewing bearings considering ring deformations was developed by Heras et al. [15].

The same happens for roller bearings, it is easy to adapt load distribution models to obtain stiffness curves. For example, the methodologies presented by Aguirrebeitia et al. in [9] and [12] retrieves the stiffness curves for crossed roller and three-row roller bearings respectively. The effect on the stiffness of uneven roller sizes or different clearances for a particular bearing design can be evaluated with the models proposed by Yu et al. [84] or Xiaoli et al. [85]. More recently, Heras et al. [95] proposed a straightforward methodology to calculate the stiffness in crossed roller slewing bearings, which was an adaptation of a previous work [15].

1.4.4 Friction torque

The study of the friction torque is one of the most prolific research fields in the scope of slewing bearings. Due to its relevancy, a formula for its calculation was proposed by the NREL [41]. This is a widely used calculation method, which can be found in many product catalogues because of its simplicity. The suggested formula is expressed below:

$$M_f = \mu \cdot \frac{D_{pw}}{2} \cdot \left(A \cdot \frac{M_t}{D_{pw}} + B \cdot F_a + C \cdot F_r \right) + M_{f0} \qquad (1.25)$$

Where M_t is the tilting moment, F_a is the axial load, F_r is the radial load and M_{f0} is the idling friction torque. The apparent friction coefficient μ depends on the type of bearing, being 0.003 for ball bearings with cage and 0.004 for ball bearings with spacers and cylindrical crossed roller bearings. Proposed values for A, B and C are 4.4, 1 and 2.2 respectively. However, some manufacturers use different coefficient values and have adapted the coefficient of friction to their own product series [96,97]. Despite the accepted use of this formula, it also presents several drawbacks. For example, it does not account for the contact angle variation and the rolling element preload is considered in a simplified manner. Besides, the contact area evolution is non-linear and depends on the applied loads, which affect to the friction torque.

Regarding research contributions for ball slewing bearings, Leblanc and Nélias [98,99] adapted, for four-point contact slewing bearings, the approach proposed by Jones [100] for angular contact ball bearings. In this works, a full sliding condition is assumed on the contacts and the imposed equilibrium of forces and moments allows solving the bearing kinematics. Once the load distribution problem is solved and knowing the kinematics, the friction torque can be directly computed. Later, Lacroix [101] proposed different methods to consider ring flexibility. All these works take into account inertial effects, which are negligible in slow turning velocities. For this reason, Joshi et al. [102] made a particularization for slow speed applications that simplified the calculation.

Heras et al. [16] recently studied the effect of manufacturing errors on the friction torque via FE simulations. A formula for the friction torque estimation was also proposed as a function of contact deformations and the osculation ratio. The effect of ring flexibility, preload and number of balls was also studied. Later, the same authors studied the capabilities and limitations of the analytical model developed by Joshi et al. [102] via a comparison with FE results [17].

Finally, a more efficient friction torque approach based on the previous contribution was presented [18], which involved the superelement technique.

Some research has also been carried out for roller bearings, but mainly for tapered roller bearings. In an early work, Palmgrem [55] proposed a general friction torque model including external load and operating speed. However, Palmgren's model results differed from experimental results. For that reason, Witte [103] developed a semi-empirical equation to estimate the friction torque in tapered roller bearings under axial and radial loads. Later, Aihara et al. [104] proposed an equation to obtain the running torque taking into consideration several lubrication phenomena. The efficiency of this model was improved by Zhou and Hoeprich [105] and Tong et al. [106], who combined this method with a static model that considered inner ring misalignment. Zhang et al. [107] also presented a model to calculate the friction torque in dry-lubricated tapered roller bearings considering roller skewing. Regarding manufacturing errors or contact geometry defects, Liu et al. [108] recently studied their effect on friction torque. There are also some publications regarding cylindrical roller bearings. Fernandes et al. [109] studied the effect of five similar lubricants on axially loaded cylindrical roller thrust bearings. Friction torque and operating temperatures were evaluated at different speeds. In another work, Fernandes et al. [110] performed a similar study but at a constant temperature. Results showed that the formulation of the lubricants has a significant influence on the friction torque. Gonçalves et al. [111] studied the influence of different greases on the friction torque in cylindrical thrust roller bearings. These tests were performed under constant load, varying rotational speed and different temperatures.

1.4.5 Fatigue calculation

The theory proposed by Lundberg and Palmgren [8,9] is generally accepted for the estimation of the bearing minimum life and it is also the basis of the ISO 281 standard [37] and ANSI/ABMA 9 and 11 standards [3, 4]. This theory was conceived to be applied to continuously rotating bearings and did not consider oscillating conditions. The NREL report [41] summarizes several life calculation methods and proposes a procedure for the fatigue life estimation in yaw and pitch wind turbine bearings. However, the limitations of this guideline promoted the development of specific research for slewing bearings.

Sawicki et al. [112] presented an analytical and FE approach for four-point contact slewing bearings fatigue life prediction considering bearing

deformation. Regarding manufacturing errors, Potočnik et al. [113] also considered possible geometrical irregularities on a double row eight-point contact bearing. Generally, the external loads that a bearing supports during its life are unknown or uncertain. For this reason, Portugal et al. [114] developed a fatigue model for multiaxial randomly loaded cases. This methodology was developed for machine components with particular working conditions and no specific fatigue calculation procedures, like slewing bearings. Recently, Menck et al. compared three approaches for the calculation of the equivalent loads required for the current lifetime calculation methods. Two of these approaches were obtained from the NREL DG03 [41] and the other one from the ISO/TS 16281:2008 [30]. It was proven that current calculation methods are conservative as they do not take account of the specific characteristics of slewing bearings. With all this, there is no accepted procedure for the slewing bearing fatigue life calculation yet.

In terms of contact fatigue, Poplawski [115] compared the bearing life of several roller profiles loaded against a flat surface according to different models (Weibull, Lundberg and Palmgren, Ioannides and Harris, and Zaretsky), assessing the benefits of this practice. Londhe et al. [116] studied the implications of raceway induction hardening on the subsurface stress variation and discussed its potential implications on bearing fatigue life. To the same regard, He et al. [117] studied the effect of the raceway hardened layer depth on the fatigue life of a three-row roller bearing. Schwack et al. [118] performed FE simulations and experimental tests to predict wear and frictional work on ball contacts. There are numerous studies regarding the latter area [119–122] but there are still no reliable models to predict rolling contact fatigue failure.

1.4.6 Finite element modelling

Finite element modelling of slewing bearings is not simple and entails several difficulties. One of the main problems lies in the large number of Degrees of Freedom (DoF) of the model, which involves a high computational cost. This is mainly caused by two reasons: the slenderness of the component and the need for refining on the rolling element-raceway contacts. Bearing FE simulations are also highly non-linear, where the sources of non-linearities are the frictional contacts and the large displacements. Materials are generally assumed to be linear-elastic, so this is not a usual source of non-linearity. Frictional contacts are required on rolling element-raceway contacts to properly simulate the contact behaviour and large displacements must be considered in

order to correctly reproduce the evolution of the contact areas. Reaching the convergence in this kind of simulations is also challenging. There is a large number of rolling element-raceway contacts in small areas and which suffer changes during the simulation; for this reason, it is necessary to create a refined mesh in the contact zones. Rolling elements can also lose contact during the loading process, causing convergence problems due to insufficiently constrained bodies.

All the aforementioned challenges that arise when modelling these components have promoted the development of efficient FE modelling strategies. These techniques are based on simplifications that reduce complexity with a minimum impact on accuracy. For the sake of clarity, strategies for ball bearings are introduced first, followed by strategies for roller bearings.

Ball bearings

The simplifications of the FE modelling were conceived in such a way that they not only simulate the elastic behaviour of the contact, but also the variation of the contact angle. Golbach proposed a method of this kind for angular contact ball bearings [123]. Figure 1.15a shows the proposed 4-node user-defined element that replaces the ball, which was created by a subroutine in Abaqus®. This mechanism, or user-defined element, represents the structural behaviour of the ball-raceway contacts. In order to replicate the evolution of the contact angle, each raceway centre is connected with rigid elements to two nodes located on the raceway (but not properly specified). Then, both race centres are connected with a non-linear spring that represents the stiffness behaviour of the contacts. The formulation proposed by Brewe and Hamrock [46] (Equation (1.5)) was applied to the non-linear spring element to model the force-deformation behaviour of the two non-conforming elastic bodies. Finally, the accuracy of the simplification was assessed via a results comparison with a solid meshed model with contact mesh refinements.

Years later, Smolnicki et al. also proposed another FE simplification for a double row two-point contact ball bearing [124,125]. In this case, the ball was also removed and replaced by a simplification, which consisted of two rigid beams and one non-linear elastic element that represent the structural behaviour of the contacts. As shown in Figure 1.15b, rigid beams link each raceway with its curvature centre, while the non-linear elastic element connects both curvature centres. However, the connection between the rigid beam and the raceway is not so clearly explained. The load-deformation $Q - \delta$

characteristic of the non-linear elastic element was defined in the form of Equation (1.26); where C and η are constants and which values are determined via FE analyses instead of using the formulation of the hertzian contact. It is worth mentioning that the non-linear elastic element has a traction only behaviour; this means that it represents the deformation of the contacts under load and no force is transmitted when there is no contact.

$$\delta = C \cdot Q^\eta \qquad\qquad (1.26)$$

The previous FE simplifications were valuable contributions, but the one proposed by Daidié et al. [126] is by far the most popular. The proposed method is almost identical to the one proposed by Golbach [123], but was explained more in detail and adapted for application to four-point contact ball bearings. In this case, the proposed ball simplification consists of two identical mechanisms, one for each contact diagonal (C_1, C_2 and C_3, C_4 in Figure 1.15c). The first step to build the mechanism consists of connecting the raceways centres with a traction-only spring element. The force-deformation behaviour of the spring element could be defined with Equation (1.5) or Equation (1.26), but authors considered it adequate to include the osculation ratio for this relationship. For that reason, an analytical formula was derived from the work proposed by Houpert [47].

Considering that the traction-only spring element represents the behaviour of the contacts on its diagonal, it seemed appropriated to stiffen the raceway in order to prevent redundant deformations. For this purpose, a rectangular rigid surface made of shell elements was placed on the contact zones, as shown in Figure 1.15c. The size of the rigid surface is calculated with the major and minor semi-axes of the contact ellipse (a, b), also calculated with the formulae proposed by Houpert [47].

Finally, each raceway centre is linked to its corresponding rigid shell by means of two rigid beam elements. This way, the deformation of the contacts is represented by the non-linear spring element and the force transmitted to the rings by the rigid beams and rigid shells, which prevent the raceway from suffering the deformations already taken into account by the spring element.

Ball-slewing bearings are usually designed with a high osculation ratio, so Daidié et al. developed the formulae to define the behaviour of the traction only-spring and to calculate the contact ellipse semi-axes for high osculation ratio values.

(a)

(b)

(c)
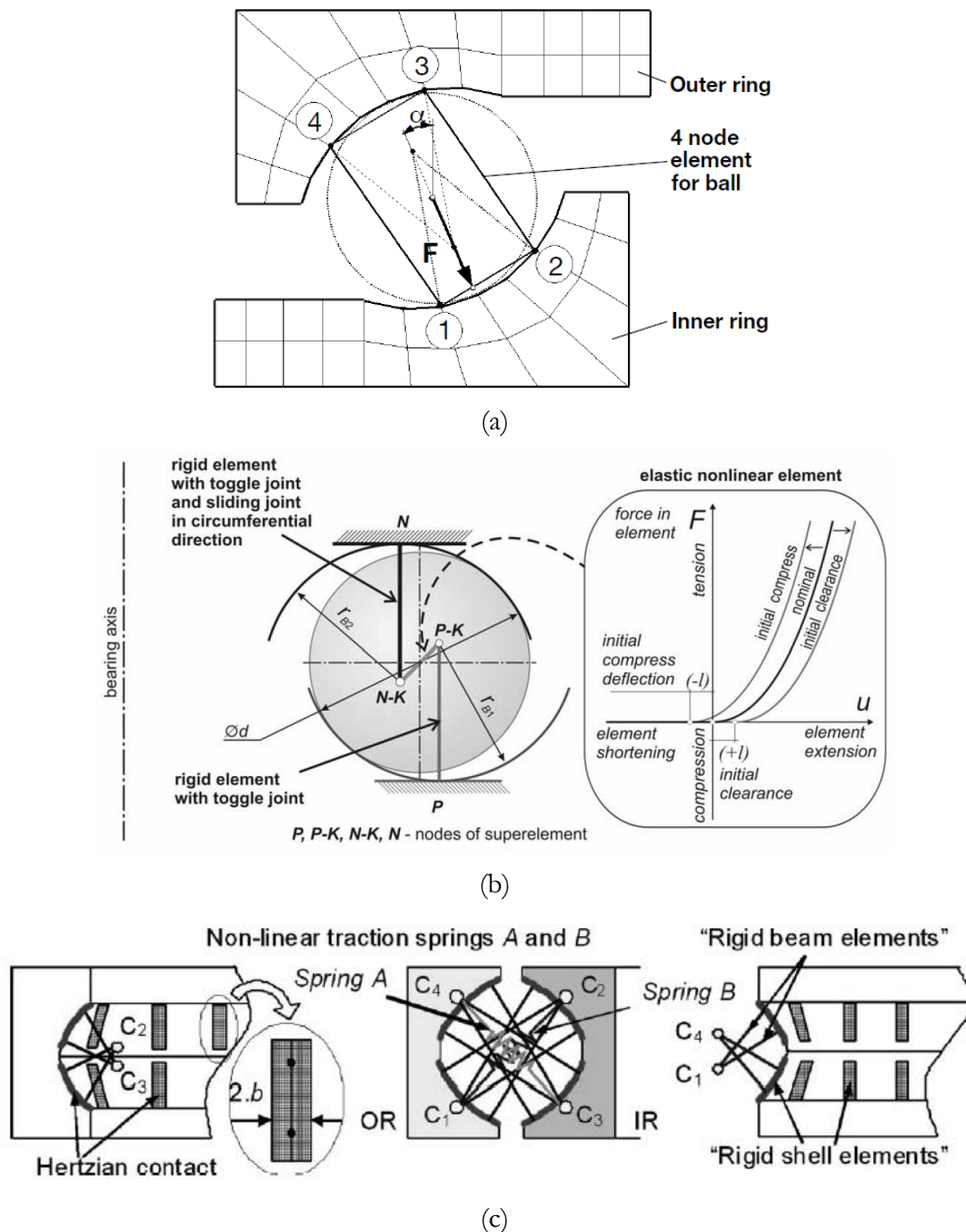
Figure 1.15 Golbach's user defined element simplification [123]; (b) Smolnicki's "superelement" [124,125]; (c) Daidié's mechanism [126].

Although the aforementioned elements used in the FE simplifications are still non-linear, rigid body motion problems caused by the loss of contact are avoided. Besides this, these techniques avoid the need to model the balls, which reduce the size of the mesh, and also avoid the need for a ball-raceway contacts definition and raceway mesh refinements. These techniques are accepted by the research community and widely used in the industry. For instance, Aguirrebeitia et al. [21] implemented Daidié's approach in a FE model to validate their

analytical model (Figure 1.16a), and proposed a method to consider ball preload by changing the length of the non-linear spring. Heras et al. [18] also implemented the mechanism in a calculation methodology involving the superelement technique for four-point contact slewing bearings. Śpiewak [127] implemented this mechanism in a two-row ball slewing bearing (Figure 1.16b) to develop a methodology to obtain the static carrying capacity. Recently, Menck et al. [128] also implemented Daidié's mechanism on a two-row ball slewing bearing (Figure 1.16c) to calculate and compare the fatigue life with different methods.

(a)

(b)

(c)
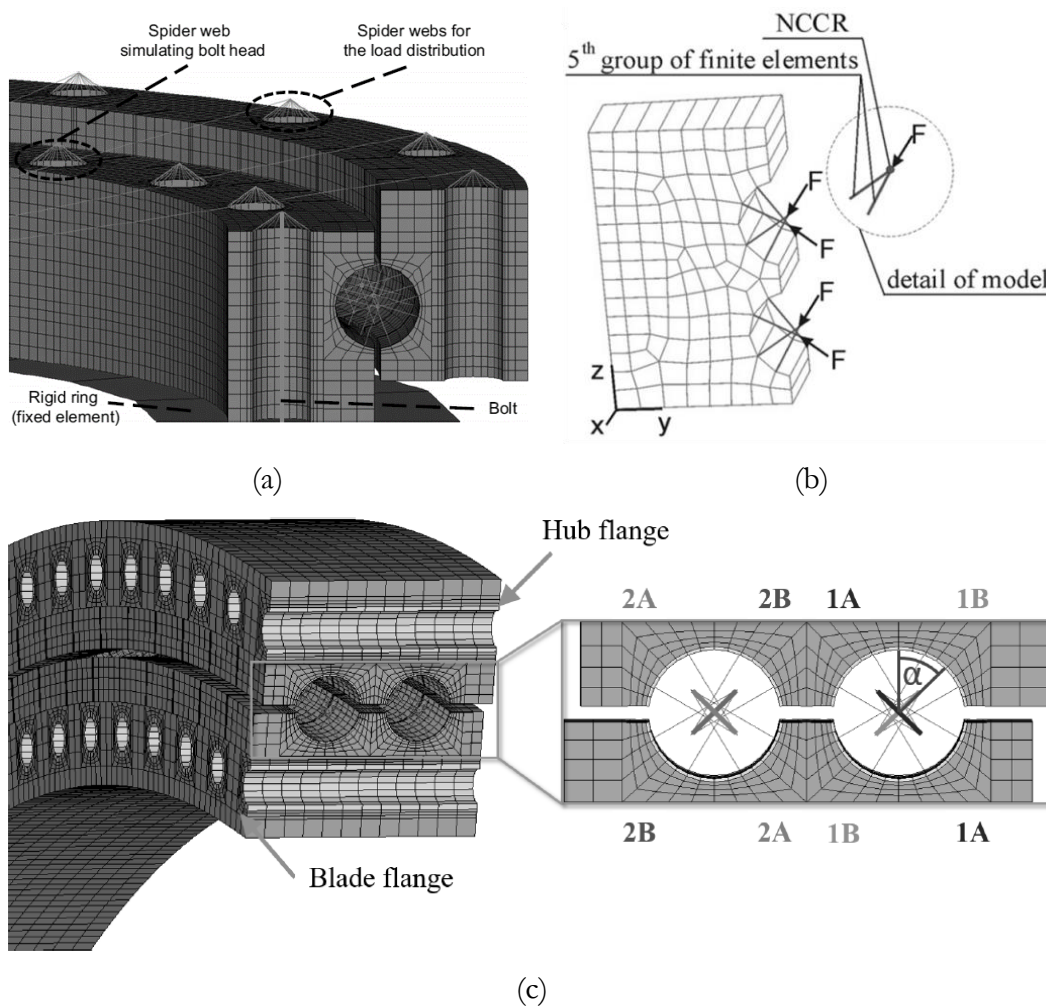
Figure 1.16 Daidie's mechanism: (a) Application on one row ball bearing [21]; (b) Application on two row ball bearing [127]; (c) Application on two row ball bearing [128].

Roller bearings

Some efficient FE modelling strategies have also been developed for roller slewing bearings. In this case, the absence of contact angle variation makes the conception of simplified FE mechanisms easier. However, it is not so easy to represent the behaviour of the roller-race contact. In his previously mentioned

work [123], Golbach also proposed a method based on a slightly crowned roller discretized into a laminae formed by two rows of n springs (Figure 1.17a). A line of rigid beam elements separates both spring rows, where each one represents the behaviour of each contact. In order to prevent possible unconstrained DoFs, the springs only transmit force in its axial direction (1 DoF). The load-deflection relationship of Equation (1.11) proposed by Palmgren [55] and included in [129] was found to be the most suitable by the author to represent the stiffness of the contacts. As there are n springs per contact, each one has $1/n$ of contact stiffness. However, if both inner and outer raceway contacts are equal, both spring rows can be combined on only one row with an equivalent stiffness. Finally, the connection between the springs and the raceway mesh is made by sharing one node on the raceway surface.

As has been specified in previous sections, roller profile geometry can be diverse. This fact may cause difficulties when it comes to representing the contact behaviour with simplified FE elements, since each roller profile retrieves a characteristic contact stiffness. To deal with this problem, Kania [130] developed a methodology where each roller is replaced by one truss (link) element. This truss element is directly connected to the raceway nodes and its mechanical characteristics are a function of the roller geometry. The methodology is divided into three stages, each one having a different purpose.

The first stage consists on the analysis of the contact zone of the roller with the raceway. The objective lies in obtaining the dependency of the approach of the bearing rings on the contact force. To this end, one FE model of the roller and raceway was performed for different roller profiles (straight, cylindrical crowned, tapered and logarithmic). The second stage is focused on determining the deformation of the raceway segment due to the placement of the truss element. To evaluate this phenomenon, a FE model of one sector of the ring raceway was built. In this model, a punctual force applied on the node where the truss element is connected to the raceway simulates its effect. Finally, the third stage calculates the equivalent deformation of the truss element as the difference between the results of stages one and two. The equivalent deformation is a key parameter for the calculation of the mechanical characteristics of the truss element depending on the roller geometry.

The methodology proposed by Kania is interesting and was carefully developed and presented. However, its practical application was not compared with results from a detailed solid-meshed FE model or experimental test, so there is no information about the accuracy of the method.

Stammler et al. [131] also proposed a roller FE simplification for the calculation of the load distribution problem in a roller-type rotor blade bearing. In order to increase the computational efficiency of the FE model, solid rollers are replaced by the mechanism shown in Figure 1.17c. This mechanism is composed by a row of four traction-only non-linear springs connected by means of rigid beams to the raceways along the rectangular contact area. The spring-beam mechanism is quite similar to that proposed by Daidié [126], but in this case there is no geometrical reason for its definition; however, this alternative was considered instead of a simple row of compression-only springs (like Golbach's simplification). According to the authors, one spring mechanism stiffens the contact but many springs result in an unstable system. Stiffness behaviour was modelled with the expressions proposed in [129] for line contacts, assessing that the comparison with contact simulations was satisfactory.

It is worth mentioning some other studies in this scope, such as the FE simplifications carried out by Molnar [132] or Claesson [133]. However, these works are not as relevant as the ones presented in this section.

(a)

(b)

(c)
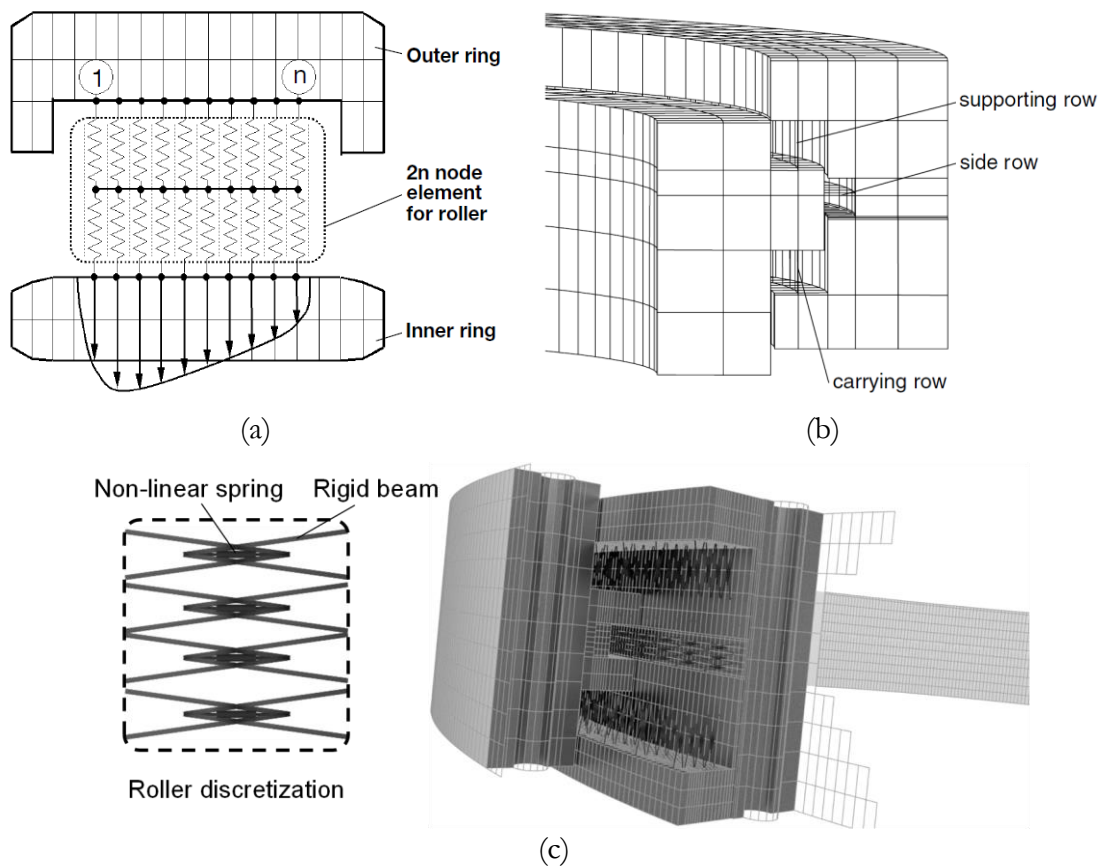
Figure 1.17 (a) Golbach's roller discretization [123]; (b) Kania's modelling [130]; (c) Mechanism proposed by Stammler et al. [131].

Recently, He et al. [117] studied the effect of the raceway hardened layer depth in the fatigue life of a three-row roller bearing. For this purpose, they implemented the roller discretization proposed by Golbach [123] on a half bearing FE model and calculated the maximum contact load. Then this load was applied on a one roller reduced FE model to study the contact stresses. As well as this, they evaluated the effect of the number of springs per roller. Four different combinations with one, two, four and eight springs were analysed, where the larger amount of springs gave the best results.

Other works

Another point of view regarding efficient FE modelling was provided by Olave et al. [77], where the superelement technique was applied to obtain a more versatile and well-founded stiffness matrix of the rings and surrounding structures. Plaza et al. in [19] also applied this technique to the bearing rings and the surrounding structures of an specific wind turbine generator in order to solve the load distribution problem. This strategy was proved to be a cost effective tool that significantly reduces the computational cost with a negligible accuracy loss. A similar method was implemented by Heras et al. [18], where the superelement technique was used to obtain the stiffness matrix of the bearing rings with the aim of implementing ring flexibility in an analytical calculation methodology.

Efficient FE models are commonly used to obtain the load distribution, stiffness, effects of the rolling element preload or bolt preload, inter alia. However, contacts are not defined in these models and some results like contact pressure distribution, truncation, friction forces, tangential or subsuperficial stresses among others cannot be evaluated. To study the behaviour of the contacts, they must be modelled using a detailed FE model. As has been mentioned, these models have more DoF and present convergence problems, such as the rolling element contact loss. This problem arises when the rings deform in such a way that the rolling elements lose contact and become unconstrained. To deal with this problem, Heras et al. [15] proposed a solution based on a very flexible cage that prevents the balls from undergoing rigid body motion.

The works mentioned in this section so far were focused on improving the computational cost and analysis convergence, but the FEM is not only a powerful tool to make bearing simulations. It can be also used to feed analytical approaches dealing with tasks that are not possible or complex to be addressed

analytically. One of these tasks, as has been mentioned, is to consider ring deformations. Zupan and Prebil [75] used FE simulations to built stiffness matrices with the flexibility of the rings and surrounding structures to feed an analytical model. Guo and Parker [94] developed a numerical method to estimate the bearing stiffness of different bearing types based on FE calculations. In terms of friction torque, Aguirrebeitia et al. [134] developed a four-point contact bearing sector FE model to measure it. The objective consisted of performing a DoE FE analysis campaign to adjust a friction torque calculation formula. This model was also used and improved by Heras at al. [16–18].

1.4.7 Experimental tests

There are numerous research works involving experimental tests with conventional bearings; however, it is more difficult to perform tests when it comes to slewing bearings. The large diameter of the majority of slewing bearings requires the use of specifically designed test rigs, which are extremely large, heavy and expensive. The most advanced ones can apply dynamic axial, radial and tilting loads while applying a rotating torque to the bearing. Besides this, surrounding structures are also, to a greater or lesser extent, represented. This allows for replicating real working conditions and performing tests introducing measured field loads. As a result, bearing deflections, wear damage and rolling contact fatigue can be accurately tested. These kinds of test rigs are located in research centres or in the facilities of the main manufacturers, mainly focussed on testing wind energy bearings. Wind power industry is currently the most powerful sector demanding this kind of component.

Test rigs like the one shown in Figure 1.18a or Figure 1.18b are commonly used by the main slewing bearing manufacturers such as Schaeffler [135], Liebherr [136], Rothe Erde [137] or Rollix [138]. For example, the Astraios [135] test bench can reproduce operational axial and moment load conditions (static and dynamic) with four axial hydraulic cylinders and simulate the weight of a rotor hub with blades by means of another four radial hydraulic cylinders.

Some test rig layouts integrate all the bearing interfaces (hub, blade, pitch drive) of the wind turbine. Figure 1.18c shows the Windbox test rig [139], which was designed to perform tests on pitch and main shaft bearings. The test rig of Figure 1.18d belongs to the Fraunhofer Institute for Wind Energy and Energy System Technology (IWES). This rig was conceived to test bearings of 3 [MW] class wind turbines. Its layout permits accurate reproduction of the operating

conditions of the pitch bearing. Stammler et al. [140] performed tests to measure the friction torque under load and compared the obtained results with different calculation models using this test bench.

Another kind of large slewing bearing test rig arranges the bearings in pairs and in a horizontal position. This layout allows for the application of a rotational movement with an external or internal pitch drive. The lower bearing is bolted to a fixed support while the upper bearing is bolted to the moveable upper frame. A force transition element is placed between both bearings to connect them and transmit the force from the upper frame to the lower support. Several hydraulic actuators act on the upper frame in such a way that loads in 6 DoF can be applied to the bearings. One example of this kind of test rig can be found in the Korea Institute of Machinery & Materials (KIMM) [141,142]. In this case, the transition element was made of steel and loads were applied to the upper frame by means of several axial and radial hydraulic actuators, as can be seen in Figure 1.18e. The Fraunhofer IWES also has a test rig of this kind at their facilities (Figure 1.18d [143]). In this case, the transition element aims to reproduce the real supporting structures. To this end, it was made of a combination of GFRP rings and steel sections that reproduce the behaviour of spar caps and shear webs. Besides this, stiffener plates were attached to the bearings in order to counteract the ovalization of the rings. In terms of loading, any combination can be applied since the upper frame is basically a hexapod (Gough–Stewart platform) with 6 DoF. Finally, the test rig of the Nanjing TECH University in China (Figure 1.18e [141]) can drive accelerated life tests on slewing bearings. In this case, there is a main bearing under study bolted to an accompanying bearing, which serves to allow. The main bearing is bolted to the upper frame and the accompanying bearing to the fixed lower frame. Axial load and tilting moment are introduced to the upper frame by two vertical hydraulic cylinders, radial load by a horizontal hydraulic cylinder and a hydraulic motor also provides rotational movement. Loads can be introduced in only 3 DoF, so this is not such a versatile test rig compared with the others. However, several research studies were conducted using this test rig [119,144,145].
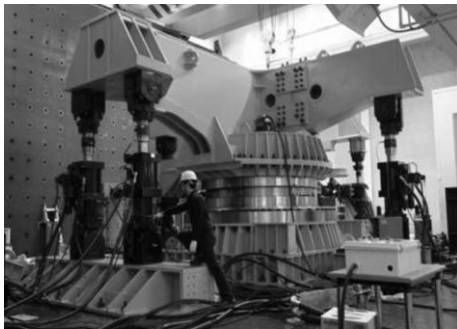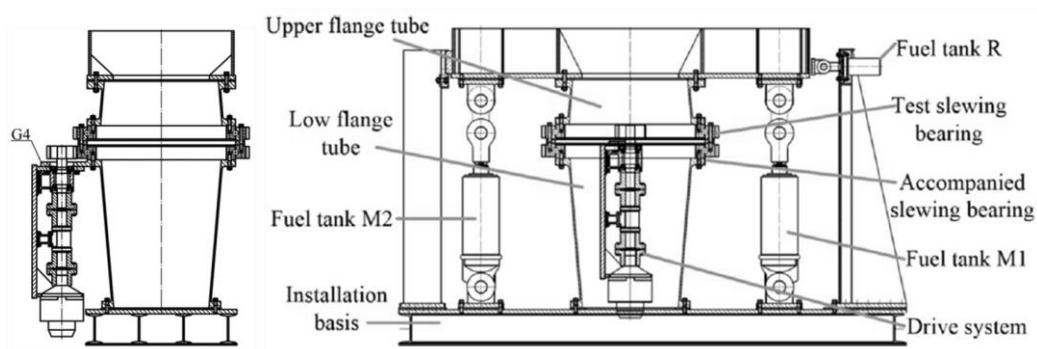
Figure 1.18 Large bearing test rigs: (a) Schaeffler Astraios test rig [135]; (b) Liebherr large bearings test rig [136]; (c) Windbox test rig [139]; (d) Pitch bearing test rig at Fraunhofer IWES [140]; (e) KIMM test rig [141]; (f) BEAT 6.1 hexapod test rig [143]; (g) Nanjing TECH University [119].

There are also modest test rigs for smaller slewing bearings, but there are not as many and they are not as sophisticated as the ones used for the wind energy industry. The test rigs of the Laboratoire de Genie Mecanique of Toulouse [146] and the Kunming University of Science and Technology in China [147] are some examples. The components of these kind of test rigs are indicated in Figure 1.19a, where the loading cylinder can be placed along the loading beam to adjust the overturning moment. Only static tests of a combination of axial and tilting moment loads can be performed; however, this load combination is commonly found in slewing bearings applications.

Joshi et al. [102] used a test rig to validate a friction torque model for slow speeds. The test rig was driven by a servomotor, with two bearings connected to the shaft. The outer rings of the bearings were attached to a housing where the axial load was applied by tightening six screws. Both the axial load and torque were measured with load cells. Another test rig to measure the friction torque is shown in Figure 1.19b. This test rig is located at the Aachen University (RWTH) and can perform friction torque and fatigue tests on large slewing bearings [148]. To allow for the rotational movement, two bearings are arranged in each test. Both bearing inner rings are connected by a bolted joint and a spacer and a stiffener plate are also placed in between to represent the stiffness of the surrounding structures. On the other side, four stiffening plates are attached to each outer ring in such a way that 56 hydraulic cylinders placed between them apply the axial load. Finally, a pitch drive generates the oscillation or continuous rotational movement to perform the tests. Finally, Hou and Wang [149] proposed an experimental methodology to measure the radial load distribution on a cylindrical roller bearing. For that purpose, they built a notched bearing housing in such a way that there were one strain gauge per roller. The complete test rig schema is represented in Figure 1.19c.

(a)

(b)

(c)
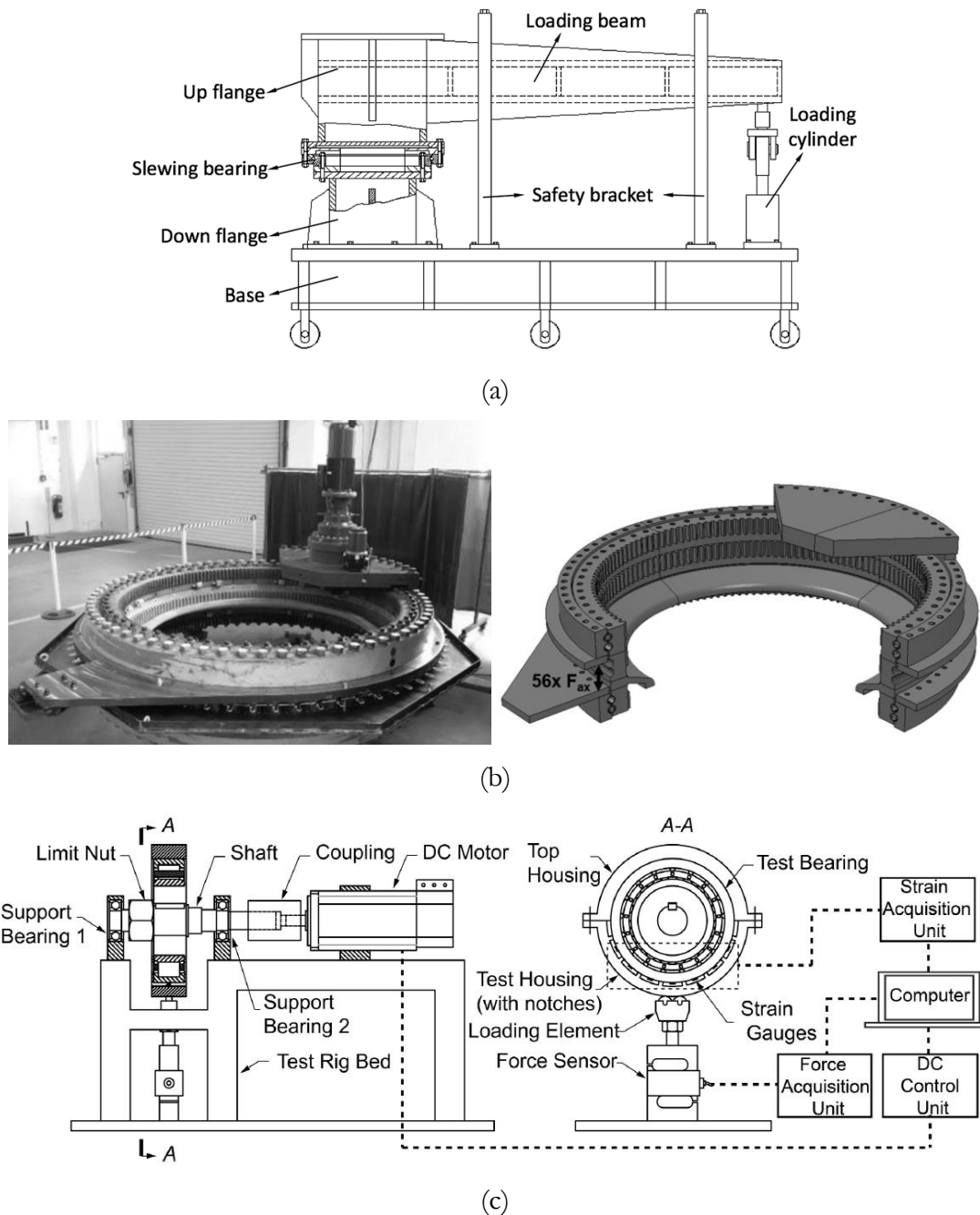
Figure 1.19 Test rigs: (a) Kunming University of Science and Technology test rig [147]; (b) RWTH test rig [148]; (c) Test rig developed by Hou and Wang [149].

1.5 Wire-race bearings literature review

As it has been mentioned, wire race bearings markets and manufacturers are increasing [4]. Nevertheless, they are far from being as popular as conventional bearings and can be considered a niche product. This results in limitations in terms of available literature, since manufacturers are obviously not interested in revealing their know-how. Besides this, no standards have yet been developed for these kind of bearings and the current ones for conventional bearings are

not directly applicable. In terms of research publications, this is not so different, although some studies can be found.

The first publication regarding wire-race bearings was provided by Shan et al. [150], where an analytical methodology to obtain the optimal preload on a non-conformal wire-race ball bearing was proposed. Figure 1.20 shows the cross-section of the bearing under study; as it can be can be seen, ball preload is determined by the thickness of the shim. Moreover, the figure shows that the cross section of the wire is circular, i.e. it has no race machined, and thus the ball-wire contact is non-conformal. The contact formulae proposed by Johnson [59] was applied to obtain the minimum and maximum preload values. The own mass of the structure can lead to a two-point contact situation, so the minimum preload should preserve the four-point contact status. On the other hand, maximum preload causes contact failure.
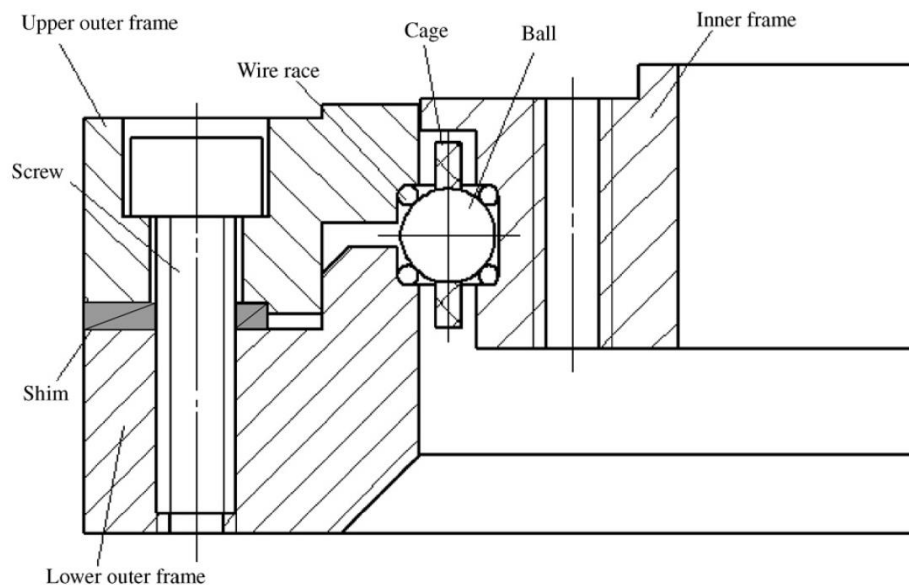
Figure 1.20 Ball wire-race bearing cross-section [150].

Some other works were published by the same authors [151–153] and others [154–156] in non-indexed journals or congress proceedings with little research interest. Besides this, these publications are not well structured, there is a lack of explanation and they fall short of scientific rigour. Nevertheless, a brief summary of their content is included in following paragraphs.

The contribution in [151] consists of applying the contact formulations developed by Johnson [59] to a ball wire contact and comparing the results with a FE simulation. As expected, good agreement was obtained and no novel conclusions were provided in this work.

An analytical model for the resolution of the radial load distribution problem was proposed in [152]. Firstly, they applied the methodology developed by Stribeck [67–69] to obtain the contact force on each ball. Then, each ball-wire contact was modelled with a spring with an equivalent contact stiffness (K_1, K_2, K_3, K_4 in Figure 1.21). Two major problems arose at this point; wire-ring contact stiffness was not being considered, and the spring mechanism was not designed to account for contact angle variations (an assumption that was not specified in the article). Finally, experimental validation showed that radial stiffness is highly dependent on the shim thickness, which was not considered in the analytical model.
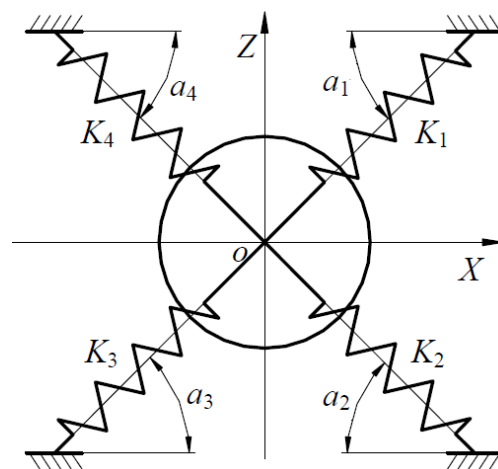
Figure 1.21 Equivalent spring model [152].

A mathematical model to obtain the stiffness matrix of a four-point contact wire-race bearing was described in [153]. To this end, a load distribution model based on Hertz contact theory is explained. Equations of the load distribution problem arranged in a matrix form retrieve the stiffness matrix of the bearing. Finally, analytical results were compared with experimental measurements. Again, experimental results show that shim thickness has a great effect on stiffness, which was not taken into account in the analytical model. Besides this, it was assumed that the wire-ring contact stiffness does not affect the bearing structural behaviour. Finally, it is stated that the model is valid, but the experimental results do not tally with the theoretical ones. In fact, they are very different.

Xiangyang et al. [154] carried out a study to evaluate whether Hertz's contact theory could be applied to the contact between a ball and a wire with no machined race, like the one in [150]. To do this, they built a FE model of the ball-wire contact and performed an analysis. The content in this publication is diffuse, the results comparison of the analytical and numerical models is not

clear, and they adduce that the deviations in the comparison are caused by the plastic deformation that Hertz did not considered in his formulae. This is an erroneous justification, since they assumed linear elastic behaviour for the material in the FE model. Ruixia and Xiangyang [155] also proposed an optimization methodology to obtain a better wire bearing design in terms of dynamic load rating. The poor explanations and the general lack of quality indicated that the contribution was far from good. Besides this, results obtained from the optimization process could have been anticipated at first glance (a rise in the ball diameter and number of balls increase the dynamic load rating).

Zhao et al. [156] carried out another optimization process to obtain the bearing geometrical parameters within limits that retrieved the minimum friction torque under certain axial and radial load values. Of course, the target function is the friction torque, which is calculated by means of a given formula; and the ball diameter, pitch diameter, contact angle and ball number are the design parameters. There are also some constraints regarding the maximum allowable contact pressure and a safety factor, amongst others. This kind of optimization method could be useful with a complete set of constraints. Usually, a designer does not have so much freedom to vary the design parameters, since the bearing has to comply with other requirements in terms of available mounting space and mechanical capabilities. Nonetheless, the main problem in this work lies with the friction torque calculation formula, since it is not contrasted or validated.

More recently, Gunia and Smolnicki carried out a couple of studies regarding stress distribution in wire-race ball bearings. Two FE models were developed in [157] to evaluate the status of the ball-wire and wire-ring contact. Due to the symmetry planes present on the geometry, only a quarter of the ball with its corresponding wire and ring sections were modelled. Figure 1.22a shows the boundary conditions, which consists of symmetry constraints and an imposed displacement in the direction of the contact angle. Various results were evaluated, such as pressure patches, contact deformations and Von Mises stress (Figure 1.22b). The main conclusion of this study was related to the truncation of the contact ellipse caused by a combination of high loads with high osculation ratios; under this situation, the ball reaches the wire edge causing a stress concentration in that area. Geometrical correction of the wire edge, such as a fillet or a logarithmical profile, was suggested to prevent this behaviour. A non-specific geometrical correction was also suggested; this statement is

questionable, since the wire-ring contact geometry was not properly defined in the article.

Another study was performed in [158], but in this case, new design parameters were evaluated. A similar FE model to the one in Figure 1.22a was used, considering different values of ball diameter, osculation ratio and a new parameter called "fill factor of the raceway (k)". This parameter measures the size of the raceway and is defined by the relation between the raceway chord and the wire diameter. In this work, ball-wire contact FE maximum pressure and Von Mises stress were compared with calculations performed with Hertz's contact formulation. The descriptions of the study cases were not clear (raceway fill factors were not specified), their selection was not the most suitable to study the parameter's main effects and to discriminate the crossed effects. Besides this, the results comparison was not the most adequate and apparent incoherencies were not successfully justified. However, the introduction of the raceway fill factor and the implications that it has in terms of contact pressure and stress distribution was a valuable contribution.

(a)   (b)

(c)
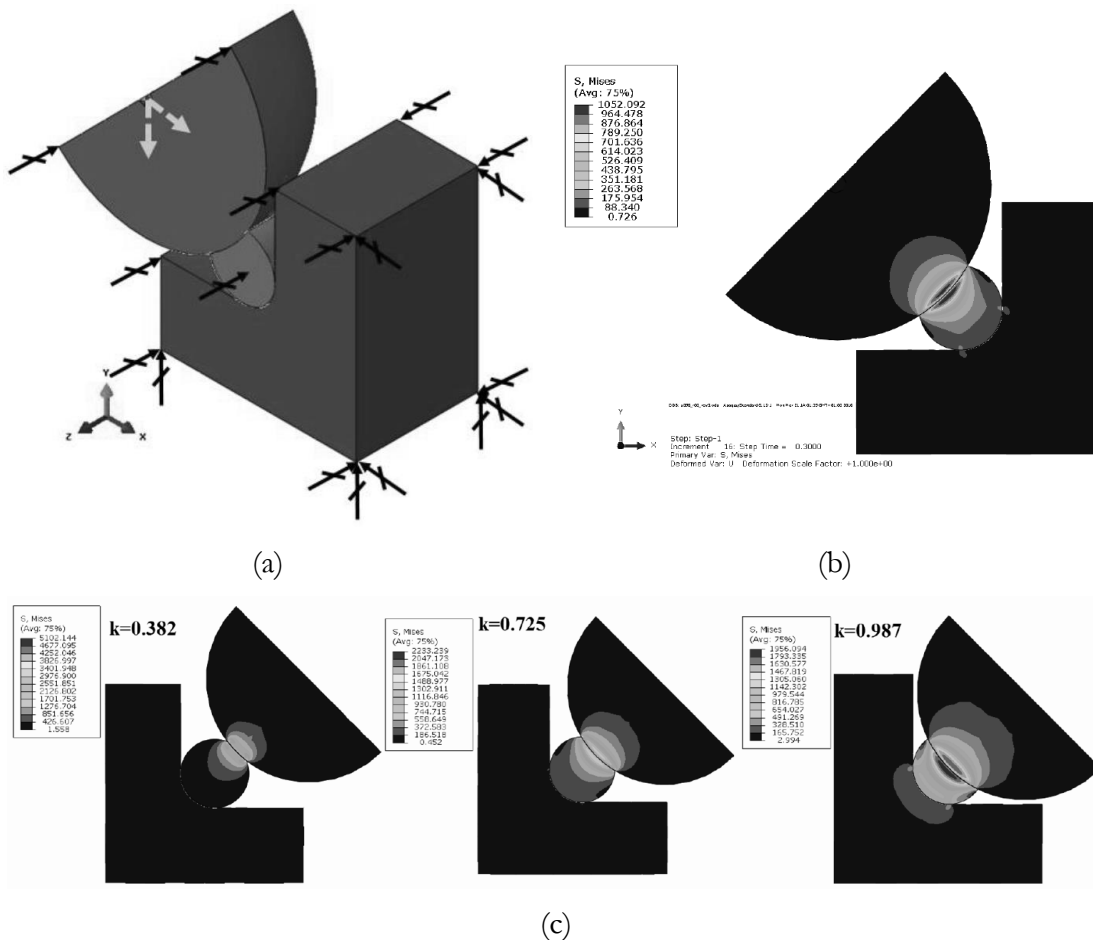
Figure 1.22 FE model geometry and boundary conditions [157]; (b) Von Mises stress results [157]; (c) Stress distribution for different values of raceway fill factor [158].

Finally, the last work presented by Gunia and Smolnicki regarding wire-race ball bearings is related to the mentioned wire edge geometry correction [159]. Figure 1.23 shows a geometrically non-corrected and corrected wire cross-section. There are many options by which to perform the edge filleting, in fact, the same corrections used for the roller profile (Figure 1.10) could be applied to the wire edges. To study the implications of this correction, three FE analyses were performed. The first FE model consisted of a regular wire-race ball bearing with an 8 [mm] diameter ball, a 2.5 [mm] diameter wire and an osculation ratio of 0.96. The other two FE models received the wire edge geometry correction in terms of a simple rounded edge fillet with a radius of 0.2 and 0.4 [mm]. Regarding the results, significant differences were found in the maximum contact pressure and Von Mises stress comparison between the FE analyses and the analytical Hertz's calculations. These deviations were related to the limitations of the analytical method. In terms of stress distribution, wire edge correction retrieved a stress reduction in the edge stress concentration, which can lead to fatigue life improvement. However, a higher fillet radius reduces the size of the effective raceway, which should lead to higher pressuresat the centre of the contact for the same applied load. Nonetheless, and according to the stress plots included in the article, the observed effect goes in the opposite direction. The concept presented in this work is quite relevant, but its materialization in this study could have been more rigorous. This is still an interesting research topic to conduct investigations for ball and roller wire race bearings.
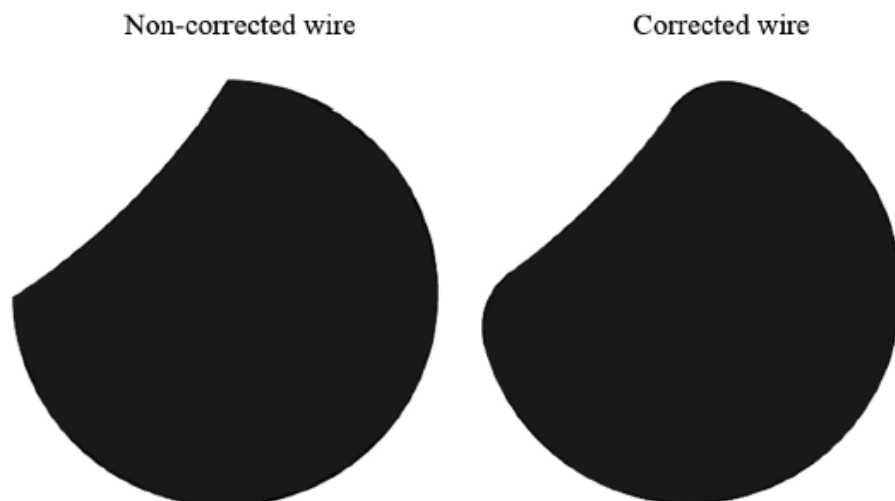
Figure 1.23 Geometrically non-corrected and corrected wire [159].

The contribution with more scientific rigour in the scope of wire-race bearings was presented by Dindar et al. [160]. The objectives of this work consisted of studying the friction sources on a double row roller wire race bearing and developing a method to estimate the friction torque under different load conditions. To fulfil the first objective, several tests with different layouts were performed with the test bench of Figure 1.24a. The test campaign consisted of combinations of axial and tilting moment load levels at different rotational speeds. The results concluded that the contribution of each friction source to the friction torque was distributed as: 10.8% upper seal (normal lip seal), 54.8% lower seal (lip seal with garter spring) and 34.5% bearing inner mechanism. According to this, proper sealing selection is one of the most important steps by which to reduce the friction torque. Friction torque also increases with growing axial load, tilting moment or rotational speed.

Regarding the second objective, the calculation procedure to estimate the friction torque is described in Figure 1.24c. First, a FE analysis (in Ansys®) must be performed to solve the load distribution problem and obtain the roller contact forces. The FE model used to this end is shown in Figure 1.24c, where it can be seen that the rollers were replaced by compression-only springs and the wires were integrated into the rings (i.e. no relative movement is allowed between the wires and the rings). Spring stiffness was calculated according to [60] and the half width of the contact area was obtained applying Hertz's contact theory [43,44]. This may seem like a good strategy, but its validity was not properly assessed. To this regard, the simplification of the wires implies the suppression of the wire-ring contacts. This way, the flexibility that the wire-ring contacts provide is ignored. Besides this, steel was defined as the material for rollers and wires, but the ring material was not specified. After the FE analysis, results were imported in a multibody model (in ADAMS®) to simulate the rolling friction and the contribution of the seals was estimated with a model generated with the results of the experimental tests. Good agreement was obtained between experimental tests and the calculation methodology.

(a)

(b)   (c)

(d)
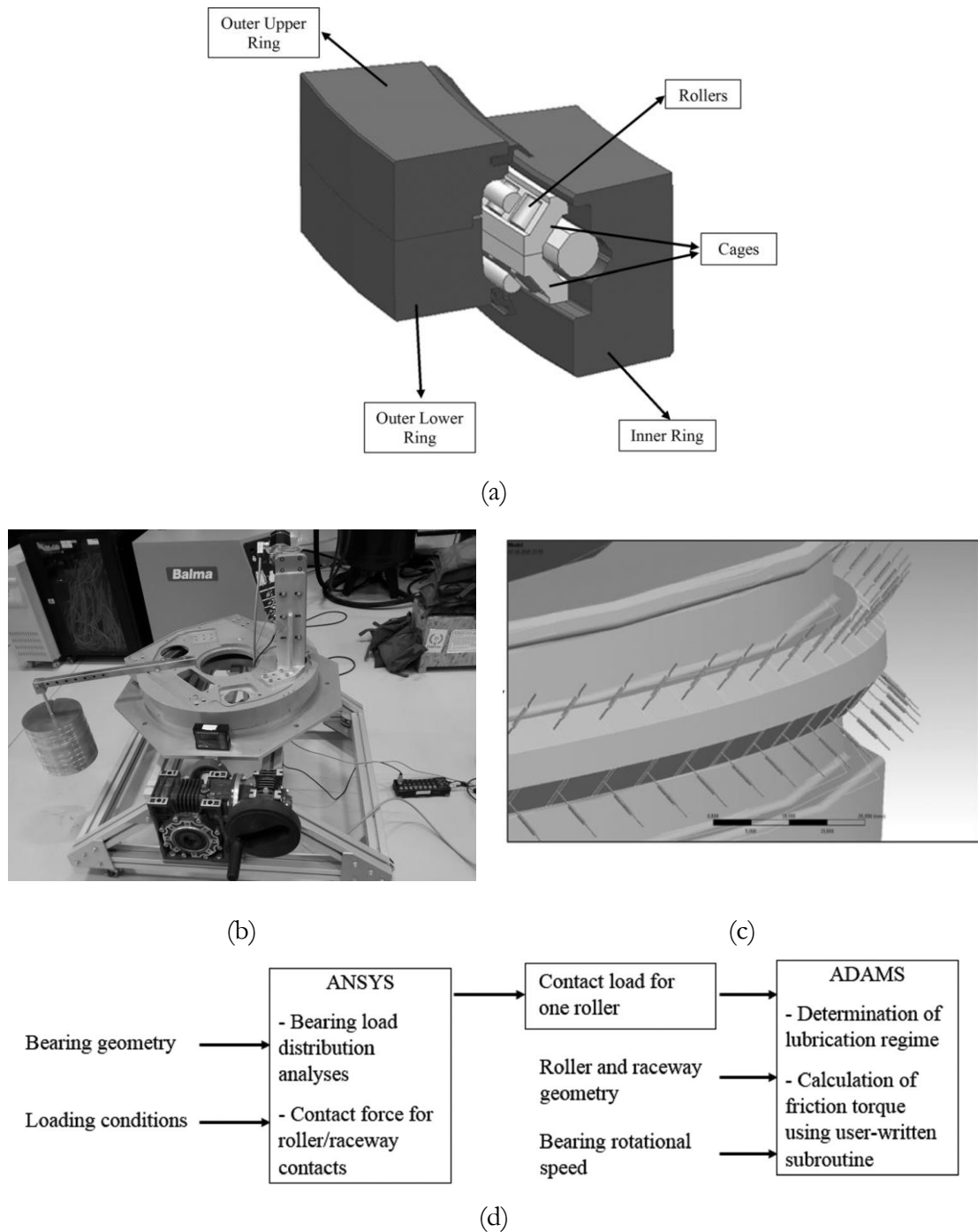
Figure 1.24 (a) Three wire-race double row roller slewing bearing [160]; (b) Friction torque test bench [160]; (c) FE roller simplification [160]; (d) Friction torque calculation procedure [160].

To bring this section to a satisfactory end, it is worth mentioning that the path is open to new scientific work and the numerous research lines available. For this reason, this thesis intends to lay the foundations regarding this matter and serve as reference for future research work.

1.6 Objectives

Considering the lack of information or scientific publications available for wire-race bearings, it was considered appropriate to carry out fundamental research about the behaviour of these kind of bearings. This will open the way to further research lines and will retrieve a better understanding of the components. Besides this, the inapplicability of the current calculation methodologies or standards generates a knowledge gap for the industry itself. To contribute towards filling that gap, the development of analytical calculation methods for the simulation of their structural behaviour and the specification of design guidelines are the main purposes of this Doctoral Thesis. As it has been presented in this chapter, there are many wire race bearing layouts. For this reason, this work is focussed on the two most popular ones: four-point contact and crossed roller wire race bearings. Based on this, the following bullet points define the specific objectives of the research work presented in this Doctoral Thesis:

The objectives are focused both on four-point contact and crossed roller wire-race slewing bearings:

- Study the structural behaviour by means of FE simulations:
    - Identify the physical phenomena that results in the structural response.
    - Compare the performance with conventional slewing bearings.
- Develop analytical models for the calculation of the load distribution problem, the static load capacity and the stiffness curves.
- Create efficient FE modelling strategies.
- Validate the analytical and FE models through experimental testing.
- Study and quantify the effect of the main design parameters in the performance.

1.7 General overview of the proposed methodology

In this Doctoral Thesis, various studies were carried out and novel approaches developed and validated to meet the proposed objectives. In order to structure the document in a simple to follow and clear manner, each study or approach is explained in a separate chapter. This section provides a general overview of the research work presented in the following chapters. The reader may find it convenient to come back to this point whilst reading the document as a reminder of which problem is being addressed in each chapter.

In Chapter 2, a study of the structural behaviour of four-point contact wire-race bearings under axial load is presented. To this end, several FE analyses were carried out to evaluate the influence on the performance of the osculation ratio, the adequate wire-ring contact lubrication and the boundary conditions. Besides this, results were compared with the equivalent conventional slewing bearings. This is a proper introductory study, since the structural behaviour is evaluated and its performance compared with the equivalent conventional slewing bearing.

Because of the effect the wire has on the wire-race slewing bearings performance, an analytical formula to obtain the wire twisting stiffness is presented in Chapter 3. This formula could prove useful in some other applications, but it was developed with the aim of implementing the wire twisting stiffness in wire-race slewing bearings analytical approaches.

Also related with four-point contact wire-race slewing bearings, Chapter 4 includes explanations about the analytical approach developed for the calculation of the stiffness, static load capacity and contact results. For this first approach, only the axial or tilting moment load cases can be considered. Besides this, rigid rings boundary conditions were assumed. This approach was developed considering the conclusions obtained in the previous chapters and consists of equations based on the stiffness of the contacts and compatibility of deformations.

Chapter 5 introduces another analytical approach, in this case for crossed roller wire-race slewing bearings. The procedure is similar to the one followed in Chapter 4, but more complex. The proposed analytical formulation is embedded into a simulation algorithm to calculate stiffness curves in the axial, radial and tilting directions together with its related static load capacities. Besides this, the load distribution problem can also be solved with any acting external load combination, retrieving the contact forces and angles on all the rollers and the maximum contact pressure. As it aims to be a complete calculation tool, both rigid and flexible rings boundary conditions can be considered.

In order to obtain a functional analytical simulation tool, the analytical approach for crossed roller wire-race slewing bearings must be validated experimentally. The experimental test campaign was carried out on a tension-compression test bench located in the Faculty of Engineering of Bilbao. To this end, two bearing designs were defined and two specimens of each one

manufactured by IRAUNDI S.A. The validation process and the obtained results are explained and discussed in Chapter 6.

As has been explained above, slewing bearing FE models are complex and computationally heavy. Needless to say that these problems are more acute when it comes to wire-race slewing bearings. For this reason, some efficient FE modelling strategies that reduce the complexity and improve the efficiency of the FE models are presented in Chapter 7. On the one hand, the simplification proposed by Daidié is implemented on a four-point contact wire-race slewing bearing. On the other hand, two alternatives are proposed for crossed roller wire-race slewing bearings. The first one consists of the implementation of the analytical approach proposed in Chapter 5 in a FE model, and the second one consists of representing the behaviour of all the contacts with a non-linear equivalent spring.

Since no design criteria is available in the literature for wire-race slewing bearings, Chapter 8 is focused on this matter. First, the main geometrical design parameters were defined for four-point contact and crossed roller wire-race slewing bearings. Then, a FE simulation campaign was carried out based on a full factorial DoE (Design of Experiments). Because of the large number of analyses and the computational cost related to each one, only the axial load case was considered. Finally, to evaluate the effect of each design parameter on the bearing structural response, main and crossed effects were evaluated on several performance indicators. As a result, some design guidelines were proposed.

Finally, Chapter 9 summarizes the main conclusions that arise from the work carried out in this Doctoral Thesis and suggests the future work to be done to this regard.

2 Structural behaviour of four-point contact wire-race bearings

2.1 Introduction

As has been mentioned, there is almost no literature regarding wire race bearings and no standards regulating the design or calculation methods. Besides this, manufacturers possess all the know-how and are wary about sharing it, which is logical from a business standpoint. However, this situation does not help promote the application of these bearings. The lack of technical information can lead to mistrust from potential customers, since they can interpret that wire race bearings are not a mature product. For this reason, it is appropriate to start with the foundations and begin the contents of this Doctoral Thesis with a study that sheds light about the performance of this kind of bearings.

In this chapter, the subject of the study is the four-point contact wire race slewing bearing, since it is one of the most popular layouts. Despite this fact, the effect of such an important design parameter as the osculation ratio has not yet been evaluated. The effect of this parameter on performance is well known for conventional slewing bearings, where a high osculation ratio makes the contact more conformal, which leads to a bigger contact ellipse. This effect is usually desirable since it increases the contact stiffness and the static load capacity. Nevertheless, an increase in the size of the contact ellipse also compromises the risk of suffering truncation. This can pose a risk for conventional bearings and an even greater risk for wire race bearings because of its limited raceway size. Another key aspect that deserves attention is the lubrication of the wire-ring contact. Manufacturers recommend lubricating this contact with grease [161], but the effects of incorrect lubrication are still unknown or not reported.

When it comes to perform a study of the structural behaviour of a component, boundary conditions play a significant role. Usually, it is desirable to represent the most realistic boundary conditions in order to obtain accurate results. This involves modelling the surrounding structures and fixing methods. However, this cannot be done in a generalist study. For this reason, it makes more sense to define different simplified boundary conditions. This way, the scope is wider and the conclusions more general.

Valuable conclusions for the comprehension of the behaviour of wire race bearings can be obtained from the study of the aforementioned parameters. However, the most interesting question is left unanswered, which is related to the performance of the bearing in comparison with conventional slewing bearings. For this reason, the results are compared with the results obtained from the equivalent conventional slewing bearing for each studied design case.

Summing up, there are 3 main objectives in this chapter. Firstly, shedding light over the working mechanisms involved in four-point contact wire race slewing bearings to understand their structural response. Secondly, evaluating the effect of the osculation ratio and wire-ring contact friction coefficient on the structural behaviour under different boundary conditions. And finally, comparing the structural performance of wire race slewing bearings with conventional slewing bearings.

To achieve these goals, several FE simulations were performed considering the sector corresponding to one ball. By applying an external axial load to the sector FE model, the working conditions of the most loaded ball under an applied axial force or a bending moment are simulated.

2.2 Case studies

Since the aim of the work was to study and compare the performance of wire bearings with conventional bearings, different analyses were carried out varying two characteristic parameters: the osculation ratio (s) and the friction coefficient (μ). In the industry, typical osculation ratio values are close to 0.943 [162] for conventional bearings and between 0.87 and 0.96 for wire bearings. In order to cover a wide spectrum, osculation ratios of 0.87 and 0.943 were chosen for this study. Regarding the friction coefficient, 0.1 is a typical value for the ball-raceway lubricated steel-steel contact pair [102,163,164]; for wire bearings, 0.1 was also used for ball-wire contact, and for wire-ring aluminium-steel contact two values were studied, 0.1 and 0.3, to evaluate the effect of the

presence or absence of lubrication on the performance of the wire bearing. The first columns of Table 2.1 summarize the five cases analysed in this work, with their corresponding parameter values.

Even for the same type of slewing bearing (conventional or wire), the axial stiffness is not the same for different values of s and μ. For this reason, to make the comparison feasible, a different axial load had to be applied to each model. This axial force was chosen to be the axial static load capacity as calculated by the analytical model proposed by Aguirrebeitia et al. [13], summarized in the last column of Table 2.1 (according to Table 2.2 geometrical data). The analytical model, thoroughly explained and validated in [13], is based on the calculation of the ball–raceway interference field caused by axial, radial and tilting displacements of the rings due to external loads (in addition to ball preload), assuming rigid rings. As the stiffness of the adjacent structures has a relevant effect on the behaviour of the bearings, two extreme situations were taken into account for each case study in Table 2.1. On the one hand, clamped rings, assuming that the rings are fixed to rigid supporting structures; on the other hand, unclamped rings, assuming that the supporting structures are rigid but the bearing rings can freely slide on them. Of course, real systems behaviour falls between these two extreme conditions. In summary, there are five case studies with two boundary conditions, which means that ten FE analyses had to be carried out.

Table 2.1 Case studies.

Case	Bearing type	s	μ (ball-wire)	μ (wire-ring)	C_{0a} [kN] [13]
1	Conventional	0.943	0.1	-	1213.1
2	Conventional	0.870	0.1	-	674.24
3	Wire	0.943	0.1	0.1	1213.1
4	Wire	0.870	0.1	0.1	674.24
5	Wire	0.870	0.1	0.3	674.24

Regarding the geometry of the bearings, the two main geometrical parameters are the ball diameter (D_w) and the bearing mean diameter (D_{pw}), which were chosen in such a way that the resulting bearing could be found in both conventional and wire bearing commercial catalogues. With regards to the geometry of the rings, each manufacturer has its own designs or can custom-build them depending on the application. In order to create a design criterion, Heras et al. performed a DoE based on the ring geometries that appear in the most relevant manufacturers' catalogues and proposed a standard parametric geometry for conventional four-point contact slewing bearings in terms of D_w and D_{pw} [15]. That methodology was applied in this study, even though wire-race bearing cross-sections are usually larger than conventional bearing sections. However, same ring geometry permits making the comparison in strictly the same conditions. It is worth pointing out that the wire housing radius (R_{wh}) is usually 100 [μm] smaller than the wire radius ($\lambda/2$).

Bolts and bolt holes were not considered because the objective of this study is to understand the structural behaviour of the component. Bolts are usually highly preloaded and this can affect the response of the bearing. For this reason, the effect of the number of bolts and the bolt preload can be the subject of another study.

Figure 2.1 shows the cross-section of both bearing types with their geometrical parameters, which values are collected in Table 2.2. It is worth mentioning that no spacers or cage were considered and the number of rolling elements (N_B) was the highest possible.

Table 2.2 Geometrical values.

D_w [mm]	D_{pw} [mm]	D_{cw} [mm]	α_0 [º]	λ [mm]	N_B	R_{wh} [mm]	R_L	R_H	R_{Lg}	H_g [mm]
16	420	-	45	-	82	-	1.9	2.15	0.1	5
16	420	20	45	6.66	82	3.23	1.9	2.15	0.1	3

(a)

(b)
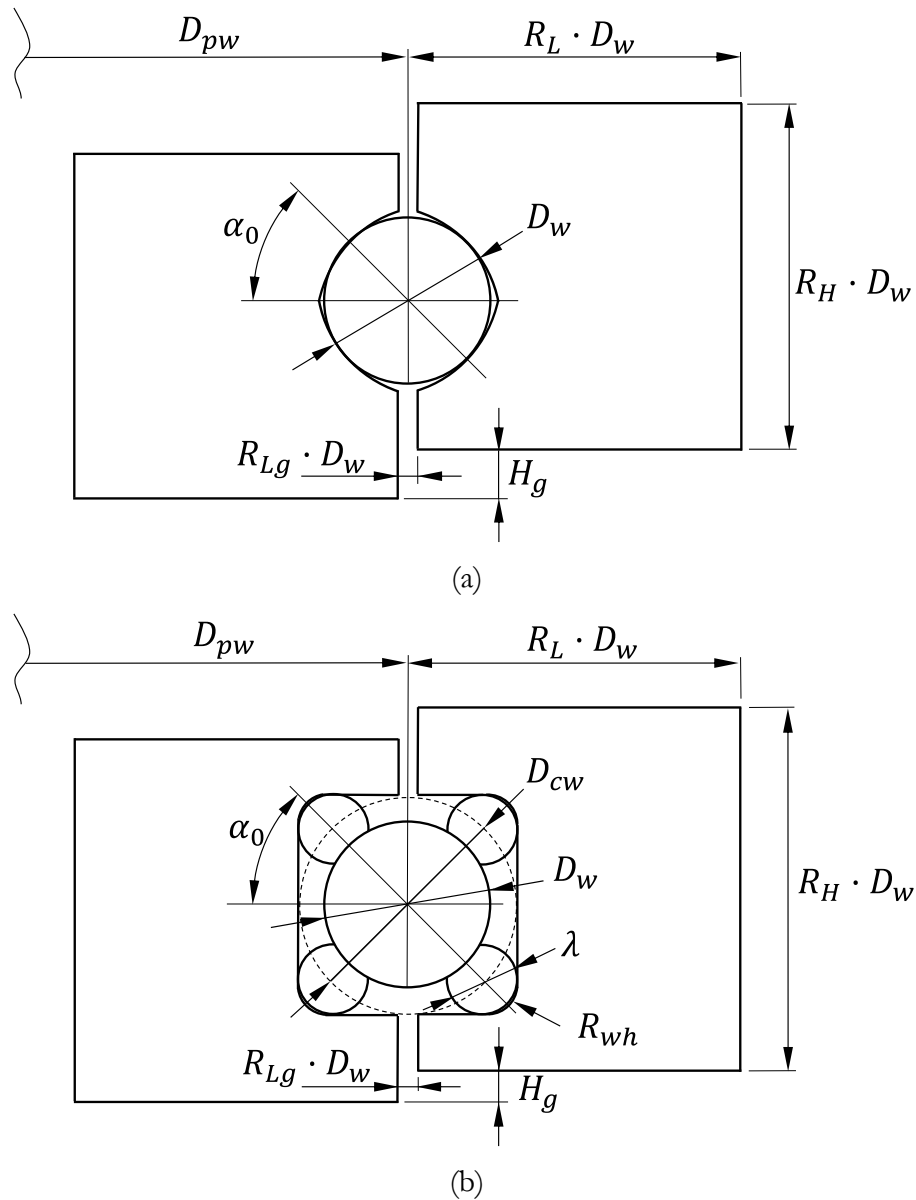
Figure 2.1 Geometry of the slewing bearings: (a) Conventional; (b) Wire-race.

2.3 FE models

As it was stated in the introduction, the basis of this study lies on FE simulations. In this section, the multiparametric FE models developed for the simulations are introduced together with the submodelling technique, which was applied to obtain more accurate results. Everything related with FE was performed with the commercial software Ansys®.

2.3.1 Half sector FE models

Selecting the axial load case for this study was not random. The axial load situation provides a cyclic symmetry load distribution, which, together with a

cyclic symmetry geometry, allows for the simplification of the whole bearing model into a one sector model. Furthermore, the one sector model has a symmetry plane that allows for the analysis of only one half sector model, significantly decreasing the number of Degrees of Freedom (DoF) and computational cost. It must be also noted that an axially loaded sector model also reproduces the load conditions of a ball in a bearing under an applied bending moment.

Regarding the materials of the models, linear elastic steel with an elastic modulus of 200 [GPa] was used for the conventional slewing bearing model. In the case of wire-race bearings, the most common layout according to commercial catalogues consists of constructing the rolling elements and the wires in steel and the rings in aluminium. For this reason, the same linear elastic steel is used for balls and wires, and linear elastic aluminium with an elastic modulus of 71 [GPa] for the rings.

Figure 2.2 shows the mesh of both bearing models. Models were meshed with the same element size in order to make a more accurate comparison between results. To this end, several partitions were performed on the geometry. The partitions with a contacting surface were meshed with second-order hexahedrons; the other partitions were meshed with second-order tetrahedrons to enable quick size transitions with high aspect ratio elements. The conventional bearing model has 321,813 DoF, whereas the wire bearing model has 614,529 DoF.

All the contacts on both models were defined as frictional with augmented Lagrange formulation, allowing for contact stiffness updating for each iteration so a maximum penetration tolerance of 1 [μm] is allowed. With regard to the friction coefficients, the data of Table 2.1 is considered.

With regards to boundary conditions, the surfaces which are intended to be in contact with the supporting structures are assumed to be rigid. The axial load is applied by means of an axial displacement normal to the surface, and, depending on the case, clamped or unclamped, on-plane displacements are allowed or not, to the rigid faces. Of course, symmetry boundary conditions were applied to the symmetry surfaces.
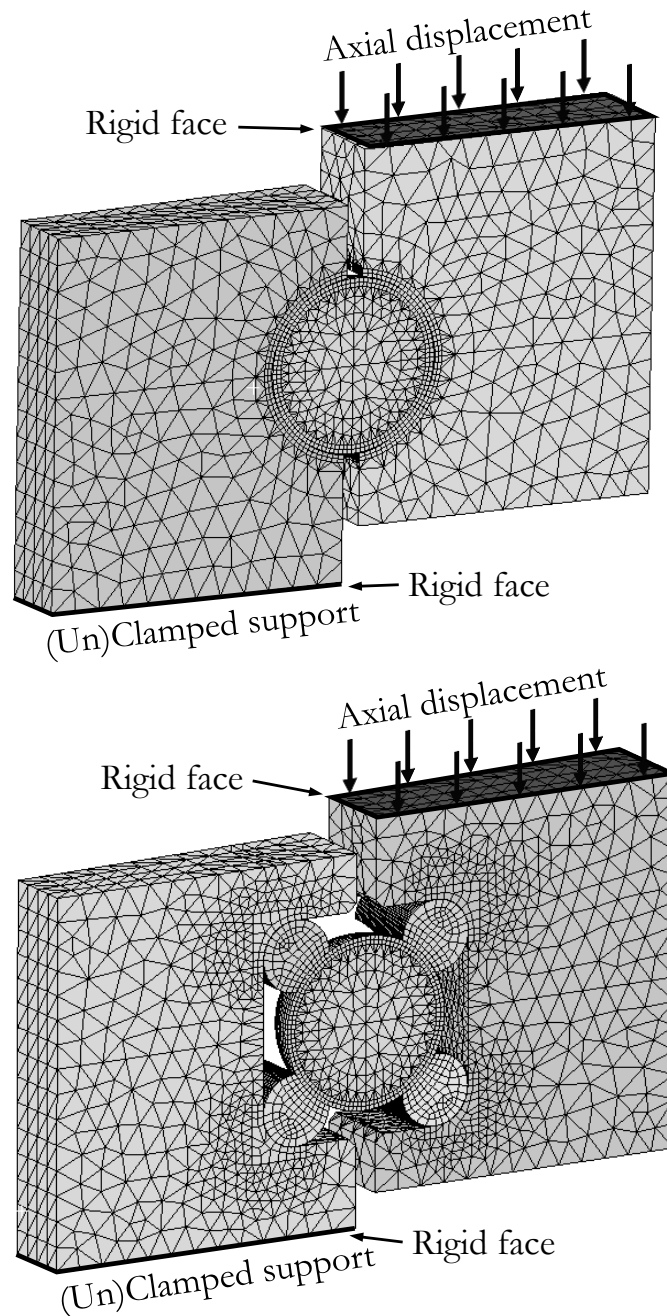
Figure 2.2 Half sector FE models

2.3.2 Submodelling technique

When accurate stress results are required in a local zone of a large FE model or assembly, an option could consist of performing a refined mesh throughout the whole model. This strategy is effective but not so efficient. In these cases, submodelling technique is proven to be a highly efficient strategy. This technique consists of creating a partition of the local zone in the complete FE model and performing the analysis with a relatively coarse mesh. This way, force and deformation results will be accurate, since the global behaviour is well represented. Nevertheless, stress results are not so reliable because of the

unrefined mesh. At this point, a new FE model with the local partition is created with a finer mesh, which boundary conditions on the interface surfaces are the displacements imported from the results of the global analysis. As a result, the deformations in the local submodel will be the same as in the global model, but the stress results much more accurate.

In this case, the global behaviour of the bearing could be accurately simulated by the half sector models. However, finer mesh is necessary around the contact surfaces in order to obtain better local contact results. For this reason, the submodelling technique was found to be a good simulation alternative, where half sector models were the global models and the contact partitions of the ball-race contacts the sub-models. Figure 2.3 illustrates the mesh of the submodels, where finer contact meshes were performed (2,416,227 DoF in the conventional bearing submodel, and 1,167,117 DoF in the wire bearing submodel).
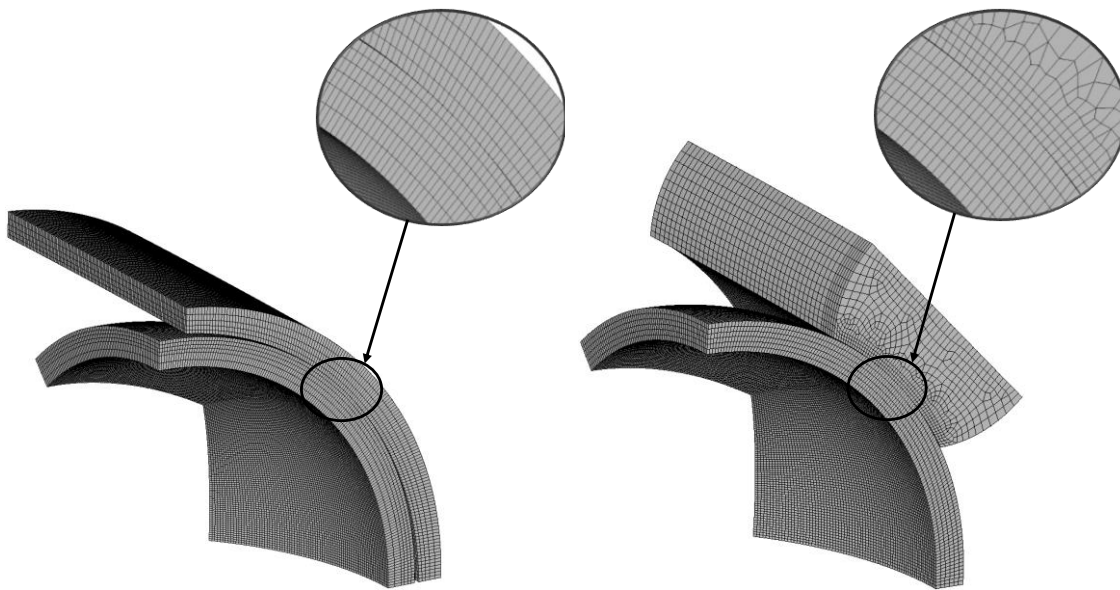
Figure 2.3 Submodels.

2.4 Results and discussion

In this section, the results obtained from the FE analyses are presented and discussed to draw the main conclusions of the study.

2.4.1 Wire twisting phenomenon

The most remarkable phenomenon that takes place during the loading process is wire twisting. When the axial displacement is applied on conventional bearings, the ball climbs the raceway, increasing the ball-raceway contact angle.

On wire bearings, the ball-wire contact force generated by the axial displacement is not aligned with the centre of the wire cross-section, and consequently a twisting moment is induced in the wire. Depending on the friction coefficient of the contacting surfaces, this moment promotes the wire twist rather than ball climbing, as in a conventional bearing. Figure 2.4a shows a detailed view of the undeformed mesh in the contact zone (note the coincident nodes along both wire-ring circumferential contact lines), and Figure 2.4b illustrates wire twist as result of the applied load. The wire twisting has a huge influence on the behaviour of the wire bearing, due to its effects on the stiffness of the bearing, contact ellipse truncation and contact forces. These effects are explained below.

(b)   (c)
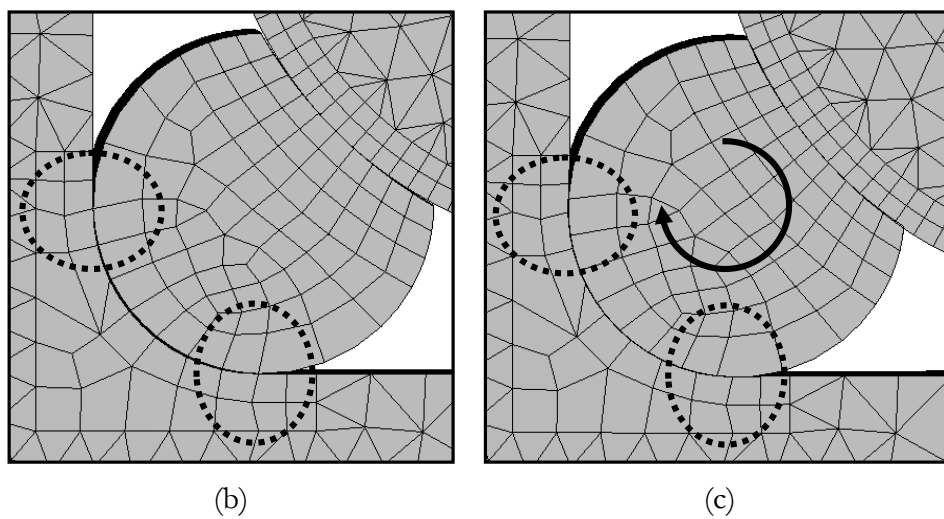
Figure 2.4 Wire twist Case 3 (unclamped situation): (a) Undeformed model; (b) Deformed model (scale x1.6).

2.4.2 Axial stiffness and static load capacity

Axial stiffness curves for each case in Table 2.1 were obtained by means of FE analyses of the half sector models in Figure 2.2. Moreover, the analytical model [13] used to fix the target axial force, was also used to obtain the stiffness curves; this analytical model assumes that the rings are rigid and only considers the deformations of the contacts, so greater stiffness is expected. Figure 2.5 shows the stiffness curves of the five cases summarized in Table 2.1, as well as the points in which the contact ellipse truncates for unclamped (Figure 2.5a) and clamped (Figure 2.5b) situations. To this end, truncation was considered to begin when the contact ellipse reaches the raceway boundaries.
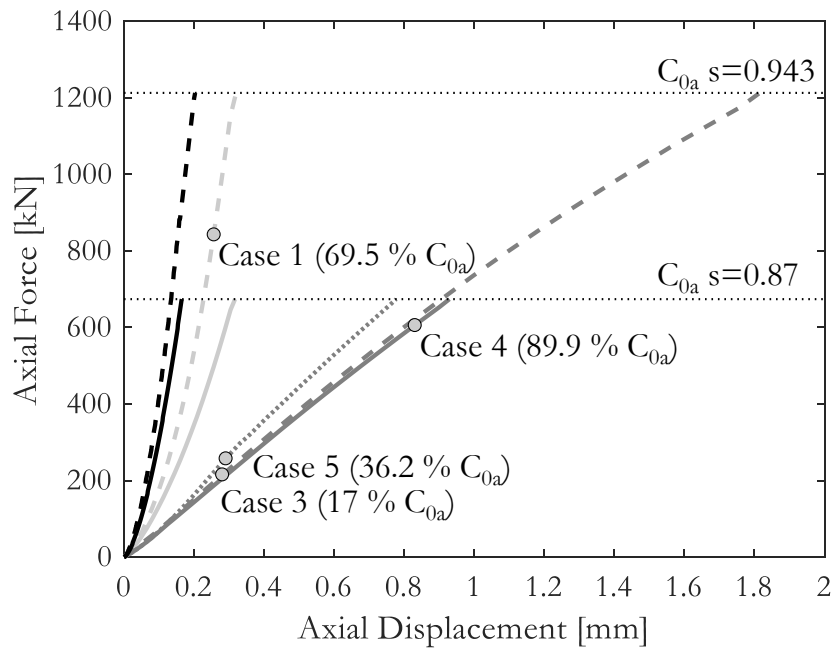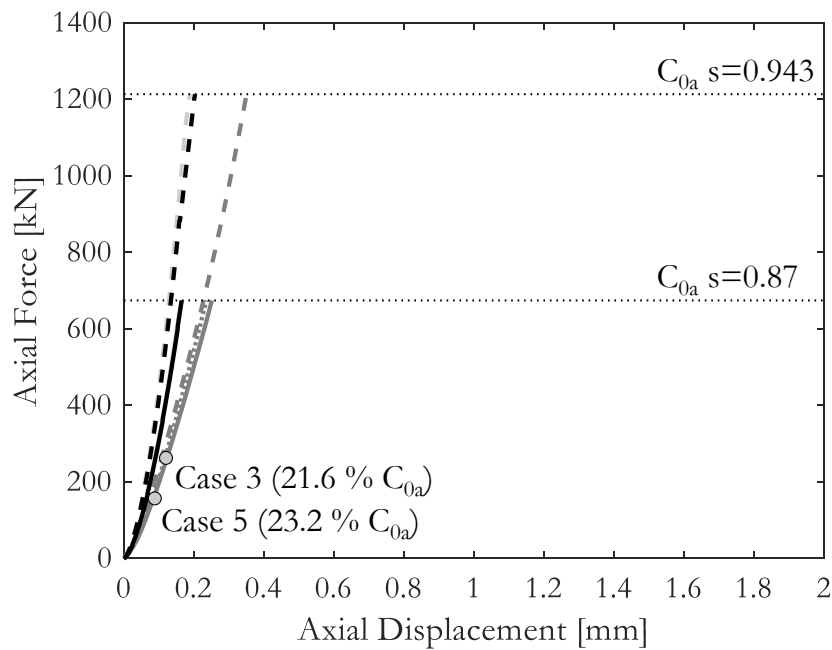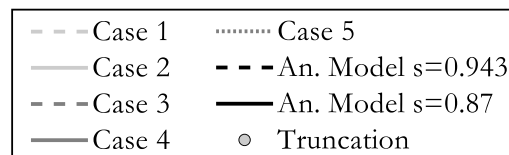
Figure 2.5 Stiffness and truncation status: (a) Unclamped situation; (b) Clamped situation.

Axial stiffness

First of all, it can be seen that the stiffness provided by the analytical model [13] fits very well with the conventional bearing models (cases 1 and 2) with a

clamped configuration, and is slightly larger for the unclamped condition. This is because the clamped condition restricts the radial deformation of the rings, thus being closer to the rigid rings assumption of the analytical model.

Wire bearing rings are built with lighter and more compliant materials and have an extra contact (wire-ring contact). These aspects, together with the wire twisting, makes them more flexible than the rings of conventional bearings. The wire twisting effect on the stiffness can be clearly appreciated observing the wire bearings with the same conformity factor value (0.87) but different wire-ring friction coefficients (0.1 and 0.3), i.e. cases 4 and 5; a larger friction coefficient decreases wire twisting and subsequently increases the axial stiffness of the bearing.

Another phenomenon to take into account is the different stiffness behaviour of each bearing type under different boundary conditions. Conventional bearings show exponential stiffness behaviour due to the exponential nature of the ball-raceway contact deformation and the variation of the contact angle. Wire bearings provide almost linear stiffness behaviour for unclamped conditions, mainly caused by the low stiffness of the rings and the slight variation of the contact angle due to the wire twisting, as will be explained in the following section. For the clamped configuration, the flexibility of the rings does not play such an important role, and therefore the response is exponential.

Axial static load capacity and contact ellipse truncation

According to Table 2.1, and as illustrated in Figure 2.5, the axial static load capacity (C_{0a}) obtained from the analytical model [13] highly depends on the contact conformity: the most conformal bearings ($s = 0.943$) have approximately twice the theoretical capacity of the less conformal ones ($s = 0.87$). However, the analytical model does not consider the truncation of the contact ellipse, which can have a huge effect on static capacity. In this context, Figure 2.5a shows that for an unclamped configuration, cases 1 and 4 behave similarly: in case 1, the conventional bearing with $s = 0.943$, started suffering truncation at 69.5% of the theoretical static load capacity and did not reach complete truncation, whereas in case 3, the wire bearing with $s = 0.87$ and $\mu = 0.1$ in the raceway-ring contact, started suffering truncation at 89.9% of its theoretical static load capacity and neither reached complete truncation.

As has been mentioned above, as the wire-ring friction coefficient increases, so does the axial stiffness because the wire twist decreases, especially in the

unclamped configuration; wire-ring friction also affects contact ellipse truncation. The wire bearing in case 5 ($\mu = 0.3$), starts truncation at 17% C_{0a} and completes it at 67.6%C_{0a}, which is clearly worse than the response in case 4 ($\mu = 0.1$). This fact demonstrates that in terms of static load capacity, the wire twisting phenomenon improves the performance since it prevents the truncation of the contact ellipse. In the clamped configuration, wire twisting is more restricted, so this phenomenon is not so critical.

Analysing the results of cases 2 and 3, both have clear disadvantages. On the one hand, the low conformity conventional bearing (case 2, with $s = 0.87$) is less optimal than the high conformity one (case 1, with $s = 0.943$) because it has half the static load capacity. On the other hand, the high conformity wire bearing (case 3, with $s = 0.943$) started and completed the truncation of the contact ellipse at very low static load capacity percentages, both for clamped and unclamped conditions.

2.4.3 Contact forces and contact angles

Normal contact force is commonly used in analytical models to obtain the contact pressure and shear stress distribution. The contact angle (α) is defined as the angle of the normal contact force with the horizontal axis. In this study, the normal contact force was obtained by means of a post processing macro in Ansys®, based on the assumption that the normal contact force is the vector sum of the normal forces in each node. In order to validate this procedure, the angle between the point of the contact ellipse with the maximum pressure and the horizontal axis was measured, and it was found to be identical to the one obtained by means of forces. Accordingly, Figure 2.6 illustrates the evolution of the ball-raceway contact angle with the normal force for each bearing under clamped and unclamped situations.

It can be seen that, in the case of conventional bearings (cases 1 and 2), the contact angle increases with the axial load due to ball climbing, which can finally result in ball-raceway contact ellipse truncation. In this sense, if the normal contact force and the contact angle are known, the dimensions of the contact ellipse can be calculated; if it reaches the raceway limit, then truncation occurs. In the case of wire bearings, wire twisting involves that the contact angle not always increases with the axial load, as illustrated in cases 3, 4 and 5. In these cases, and for low load values, the contact angle increases as in conventional bearings, because ball climbing occurs because of the lack of wire twisting; however, from an specific axial load onwards, wire twisting starts and

consequently the contact angle decreases. Due to this complex behaviour, the study of the contact ellipse truncation in wire bearings is not as straightforward as it is for conventional bearings.
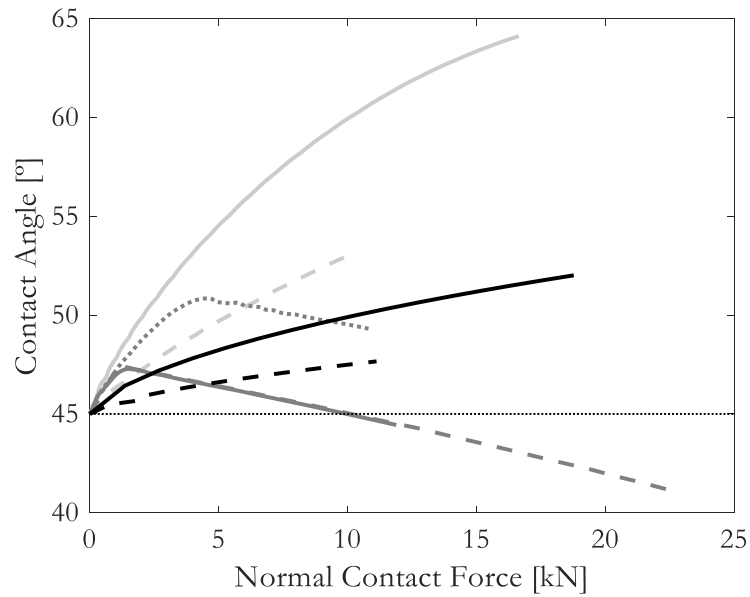
(a)
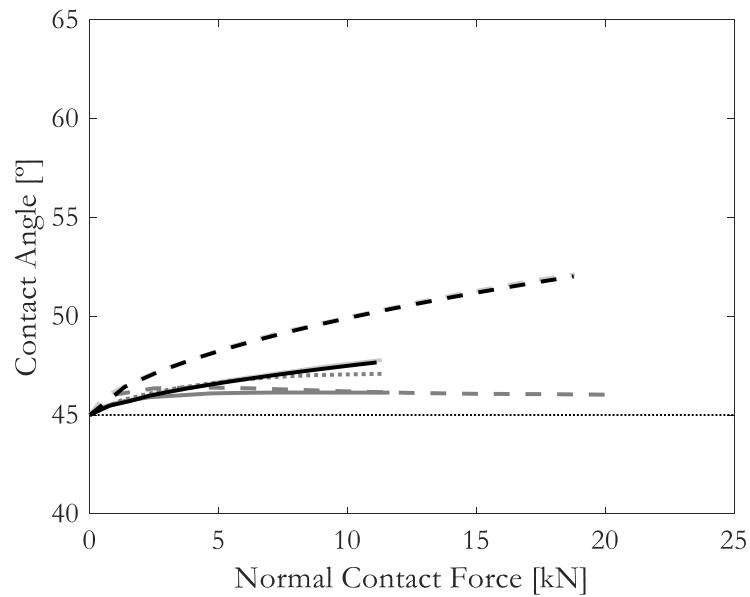
(b)
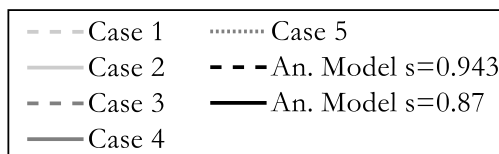
Figure 2.6 Contact forces and angles: (a) Unclamped situation; (b) Clamped situation.

2.4.4 Contact pressure distribution

As the schematic illustration in Figure 2.7 shows, wire twisting involves a contact angle decrease. This phenomenon prevents the ball from climbing and as a consequence, the contact ellipse remains centred on the wire raceway. This statement is demonstrated by the plots in Figure 2.8, which show the contact pressure distribution along the major semi-axis of the contact ellipse for increasing load values. Each pressure point on the plots corresponds to the pressure on one contact element, which was obtained as the average of the element nodal pressures (with the ETABLE command in Ansys®).

Since the studied phenomena are more evident under unclamped boundary conditions, only the results for those cases are represented. For conventional bearings (case 1 and case 2 in Figure 2.8), contact ellipse moves towards the raceway limits as the load increases, and consequently the contact angle increases. On the contrary, for the wire bearing in case 4, Figure 2.8c shows how the contact ellipse remains centred, even though Figure 2.6a shows that the contact angle clearly decreases according to Figure 2.7. Finally, if the wire-ring friction coefficient is increased (case 5), Figure 2.6a and Figure 2.8d show that a larger load is needed for wire twisting to start, which initially tends more towards ball climbing and therefore contact ellipse truncation. As a consequence, ball-raceway contact angle alone is not enough to study contact ellipse truncation in wire bearings. Wire twisting must also be taken into account; this aspect is especially critical if simplified analytical models are to be developed.
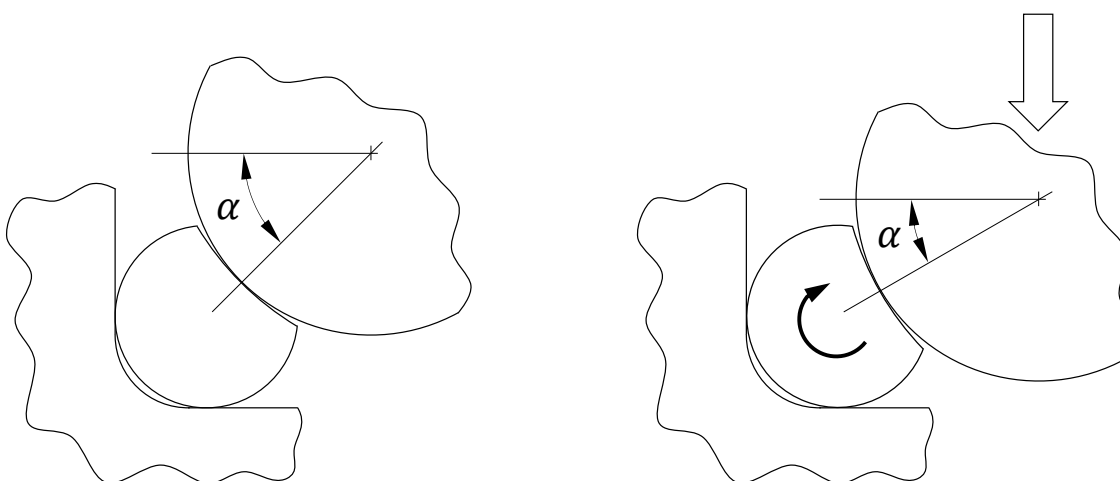
Figure 2.7 Structural response of the wire bearing under axial load.
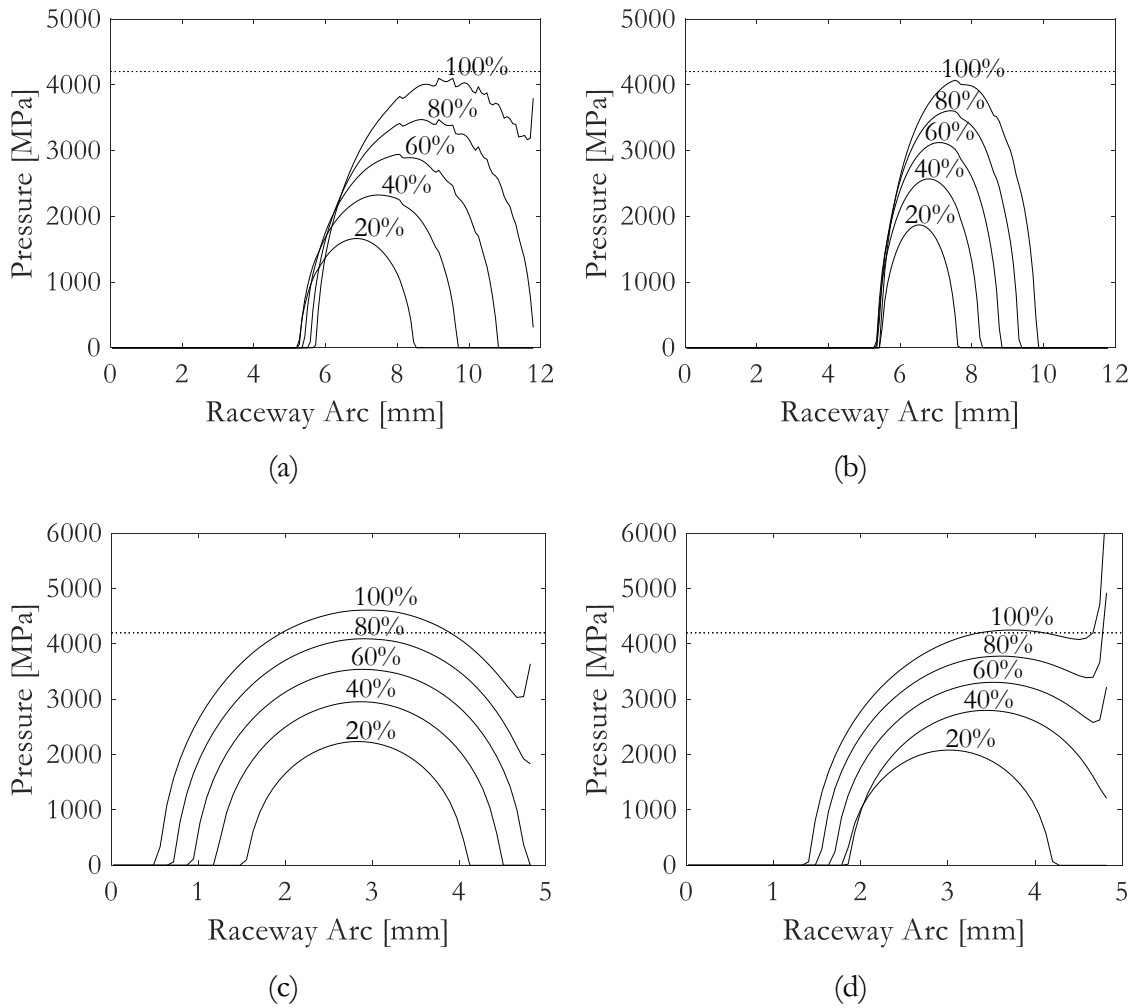
Figure 2.8 Evolution of the pressure along the major semi-axis of the contact ellipse during the loading process (unclamped conditions): (a) Case 1; (b) Case 2; (c) Case 4; (d) Case 5.

Figure 2.9 shows the contact ellipses of the four plots in Figure 2.8 for the 100% of the target axial load (theoretical static load capacity). Note that, according to Figure 2.8, the maximum pressure is not exactly 4200 [MPa] for that load value, as it should be. The static load capacity in Table 2.1 was calculated using the analytical model, which considers rigid rings; as the rings are flexible in the FE model, the contact angles and normal forces are slightly different from those predicted by the analytical model, as is the maximum contact pressure.
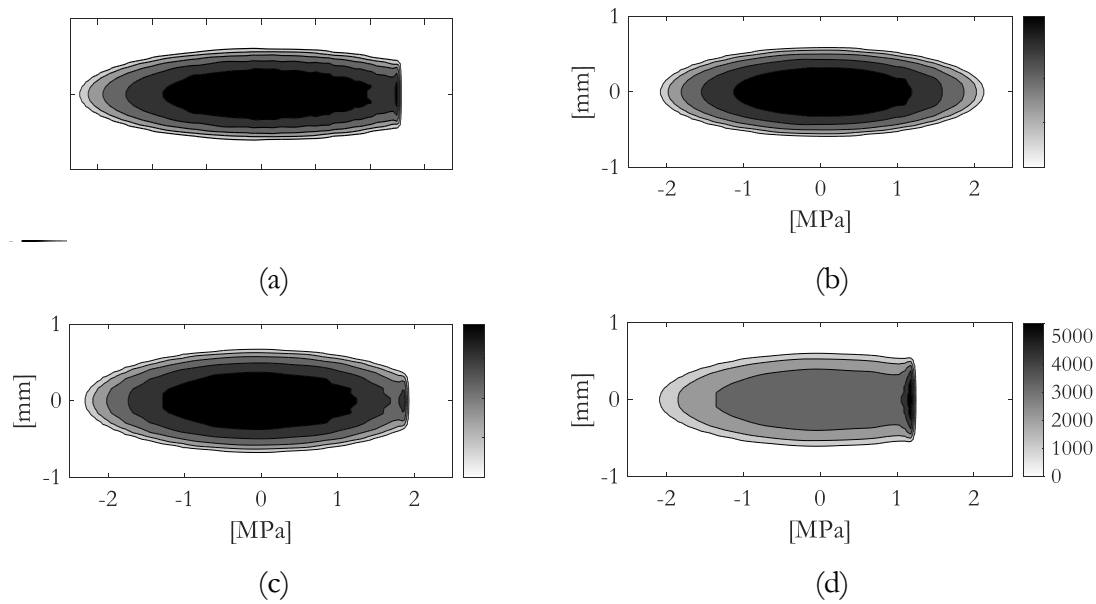
Figure 2.9 Pressure contact ellipse 100% of the target axial load (unclamped conditions): (a) Case 1; (b) Case 2; (c) Case 4; (d) Case 5.

2.4.5 Final remarks

As a final summary, it is worth mentioning that wire race slewing bearings are more flexible in comparison with conventional slewing bearings because of the wire twisting phenomenon and the aluminium rings. Nevertheless, wire twisting prevents the ball from climbing over the raceway, keeping the contact centred in the raceway and preventing contact ellipse truncation. For this reason, wire-ring contact lubrication is so crucial to allow the wire to twist. Despite the benefits of this behaviour in terms of ellipse truncation, the short length of the raceway is not compatible with high osculation ratios, since the large contact ellipse could easily reach the raceway edges anyway.

3 Wire twisting stiffness analytical formula

3.1 Introduction

Wire twisting phenomenon was introduced and explained in the previous chapter, with its relevance proved in wire bearings structural behaviour. For this reason, the correct modelling of the twisting stiffness of the wire can be decisive to correctly assess the load distribution among the rolling elements and therefore the overall mechanical behaviour of the bearing in a potential analytical model. In addition, this twisting stiffness can be implemented in simplified FE models to assess the global mechanical behaviour of bearings and their surrounding structures.

In records such as [165], there are many formulae for the elastic behaviour of many elements under several actions, where the case of slender circular rings is most similar to the wire geometry. Nevertheless, there are two main reasons that underpin the need to develop a specific analytical formula. On the one hand, formulae in [165] are frequently tricky and careful implementation is needed to avoid eventual mistakes. This does not dismiss the value of the current formulations, but emphasizes the need for simpler formulae. On the other hand, the results of the FE analyses performed in the previous chapter, indicate how the wire behaves under realistic boundary conditions. Besides this, the wire twisting phenomenon was identified, so the need to characterize this twisting stiffness also arose. To this end, realistic elastic differential deformation assumptions can be made to accurately approach the real behavior of the wire. Regarding this, the concentrated loads transmitted by the ball-raceway contacts exert a quasi-distributed twisting moment. As a result, the wire twists with respect to its circumferential axis in such a way that the circumferential "fibers" do not bend noticeably and only deform circumferentially.

In this chapter, analytical expressions to calculate the twisting stiffness of two different wire geometries are presented. The selected geometries are the most common for wire-race ball bearings and correspond to the circular and race shaped wire section. Finally, in order to validate the proposed formulae, results are compared with FE simulations.

3.2 Twisting stiffness of a circular section wire

For the first approach, a circular sector wire is considered due to its simplicity. Figure 3.1 shows a wire sector with a span angle of $\beta = 2 \cdot \pi / N_B$ corresponding to the span of one rolling element, where N_B is the rolling element number. This sector has a cyclic-symmetry condition under axial load, in such a way that the rest of the sectors behave the same.
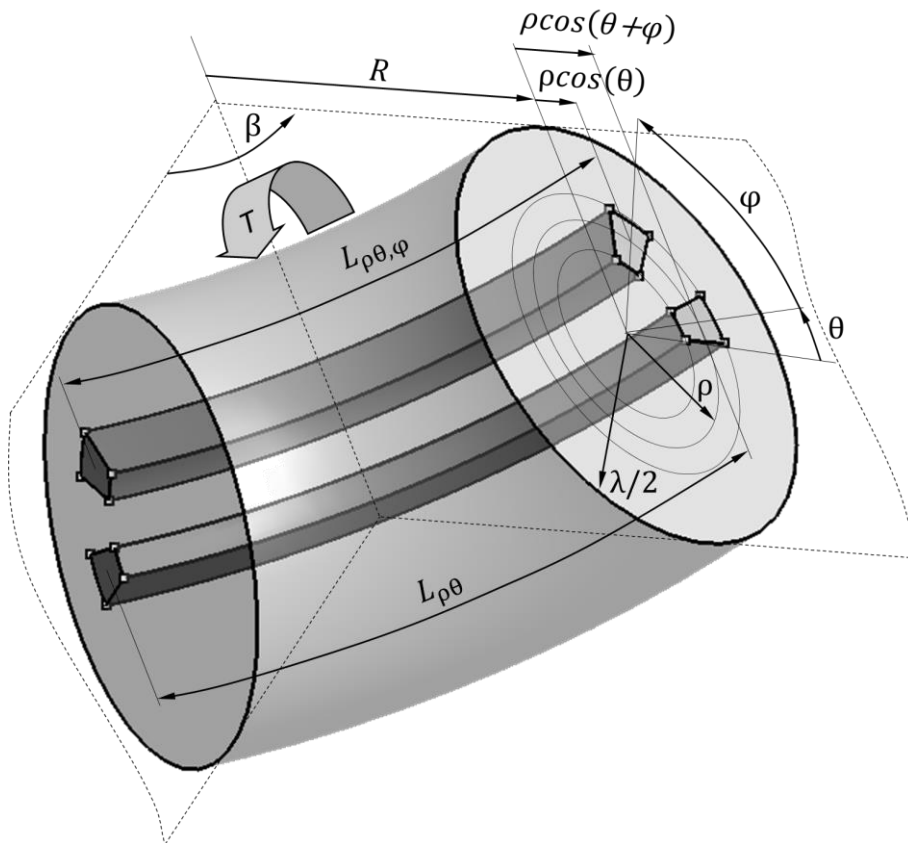
Figure 3.1 Wire sector corresponding to one rolling element.

It will be assumed that a differential element located in polar coordinates $\{\rho, \theta\}$ with a length of $L_{\rho\theta}$, will vary in length to $L_{\rho\theta,\varphi}$ when the wire twists an angle of φ due to a twisting moment:

$$L_{\rho\theta} = \beta \cdot (R + \rho \cdot cos(\theta))$$
$$L_{\rho\theta,\varphi} = \beta \cdot (R + \rho \cdot cos(\theta + \varphi)) \tag{3.1}$$
$$\Delta L_{\rho\theta,\varphi} = L_{\rho\theta,\varphi} - L_{\rho\theta} = \beta \cdot \rho \cdot (cos(\theta + \varphi) - cos(\theta))$$

The differential force needed to perform this length variation can be expressed as the tractive-compressive stiffness differential constant dK multiplied by the length variation $\Delta L_{\rho\theta,\varphi}$ as follows:

$$dF_{\rho\theta,\varphi} = dK_{\rho\theta} \cdot \Delta L_{\rho\theta,\varphi}$$
$$dK_{\rho\theta} = \frac{E \cdot dA_{\rho\theta}}{L_{\rho\theta}} \tag{3.2}$$
$$dA_{\rho\theta} = \rho \, d\rho d\theta$$

And the virtual work contribution of that differential force along the length variation:

$$dW_{\rho\theta,\varphi} = dF_{\rho\theta,\varphi} \cdot \Delta L_{\rho\theta,\varphi}$$
$$dW_{\rho\theta,\varphi} = E \cdot \frac{\left(\Delta L_{\rho\theta,\varphi}\right)^2}{L_{\rho\theta}} \cdot \rho \, d\rho d\theta \tag{3.3}$$
$$dW_{\rho\theta,\varphi} = \beta \cdot E \cdot \frac{(cos(\theta + \varphi) - cos(\theta))^2}{(R + \rho \cdot cos(\theta))} \cdot \rho^3 \, d\rho d\theta$$

The sum of the differential virtual work for all the differential elements over the section of the wire must be equal to the virtual work done by the twisting moment T along the angle φ. From that equality, the twisting moment can be expressed as:

$$T = \frac{\beta \cdot E}{\varphi} \iint_A \frac{(cos(\theta + \varphi) - cos(\theta))^2}{(R + \rho \cdot cos(\theta))} \cdot \rho^3 \, d\rho d\theta \tag{3.4}$$

For small twisting angles (φ) and for a wire mean radius (R) much larger than the wire section radius $\lambda/2$, the previous expression can be simplified:

$$(cos(\theta + \varphi) - cos(\theta))^2 \cong \varphi^2 \cdot sin^2(\theta)$$
$$R + \rho \cdot cos(\theta) \cong R \tag{3.5}$$
$$T \cong \frac{\varphi \cdot \beta \cdot E}{R} \iint_A \rho^3 \cdot sin^2(\theta) \, d\rho d\theta$$

This last equation allows defining the twisting stiffness constant as the twisting moment (T) over the twisting angle (φ):

$$K_T = \frac{\beta \cdot E}{R} \iint_A \rho^3 \cdot sin^2(\theta) \, d\rho d\theta \qquad (3.6)$$

For a circular section, the integral in Eq. (3.6) is easily solved since the integration limits are constant and independent:

$$K_T = \frac{\beta \cdot E}{R} \int_0^{2\pi} sin^2(\theta) \left[\int_0^{\lambda/2} \rho^3 \, d\rho \right] d\theta$$

$$K_T = \beta \cdot E \cdot \frac{\pi \cdot (\lambda/2)^4}{4 \cdot R} \qquad (3.7)$$

Considering the definition for the span angle (β) as a function of the ball number in the bearing, the following expression is obtained:

$$K_T = \frac{E \cdot (\lambda/2)^4}{N_B \cdot R} \cdot \left(\frac{\pi^2}{2} \right) \qquad (3.8)$$

3.3 Twisting stiffness of a race shaped section wire

The wire for most ball bearing applications has a race shaped geometry, which consists on a circular section from which another non-centred circle is substracted. Figure 3.2 shows the geometric parameters of this section expressed in polar coordinates.
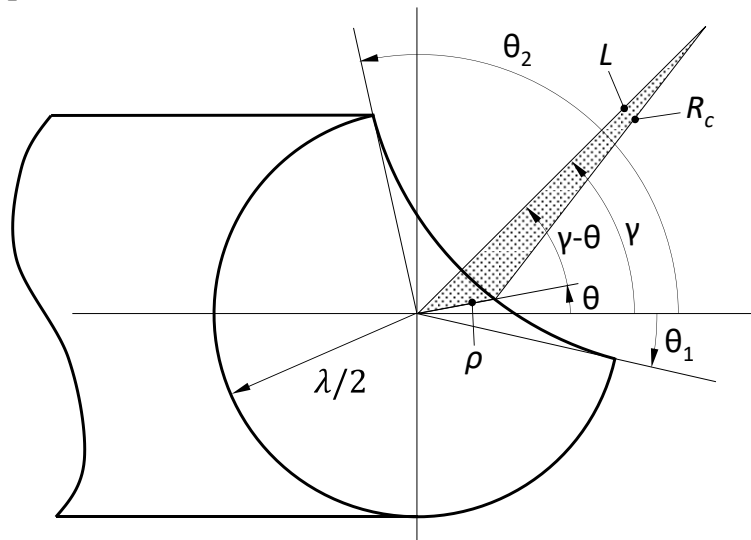
Figure 3.2 Geometrical parameters of the race shaped wire section.

The integral in Eq. (3.6) must be split into two parts. In fact, definite integral I_1 in Eq. (3.9) can be easily solved as in Eq. (3.7) since the integration limits are independent for the two polar variables, but integral I_2 must be solved for $\rho(\theta)$ from θ_1 to θ_2.

$$I = \iint_A \rho^3 \cdot sin^2(\theta)\, d\rho d\theta = I_1 + I_2$$

$$I_1 = \int_{\theta_2}^{2\pi+\theta_1} sin^2(\theta) \cdot \left[\int_0^{(\lambda/2)} \rho^3\, d\rho \right] d\theta \tag{3.9}$$

$$I_2 = \int_{\theta_1}^{\theta_2} sin^2(\theta) \cdot \left[\int_0^{\rho(\theta)} \rho^3\, d\rho \right] d\theta$$

Then, integral I_1:

$$I_1 = \int_{\theta_2}^{2\pi+\theta_1} sin^2(\theta) \cdot \left[\int_0^{(\lambda/2)} \rho^3\, d\rho \right] d\theta = \frac{(\lambda/2)^4}{4} \cdot \left[\frac{\theta}{2} - \frac{sin(2\theta)}{4} \right]_{\theta_2}^{2\pi+\theta_1}$$

$$I_1 = \frac{(\lambda/2)^4}{4} \cdot \left(\pi + \frac{(\theta_1 - \theta_2)}{2} + \frac{(sin(2\theta_2) - sin(2\theta_1))}{4} \right) \tag{3.10}$$

For integral I_2, the equation of a non-centered circumference is derived in the form of $\rho(\theta)$ in first place. Applying the law of the cosine to the shaded triangle in Figure 3.2:

$$R_c^2 = L^2 + \rho(\theta)^2 - 2 \cdot L \cdot \rho(\theta) \cdot cos(\gamma - \theta) \tag{3.11}$$

Solving for the first value of $\rho(\theta)$ which fulfills Eq. (3.11),

$$\rho(\theta) = L \cdot cos(\gamma - \theta) - \sqrt{R_c^2 - L^2 \cdot sin^2(\gamma - \theta)} \tag{3.12}$$

Therefore, integral I_2 can be solved as:

$$I_2 = \frac{1}{4} \cdot \int_{\theta_1}^{\theta_2} sin^2(\theta) \cdot \rho(\theta)^4\, d\theta$$

$$I_2 = \frac{(\lambda/2)^4}{4} \cdot \int_{\theta_1}^{\theta_2} sin^2(\theta) \cdot \tag{3.13}$$

$$\cdot \left(\frac{L}{(\lambda/2)} cos(\gamma - \theta) - \sqrt{\left(\frac{R_c}{(\lambda/2)}\right)^2 - \left(\frac{L}{(\lambda/2)}\right)^2 \cdot sin^2(\gamma - \theta)} \right)^4 d\theta$$

Which must be solved numerically for $R_c/(\lambda/2)$, $L/(\lambda/2)$ and γ. Regarding the integration limits for both integrals, depending on the geometrical parameters in Figure 3.2, the values for θ_1 and θ_2 can be derived, performing $\rho(\theta) = (\lambda/2)$ in Eq.(3.14):

$$\begin{aligned} \theta_1 &= \gamma - arccos\left(\frac{1 + (L/(\lambda/2))^2 - (R_c/(\lambda/2))^2}{2(L/(\lambda/2))}\right) \\ \theta_2 &= \gamma + arccos\left(\frac{1 + (L/(\lambda/2))^2 - (R_c/(\lambda/2))^2}{2(L/(\lambda/2))}\right) \end{aligned} \tag{3.14}$$

At this point, a DoE is planned to obtain an engineering formula in order to make a reasonable approximation for integrals in Eq. (3.9). The arranged DoE is a full factorial and it was done for the values in Table 3.1. These parameters were not randomly chosen, they are within the limits generally adopted by the manufacturers.

Table 3.1 Integral in Eq. (3.10) for geometrical parameters within the common design range, valid for $\gamma = \pi/4$, $\gamma = 3\pi/4$, $\gamma = 5\pi/4$ and $\gamma = 7\pi/4$.

$R_c/(\lambda/2)$	$L/(\lambda/2)$	$L/(\lambda/2) - R_c/(\lambda/2)$	$I/(\lambda/2)^4$
2.00	2.25	0.25	0.522088805
2.50	2.75	0.25	0.513905797
3.00	3.25	0.25	0.503645074
2.00	2.50	0.50	0.609857837
2.50	3.00	0.50	0.604207922
3.00	3.50	0.50	0.600254386
2.00	2.75	0.75	0.708211997
2.50	3.25	0.75	0.705624706
3.00	3.75	0.75	0.703774932
2.00	3.00	≥ 1	$\pi/4$
2.50	3.50	≥ 1	$\pi/4$
3.00	4.00	≥ 1	$\pi/4$
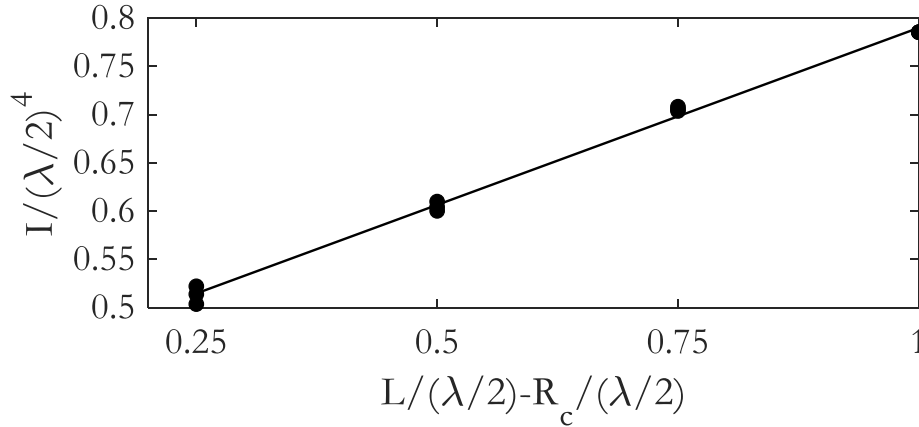
From Table 3.1 it can be reasonably concluded that the value of the Integral has a strong linear relationship with parameter $(L/(\lambda/2) - R_c/(\lambda/2))$ and second order dependences can be mispriced. The following equation can be derived via Least Squares, forcing the integral to be $\pi/4$ for $(L/(\lambda/2) - R_c/(\lambda/2)) = 1$:

$$I \approx (\lambda/2)^4 \cdot \left(\frac{\pi}{4} - 0,36 \cdot \left[1 - \left(\frac{L}{(\lambda/2)} - \frac{R_c}{(\lambda/2)}\right)\right]\right) \qquad (3.15)$$

Then, the stiffness constant can be expressed as:

$$K_T = \beta \cdot E \cdot \frac{(\lambda/2)^4}{R} \cdot \left(\frac{\pi}{4} - 0.36 \cdot \left[1 - \left(\frac{L}{(\lambda/2)} - \frac{R_c}{(\lambda/2)}\right)\right]\right)$$

$$K_T = \frac{E \cdot (\lambda/2)^4}{N_B \cdot R} \cdot \left(\frac{\pi^2}{2} - 0.72 \cdot \pi \cdot \left[1 - \left(\frac{L}{(\lambda/2)} - \frac{R_c}{(\lambda/2)}\right)\right]\right) \qquad (3.16)$$

3.4 Correlation with FE models

3.4.1 Simplified load cases

The first step to check the validity of the formulae involved both circular and race shaped wire sections being modelled in Ansys®, considering the assumptions made for the development of the formulae. Table 3.2 shows the geometrical parameters used for the validation FE models, which are shown in Figure 3.3. It was deemed appropriate to create two FE models per section type, one 2D axisymmetric FE model and another 3D cyclic symmetric FE model. This way, the effect of the boundary conditions can be evaluated. In the 2D models, the twist is imposed to the whole section, while in the 3D models, the twist is imposed on both lateral sections. Besides this, symmetry boundary

conditions were applied in the 3D model. Finally, in order to prevent rigid body motion and avoid convergence problems, the central node of the sections with applied boundary conditions is fixed.

Table 3.2 Geometrical parameters for the validation.

E [GPa]	N_B	R [mm]	$\lambda/2$ [mm]	$R_c/(\lambda/2)$ [mm]	$L/(\lambda/2)$ [mm]	γ [º]
210	82	227	3.3	-	-	-
210	82	227	3.3	3	3.5	45

(a)   (b)

(c)   (d)
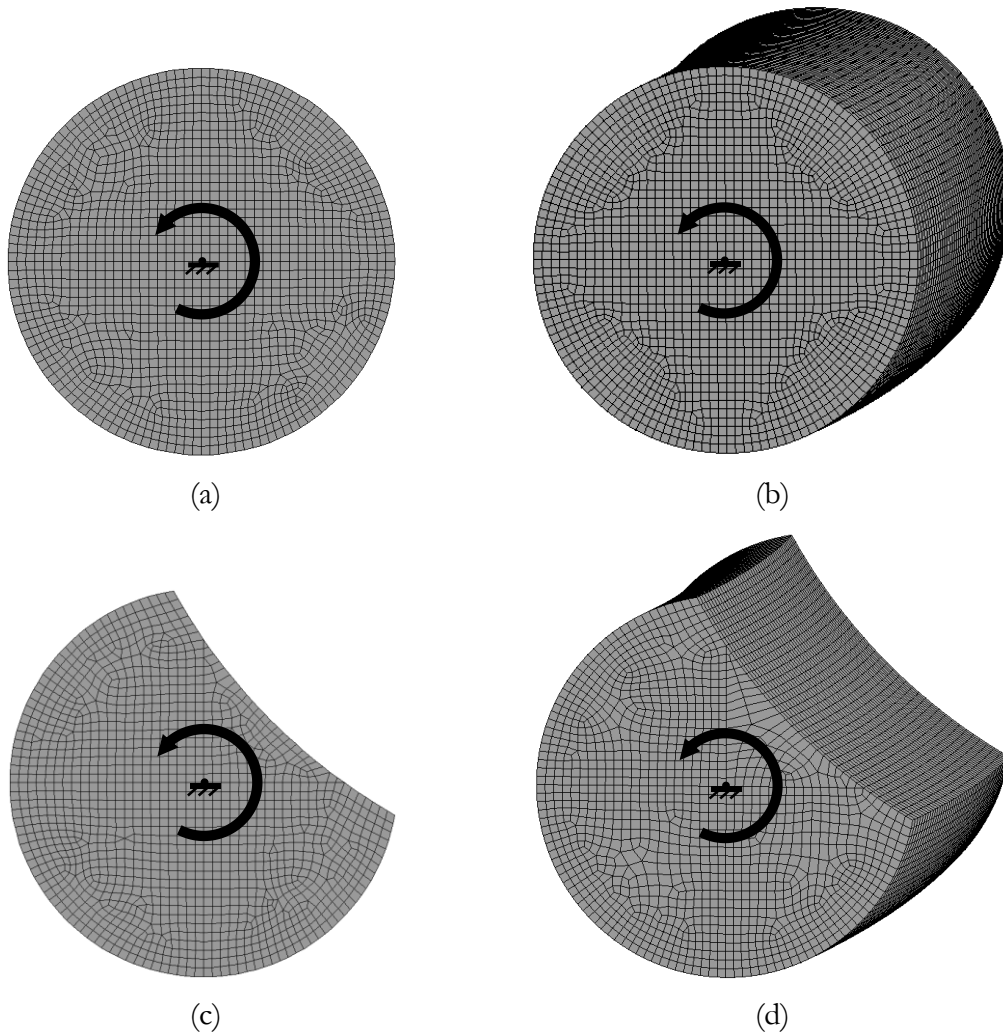
Figure 3.3 FE models: (a) Circular section 2D model; (b) Circular section 3D model; (c) Race shaped section 2D model; (d) Race shaped section 3D model.

After performing the FE analyses, the behaviour observed between the 2D and 3D models was identical. Because of this and for simplification reasons, only the stiffness results of the 2D model are included in Figure 3.4. The behaviour of the circular section does not depend on the positive or negative direction of the twist. However, the race shaped section shows stiffer behaviour when the twist is applied in a counter clockwise direction. The behaviour of $\gamma = 45°$ was shown only, since the case $\gamma = 135°$ behaves the same, but for the opposite sign of the twisting angle.

Circular section twisting stiffness

Race shaped section twisting stiffness
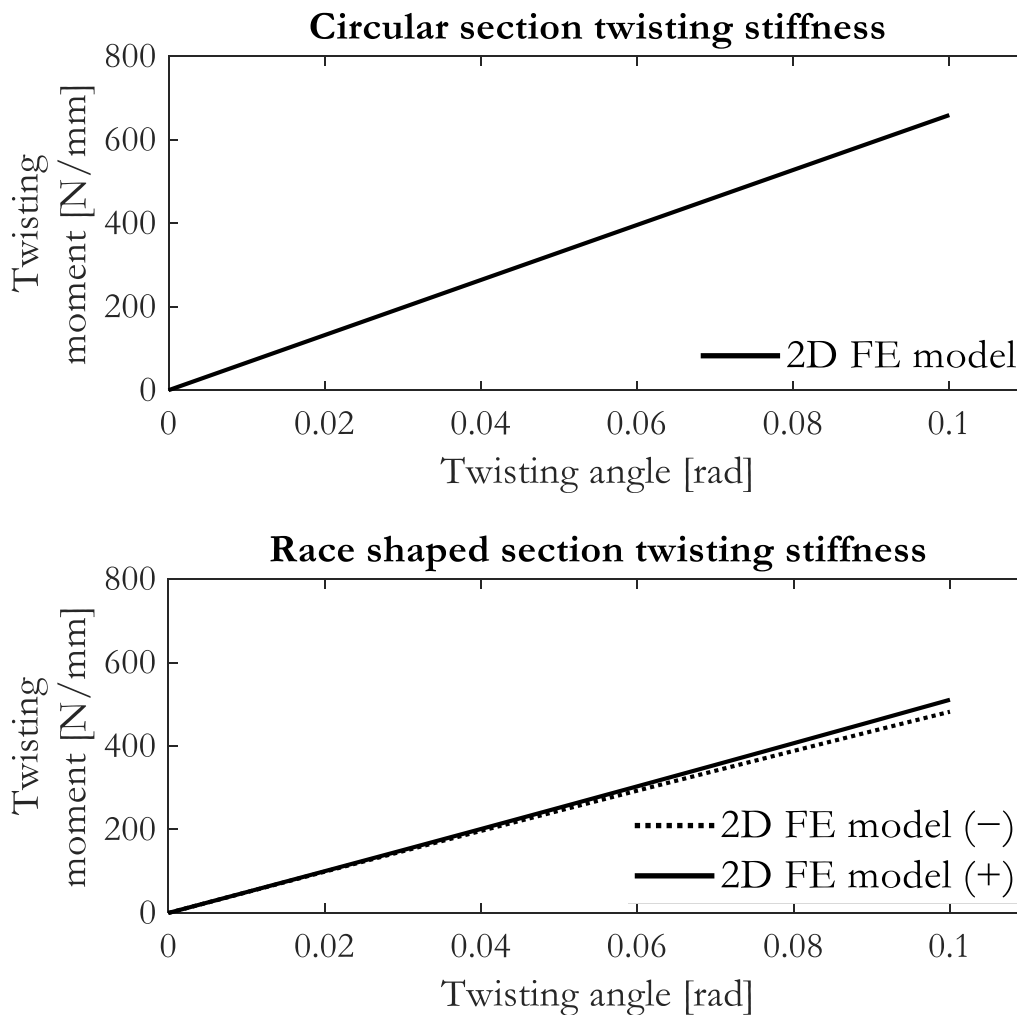
Figure 3.4 Twisting stiffness of the 2D axisymmetric FE model.

Twisting stiffness is very linear for both circular and race shaped sections, so it is fair to compare FE and analytical results with stiffness constants and obtain the deviation in terms of error. The first stiffness constant defined (K), results from the application of a linear regression to the FE results. This stiffness constant represents the stiffness along the entire range. The second stiffness constant K^{Origin} refers to the stiffness of the first load step of the FE model, i.e. considering the initial undeformed geometry. As the analytical model is

based on this undeformed geometry, K^{Origin} coincides with the analytical stiffness, and its value is the same for any twisting direction. However, as the twisting angle increases, the wire section rotates and therefore its stiffness varies. In contrast to the analytical model, the FE model accounts for this phenomenon (large displacements), and for that reason FE and analytical stiffness values are slightly different. Despite all these considerations, the discrepancies between the analytical and FE model are negligible, as can be seen in the stiffness constants comparison of Table 3.3 and the relative error obtained.

Table 3.3 Twisting stiffness constants.

	K	K^{Origin}	$K^{An.}$	Error K	Error K^{Origin}
		[N·mm/rad]		[%]	[%]
2D Circular sec.	6596	6602	6602	0.1	0.0
3D Circular sec.	6591	6598	6602	0.2	0.1
2D Race shaped sec.	5080 (+) 4854 (−)	4975	5089	0.2 4.6	2.3
3D Race shaped sec.	5075 (+) 4850 (−)	4970	5089	0.3 4.7	2.4

3.4.2 Realistic load case

To further explore the validity of the stiffness constant calculated using the analytical approach, a more realistic load case shown in Figure 3.5 was considered. In this case, a rigid support for the wire was modelled, as well as a rigid ball as a loading element. The ball approaches the wire in such a direction that finally contact occurs almost on the edge of the wire, which is the situation in which the distribution of applied torque is the furthest possible from the theoretical assumption. Analyses were done for friction coefficients $\mu = 0$ and $\mu = 0.1$ for the three contact pairs defined in the model, with the latter case being a very typical one for four-point contact wire-race slewing bearings.
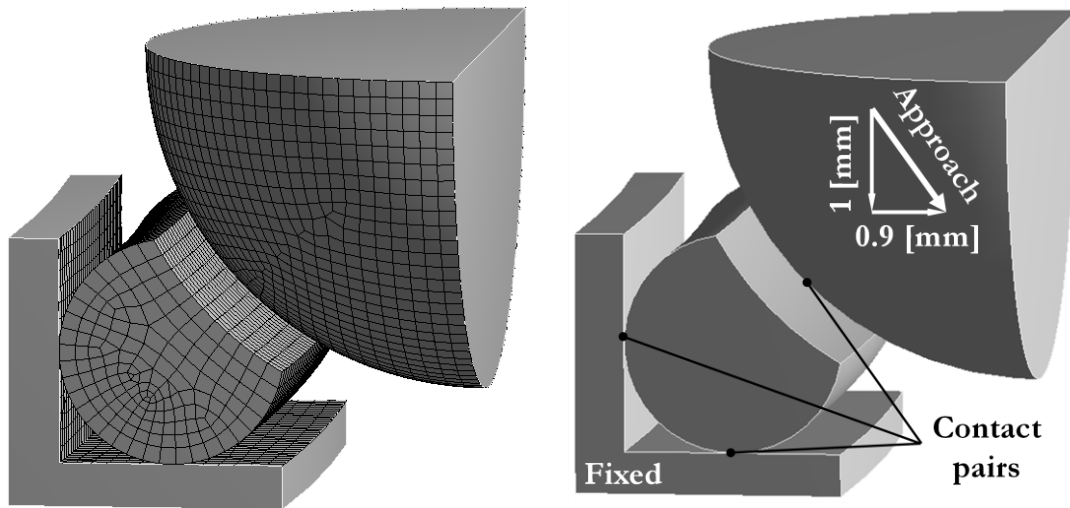
Figure 3.5 Realistic load case FE model: (a) Mesh; (b) Loads and boundary conditions.

Figure 3.6 shows the FE results in terms of contact pressure distribution and wire deformation. Regarding the contact pressure results, the distribution on the top corresponds to the first load step and the one on the bottom to the final displacement condition. It can be observed how the load acts on the lower edge of the wire generating a twisting torque. The displacement imposed on the ball is the same for $\mu = 0$ and $\mu = 0.1$ cases, as is the displacement (and twisting angle) of the wire.
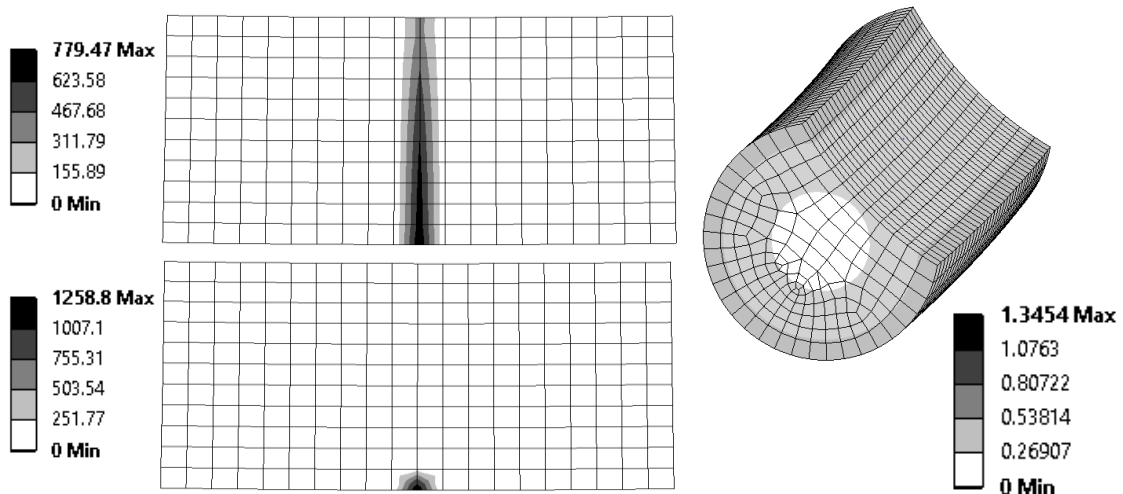
Figure 3.6 Pressure distribution (in [MPa]) and wire deformation (in [mm]).

In order to evaluate the influence of the wire-ring contact behaviour, the wire twisting stiffness is calculated for both cases. Figure 3.7 shows the displacements and reaction forces, where it can be seen that there are friction forces only in the $\mu = 0.1$ case. These friction forces also generate a larger ball-wire contact force in order to achieve the static equilibrium.
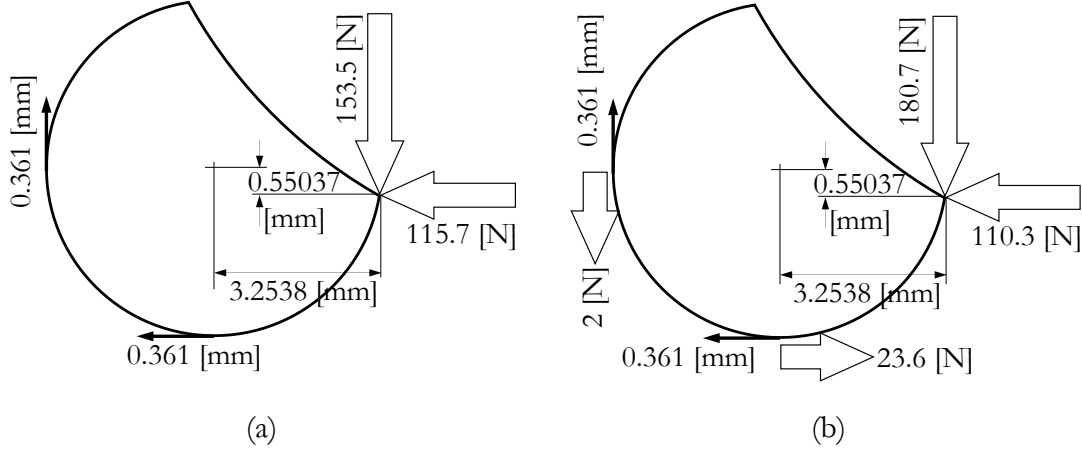
Figure 3.7 Displacements and friction forces: (a) $\boldsymbol{\mu} = 0$ case; (b) $\boldsymbol{\mu} = 0.1$ case.

As a result, the wire twisting stiffness is obtained in Equations (3.17) and (3.18) for the $\mu = 0$ and $\mu = 0.1$ cases respectively. Both twisting stiffnesses are identical regardless of the friction coefficient, as initially expected.

$$T = 153.5 \cdot 3.2538 + 115.7 \cdot 0.55037 = 564 \ [N \cdot mm]$$
$$\varphi = 0.361 \cdot 3.3 = 0.11 \ [rad] \tag{3.17}$$
$$K = T/\varphi = 5146 \ [N \cdot mm/rad]$$

$$T = 180.7 \cdot 3.2538 + 110.3 \cdot 0.55037 - (2.0 + 23.6) \cdot 3.3$$
$$T = 564 \ [N \cdot mm]$$

$$\varphi = 0.361 \cdot 3.3 = 0.11 \ [rad]$$
$$K = T/\varphi = 5146 \ [N \cdot mm/rad]$$

$$\tag{3.18}$$

Finally, Figure 3.8 shows the comparison between the FE and the analytical results. It can be observed that the analytical stiffness approaches satisfactorily the FE results for both frictionless and frictional contact conditions. In terms of stiffness constants, Table 3.4 features the values of K and K^{Origin} of both FE models and the analytical formulae. The relative error of the analytical stiffness constant is also obtained, which is small for K but larger for K^{Origin}. There is no evident cause for this behaviour, since the more realistic situation can lead to the appearance of eventual hidden phenomena. However, the sound overall performance of the analytical formulae assesses the validity of the proposed wire twisting calculation method.
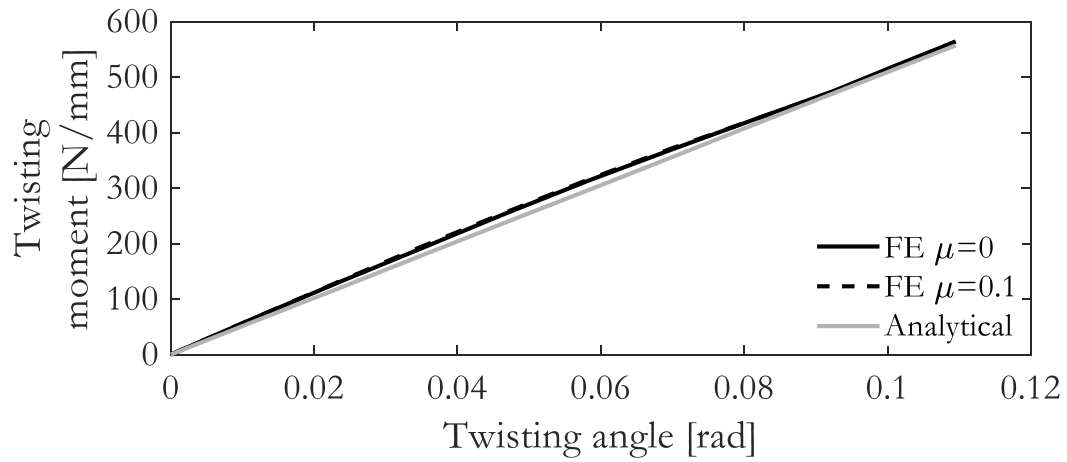
Figure 3.8 Stiffness constants calculation for: (a) $\mu = 0$; (b) $\mu = 0.1$.

Table 3.4 FE and analytical stiffness constants.

	K	K^{Origin}	$K^{An.}$	Error K	Error K^{Origin}
	[N·mm/rad]			[%]	[%]
FE $\mu = 0$	5209	5641	5089	2.3	9.8
FE $\mu = 0.1$	5215	5641	5089	2.4	9.8

4 Four-point contact wire-race bearing analytical model

4.1 Introduction

Finite Element simulations are a common tool used in the design stage of a component, as many results can be obtained accurately. Nevertheless, simulations are complex, computationally costly and require experienced structural analysts to perform them. Another strategy lies in performing simulations with analytical calculation tools. These tools are based on analytical models, which represent the physical phenomena that define the structural behaviour of the component. These tools are easier to use for the end user, and faster and simpler. For these reasons, analytical calculation tools are an alternative to take into consideration for preliminary designs or for components whose structural behaviour is well known. However, the main disadvantage of analytical models lies in the need to assume simplifications for development purposes. This means that the tool is applicable and accurate only if all the assumptions made are fulfilled by the component being designed. Analytical models usually have ranges of applications or preliminary considerations, which makes them not as versatile and accurate as FE.

A four-point contact wire-race slewing bearing analytical model is presented in this chapter. Given the complexity of the component, only axial or tilting moment load cases are considered for this first approach. In order to consider any bearing geometry, the analytical model is based on parametric equations. The analytical model can be used to obtain the bearing stiffness, static load capacity, contact force and contact angle. In the following sections, the foundations and the formulation of the analytical model is explained together with the validation carried out via a comparison with a FE reference model.

4.2 Analytical model

4.2.1 Assumptions and simplifications

As for every analytical modelling, the first step consisted in recognizing the underlying phenomena and designing a strategy to screen them in a simple way. This work was already carried out in Chapter 2, where it was stated that the most relevant phenomena that affects the structural behaviour of the four-point contact wire-race slewing bearings are the ball climbing and wire twisting phenomena. Of course, the stiffness of the contacts have a significant effect on the structural response of the bearings and must be modelled properly.

Once the structural behaviour of the component has been studied, the next step consists of making the necessary number of assumptions and simplifications that allow for the analytical model to be developed. Of course, these assumptions and simplifications suppress the possibility of calculating certain results and may introduce slight errors; however, the advantages of the analytical model clearly outweigh these limitations.

First, it can be assumed that the deformations of one sector with one rolling element do not affect the adjacent sectors; the large mean diameter and the cyclic symmetry of the geometry allow for this simplification to be made. This way, the structural response of the whole bearing can be obtained as the sum of the structural response of all the independent sectors. However, this does not mean that the twisting stiffness of the wire is not considered.

The second assumption is related with the loading, where only the axial load is considered. This allows for the calculation of the response of the bearing under axial load, tilting moment or a combination of both. On the one hand, it is only necessary to solve one sector to obtain the whole bearing response under axial load. On the other hand, a tilting moment or a combination of tilting moment and axial load can be distributed as a different axial load acting on each sector.

Thirdly, a sector supporting axial load always transmits the load through one diagonal (two-point contact situation). This happens during the entire loading process only if the rolling element is not preloaded. As a result of the two-point contact situation, there is no need to model the other two contacts.

The fourth assumption is related to the stiffness of the inner and outer rings, which is almost identical for large mean diameters. As a result, a symmetry can

be applied in such a way that only the contacts corresponding to one of the two sides of the contact diagonal are modelled, i.e. one ball-wire contact and the corresponding wire-ring contact pair.

Finally, this is a first approach to represent the structural behaviour of these kind of bearings. For this reason, the strategy to follow is in line with other works introduced included in Section 1.4.2 and related to bearing analytical models. In these works, the analytical models are firstly developed considering boundary conditions that assume rigid rings, i.e. only considering local deformation of the contacts. On this basis, the flexibility of the rings can be later implemented in future works.

4.2.2 Contact stiffness calculation

To properly represent the structural response of the bearing, it is necessary to obtain the expressions that relate the forces and deformations of the contacts. In this case, analytical formulae available in the literature were found adequate to serve this purpose. The literature review about the normal contact problem was carried out in Section 1.4.1, so there is no need on deepen into the topic.

During recent years, the simplified formulation proposed by Houpert [47] has been widely used to represent the behaviour of the ball-raceway contact. For this reason, the decision to use this formulation for the ball-wire contact was almost immediate. Even though the proposed engineering approaches simplify the Hertz's formulation [43,44], some mathematical operations were performed in order to simplify even more this formulation. All these mathematical procedures are attached in Appendix A, and only the final expressions that were used for this analytical model are included here. The contact behaviour in terms of force/deformation is represented by Equation (4.1). Because of the nature of the problem, there are two possibilities by which to obtain the stiffness constant k_B , which depends on the osculation ratio of the contact (s).

$$Q = k_B \cdot \delta^{\frac{3}{2}}$$

$$k_B = \begin{cases} \dfrac{102456.8 \cdot D_w^{1/2}}{(1-s)^{0.2919}} & for\ 0 < s < 0.886 \\[4mm] \dfrac{88222.45 \cdot D_w^{1/2}}{(1-s)^{0.3621}} & for\ 0.886 < s < 0.992 \end{cases} \qquad (4.1)$$

Regarding the wire-ring contacts, plain strain conditions were considered, assuming a cylinder-elastic half-space contact under a distributed compressive load. This situation does not really happen, but these assumptions must be made in order to simplify the model. On the one hand, the large curvature radius on slewing bearings allows the cylinder-plane assumption to be taken into account. On the other hand, each ball acts as a punctual load over the wire raceway. However, a high filling ratio reduces the closure between contacts, which allows the contact force to be considered as a distributed load. As was explained in detail in the introduction chapter, there are many formulations that can be used for the cylinder-plane contact. In order to assess their accuracy, the stiffness results obtained with different formulations are compared with cylinder elastic half-space contact FE model results.

The line contact formulations proposed by Puttock [56], Tripp [58] and Johnson [59] and Hamrock [60] were considered for the comparison. More information about these formulations can be found in the introduction chapter. These formulations can be found in Equations (1.14), (1.16) and (1.19) respectively.

The FE model used for the comparison (shown in Figure 4.1) was built considering the 2D plane strain assumption. The surface was divided into various partitions to perform a fine mesh in the vicinity of the contacts and allow a transition to coarser elements in the interior zones. The contact was defined as frictionless, according to the assumptions made in the formulations. Defining the contact as frictional would have had no implications, since the aim of the analysis is to study the normal contact problem. The Augmented Lagrange formulation was defined, contact stiffness was updated each iteration and the penetration tolerance was set as 1 [μm]. Symmetry boundary conditions were applied to the edges of the symmetry plane, the other two edges of the elastic half-space were fixed and load was applied as an imposed displacement on the upper cylinder edge.
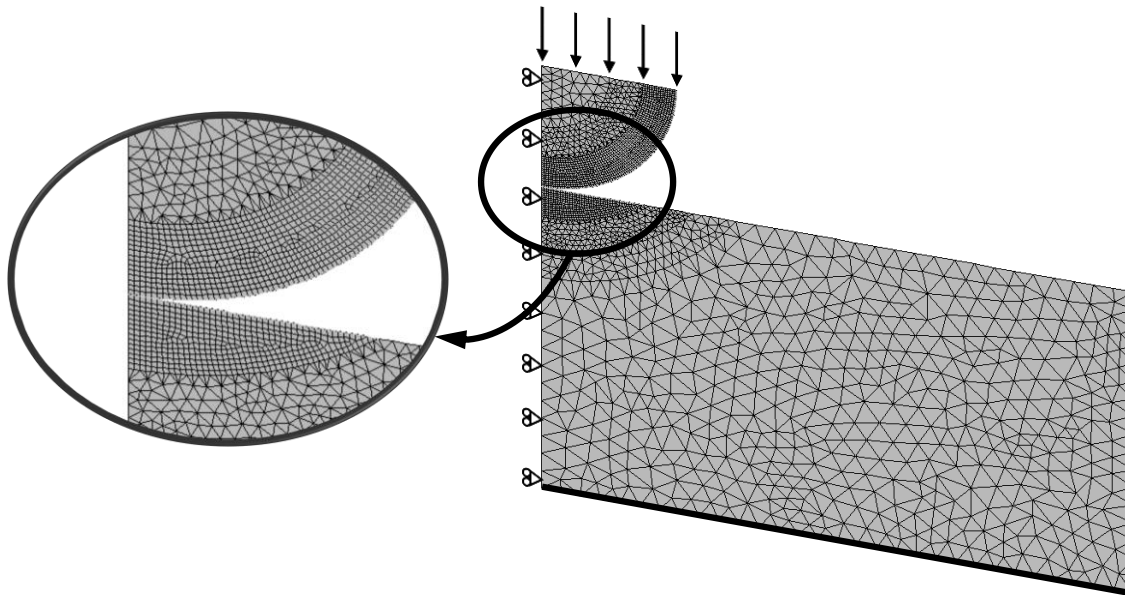
Figure 4.1 2D plane strain FE model for the cylinder-plane formulations validation.

Table 4.1 features the geometrical parameters and material properties of the study case. The proposed analytical formulations allow for the calculation of the contact deformation between bodies of different materials, which is quite convenient for the wire-ring contact case. As has already been stated, rolling elements and wires are manufactured with hardened steel while rings are commonly made of aluminium. To be thorough, analytical formulations were compared with FE results for two cases: steel-steel and steel-aluminium contacts.

Table 4.1 Geometrical parameters and material properties.

D_w [mm]	L [mm]	E_{Steel} [GPa]	$E_{Al.}$ [GPa]	ν_{Steel}	$\nu_{Al.}$
8	4	200	70	0.3	0.33

At this point, the loading level that must be applied needs to be defined. The accepted convention proposed by the ISO-76 standard [24,25] states that contact failure occurs at a contact pressure value of 4000 [MPa], which is obtained in an elastic calculation. For this reason, the maximum contact force in both study cases was the one that reached that pressure value in the steel-steel contact FE model. It is true that the steel-aluminium contact may fail at a lower contact force value, but the purpose of this comparison lies in validating some analytical formulations.

The results of the steel-steel contact study case are shown in Figure 4.2a. On the one hand, a perfect match is achieved between the formulation proposed by Puttock [56] and FE results. On the other hand, the formulations of Tripp [58] and Johnson [59] and Hamrock [60] present a significant deviation. Regarding the results of the steel-aluminium contact study case, the formulation proposed by Puttock [56] differs a little from the results obtained using the FE analysis and the other two formulations resulted in a more pronounced deviation.
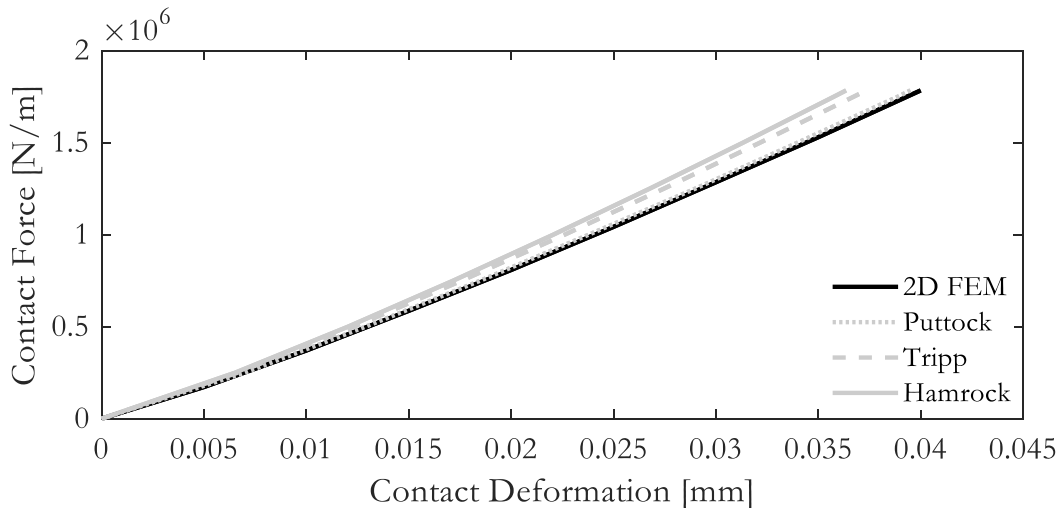
(a)
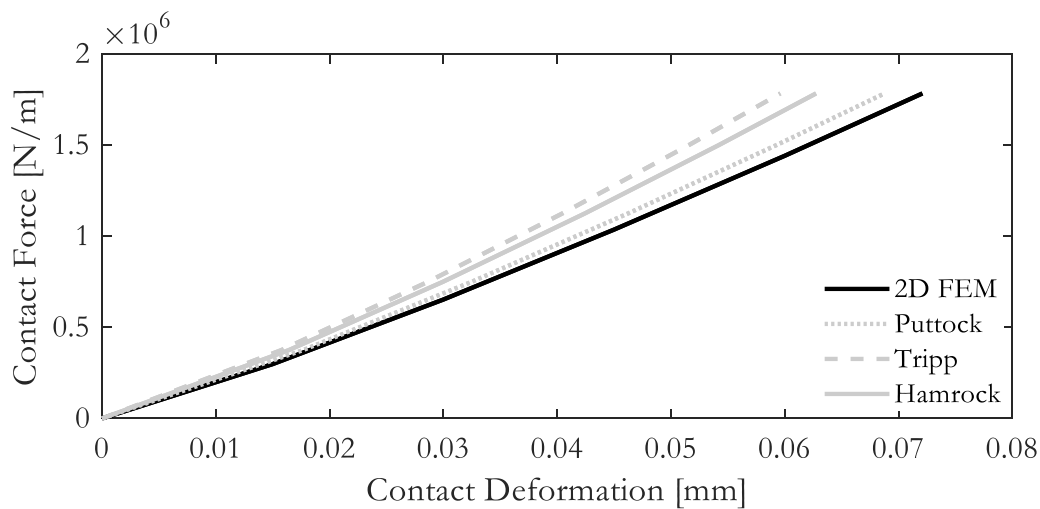
(b)

Figure 4.2 Validation of the analytical cylinder-plane formulations: (a) Steel cylinder-Steel halfspace; (b) Steel cylinder-Aluminium halfspace.

According to the observed results, it appears appropriate to choose the formulation developed by Puttock [56] to represent the stiffness behaviour of the wire-ring contact.

4.2.3 Description of the analytical approach

The description and the mathematical background of the analytical model is presented in this section. The proposed analytical model is based on a mechanism built with rigid beams and springs. Linear springs are used to represent the normal contact behaviour and a torsional spring is also used to represent the twisting stiffness of the wire. The role of the rigid beams consists of transmitting the forces and moments through the structure.

Figure 4.3 shows the mechanism created for the analytical model. The modelling of the ball-wire contact was adapted from the simplified mechanism proposed by Golbach [123], Smolnicki et al. [124,125] and Daidié et al. [126]. The ball-wire contact behaviour is represented by a tension-only spring. This spring is not randomly positioned. It must connect the centres of the raceway arcs. In this case, due to the symmetry simplifications, the spring connects one raceway arc centre and the centre of the ball. This spring is attached to a rigid beam that transmits the forces and moments to the wire centre through a torsional spring, which represents the torsional stiffness of the wire. The wire is considered to be a rigid body, which, under the action of the transmitted forces, compresses the springs that represent the response of the wire-ring contacts.
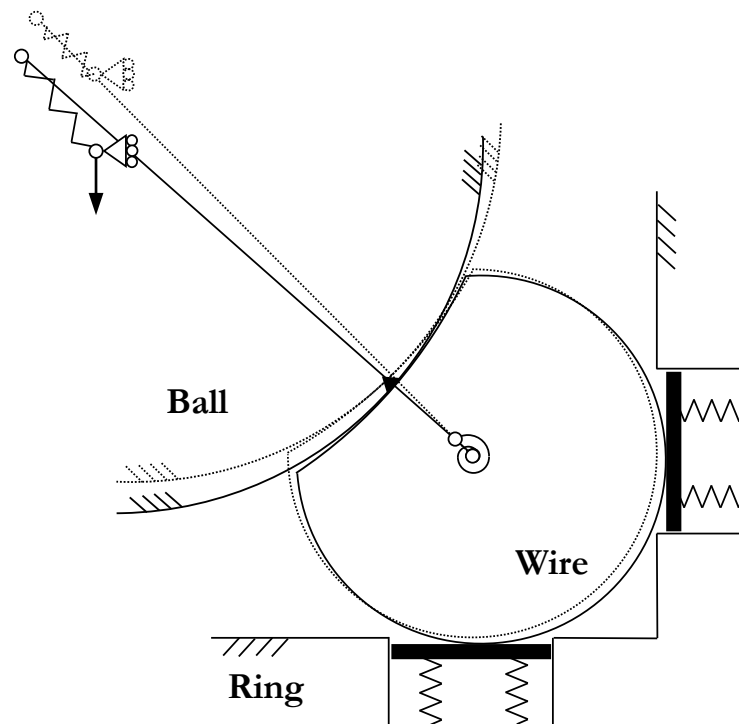
Figure 4.3 Deformed and undeformed (dotted) shapes of the mechanism for the analytical model.

The deformed shape of the mechanism reveals that the wire twisting phenomenon can be represented. Besides, ball climbing is also considered, since the contact angle is defined by the angular position of the tension-only spring.

Regarding friction forces, ball-wire contact is assumed to be rolling, so they were considered negligible. However, wire-ring contact friction forces must be considered. Otherwise, nothing would counteract the generated twisting moment and the equilibrium would be unreachable. Modelling the wire-ring friction forces is not straightforward. In preliminary FE simulations, it was found that at the beginning of the loading process both contacts are in stick. Shortly after, the ball climbs over the raceway and generates the enough twisting moment to turn one of the contacts into slip (Figure 4.4a). This situation continues until the static load capacity is reached (Figure 4.4b). Eventually, and under less restrictive boundary conditions, both contacts may be in slip.

(a)

(b)

☐ Near	☐ Sliding	■ Sticking
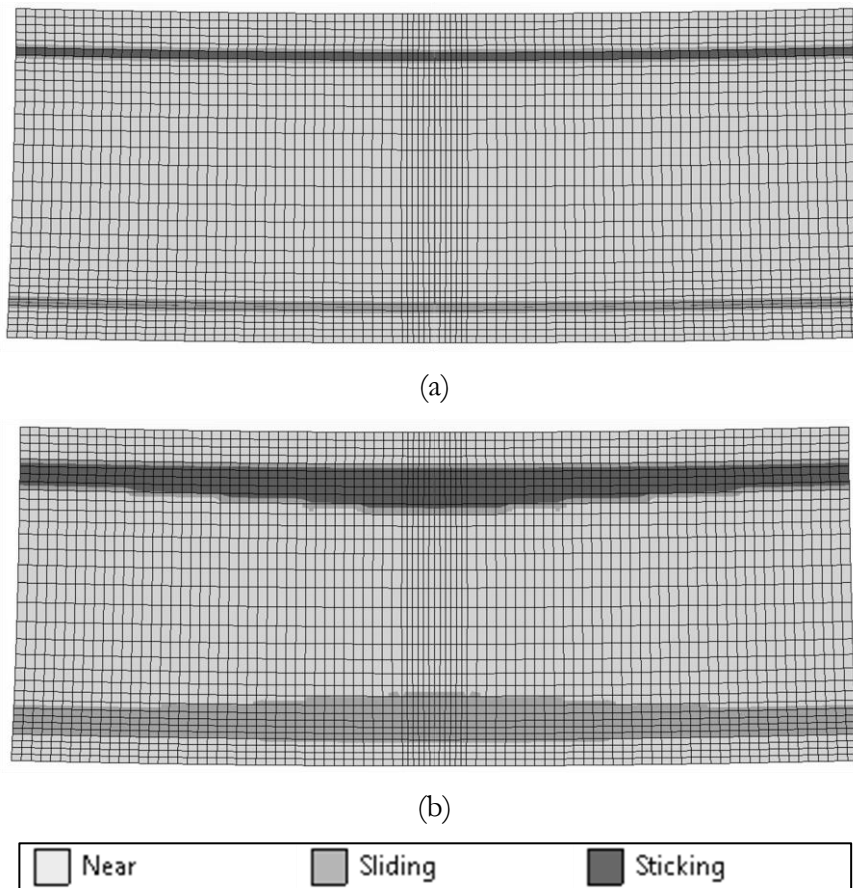
Figure 4.4 Wire-ring contact status: (a) One contact starts to slide at 10% C_{0a}; (b) Contact status at 100% C_{0a}.

Now it is clear that there are three different alternatives for the wire-ring contacts status: stick-stick, slip-stick and slip-slip. The initial stick-stick situation is the most problematic, since the friction forces of both contacts are lower

than the friction coefficient multiplied by the normal contact forces. This means that they are variables of the system. However, it is very complicated to define the tangential contact problem and no simple solution was found.

The difficulty of modelling the tangential problem together with the fugacity of the phenomenon, lead to us ignoring this initial situation and assuming that the initial situation is slip-stick. This assumption may lead a minor error, but makes the definition of the analytical model feasible. In this situation, the tangential force of the contact in slip is easily defined with the Coulomb contact theory. However, the frictional force of the contact in stick is still a variable. For this reason, an additional equation must be included. This equation is based on the compatibility of deformations that occur when the wire rolls over the stick contact area.

During the loading process, the contact in stick can switch to slip. This happens if the friction force variable reaches the value of the contact normal force multiplied by the friction coefficient. If this happens, the friction force is modelled this way and the equation that defines the rolling contact is supressed.

The previous problem with the status of the wire-race contacts can vary depending on the boundary conditions. For example, deformations under rigid rings boundary conditions are small, so the predominant situation is the slip-stick. However, greater deformations occur under clamped or unclamped boundary conditions. This leads to more freedom for the wire to twist, so the slip-slip situation is reached quickly.

With the structural behaviour of the analytical model explained, it is time to present the equations that define it. To do so, it is appropriate first to present Figure 4.5 and Figure 4.6, where geometrical parameters, geometrical variables and reaction forces are shown.

In these drawings, L_{RC} is the distance between the centres of the raceway and wire and d is the vertical and horizontal projection of the ball-wire contact spring. y_B is the axial displacement input (half of the total bearing sector deformation). Regarding the displacements of the mechanism, x_w, y_w and θ_w are the displacements and twisting angle of the wire centre, and x_{RC} and y_{RC} are the displacements of the raceway centre. In terms of forces, N_1, N_2 and T_2 are the reaction forces on the wire-ring contacts and F_B the ball-wire normal contact force.
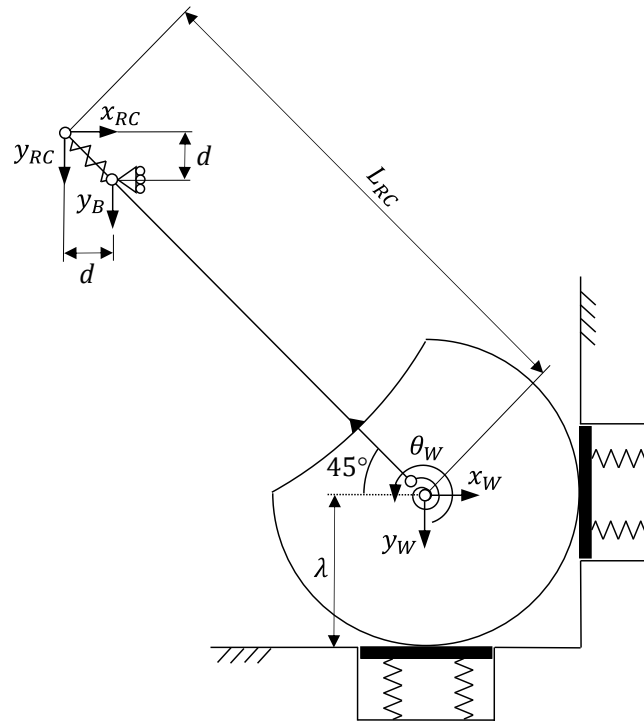
Figure 4.5 Geometrical parameters and DoF of the analytical model.
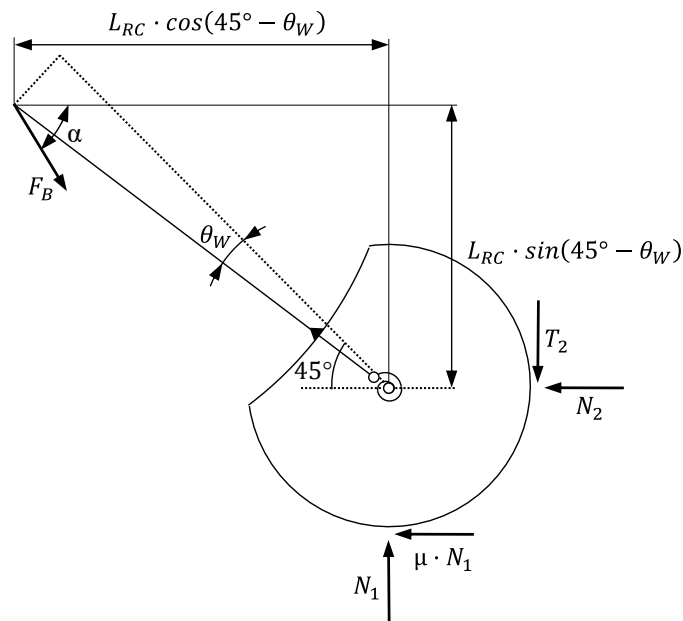
Figure 4.6 Reaction forces in the mechanism.

The equations that form the system come from well-differentiated sources. The first group composed of Equations (4.2)-(4.4) comes from the equilibrium of forces and moments. As has been mentioned previously, under the action of high loads both wire-ring contacts can slide. This situation occurs when the tangential force of the contact in stick (T_2) reaches the slip limit defined as $\mu \cdot N_2$. Beyond that point, T_2 is no longer a variable and must be replaced by $\mu \cdot N_2$.

The second group of equations is formed by the force-deformation relationships. Equation (4.5) represents the behaviour of the ball-wire contact and Equations (4.6) and (4.7) the behaviour of the wire-ring contacts. Additionally, the wire twisting resistance provided by the torsional spring is included in Equation (4.8), where M_w is the twisting moment and k_{tw} the twisting stiffness.

The third group is obtained from the compatibility of deformations relationships. Equations (4.9) and (4.10) relate the displacements of both rigid beam ends, while Equation (4.11) defines the movement of the ball-wire contact spring if one of its ends is displaced vertically.

Finally, as mentioned in previous sections, slip condition is assumed on one wire-ring contact and stick on the other. This assumption implies the need to imposethe rolling condition of Equation (4.12), which forces the wire to roll over the contact in stick. It is worth remembering that this equation must be supressed in case the contact in stick turns to slip.

$$F_B \cdot cos(\alpha) - N_2 - \mu \cdot N_1 = 0 \tag{4.2}$$

$$F_B \cdot sin(\alpha) - N_1 - T_2 = 0 \tag{4.3}$$

$$T_2 \cdot \lambda/2 - \mu \cdot N_1 \cdot \lambda/2 + F_B \cdot L_{RC} \cdot [sin(\alpha) \cdot cos(45° - \theta_W) - \\ - cos(\alpha) \cdot sin(45° - \theta_W)] - M_w = 0 \tag{4.4}$$

$$F_B = k_B \cdot [\sqrt{(d + y_B - y_{RC})^2 + (d - x_{RC})^2} - \sqrt{2 \cdot d^2}]^{2/3} \tag{4.5}$$

$$x_w = \frac{N_2}{2 \cdot a} \cdot \left(\frac{1 - v_1^2}{\pi \cdot E_1} + \frac{1 - v_2^2}{\pi \cdot E_2}\right) \cdot \left[1 + ln\left(\frac{8 \cdot a^2}{\left(\frac{1 - v_1^2}{\pi \cdot E_1} + \frac{1 - v_2^2}{\pi \cdot E_2}\right) \cdot \frac{N_2}{2 \cdot a} \cdot \lambda}\right)\right] \tag{4.6}$$

$$y_w = \frac{N_1}{2 \cdot a} \cdot \left(\frac{1 - v_1^2}{\pi \cdot E_1} + \frac{1 - v_2^2}{\pi \cdot E_2}\right) \cdot \left[1 + ln\left(\frac{8 \cdot a^2}{\left(\frac{1 - v_1^2}{\pi \cdot E_1} + \frac{1 - v_2^2}{\pi \cdot E_2}\right) \cdot \frac{N_1}{2 \cdot a} \cdot \lambda}\right)\right] \tag{4.7}$$

$$M_w = k_{tw} \cdot \theta_w \tag{4.8}$$

$$x_{RC} = x_w - L_{RC} \cdot [cos(45° - \theta_w) - cos(45°)] \tag{4.9}$$

$$y_{RC} = y_w - L_{RC} \cdot [sin(45° - \theta_w) - sin(45°)] \tag{4.10}$$

$$tan(\alpha) = \frac{d + y_B - y_{RC}}{d - x_{RC}} \tag{4.11}$$

$$y_W = \lambda/2 \cdot sin(\theta_w) \tag{4.12}$$

4.3 FE validation

Once the system of equations of the analytical model is defined, an algorithm was programmed in Matlab® in order to carry out the solution process. The results obtained from the algorithm after simulating a reference geometry until its static load capacity are compared with FE simulation results. The wire-race bearing geometry presented in Chapter 2 was considered to serve as a reference geometry for the validation. Table 2.2 contains the most relevant geometrical data and material properties of the reference geometry. The FE model used in Chapter 2 was also useful to perform the FE simulation for the validation. However, in this case, rigid rings boundary conditions are considered, which consist of rigid exterior surfaces of the rings. FE model mesh and boundary conditions are shown in Figure 4.7 together with the load application method. External axial displacement is applied on the rigid surfaces of the model until the static load capacity of the bearing, obtained using the methodology proposed in [13], is reached (674.24 [kN]). The validation process consists of comparing results of both models in terms of bearing stiffness, contact normal force, contact angle and wire twist.
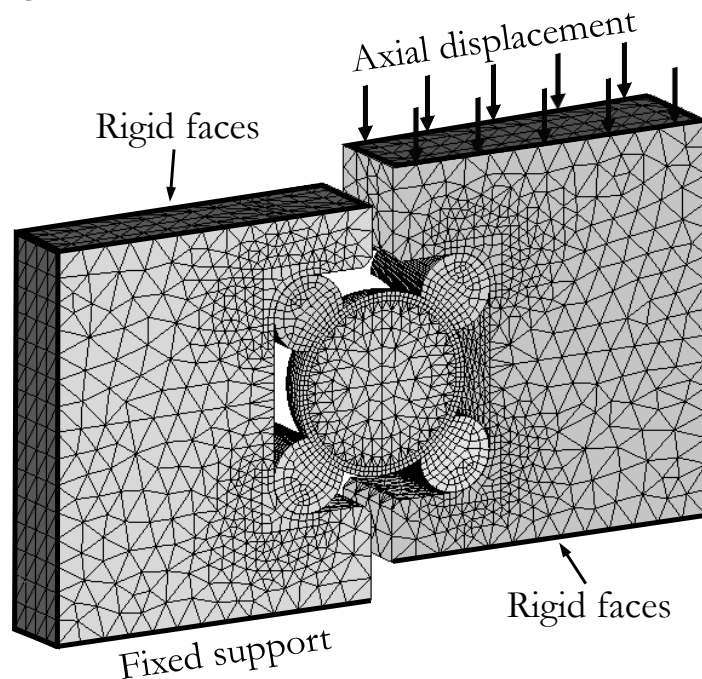
Figure 4.7 FE model for the validation.

4.3.1 Axial stiffness

Bearing stiffness is one of the most relevant performance indicators that represent the structural behaviour of the bearing. For this reason, it is logical to present this comparison in the first place. Figure 4.8 shows the bearing force-deformation curves, where good agreement is observed for moderate loads. However, differences in the curvature results in a significant deviation for high load values. Table 4.2 gathers the relative errors that exist at different levels of the static load capacity.
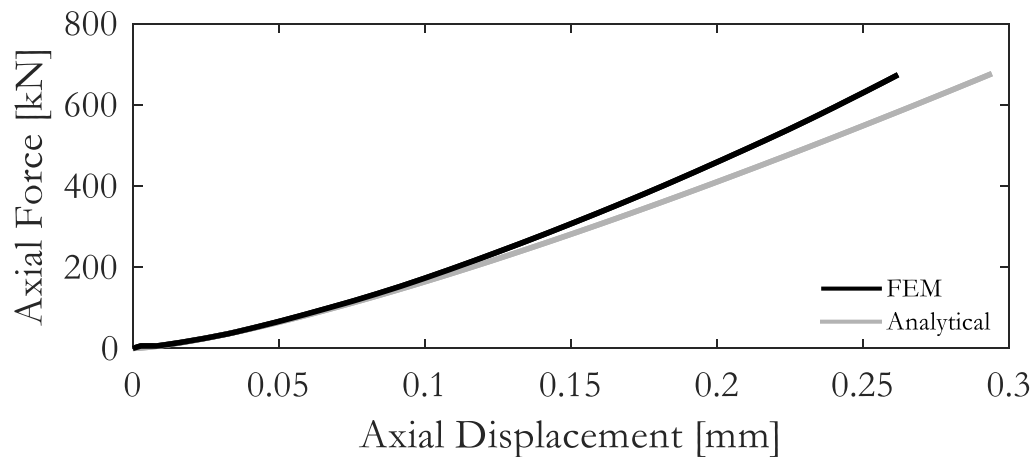
Figure 4.8 Bearing axial stiffness results.

Table 4.2 Relative error at different levels of C_{0a}.

[%] C_{0a}	25	50	75	100
Error	3.9	7.3	9.5	12.2

4.3.2 Ball-wire contact force and contact angle

Regarding the ball-wire contact, normal contact force and contact angle are relevant results to take into consideration in order to assess the validity of the analytical model. Normal contact force can be used to obtain the maximum contact pressure and, therefore, the static axial load capacity of the bearing. Moreover, the pressure distribution can be calculated in combination with the contact angle evolution, which is useful as an indicator of the contact ellipse truncation. Ball-wire contact results are shown in Figure 4.9, where identical behaviour is observed between normal contact force and bearing stiffness results. Regarding the contact angle, FE results show an initial rise followed by subsequent stabilization. The initial rise comes from the ball climbing over the

race caused by an initial stick situation on both wire-ring contacts, and the stabilization from the slip situation in the inner contact and stick in the upper, which allow the wire to twist. The analytical model is able to represent the second stage, but not the initial rise because it does not consider the initial stick situation in both wire-ring contacts. Despite the difference in the contact angle plot, it must be pointed out that the maximum error is less than one degree.
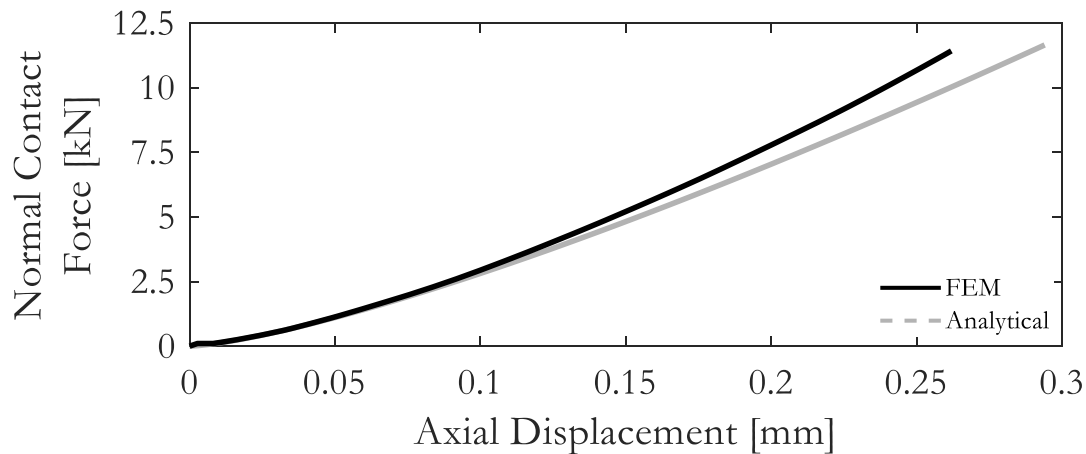
(a)
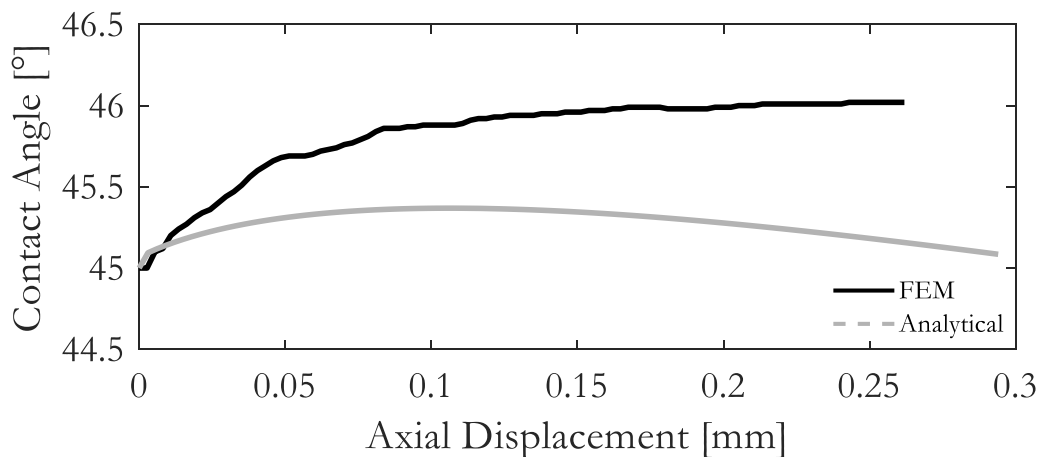
(b)

Figure 4.9 Ball-raceway contact results: (a) Normal contact force, (b) Contact angle.

4.3.3 Wire twist

Wire twist may not be one of the most important performance indicators, but it can reveal how the analytical model represents the bearing behaviour. Figure 4.10 shows how the wire remains at the initial position for a while and starts twisting later in the FE results. Once again, this situation results from the initial stick-stick situation in both wire-ring contacts. Despite this initial deviation, the

analytical model can quite accurately represent the behaviour once the initial situation is overcome, given the curves identical trend.
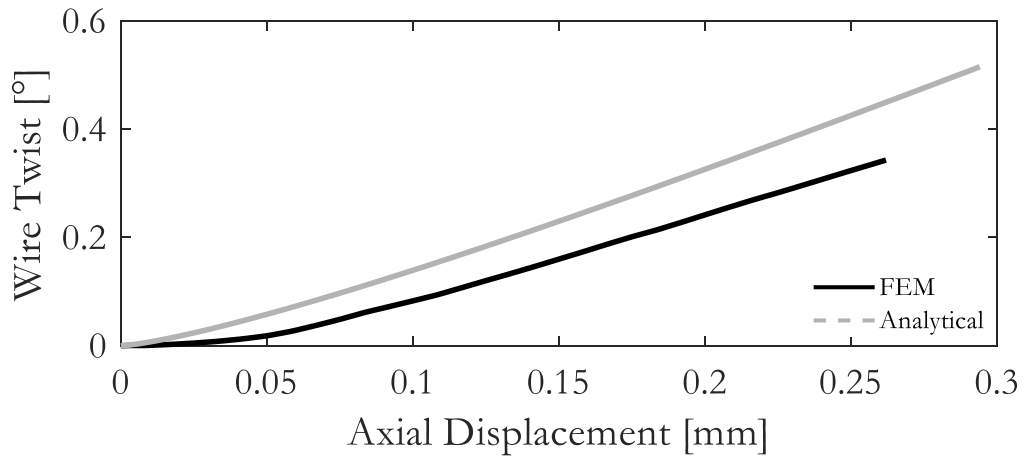
Figure 4.10 Wire twist results.

4.3.4 Influence of the wire twisting stiffness

Having provided the results of the validation, it is worth evaluating the effect of the wire twisting stiffness on the structural response of the bearing. Wire twisting stiffness generates a twisting moment that is in the opposite direction to the twisting moment generated by the contact force. For this reason, the comparison between these two twisting moments provides information about the influence of the wire twisting stiffness.

According to the geometrical data of the reference bearing, the formulation proposed in the previous chapter retrieves a wire twisting stiffness (k_{tw}) value of 4,670 [N·mm/rad]. To obtain the twisting resistance provided by the wire (M_w), it is only necessary to multiply k_{tw} by the wire twisting value.

The twisting moment generated by the contact force (M_B) can be easily obtained from Equation (4.4) as follows:

$$M_B = F_B \cdot L_{RC} \cdot (sin(\alpha) \cdot cos(45° - \theta_W) - cos(\alpha) \cdot sin(45° - \theta_W) \quad (4.13)$$

With this information, Table 4.3 compiles the values of both subjects under study for different levels of the C_{0a}. In addition to this, the relative value of M_w over M_B is calculated to evaluate the influence of the wire twisting stiffness. It can be observed that the contribution of the wire twisting stiffness is not negligible, but not so relevant. However, the wire twisting values obtained with the analytical model are larger than the ones calculated using the FE model.

This means that the real contribution of the wire twisting stiffness may be even lower.

Table 4.3 Wire twisting moment comparison.

C_{0a} [%]	M_B [$N \cdot mm$]	M_w [$N \cdot mm$]	Ratio [%]
25	288.73	11.63	4.0
50	679.8	22.15	3.3
75	1058.5	32.16	3.0
100	1401.8	41.81	3

4.4 Simplified formulation

Because of the relatively low effect of the wire twisting stiffness on the bearing structural response, a simplified analytical model was also proposed. This simplified formulation do not consider the torsional spring that represents the wire twisting stiffness. This way, the rigid beam is fixed to the wire. This modification does not involve major modifications, since only the terms related to the torsional spring are suppressed. The resulting system of equations of the simplified formulation is presented below:

$$F_B \cdot cos(\alpha) - N_2 - \mu \cdot N_1 = 0 \tag{4.2}$$

$$F_B \cdot sin(\alpha) - N_1 - T_2 = 0 \tag{4.3}$$

$$T_2 \cdot \lambda/2 - \mu \cdot N_1 \cdot \lambda/2 + F_B \cdot L_{RC} \cdot [sin(\alpha) \cdot cos(45° - \theta_W) - \\ - cos(\alpha) \cdot sin(45° - \theta_W)] = 0 \tag{4.14}$$

$$F_B = k_B \cdot [\sqrt{(d + y_B - y_{RC})^2 + (d - x_{RC})^2} - \sqrt{2 \cdot d^2}]^{2/3} \tag{4.5}$$

$$x_w = \frac{N_2}{2 \cdot a} \cdot \left(\frac{1 - v_1^2}{\pi \cdot E_1} + \frac{1 - v_2^2}{\pi \cdot E_2}\right) \cdot \left[1 + ln\left(\frac{8 \cdot a^2}{\left(\frac{1 - v_1^2}{\pi \cdot E_1} + \frac{1 - v_2^2}{\pi \cdot E_2}\right) \cdot \frac{N_2}{2 \cdot a} \cdot \lambda}\right)\right] \tag{4.6}$$

$$y_w = \frac{N_1}{2 \cdot a} \cdot \left(\frac{1-v_1^2}{\pi \cdot E_1} + \frac{1-v_2^2}{\pi \cdot E_2} \right) \cdot \left[1 + ln \left(\frac{8 \cdot a^2}{\left(\frac{1-v_1^2}{\pi \cdot E_1} + \frac{1-v_2^2}{\pi \cdot E_2} \right) \cdot \frac{N_1}{2 \cdot a} \cdot \lambda} \right) \right] \qquad (4.7)$$

$$x_{RC} = x_w - L_{RC} \cdot [cos(45° - \theta_w) - cos(45°)] \qquad (4.9)$$

$$y_{RC} = x_{RC} - L_{RC} \cdot [sin(45° - \theta_w) - sin(45°)] \qquad (4.10)$$

$$tan(\alpha) = \frac{d + y_B - y_{RC}}{d - x_{RC}} \qquad (4.11)$$

$$y_W = \lambda/2 \cdot sin(\theta_w) \qquad (4.12)$$

It can be seen how the system of equations is almost identical, only Equation (4.14) has undergone a minor modification and Equation (4.8) has been supressed.

In terms of accuracy, the suppression of the torsional spring has no effect at all on the results of the analytical model. For this reason, it seems reasonable to continue with future developments based on the simplified analytical model.

4.5 Final remarks

This chapter presents an analytical model which was conceived as a simulation and design tool. Even though this path seemed to be focussed in the right direction, there is still margin for improvement. The adequate modelling of the initial contact status and its transition from stick to slip could result in a significant quality leap in comparison with the current formulation. Having said this, it is worth pointing out that it is no simple task.

In this case, only axial behaviour is considered. It is true that this analytical model could be used to simulate tilting moment loads, since the behaviour of one bearing sector is the same, but the radial load case can be quite different. Nevertheless, the concepts presented in this contribution can be used as a solid foundation for a more complete analytical model where the whole load distribution model could be properly solved.

5 Crossed roller wire-race bearing analytical model

5.1 Introduction

The advantages that analytical models provide with respect to FE simulations were introduced in the previous chapter. However, they could not be evaluated in a practical manner, since the proposed analytical model was only suitable for the axial load case. In this case, the purpose of the modelling are the crossed roller wire-race slewing bearings. Some of the knowledge and procedures explained in the previous chapter are also applied in this one, but some other aspects and considerations are completely different.

The analytical model is based on equations that represent the structural response of one sector with one rolling element under imposed external axial and radial displacements. These equations can represent the local deformations on the contacts or even consider the flexibility of the rings. To this end, a DoE with reduced FE models was performed. Once the behaviour of one sector is analytically formulated, a simulation algorithm is programmed to obtain the stiffness curves of the bearing and solve the load distribution problem. Finally, results obtained with the analytical calculation tool are compared with FE results with validation purposes.

The previously described steps are represented in Figure 5.1 together with the related work that will be dealt with in Chapter 7. At this point, there is no need to explain the advantages of performing analytical calculations considering the flexibility of the rings. In addition, the possibility of considering only the stiffness of the contacts may also apply. On the one hand, it is useful to compare designs of different manufacturers ensuring the same boundary conditions whilst, on the other, the analytical formulation can be implemented in a FE model to replace the wires and the rollers. This way, not only the flexibility of the rings but also the stiffness of the adjacent structures can be also considered.

As it has been pointed out, the development of this efficient FE modelling strategy will be presented in Chapter 7.
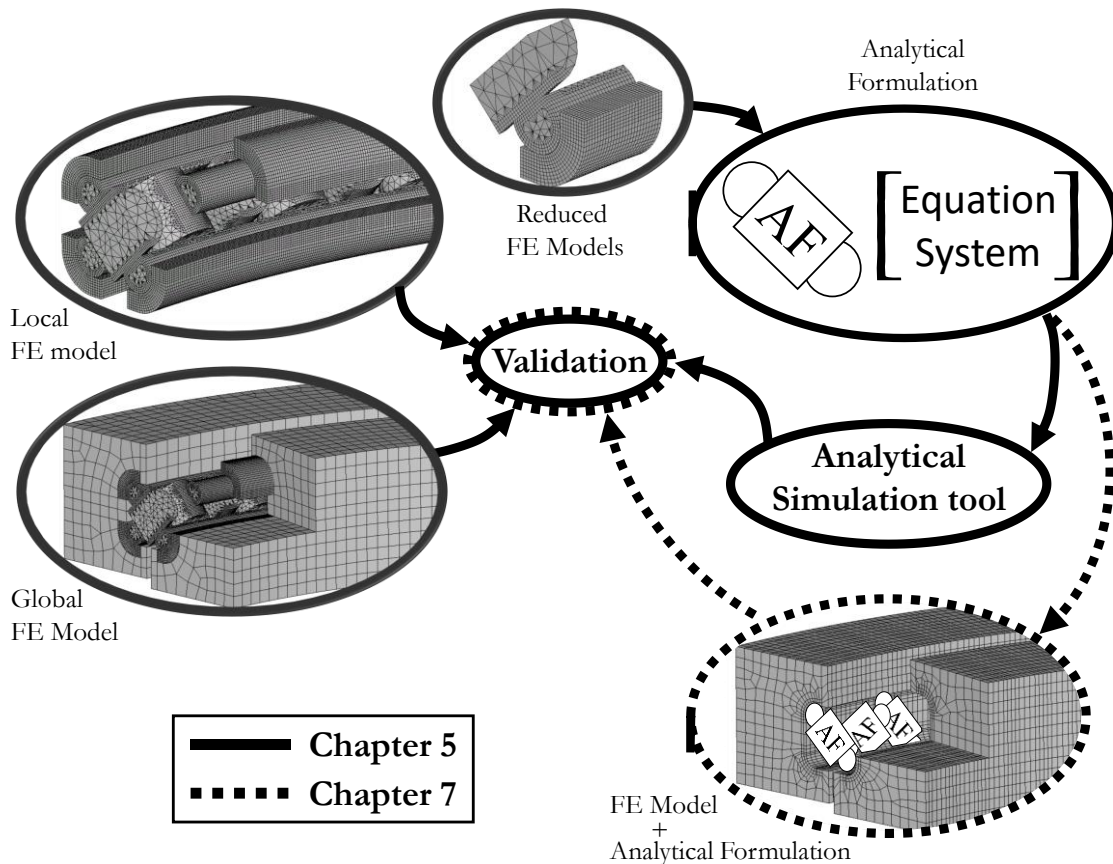
Figure 5.1 Summary of the development, implementation and validation of the analytical formulation.

5.2 Analytical formulation for one sector

5.2.1 Assumptions and simplifications

In contrast to the four-point contact wire race slewing bearings, there is no previous work in this Doctoral Thesis regarding crossed roller wire-race slewing bearings. Therefore, the structural behaviour of this kind of bearings was completely unknown at the early stages of development. For this reason, it was considered appropriate to perform preliminary FE analysis to evaluate and study the phenomena that occur under load. To this end, there was no need to create a complex FE model; a half-sector cyclic symmetry FE model subjected to axial load was enough. The FE model developed for these analyses is the same that was later used in the validation process, which is properly introduced in detail in Section 5.5.

Some relevant phenomena were observed during these calculations. For example, the roller-wire contact remains in stick. This can be seen in the contact status represented in Figure 5.2a. As a result, the wire-roller-wire can be considered to behave as a single solid. This assumption significantly simplifies the conception of the analytical model.

(a)

(b)

☐ Near   ▨ Sliding   ■ Sticking
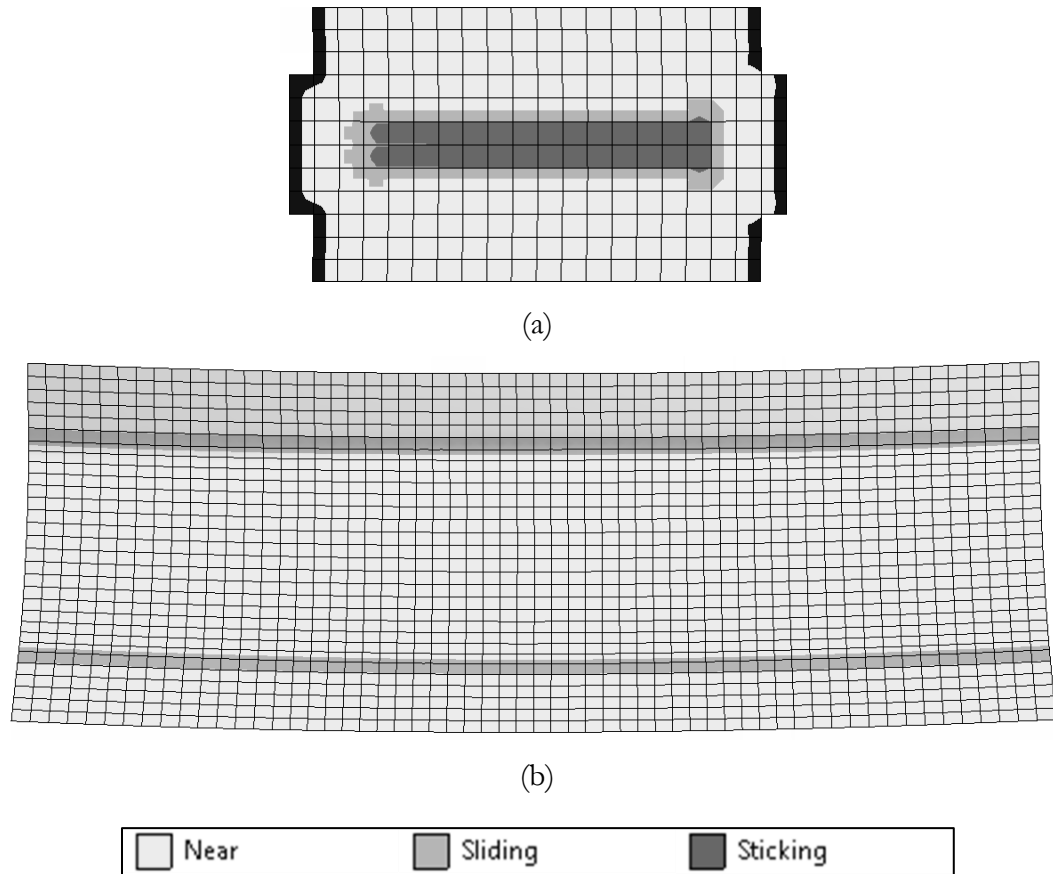
Figure 5.2 Contact status: (a) Roller-wire contact (results on the roller surface); (b) Wire-ring contacts.

The latter phenomenon also affects the wire-ring contacts status. When an external displacement is applied, the compatibility of deformations forces the wire-roller-wire to rotate. As it turns as a single solid, the wire-ring contacts are forced to slip (Figure 5.2b). This situation is highly advantageous when it comes to the development of the analytical model, since the friction forces can be modelled applying the Coulomb friction model. This means that the tangential forces are equal to the normal force multiplied by the friction coefficient . However, as can be seen in Figure 5.3, the rotation direction of the single solid depends on the direction of the external applied displacement.
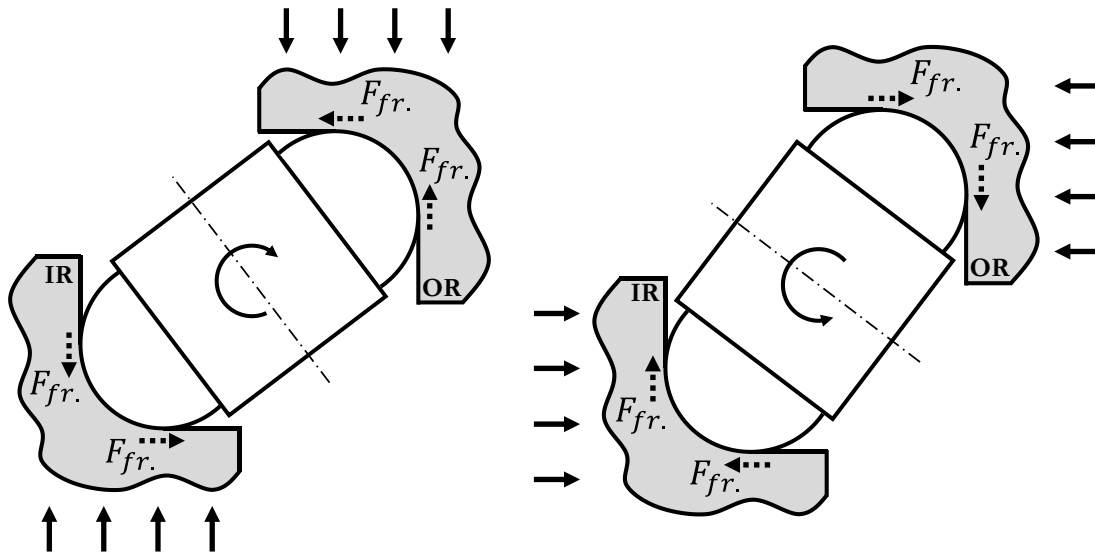
Figure 5.3 Wire-roller-wire rotation and wire-ring friction forces ($\boldsymbol{F_{fr.}}$) (IR and OR indicate inner and outer ring).

The latter dependency forces to calculate the predominant external applied displacement that is exerted on the bearing sector. This can be easily carried out if each sector is considered to deform independently, in such a way that the deformation of one sector does not affect the adjacent ones. This consideration also allows for the development of the analytical model for one sector and to solve each one separately to ultimately compile the results and obtain the bearing response.

5.2.2 Description of the analytical approach

The procedure to develop the analytical model is quite similar to the one proposed in the previous chapter. However, the analytical formulation developed for one bearing sector is more versatile in this case, as all types of loads are considered. It is also based on a geometrical interference model, where the system of equations consists of the compatibility of deformations, force-deformation relationships and equilibrium of forces. These type of bearings are composed by rollers in two orientations, so it is necessary to differentiate them. Hereinafter, rollers shown in Figure 5.3 will be called type A rollers and the ones oriented in the other direction, type B rollers. For the sake of clarity, explanations in this section will be made on the basis of type A rollers. The procedure by which to obtain the expressions of the analytical model for type B rollers is identical, as is the system of equations of the analytical model. The only difference lies in the load distribution model and results postprocessing, which require special attention.

Figure 5.4 shows the deformed shape of a generic type A roller sector i under axial Δ_A^i and radial Δ_R^i displacements. Considering that the analytical model is developed for slewing bearings, it is fair to say that the stiffness provided by both inner and outer rings is almost the same. Under this assumption, half displacement is applied to each ring, since there is a symmetry point at the centre of the roller. The sector displacements generate contact interferences and the subsequent geometrical deviations: Δ_1^i and Δ_2^i are the wire-ring interferences on the horizontal and vertical contacts, respectively, Δ_3^i is the roller-wire interference, and α_0 and α^i are the initial (unloaded) and final (loaded) contact angles, respectively. In terms of geometrical parameters, D_W is the roller diameter, λ the wire diameter and D_{CW} the distance between wire centres (see Figure 5.4).
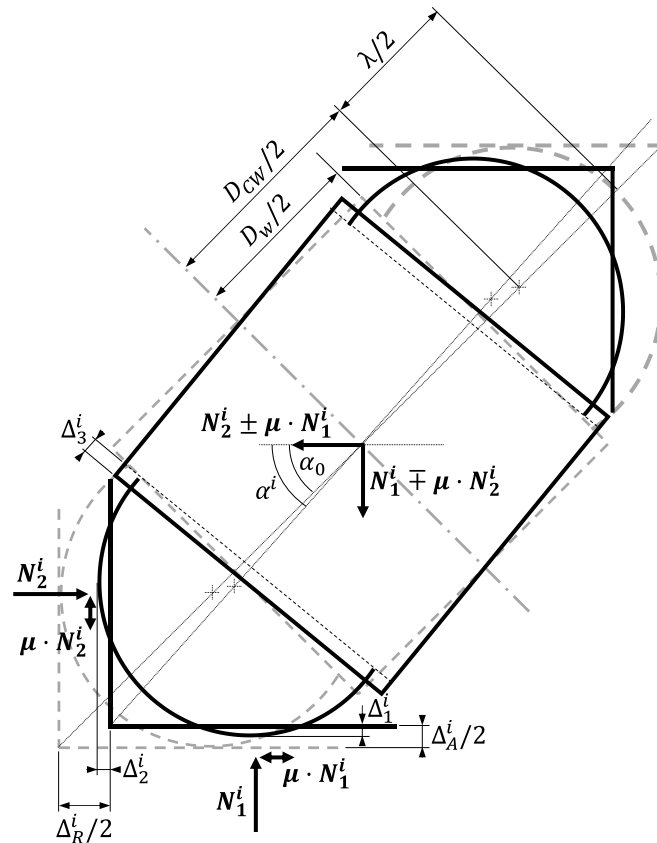
Figure 5.4 Analytical model for type A roller: Deformations and forces.

Regarding the forces that appear on the contacts due to the interferences, only the wire-ring normal contact forces (N_1^i, N_2^i) are considered to be system variables. Friction forces are represented by multiplication by the friction coefficient of friction μ, since both contacts are assumed in slip. In a general case with both axial and radial displacements, the dominant component must be identified and then the direction of the friction forces accordingly defined; thus, if $\Delta_A^i > \Delta_R^i \cdot \tan(\alpha_0)$, the axial component prevails, and vice versa. If $\Delta_A^i =$

$\Delta_R^i \cdot \tan(\alpha_0)$, the friction forces must be set to zero because the wire does not twist. The roller-wire contact always remains in stick, so the calculation of the contact forces is not so straightforward. Total contact force is the force that generates the equilibrium of the system, which is a combination of the latter forces and will be addressed later.

Figure 5.5 shows the deformation compatibility between the imposed sector displacements and the resulting contact angle and interferences.
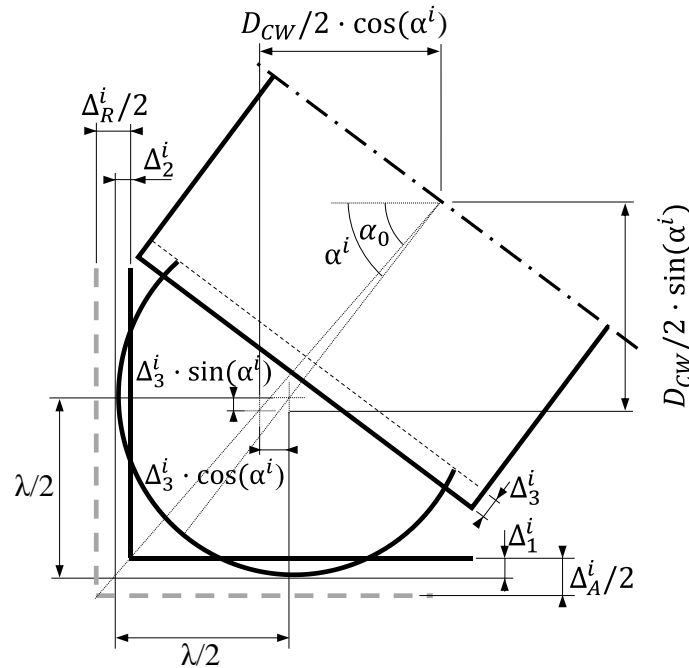
Figure 5.5 Analytical model for type A roller: Geometrical relationships.

Finally, based on all the considerations already pointed out, the system of equations that defines the analytical model can be presented. As friction forces direction depends on the prevailing relative displacement between rings, a plus-minus ($\pm, \mp$) sign strategy was considered to be appropriate. The upper signs correspond to prevailing Δ_A^i and the lower signs to prevailing Δ_R^i. This way, both equation systems for each case can be represented as a single set.

The first group formed by Equations (5.1) to (5.3) consists of force-deformation relationships, where k_1, k_2 and k_3 are stiffness constants. Depending on the value of these constants, they can represent the local or global behaviour of the bearing. Local behaviour only considers the local deformations of the contacts, while the global behaviour also represents the flexibility of the rings. The value of these constants depends on the bearing geometry and its calculation method will be explained in the next section, together with the reason behind its linear behaviour assumption.

Equations (5.4) and (5.5) represent the compatibility of deformations. These equations relate the initial geometry with the deformed system under the action of imposed external displacements.

The last Equation (5.6) is obtained from the equilibrium of moments with respect to the wire centre.

$$N_1^i = k_1 \cdot \Delta_1^i \tag{5.1}$$

$$N_2^i = k_2 \cdot \Delta_2^i \tag{5.2}$$

$$\left(N_2^i \pm \mu \cdot N_1^i\right) \cdot cos(\alpha^i) + \left(N_1^i \mp \mu \cdot N_2^i\right) \cdot sin(\alpha^i) = k_3 \cdot \Delta_3^i \tag{5.3}$$

$$D_{CW}/2 \cdot cos(\alpha_0) = \Delta_R^i/2 - \Delta_2^i + \left(D_{CW}/2 - \Delta_3^i\right) \cdot cos(\alpha^i) \tag{5.4}$$

$$D_{CW}/2 \cdot sin(\alpha_0) = \Delta_A^i/2 - \Delta_1^i + \left(D_{CW}/2 - \Delta_3^i\right) \cdot sin(\alpha^i) \tag{5.5}$$

$$\begin{aligned}
N_2^i \cdot \left(\left(D_{CW}/2 - \Delta_3^i\right) \cdot sin(\alpha^i)\right) &- N_1^i \cdot \left(\left(D_{CW}/2 - \Delta_3^i\right) \cdot cos(\alpha^i)\right) \\
\pm \mu \cdot N_1^i \cdot \left(\left((\lambda/2 - \Delta_1^i) + \left(D_{CW}/2 - \Delta_3^i\right) \cdot sin(\alpha^i)\right) &\pm \\
\pm \mu \cdot N_2^i \cdot \left((\lambda/2 - \Delta_2^i) + \left(D_{CW}/2 - \Delta_3^i\right) \cdot cos(\alpha^i)\right) &= 0
\end{aligned} \tag{5.6}$$

The resolution of this non-linear system of equations obtains the results for one individual sector in terms of the system variables. Nevertheless, roller-wire contact forces do not form part of the equation system; they are relevant results though, since they indicate the static load capacity of the bearing. To obtain these forces, simple geometrical relationships can be applied. Total contact force and angle are obtained with Equations (5.7) and (5.8). The latter force can be projected on the normal and tangential directions. The normal contact line is defined by the contact angle α^i, so the projected forces can be obtained by means of Equations (5.9) and (5.10).

$$F_{Tot.}^i = \sqrt{\left(N_1^i \mp \mu \cdot N_2^i\right)^2 + \left(N_2^i \pm \mu \cdot N_1^i\right)^2} \tag{5.7}$$

$$\alpha_{Tot.}^i = atan\left(\frac{\left(N_1^i \mp \mu \cdot N_2^i\right)^2}{\left(N_2^i \pm \mu \cdot N_1^i\right)^2}\right) \tag{5.8}$$

$$F_N^i = F_{Tot}^i \cdot cos\left(\alpha_{Tot}^i - \alpha^i\right) \tag{5.9}$$

$$F_{Tg}^i = F_{Tot}^i \cdot sin\left(\alpha_{Tot}^i - \alpha^i\right) \tag{5.10}$$

5.3 Stiffness constants approach

5.3.1 Study of the contact behaviour

The purpose of the analytical model relies on serving as a multiparametric simulation tool, where every bearing geometry can be properly simulated. For this reason, the formulation includes constants such as geometrical or operational parameters, which can change depending on the bearing under study. With regard to the latter, stiffness constants k_1, k_2 and k_3 are not an exception.

In general, contact stiffness formulations that can be found in the literature were developed considering simple contact geometries under specific loads and boundary conditions. In the case of cylinder-plane contact, formulae were developed considering plane strain assumption. This means that the applied load is distributed along the cylinder and the plane surface is part of an elastic half-space. In this case, roller-wire and wire-ring contacts do not match these assumptions. Roller-wire contact is a cylinder-plane contact with a distributed load, but the wire is far from being an elastic half-space. This means that the stress and deformation distribution on the wire is quite different from that expected by the formulations. Wire-ring contacts can be considered as cylinder-plane contacts, but in this case, the load transmitted by the roller cannot be assumed as distributed. Besides this, there are rollers in two different directions, so a certain wire has a roller contact every two sectors ($360°/N_R \cdot 2$), which is a significant distance between contacts. For all these reasons, the behaviour of the contacts had to be studied in greater detail.

Preliminary FE simulations were carried out in Ansys® with the FE model of Figure 5.6(a) to study the response of the contacts. Only one eighth of a sector was modelled taking advantage of the cyclic symmetry and symmetry planes. As usual for these kind of bearings, steel was selected as the material for the roller and wire, and aluminium for the rings. It is worth mentioning that only a partition of the ring with a depth of $\lambda/2$ was modelled, since it was considered enough to contain the local effects of the contact. All contacts were defined as frictional ($\mu = 0.1$) with a penetration tolerance of 0.1 [μm]. The external surfaces of the ring partition were clamped, and symmetry boundary conditions were applied to the cyclic symmetry cutting surfaces. Finally, the load was applied to the roller as a displacement δ in the direction of the contact angle, until the static load capacity was reached.

The response of each contact in terms of stiffness can be obtained from the normal contact forces (N_1, N_2, N_3) and normal contact deformations ($\delta_1, \delta_2, \delta_3$) shown in Figure 5.6 (b). The deformations of wire-ring contacts are defined as the horizontal and vertical displacements of the wire centre, and therefore the roller-wire deformation is the difference between the imposed displacement and the wire centre displacement. This way, the evolution of the contact stiffness can be studied via force-deformation plots. Figure 5.6(c) shows the stiffness curve of a wire-ring contact for a given generic bearing geometry, which is enough to observe the contact behaviour. This plot revealed that the force-deformation response can be divided into two sections; in the first section the behaviour is linear and suffers a slight stiffening in the second one.

(a)　　　　　　　　　　　　　(b)

(c)
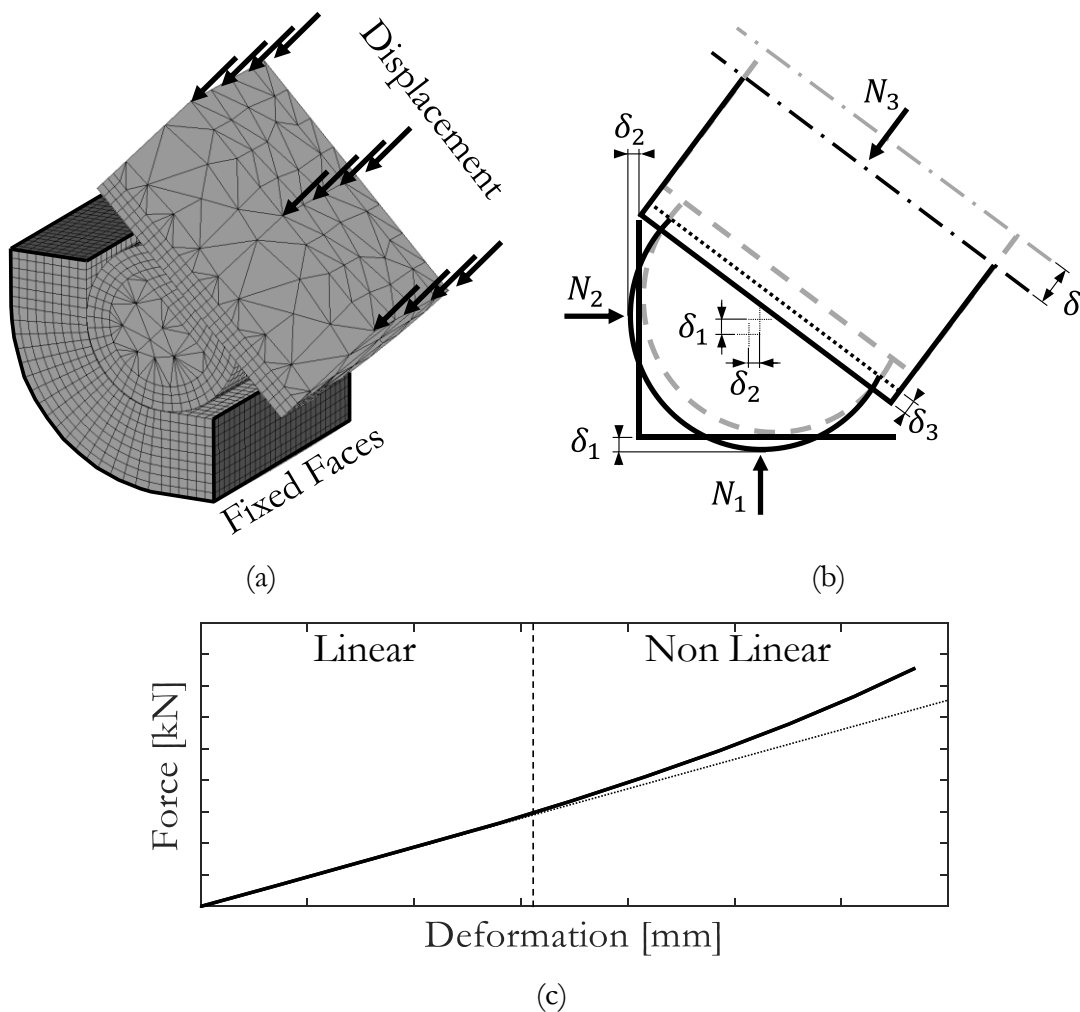
Figure 5.6 (a) Local FE model; (b) Forces and displacements in the reduced FE model; (c) Wire-ring contact force/deformation curve.

This variation in the stiffness behaviour is caused by the modification of the wire-ring contact geometry. These bearings are designed with a gap between the wire and the ring. When low or moderate loads are applied to the bearing,

this gap remains open and the forces are transmitted through two contact lines. Figure 5.7(a) shows the contact status of generic wire-ring contacts under this condition. Nevertheless, this gap closes as a consequence of the contact deformation suffered under high load values. This situation is represented in Figure 5.7(b), where the contact status indicates that the gap has disappeared and a significant area has turned to stick.

(a)

(b)
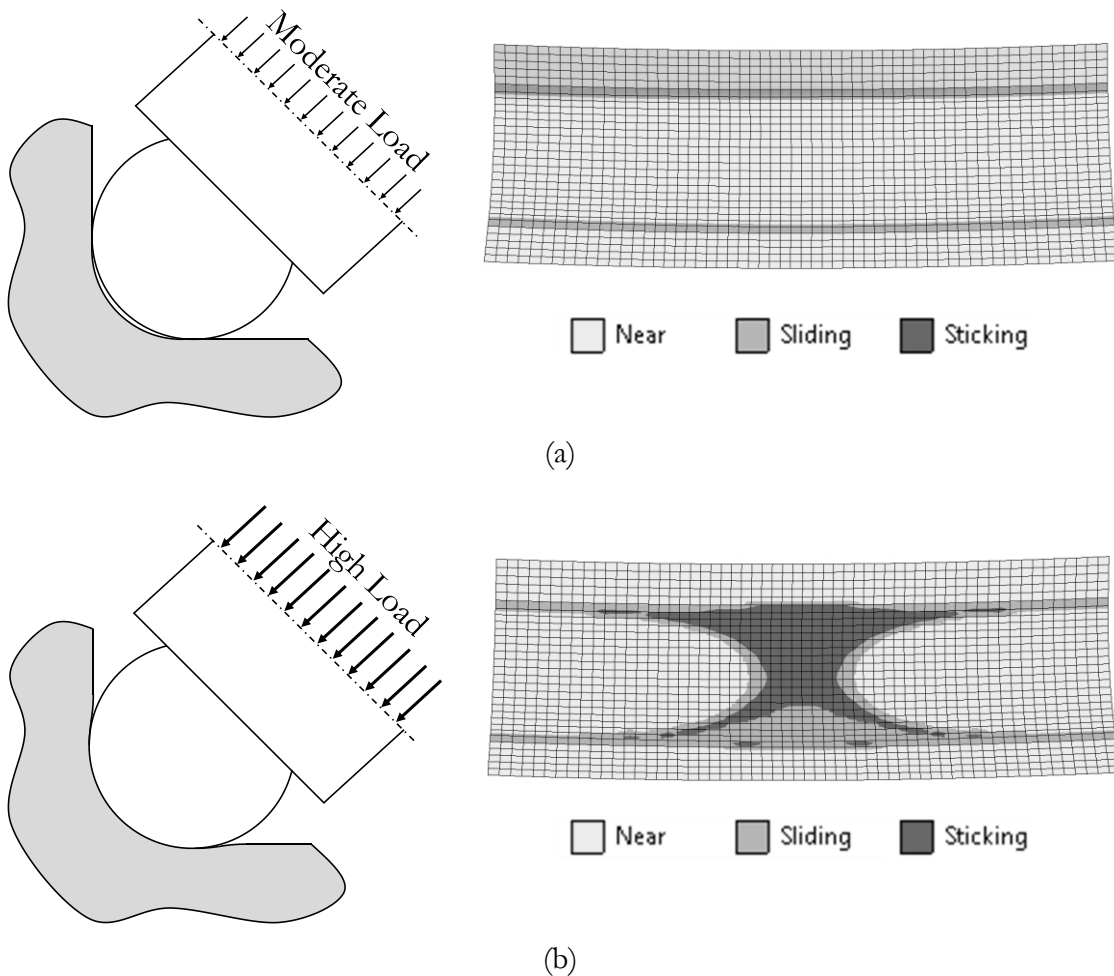
Figure 5.7 Wire-Ring gap closure phenomenon schema and pressure distribution: (a) Open gap; (b) Closed Gap.

There is an inherent difficulty when it comes to representing the contact behaviour analytically. For this reason, only the linear section of the stiffness curve was considered to represent the stiffness of the contact. In this sense, accurate results will be obtained for low and moderate loads, and conservative results for high loads. This decision could pose a problem for certain applications, but considering the applied safety coefficients and bearings design criteria, it is fair to say that accurate results are obtained in the design area.

5.3.2 Design of Experiments

At this point, FE simulations seems to be an appropriate way for the calculation of k_1, k_2 and k_3. Nevertheless, the idea of performing FE simulations for each bearing geometry and introducing the stiffness constants in the analytical model is not practical. For this reason, the best option consisted in performing a Design of Experiments (DoE) FE campaign and approach polynomial formulae to the results. This way, the values of the stiffness constants can be obtained immediately for every bearing geometry within the design space.
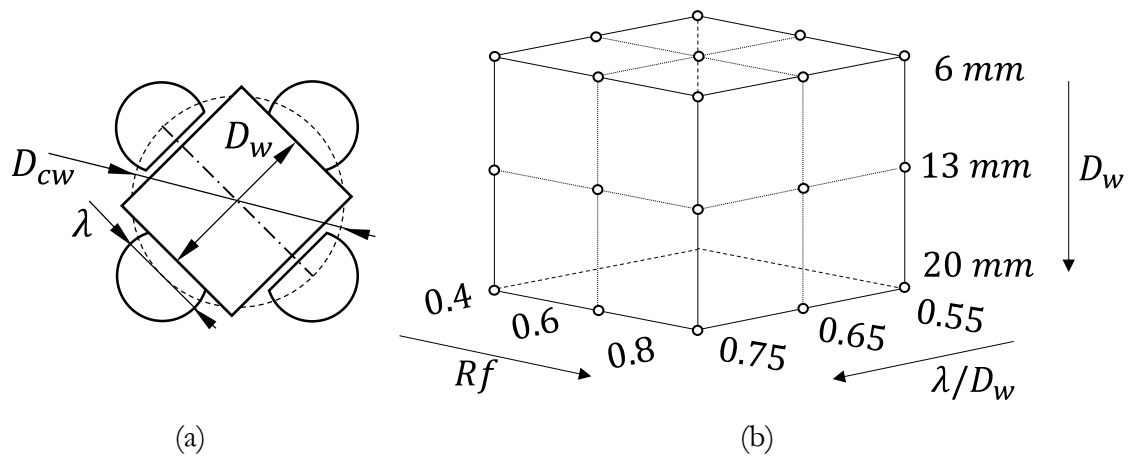
Figure 5.8 Contact geometry parameters.

The parameters selected for the DoE are directly related with the contact geometry definition, as shown in Figure 5.8a. The main geometrical parameter that defines the proportions of the bearing cross-section, is the rolling element diameter (D_w). For this reason, it deserved to be the first parameter of the DoE. Besides, the other parameters were normalized with respect to D_w in order to obtain coherent values in the matrix of experiments. The ratio between the wire and roller diameter (λ/D_w) was the second parameter, since it defines the contact geometry of the wire-ring contact and the potential size of the raceway. Equation (5.11) defines the third parameter, which indicates the size of the wire raceway in terms of how much wire material was machined to create it. A null raceway factor (Rf) value means that no race has been machined on the wire so the contact is non-conformal $(Rf = 0 \rightarrow D_w + \lambda = D_{cw})$. Moreover, a Rf value equal to 1 indicates that half of the wire section was removed $(Rf = 1 \rightarrow D_w = D_{cw})$.

$$Rf = 1 + \frac{1}{\lambda/D_w} - \frac{1}{\lambda/D_{cw}} \tag{5.11}$$

Once the parameters are defined, the number of design points and the range of the parameters must be defined. A 3 level full factorial DoE was considered to be good enough to represent the main and crossed effects in addition to non-linearities. The matrix of experiments shown in Figure 5.8b contains the 27 design points and the values of the design parameters, which are based on catalogue values [28] and information provided by Iraundi S.A.

5.3.3 FE models

The multiparametric FE models developed for the simulation campaign are addressed in this section. Depending on the method used to obtain k_1, k_2 and k_3, they can represent the local deformations of the contacts (local behaviour) or include the flexibility of the rings (global behaviour). To achieve this, two multiparametric FE models were developed (see Figure 5.10), one for the type A roller and another one for the type B roller, from where local and global stiffness results can be obtained. As will be explained later, this is possible because these FE models are basically the local FE model of Figure 5.6a with extended ring geometry.

A problem arose when trying to model the ring geometry, since the same bearing geometry can have multiple ring sizes. To deal with this problem, the standard ring geometry proposed in [15] was used. This standard geometry defines the four-point contact slewing bearing ring geometry according to D_w. It is true that it was not designed for wire-race bearings and it is not directly applicable; however, it obtains good results if the ring geometry is defined as a function of the housing H, instead on D_w. The standard wire-race bearing ring geometry is shown in Figure 5.9, and the parameters that define the dimensions in Table 5.1. It was proven that common values of D_{pw} and fill factor did not have effect the stiffness constant values.
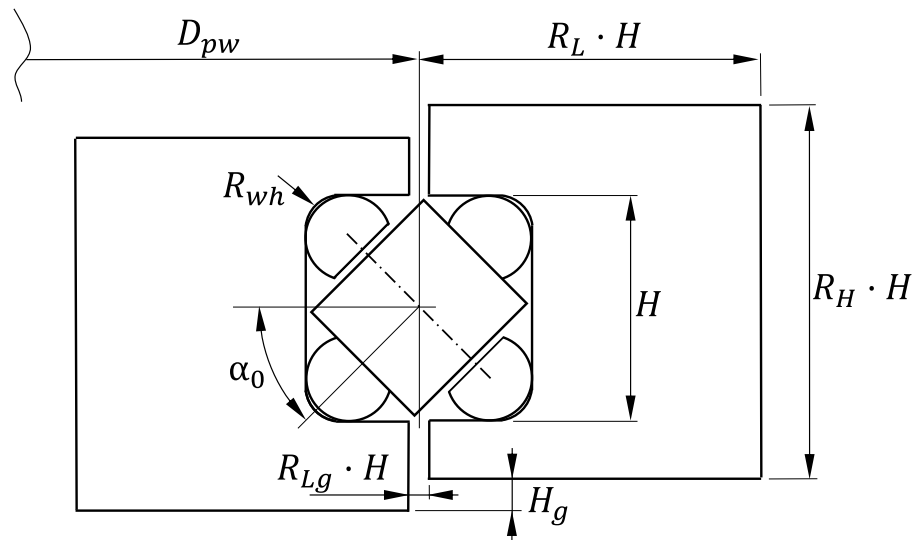
Figure 5.9 Wire-race bearing standard geometry according to [15].

Table 5.1 Standard geometry parameters [15].

D_{pw}	α_0	Fill Factor	R_{wh}	R_L	R_H	R_{Lg}	H_g
[mm]	[°]	[%]	[mm]				[mm]
420	45	100	3.9	1.9	2.15	0.1	3

Once the ring geometry is established, the multiparametric FE models for the calculation of the global stiffness constants can be presented. These two models are shown in Figure 5.10, where it can be seen how the models consist of the local model mesh with additional ring geometry. This ring add-on was meshed with larger second order hexahedrons and connected to the ring contact partition via a bonded contact based on a penalty formulation and with a penetration tolerance of 3 [μm]. The average DoF of the models was approximately 371,535. The load was also introduced as an imposed displacement in the direction of the contact angle, until the static load capacity [9] was reached. In terms of boundary conditions, the surface in contact with the surrounding structures was fixed and symmetry boundary conditions were applied to the symmetry faces.

(a)   (b)
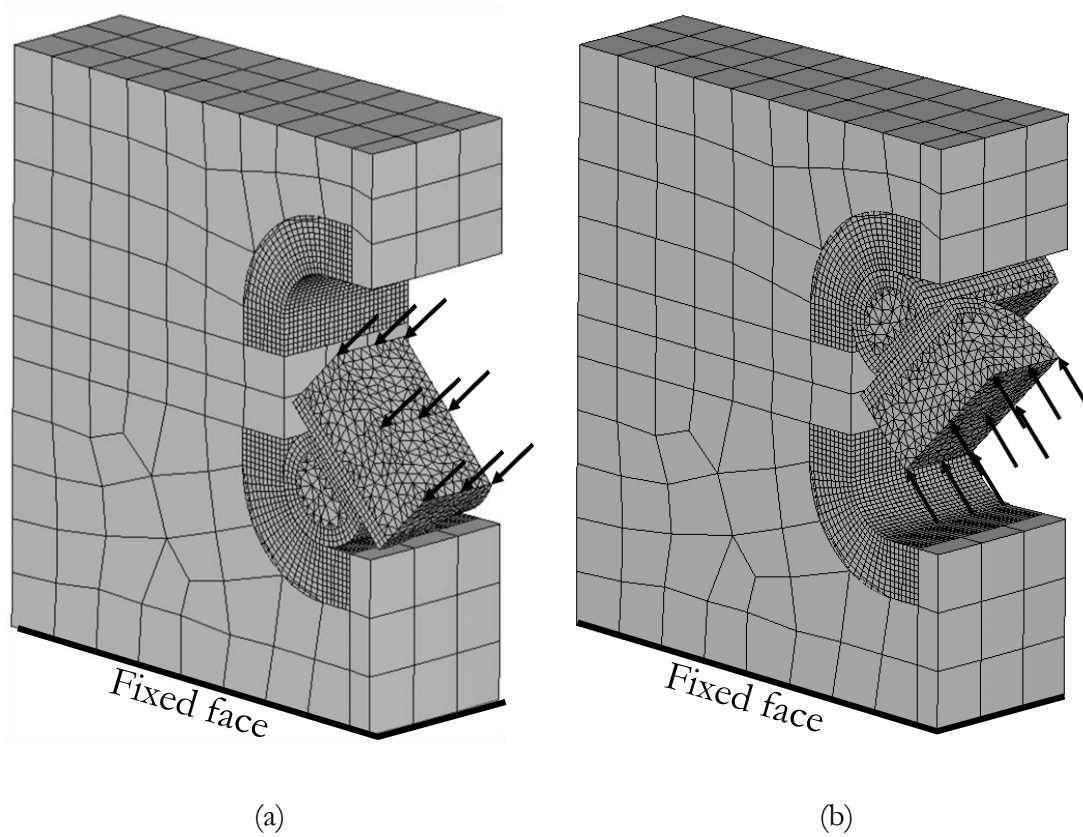
Figure 5.10 FE models for the calculation of the global stiffness constants: (a) Type A roller; (b) Type B roller.

The procedure to obtain the local force-deformation results was identical to the one used in the previous section. The only difference lies in the calculation of δ_1 and δ_2, that, for these models, is the relative displacement between the wire centre and the end of the refined ring zone. For the global force-deformation results, δ_1 and δ_2 not only represent the local deformations of the contacts within the defined refined volume, but also the deformations of the ring in its direction. To achieve this, the considered deformations are the displacements of the wire centre, which includes the contact stiffness and the flexibility of the rings.

Finally and according to the matrix of experiments, a total of 27 design points per FE model results in a 54 FE analyses campaign, with the related pre and postprocessing tasks.

5.3.4 Results and formulae approach

As has already been mentioned, only the initial linear section of the stiffness curves was considered for the approximation. The stiffener non-linearity occurred at around 35-53% of the static load capacity, within the scope of the

defined DoE. This means that the stiffness constants are accurate from zero until that range and more flexible from there on, which can be considered as conservative. Figure 5.11 shows the results of the FE simulations and k_1, k_2 and k_3 approximations for the central point of the matrix of experiments (see Figure 5.8b). Stiffness constants values for this case, which gave the approximate lines in the plots, are compiled in Table 5.2.
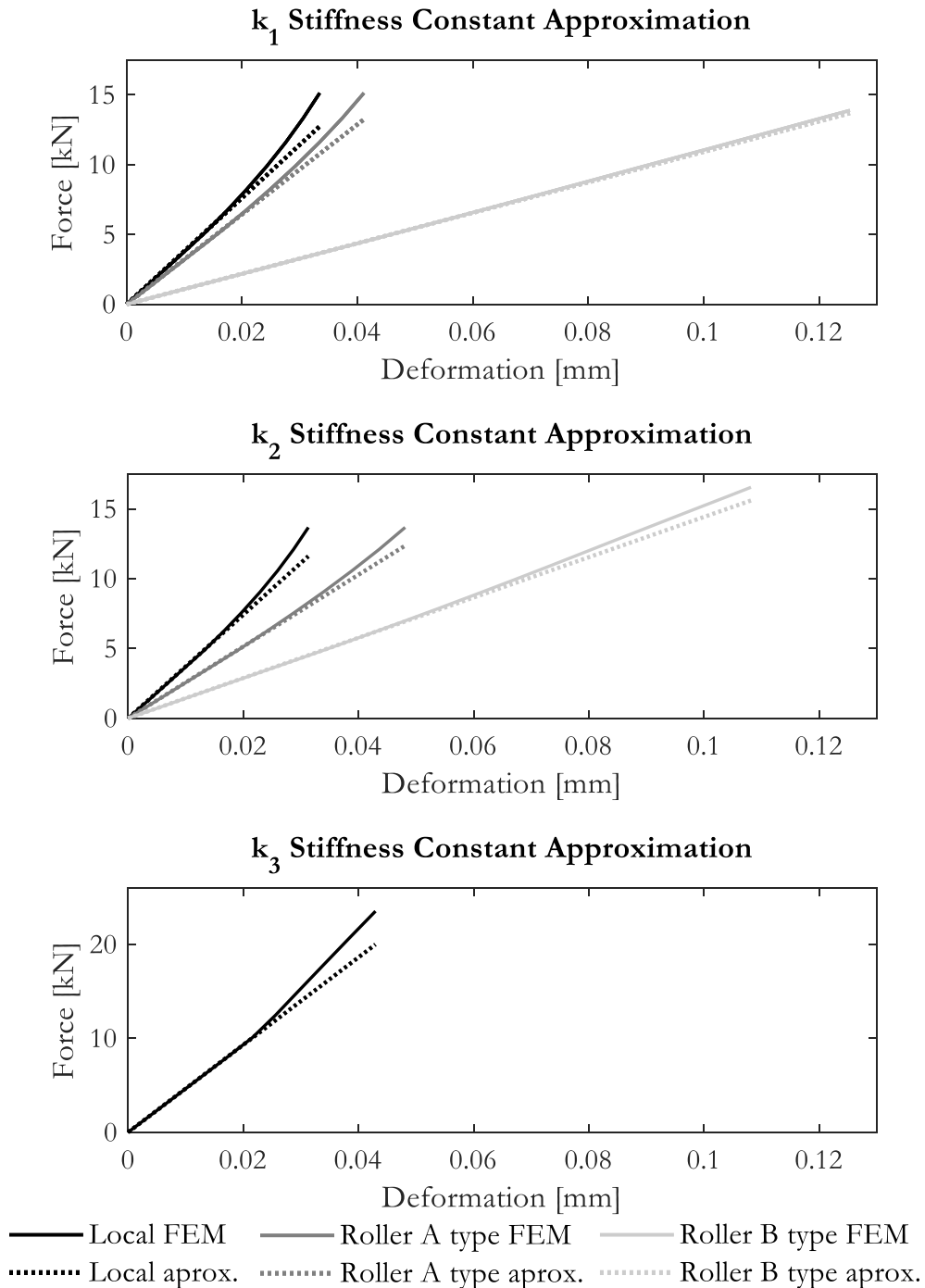
Figure 5.11 Comparison between FEM results and k_1, k_2 and k_3 approximated lines.

Table 5.2 Stiffness constants values of the DoE central case.

$[N/m] \times 10^6$	Local	Global	
		Type A roller	Type B roller
k_1	411.4	341.5	109.9
k_2	398.5	268.6	147.4
k_3	508.8	502.5	498.3

As can be expected, k_1 and k_2 local results (which consider only contact deformations) are more rigid than the global ones (which also consider ring deformations). In addition, type B roller global results are much more flexible because of the longer path followed by the load. In contrast, the type A roller load path is basically a diagonal between fixed faces. Regarding k_3, local and global results tally. This is not surprising, since the flexibility of the rings is considered in the wire-ring contacts (k_1 and k_2) and not in the roller-wire contact (k_3).

Results in all design points of the DoE are quite similar to the latter ones, so it was found appropriate to approach one engineering formula to each stiffness constant for the local and global cases. This results in a total of seven expressions, three for k_1 (local, global for type A rollers and global for type B rollers), three for k_2 (idem) and one for k_3. Different functional forms were considered to approach the results and obtain a simple and accurate formula. A polynomial form that included first order, second order and cross terms was finally used. The terms were adjusted to the results by the least squares method and the ones that had no relevance were supressed in order to simplify the formula. The following polynomial formula was the result of this approach:

$$k = c + c_{Dw} \cdot D_{wn} + c_\lambda \cdot \lambda_n + c_{Rf} \cdot Rf_n +$$
$$+c_{Dw\lambda} \cdot D_{wn} \cdot \lambda_n + c_{DwRf} \cdot D_{wn} \cdot Rf_n \tag{5.12}$$

Being:

$$D_{wn} = (D_w - 13)/(20 - 13) \tag{5.13}$$

$$\lambda_n = (\lambda/D_w - 0.65)/(0.75 - 0.65) \qquad (5.14)$$

$$Rf_n = (Rf - 0.6)/(0.8 - 0.6) \qquad (5.15)$$

Where coefficients c, c_{Dw}, c_λ, c_{Rf}, $c_{Dw\lambda}$ and c_{DwRf} are listed in Table 5.3. D_w must be expressed in [mm] for the proper calculation of D_{wn}. It was proven that second order terms and the cross term between Rf_n and λ_n did not have significance, so they were removed.

Table 5.3 Coefficient values for the stiffness constants formula.

Local						
$[N/m] \times 10^6$	c	c_{Dwn}	$c_{\lambda n}$	c_{Rfn}	$c_{Dw\lambda}$	c_{DwRf}
k_1	379.0	219.5	58.0	-49.5	34.3	-30.3
k_2	368.4	209.4	54.6	-47.9	33.3	-26.3
k_3	467.1	253.0	50.7	66.2	27.5	35.5
Global type A roller						
$[N/m] \times 10^6$	c	c_{Dwn}	$c_{\lambda n}$	c_{Rfn}	$c_{Dw\lambda}$	c_{DwRf}
k_1	331.1	189.8	52.4	-40.9	30.4	-25.6
k_2	262.1	150.9	33.7	-27.8	19.8	-17.5
Global type B roller						
$[N/m] \times 10^6$	c	c_{Dwn}	$c_{\lambda n}$	c_{Rfn}	$c_{Dw\lambda}$	c_{DwRf}
k_1	111.1	66.1	6.1	-8.2	4	-5.2
k_2	150.4	91.1	17.3	-9.5	11.6	-7.4

The relative error of the approaches was less than 5% for any case within the defined design space. Besides this, linear or almost linear behaviour was observed among the main and crossed effects.

5.4 Simulation algorithm for all the sectors

All the information presented until now has been focused on representing the structural response of one wire-race bearing sector with any geometry. This methodology has little applicability on its own, since it can only calculate the response of one sector under axial and radial external displacements. However, a true simulation tool must obtain bearing stiffness curves and solve the load distribution problem for the whole bearing. For this reason, it was necessary to build a simulation algorithm with those capabilities. This task may seem simple considering that the analytical formulation has already been developed. Nevertheless, it is not so straightforward to achieve the proposed goals.
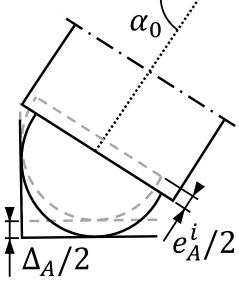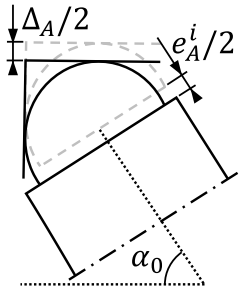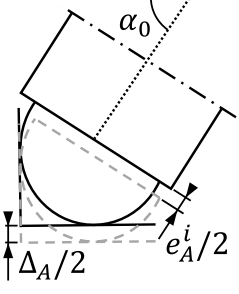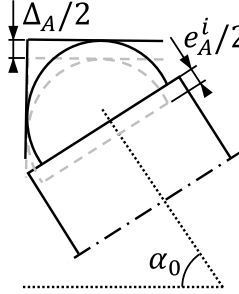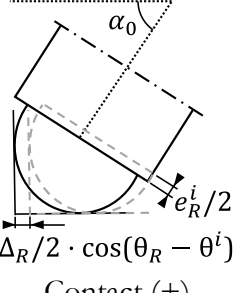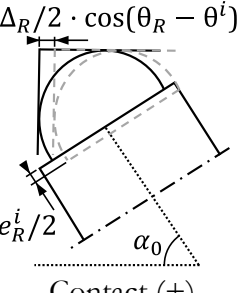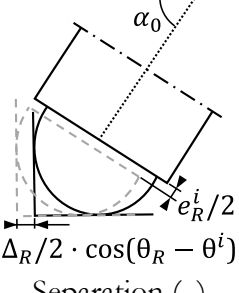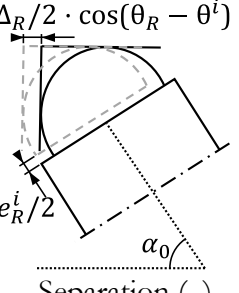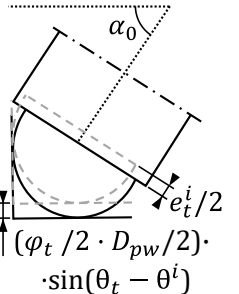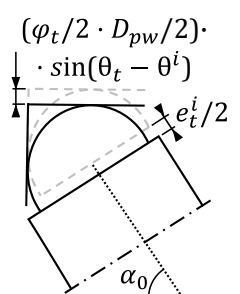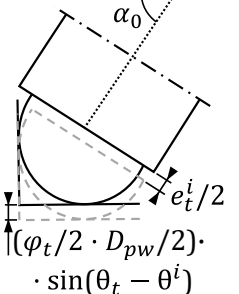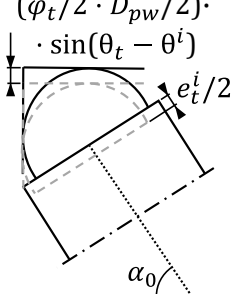
The first step consisted of developing an algorithm that obtained the structural response of the whole bearing under certain external imposed displacements. Of course, this algorithm is based on the analytical formulation for one sector previously introduced. Once the structural response of the bearing can be calculated, a simulation algorithm based on nested functions is proposed. In order to simplify understanding, explanations start on the surface and expand into the algorithm. The first subsection introduces the main block, the most superficial level. Next, two blocks can be found; one to obtain the static load capacity and stiffness, and another with the optimization process that solves the load distribution problem.

5.4.1 Bearing solver

The bearing solver block, as its name suggests, is responsible for calculating the structural response of the bearing under external applied displacements. The proposed algorithm solves the analytical formulation for each sector and gathers the results to obtain the response of the whole bearing.

The first step to solve the formulation for one sector i consists of calculating the external displacements that are applied over it. The bearing can be subjected to three different external imposed displacements: axial (Δ_A), radial (Δ_R) and tilting angle (φ_t) with their respective orientations (θ_R, θ_t). Besides this, a rolling element preload (δ_p) can be introduced, where the contact interference can be represented as a combination of axial and radial external imposed

displacements. Finally, sector external applied displacements are calculated with Equations (5.16) and (5.17), which are based on the schema in Figure 5.12. The first equation calculates the axial displacement applied to one sector (Δ_A^i) as the contributions of the bearing imposed axial displacement (Δ_A), tilting angle (φ_t) and the axial component of the preload (δ_p). The second equation distributes the radial imposed displacement (Δ_R) to each bearing sector (Δ_R^i) and also considers the radial component of the preload (δ_p).

$$\Delta_A^i = \Delta_A + \varphi_t \cdot D_{pw}/2 \cdot sin(\theta_t - \theta^i) + \delta_p \cdot sin(\alpha_0) \qquad (5.16)$$

$$\Delta_R^i = \Delta_R \cdot cos(\theta_R - \theta^i) + \delta_p \cdot cos(\alpha_0) \qquad (5.17)$$

Figure 5.12 External imposed displacements.

The next step after calculating the displacements that one sector i supports, consists of evaluating whether the rolling element suffers compression or loses the contact. To this end, the theoretical contact interference (e^i) must be calculated. The interferences that generate each type of displacement for each roller type are indicated in Table 5.4, where the sign of the interference is positive if compression occurs and negative if the contact surfaces move away. The contact interference (e^i) is obtained in Equation (5.18) as the sum of the interferences generated by each type of displacement (e_A^i, e_R^i, e_t^i) and the preload; if the value of e^i is positive, contact happens.

$$e^i = e_A^i + e_R^i + e_t^i + \delta_p \qquad (5.18)$$

Table 5.4 Contact interferences for pure load cases.

Axial ring displacement Δ_A

Compression direction		Tension direction	
Type A roller	Type B roller	Type A roller	Type B roller
Contact (+)	Separation (−)	Separation (−)	Contact (+)

$$e_A^i = \Delta_A \cdot sin(\alpha_0)$$

Radial ring displacement Δ_R

$(\theta_R - 90°) < \theta^i < (\theta_R + 90°)$		$(\theta_R + 90°) < \theta^i < (\theta_R - 90°)$	
Type A roller	Type B roller	Type A roller	Type B roller
Contact (+)	Contact (+)	Separation (−)	Separation (−)

$$e_R^i = \Delta_R \cdot \cos(\theta_R - \theta^i) \cdot \cos(\alpha_0)$$

Angular ring displacement φ_t

$(\theta_t - 180°) < \theta^i < (\theta_t)$		$(\theta_t) < \theta^i < (\theta_t + 180°)$	
Type A roller	Type B roller	Type A roller	Type B roller
Contact (+)	Separation (−)	Separation (−)	Contact (+)

$$e_t^i = (\varphi_t \cdot D_{pw}/2) \cdot \sin(\theta_t - \theta^i) \cdot \sin(\alpha_0)$$

Both steps explained until this point are carried out for each sector at the beginning of the loop, as the flowchart in Figure 5.13 illustrates. After this, the path splits in two. If the contact interference is negative, the rings separate from each other and contact does not happen. In this case, the variables of the system of equations are set to zero and the contact angle to its initial value. This way, there is no need to solve the system of equations, which is more efficient in terms of computational cost.
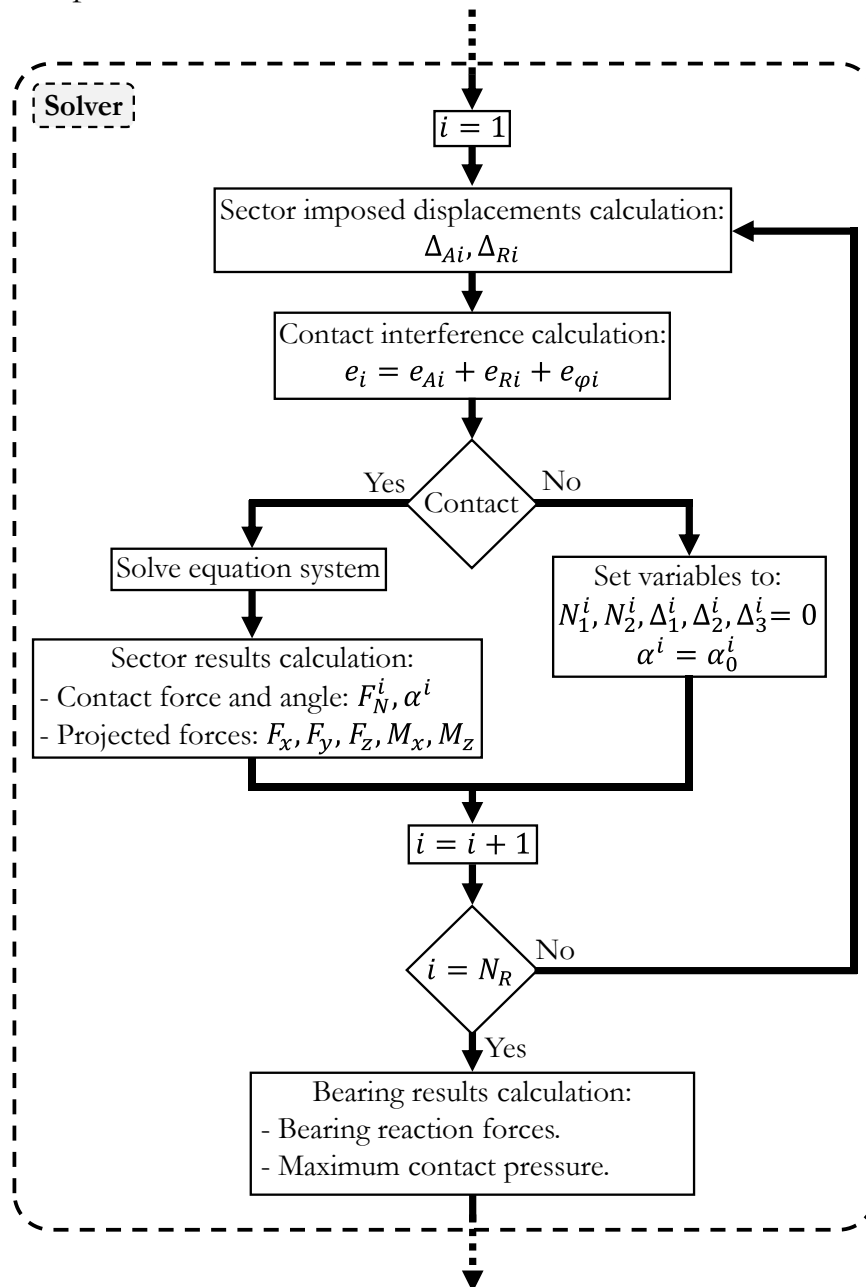
Figure 5.13 Solver block flowchart.

On the other hand, if the contact interference is positive, compression of the rolling element occurs and the system formed by Equations (5.1) to (5.6) is solved depending on the predominant (Δ_A^i, Δ_R^i). The sector calculation does not

end here, since the results are oriented in the radial direction defined by θ^i. In order to gather force results and obtain the reactions on the bearing, the results of each sector have to be referred to one reference coordinate system. Figure 5.14 shows the sector reaction forces and the distances to the axes of the reference coordinate system for type A and type B rollers (subscripts A or B). Based on that, Equations (5.19), (5.20) and (5.21) projects sector reaction forces results on the reference coordinate system, and Equations (5.22) to (5.23) also calculates the moments generated. It is worth recalling that friction forces direction varies depending on the predominant (Δ_A^i, Δ_R^i), so the same plus-minus $(\pm, \mp)$ criterion employed for the sector analytical formulation is used (upper signs for predominant Δ_A^i and lower signs for predominant Δ_R^i).

(a)

(b)

Figure 5.14 Inner ring reaction forces and distances to the bearing center: Type B roller; Type A roller.

$$F_x^i = \left(N_{2A}^i \pm \mu \cdot N_{1A}^i\right) \cdot cos(\theta^i)$$
$$F_x^i = \left(N_{2B}^i \pm \mu \cdot N_{1B}^i\right) \cdot cos(\theta^i)$$

(5.19)

$$F_y^i = \left(N_{1A}^i \mp \mu \cdot N_{2A}^i\right)$$
$$F_y^i = \left(-N_{1B}^i \pm \mu \cdot N_{2B}^i\right)$$

(5.20)

$$F_z^i = \left(N_{2A}^i \pm \mu \cdot N_{1A}^i\right) \cdot sin(\theta^i)$$
$$F_z^i = \left(N_{2B}^i \pm \mu \cdot N_{1B}^i\right) \cdot sin(\theta^i)$$

(5.21)

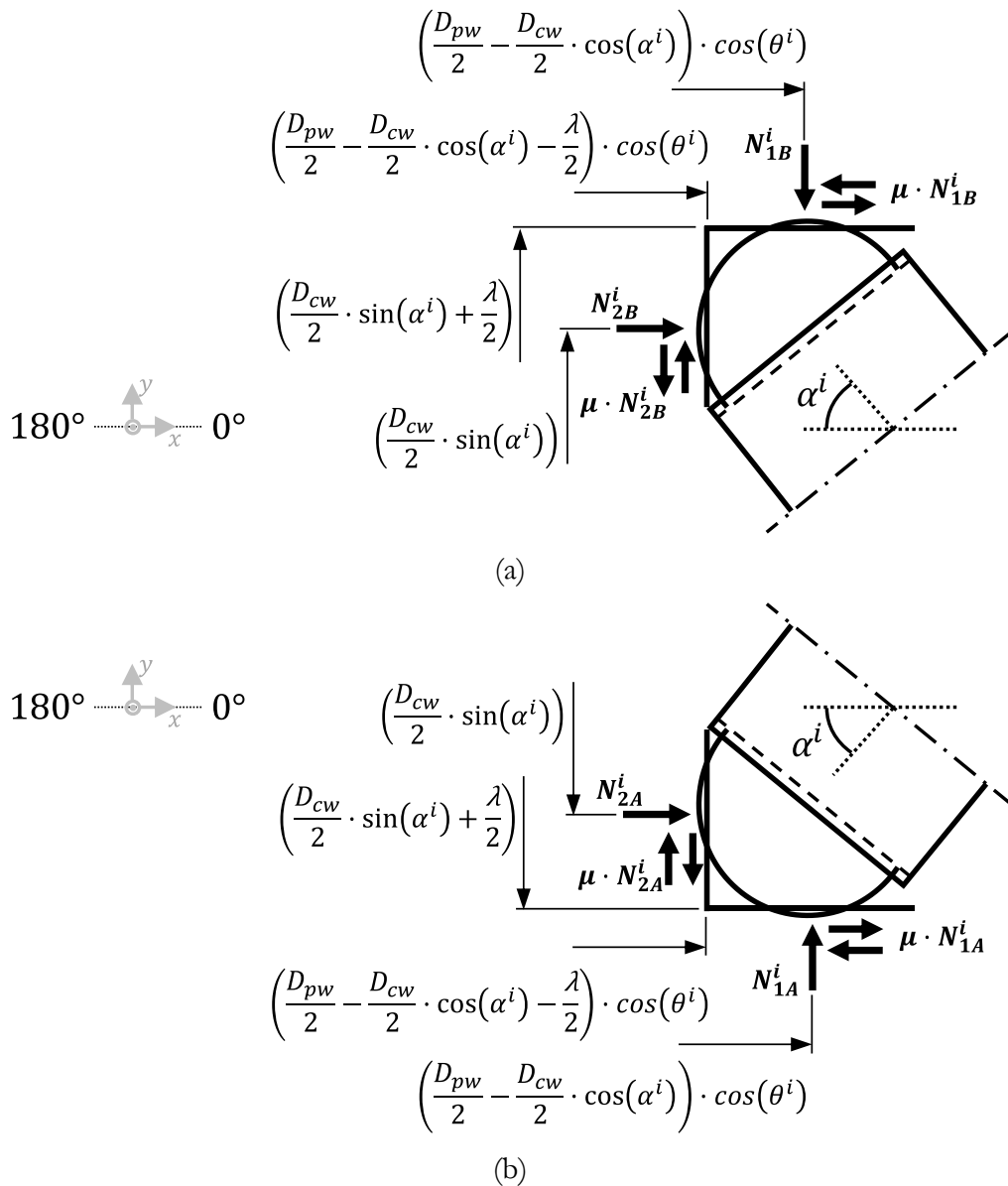$$M_x^i = -N_{1A}^i \cdot \left(\frac{D_{pw}}{2} - \frac{D_{cw} \cdot cos(\alpha^i)}{2}\right) \cdot sin(\theta^i) \mp \mu \cdot N_{1A}^i \cdot sin(\theta^i) \cdot$$
$$\cdot \left(\frac{D_{cw}}{2} \cdot sin(\alpha^i) + \frac{\lambda}{2}\right) - N_{2A}^i \cdot sin(\theta^i) \cdot \left(\frac{D_{cw}}{2} \cdot sin(\alpha^i)\right) \pm$$
$$\pm \mu \cdot N_{2A}^i \cdot \left(\frac{D_{pw}}{2} - \frac{D_{cw} \cdot cos(\alpha^i)}{2} - \frac{\lambda}{2}\right) \cdot sin(\theta^i)$$

(5.22)

$$M_x^i = N_{1B}^i \cdot \left(\frac{D_{pw}}{2} - \frac{D_{cw} \cdot cos(\alpha^i)}{2}\right) \cdot sin(\theta^i) \pm \mu \cdot N_{1B}^i \cdot sin(\theta^i) \cdot$$
$$\cdot \left(\frac{D_{cw}}{2} \cdot sin(\alpha^i) + \frac{\lambda}{2}\right) + N_{2B}^i \cdot sin(\theta^i) \cdot \left(\frac{D_{cw}}{2} \cdot sin(\alpha^i)\right) \mp$$
$$\mp \mu \cdot N_{2B}^i \cdot \left(\frac{D_{pw}}{2} - \frac{D_{cw} \cdot cos(\alpha^i)}{2} - \frac{\lambda}{2}\right) \cdot sin(\theta^i)$$

$$M_z^i = N_{1A}^i \cdot \left(\frac{D_{pw}}{2} - \frac{D_{cw} \cdot cos(\alpha^i)}{2}\right) \cdot cos(\theta^i) \pm \mu \cdot N_{1A}^i \cdot cos(\theta^i) \cdot$$
$$\cdot \left(\frac{D_{cw}}{2} \cdot sin(\alpha^i) + \frac{\lambda}{2}\right) + N_{2A}^i \cdot cos(\theta^i) \cdot \left(\frac{D_{cw}}{2} \cdot sin(\alpha^i)\right) \mp$$
$$\mp \mu \cdot N_{2A}^i \cdot \left(\frac{D_{pw}}{2} - \frac{D_{cw} \cdot cos(\alpha^i)}{2} - \frac{\lambda}{2}\right) \cdot cos(\theta^i)$$

(5.23)

$$M_z^i = -N_{1B}^i \cdot \left(\frac{D_{pw}}{2} - \frac{D_{cw} \cdot cos(\alpha^i)}{2}\right) \cdot cos(\theta^i) \mp \mu \cdot N_{1B}^i \cdot cos(\theta^i) \cdot$$
$$\cdot \left(\frac{D_{cw}}{2} \cdot sin(\alpha^i) + \frac{\lambda}{2}\right) - N_{2B}^i \cdot cos(\theta^i) \cdot \left(\frac{D_{cw}}{2} \cdot sin(\alpha^i)\right) \pm$$
$$\pm \mu \cdot N_{2B}^i \cdot \left(\frac{D_{pw}}{2} - \frac{D_{cw} \cdot cos(\alpha^i)}{2} - \frac{\lambda}{2}\right) \cdot cos(\theta^i)$$

Once the results for all the sectors have been calculated ($i = N_R$), it is time to gather the results and obtain the response of the bearing. This is an easy task, since the force reaction results for every sector are referred to the same

Cartesian coordinate system. Equations (5.24) gathers the results of the sectors to obtain the response of the bearing.

$$F_x = \sum_{i=1}^{N_B} F_x^i \quad F_y = \sum_{i=1}^{N_B} F_y^i \quad F_z = \sum_{i=1}^{N_B} F_z^i \quad M_x = \sum_{i=1}^{N_B} M_x^i \quad M_z = \sum_{i=1}^{N_B} M_z^i \quad (5.24)$$

Nevertheless, these results are not the output of the solver. It is more convenient for the methodology to retrieve the forces in the direction of the imposed displacements, which are the inputs. To this end, Equations (5.25) and (5.26) transform the forces and moments in the x and z directions into the θ_R and θ_t directions. The force in the y direction does not require transformation, since it coincides with the axial direction.

$$F_R = F_x \cdot cos(\theta_R) + F_z \cdot sin(\theta_R) \qquad (5.25)$$

$$M_t = M_x \cdot cos(\theta_t) + M_z \cdot sin(\theta_t) \qquad (5.26)$$

The last indicator to be calculated is the maximum contact pressure. To this end, the first step consists of identifying the highest loaded rolling element. Then, the maximum contact pressure is calculated using Equation (1.23). Finally, results are exported as output and the solver block is completed. This is the deepest block in the simulation algorithm, but it was considered appropriate to introduce it in first place to simplify the understanding of the whole algorithm.

5.4.2 Main block

Once the bearing solver block is explained properly, the whole structure of the simulation algorithm can be introduced. To this end, blocks will be explained from the surface to the interior of the algorithm. This block is relatively simple, as it can be seen in the Figure 5.15 flowchart. The first part consists in collecting and checking the geometrical parameters of the bearing. On the one hand, if any of the data is inconsistent, an error message pops up and the simulation aborts the calculation. This happens if the number of rollers is uneven or if it exceeds the maximum allowable number. Besides this, contact may not occur if the roller diameter is too small or the wire cross-section can be too small if the roller diameter is too big. On the other hand, there are minor inconsistencies that the user must only be notified of by means of a warning message. For example, there could be interference between the roller and the

ring which can be solved by means of slight machining on the ring. In addition, notice must also be provided if the values of the data do not fall within the design space of the DoE. Once the data has been checked, the user can select the problem to solve, the static load capacity and stiffness, or the load distribution problem. The first option obtains the local and global force-deformation curves for pure axial, radial and tilting moment loads until the static load capacity. Besides this, for comparison purposes, static load capacity is also calculated with the expressions proposed in the ISO-76 standard [24,25]. If the user is interested in solving the load distribution problem, the external applied loads must be also introduced. These loads are a combination of axial (F_A^{input}), radial (F_R^{input}) and tilting moment (M_t^{input}) loads, with their respective angular orientation ($\theta_R^{input}, \theta_t^{input}$). The resolution of this problem provides the contact status (contact or no contact) of all the rolling elements, the contact forces, contact angles and the maximum contact pressure.
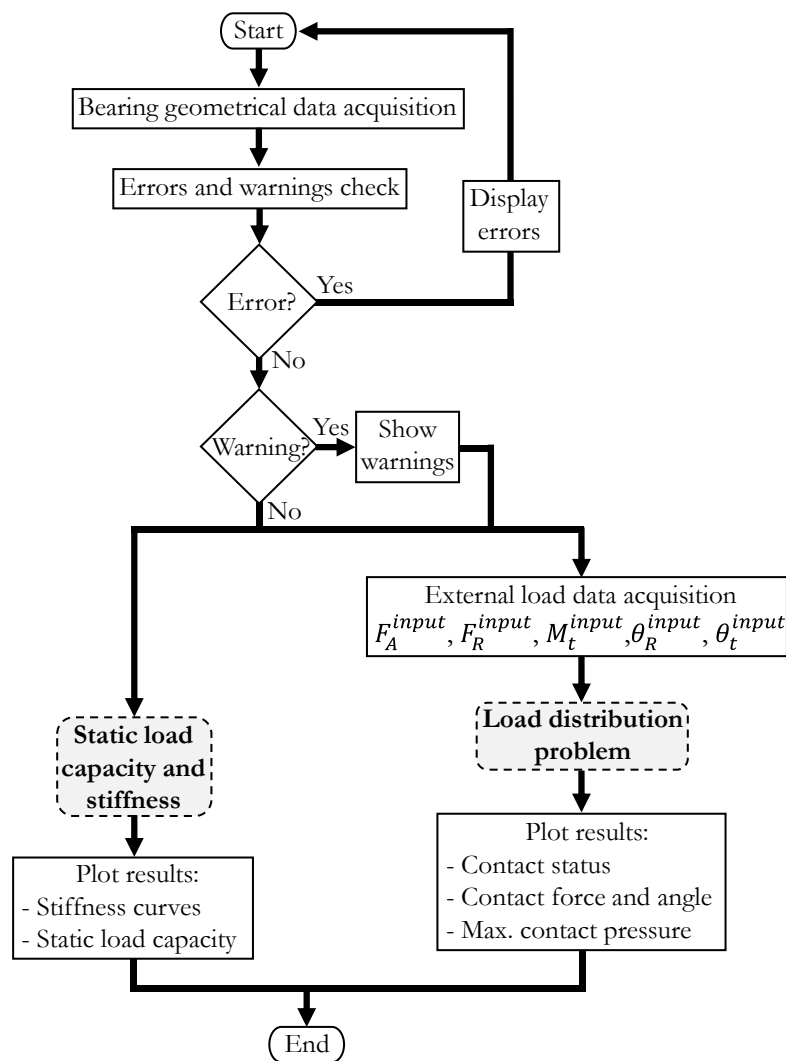
Figure 5.15 Main block flowchart.

5.4.3 Static load capacity and stiffness block

This routine is ordered from the main block, and its function consists in obtaining the static load capacity and stiffness curve for each pure load case (axial, radial and tilting). Figure 5.16 illustrates the flowchart of this block, where the first step is focused on calculating the maximum allowable contact force. Several explicit formulae can be found in the literature; however, the best results were obtained from a formula derived from the reference book written by Harris and Kotzalas [31]. These expressions have been previously introduced in Section1.4.1 as Equation (1.23) and Equation (1.24), which can be used to obtain the steel-steel contact pressure (σ) at any point of the contact patch and the contact semiwidth (b). These equations can be combined to obtain the maximum allowable contact force of Equation (5.27), which happens to be in the centre of the contact $y = 0$ [mm] at 4000 [MPa] of contact pressure [24,25]. It is also worth mentioning that the units of this formula are [N] and [mm].

$$Q_{max} = 221.5 \cdot l \cdot D_W \qquad (5.27)$$

Figure 5.16 Static load capacity and stiffness block flowchart.

The next step consists of calculating the axial, radial and tilting displacements imposed on the rings, which generate the maximum allowable contact force. To this end, a simple i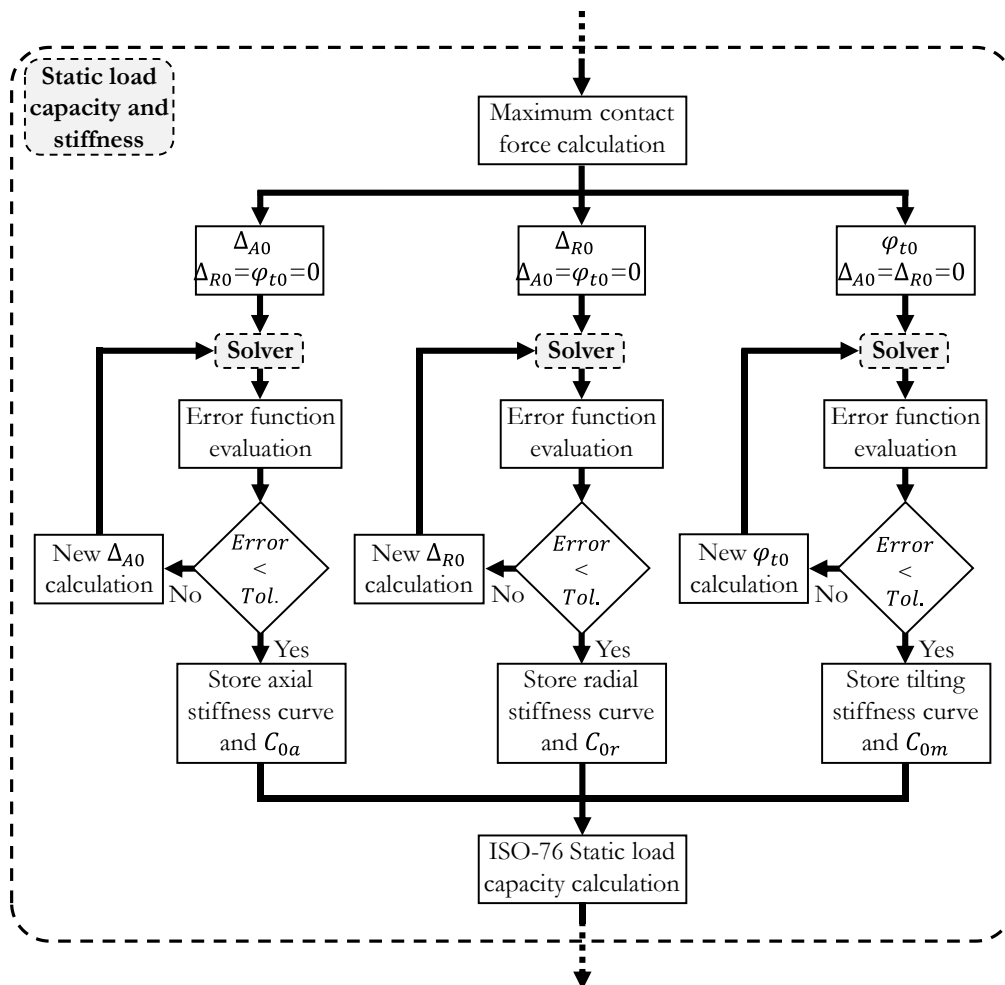terative process was programmed for each pure load case. This process starts setting an initial approximate solution, which is basically a small value of imposed pure displacement $(\Delta_{A0}, \Delta_{R0}, \varphi_{t0})$. Then, this displacement input is entered in the solver block, which calculates the contact forces, contact angles and bearing reaction forces resulting from the application of the imposed displacements. After this, the error function of Equation (5.28) is evaluated, which consists of the square of the difference between the maximum allowable contact force (Q_{max}) and the normal contact force of the most loaded roller (F_N).

$$Error = (Q_{max} - F_N)^2 \qquad (5.28)$$

The first iteration always obtains a significant error, so a new value of imposed displacement closer to the solution has to be calculated and entered in the solver block again. The new displacement value is calculated by multiplying the displacement of the current iteration by the coefficient of Equation (5.29). This coefficient (C_s) relates the target force (Q_{max}) with the result of the current iteration (F_N). The iterative process is repeated until the error is smaller than the tolerance $(tol. = 10\ [\text{N}^2])$, which happens to be quite quickly.

$$C_s = Q_{max}/F_N \qquad (5.29)$$

Once the iterative process converges to a solution, bearing force-deformation plots and the static load capacity are saved.

5.4.4 Load distribution problem block

As indicated in the previous section, imposed displacements are the inputs, and reaction forces the outputs of the solver block. However, the load distribution problem has applied forces as inputs and deformations as outputs. Dealing with this issue may seem simple, but solving this problem is far from easy, since this is the most complex block of the methodology.

The non-linear nature of the solver block demands an iterative process to solve the load distribution problem. This iterative process is more complex than the previous one, where it was only necessary to find the displacement that generated the target force in the same direction. In this case, the objective

consists in finding the combination of the three displacements that generate the desired reaction forces. The fact that three variables appear now calls for a robust iterative process. For this reason, a Taylor series based optimization process was considered a good option. Equations (5.30), (5.31) and (5.32) are the Taylor series that relate the variability of the external forces to the deformations of the bearing, where superscript j indicates the iteration number.

$$F_A^{j+1} = F_A^j + \left.\frac{\partial F_A}{\partial \Delta_R}\right|_{\Delta_R^j} \cdot \left(\Delta_R^{j+1} - \Delta_R^j\right) +$$

$$+ \left.\frac{\partial F_A}{\partial \Delta_A}\right|_{\Delta_A^j} \cdot \left(\Delta_A^{j+1} - \Delta_A^j\right) + \left.\frac{\partial F_A}{\partial \varphi_t}\right|_{\varphi_t^j} \cdot \left(\varphi_t^{j+1} - \varphi_t^j\right) \tag{5.30}$$

$$F_R^{j+1} = F_R^j + \left.\frac{\partial F_R}{\partial \Delta_R}\right|_{\Delta_R^j} \cdot \left(\Delta_R^{j+1} - \Delta_R^j\right) +$$

$$+ \left.\frac{\partial F_R}{\partial \Delta_A}\right|_{\Delta_A^j} \cdot \left(\Delta_A^{j+1} - \Delta_A^j\right) + \left.\frac{\partial F_R}{\partial \varphi_t}\right|_{\varphi_t^j} \cdot \left(\varphi_t^{j+1} - \varphi_t^j\right) \tag{5.31}$$

$$M_t^{j+1} = M_t^j + \left.\frac{\partial M_t}{\partial \Delta_R}\right|_{\Delta_R^j} \cdot \left(\Delta_R^{j+1} - \Delta_R^j\right) +$$

$$+ \left.\frac{\partial M_t}{\partial \Delta_A}\right|_{\Delta_A^j} \cdot \left(\Delta_A^{j+1} - \Delta_A^j\right) + \left.\frac{\partial M_t}{\partial \varphi_t}\right|_{\varphi_t^j} \cdot \left(\varphi_t^{j+1} - \varphi_t^j\right) \tag{5.32}$$

In the previous equations, forces of iteration $j + 1$ are actually the input forces. The terms of the previous equations can be rearranged in the matrix form of Equation (5.33). This way, the Jacobian matrix, the vector of independent terms and the vector of unknowns, which are the displacements of iteration $j + 1$, compose the system of equations.

$$
\begin{bmatrix}
\left.\dfrac{\partial F_A}{\partial \Delta_A}\right|_{\Delta_A^j} & \left.\dfrac{\partial F_A}{\partial \Delta_R}\right|_{\Delta_R^j} & \left.\dfrac{\partial F_A}{\partial \varphi_t}\right|_{\varphi_t^j} \\[2ex]
\left.\dfrac{\partial F_R}{\partial \Delta_A}\right|_{\Delta_A^j} & \left.\dfrac{\partial F_R}{\partial \Delta_R}\right|_{\Delta_R^j} & \left.\dfrac{\partial F_R}{\partial \varphi_t}\right|_{\varphi_t^j} \\[2ex]
\left.\dfrac{\partial M_t}{\partial \Delta_A}\right|_{\Delta_A^j} & \left.\dfrac{\partial M_t}{\partial \Delta_R}\right|_{\Delta_R^j} & \left.\dfrac{\partial M_t}{\partial \varphi_t}\right|_{\varphi_t^j}
\end{bmatrix}
\cdot
\begin{pmatrix} \Delta_A^{j+1} \\[1ex] \Delta_R^{j+1} \\[1ex] \varphi_t^{j+1} \end{pmatrix}
=
$$

$$
=
\begin{pmatrix}
F_A^{input} - F_A^j + \left.\dfrac{\partial F_A}{\partial \Delta_A}\right|_{\Delta_A^j} \cdot \Delta_A^j + \left.\dfrac{\partial F_A}{\partial \Delta_R}\right|_{\Delta_R^j} \cdot \Delta_R^j + \left.\dfrac{\partial F_A}{\partial \varphi_t}\right|_{\varphi_t^j} \cdot \varphi_t^j \\[3ex]
F_R^{input} - F_R^j + \left.\dfrac{\partial F_R}{\partial \Delta_A}\right|_{\Delta_A^j} \cdot \Delta_A^j + \left.\dfrac{\partial F_R}{\partial \Delta_R}\right|_{\Delta_R^j} \cdot \Delta_R^j + \left.\dfrac{\partial F_R}{\partial \varphi_t}\right|_{\varphi_t^j} \cdot \varphi_t^j \\[3ex]
M_t^{imput} - M_t^j + \left.\dfrac{\partial M_t}{\partial \Delta_A}\right|_{\Delta_A^j} \cdot \Delta_A^j + \left.\dfrac{\partial M_t}{\partial \Delta_R}\right|_{\Delta_R^j} \cdot \Delta_R^j + \left.\dfrac{\partial M_t}{\partial \varphi_t}\right|_{\varphi_t^j} \cdot \varphi_t^j
\end{pmatrix}
$$

$$(5.33)$$

Partial derivatives were obtained according to the following expressions:

$$
\left.\frac{\partial F_A}{\partial \Delta_A}\right|_{\Delta_A^j} = \frac{F_A(\Delta_A^j + \varepsilon, \Delta_R^j, \varphi_t^j) - F_A(\Delta_A^j, \Delta_R^j, \varphi_t^j)}{\varepsilon}
$$

$$
\left.\frac{\partial F_A}{\partial \Delta_R}\right|_{\Delta_R^j} = \frac{F_A(\Delta_A^j, \Delta_R^j + \varepsilon, \varphi_t^j) - F_A(\Delta_A^j, \Delta_R^j, \varphi_t^j)}{\varepsilon}
$$

$$
\left.\frac{\partial F_A}{\partial \varphi_t}\right|_{\varphi_t^j} = \frac{F_A(\Delta_A^j, \Delta_R^j, \varphi_t^j + \varepsilon) - F_A(\Delta_A^j, \Delta_R^j, \varphi_t^j)}{\varepsilon}
$$

$$(5.34)$$

$$...$$

Where ε is a coefficient small enough to ensure the convergence. This value is initially set to 0.1, but the optimization process do not always converge at first. If that happens, ε is divided by 10 and the optimization starts again. This strategy has shown good results, since convergence is usually achieved in few iterations.

As it can be observed in the flowchart of Figure 5.17, the initial solution considered for the first iteration of the optimization ($j = 1$) consists on null displacements. After this, four simulations are performed: one with the initial solution and other three where ε is added independently to each displacement of the initial solution. Then, the Jacobian matrix and the vector of independent terms can be built from the results of the simulations. The resolution of the system of Equations (5.33) retrieves the optimized displacements Δ_A^{opt}, Δ_R^{opt} and

φ_t^{opt}, which are presumably closer to the desired solution. These optimized displacements are introduced in the solver block, and the optimized loads F_A^{opt}, F_R^{opt} and M_t^{opt} calculated. To evaluate if the optimized displacements retrieve the desired target loads, the function error of Equation (5.35) is evaluated. This equation gathers the squares of the differences between the optimized loads and the input target loads. The optimization process is restarted if the error function is greater than the tolerance (1% of the input force values), but considering the optimized displacements of the current iteration as initial solution. In contrast, if the error function is smaller than the tolerance, the optimization process is completed.

$$Error = \left(F_A^{input} - F_A^{opt}\right)^2 + \left(F_R^{input} - F_R^{opt}\right)^2 + \left(M_t^{imput} - M_t^{opt}\right)^2 \quad (5.35)$$
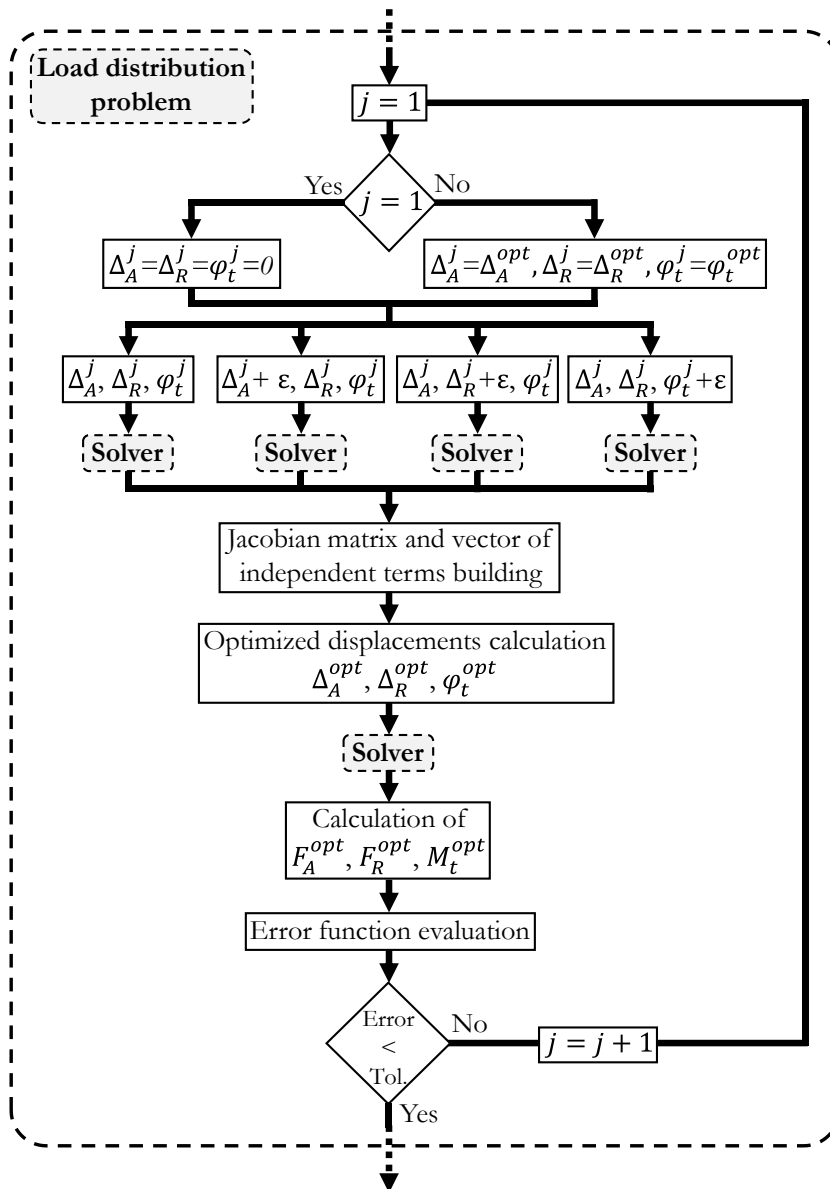

Figure 5.17 Load distribution problem block flowchart.

5.5 FE validation

The validation process followed to assess the accuracy of the simulation tool is presented in this section. The procedure is similar to the one used in Chapter 4, which consisted of a comparison between FE and analytical results. This is a good alternative to assess the accuracy of the simulation tool, since the loads and boundary conditions considered in the simulation tool can be replicated in FE. Nevertheless, it is very difficult to perform FE calculations with combined load cases, because of the large size and convergence problems that they imply. For this reason, the simulations carried out for the validation consisted of pure axial, radial and tilting moment load cases. Besides this, two different cases have to be modelled: the local and the global structural behaviour. The local case only represents the stiffness of the contacts and the global case includes the flexibility of the rings. These two cases have implications on the modelling and the boundary conditions of the FE models.

The first step to start the FE validation process consists of defining a reference bearing geometry. Geometrical and operational data of the reference bearing geometry are gathered in Table 5.5. These parameters are close to the ones used in previous chapters and similar values can be also found in the industry. Finally, this geometry is entered in the FE models and in the simulation tool to perform the results comparison.

Table 5.5 Reference bearing geometry data.

D_{pw} [mm]	D_w [mm]	λ [mm]	Rf	α_0 [°]	δ_p [µm]	N_R	μ
420	14	8	0.5	45	20	94	0.1

The first FE models to be presented are the ones used for the axial load case, since they are the most simple. Axial load and bearing geometry are cyclic symmetric, so a one sector FE model could be modelled to represent the behavior of the whole bearing. In addition to this, a sector of the bearing has a symmetry plane, so just half a bearing sector is enough for the axial load validation. Figure 5.18 shows the FE models developed for the validation of this load case and the applied boundary conditions. It is worth mentioning that the mesh is identical to the one used in the FE models to obtain the stiffness constant values (Figure 5.10).

Only the ring contact zones were considered for the local FE model and the whole ring for the global FE model. Roller-wire and wire-ring contacts were defined as frictional with Augmented Lagrange formulation, a friction coefficient of $\mu = 0.1$, a maximum penetration tolerance of 1 [µm] and updating the contact stiffness each iteration. Just in case a preload needs to be applied to the rolling element, this can be done by applying a contact offset on the roller-wire contact in a preliminary load step. The bonded contact defined to connect the contact ring partition with the rest of the ring in the global FE model, was defined with a maximum penetration tolerance of 3 [µm] and a pure penalty formulation.

In terms of boundary conditions, symmetry boundary conditions were applied on all symmetry faces of both FE models. The external load was applied via imposed displacements on certain faces of the outer ring. These imposed displacements were applied in the axial direction, constraining the DoF in the other two directions. These faces were the cutting faces on the local FE model and the faces that link the bearing with the surrounding structures on the global FE model. The same faces of the inner ring were fixed in order to avoid rigid body motion.
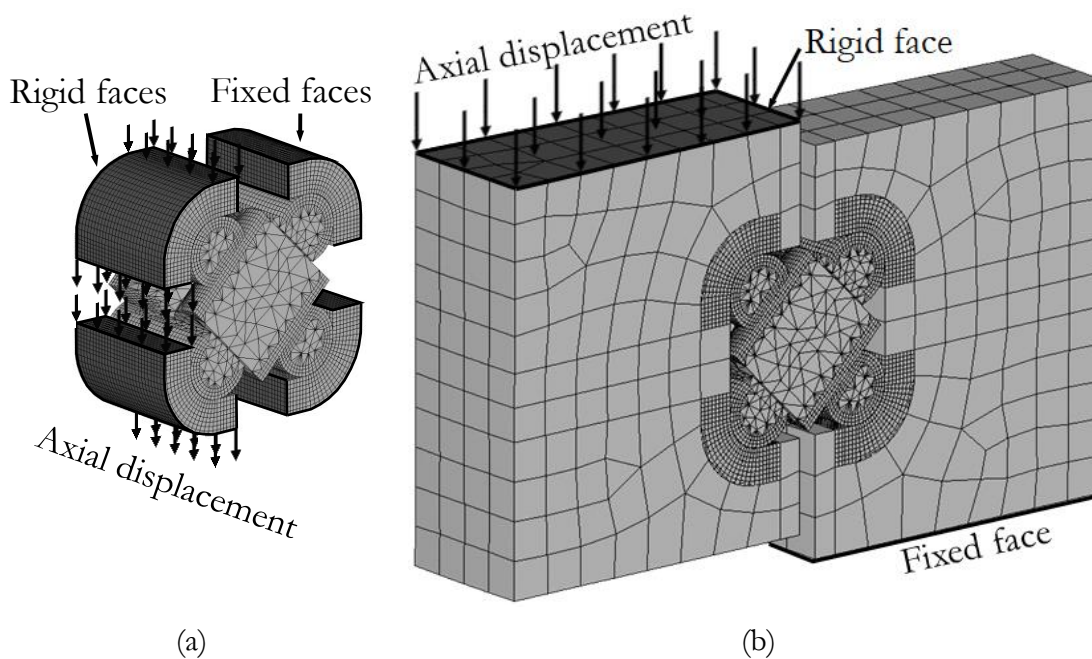

(a)   (b)

Figure 5.18 Sector FE validation models: (a) Local; (b) Global;

With the FE models for the axial load case presented, it is time to present the FE models for the radial and tilting moment load cases. These load cases are not cyclic symmetric, but do have a symmetry plane. This simplification allows

for building only half bearing FE models, which are larger than the previous ones but far more efficient than whole bearing models.

It is simple to build these models after the creation of the half sector FE models, since it is only necessary to perform a circular pattern along 180 [°] with the revolution axis in the centre of the bearing. To avoid convergence problems, only rollers that suffer compression were modelled. It is easy to identify them by applying the methodology presented in section 0. Figure 5.19 shows the mesh and boundary conditions for each local and global FE model. The radial and tilting moment loads are applied by means of a remote node created in the centre of the bearing. This remote node is rigidly linked to the surfaces where the load is applied, and transmits radial or tilting angle external displacements.
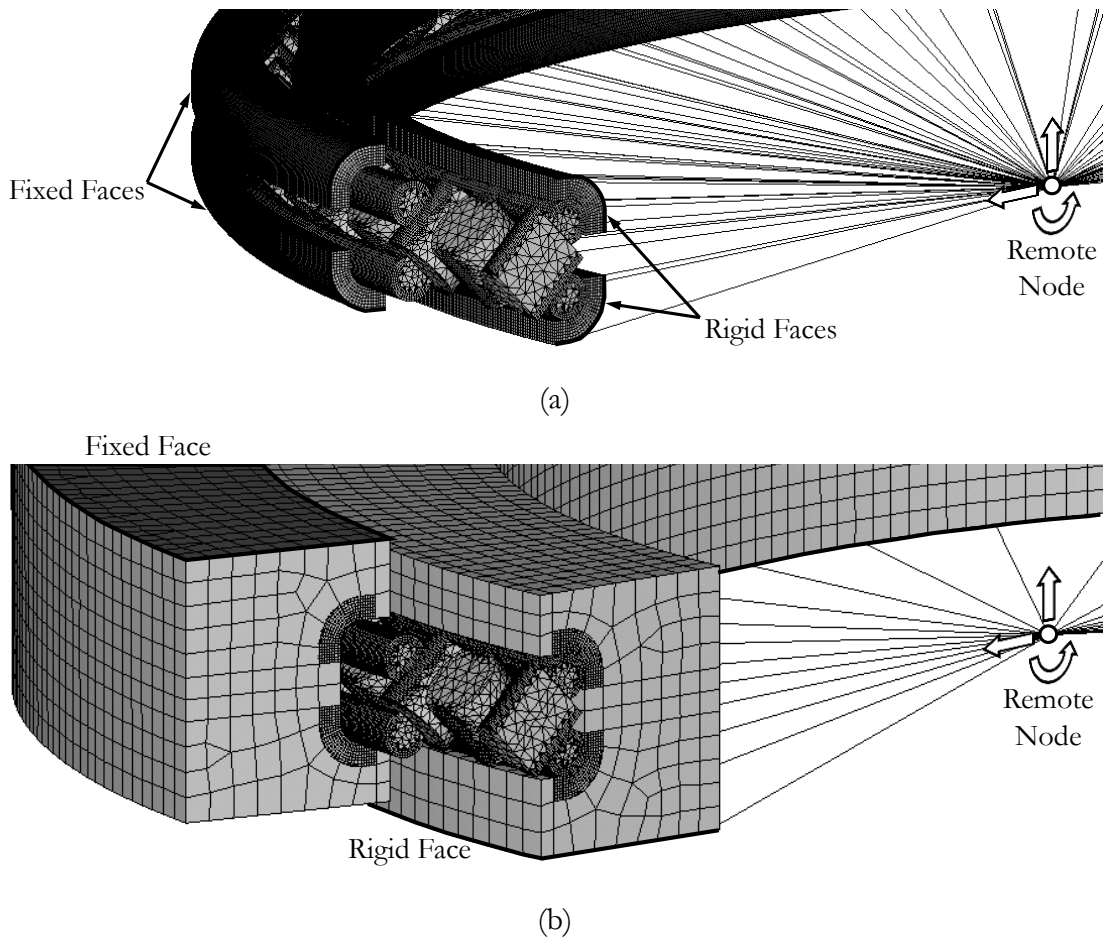

(a)

(b)

Figure 5.19 Half bearing FE validation models: (a) Local; (b) Global.

Stiffness curves, normal contact force and contact angle distribution were the performance indicators selected for the validation. Besides this, it is important to verify that the analytical simulation tool properly calculates the static load capacity. To this end, the FE contact pressure distribution at the static load

capacity computed by the analytical model is compared with the theoretical limit of 4000 [MPa].

Figure 5.35, Figure 5.36 and Figure 5.37 show the stiffness curves comparison for the local and global models of the three pure load cases studied. Stiffness curves reach the static load capacity calculated with the analytical simulation tool, which happens when the maximum allowable contact pressure is reached in the most loaded roller. Since the analytical tool can perform calculations with preloaded and non-preloaded rollers, it was considered adequate to validate both alternatives. However, preload could only be applied for the axial load case, because it was the only load case that did not present convergence problems. The other two load cases were unable to converge due to the loss of contact when the load started to be applied (all the contacts were loaded initially because of the preload).

Both analytical and FE results match fairly well at first glance. It can be seen that the non-linear behavior of the non-preloaded FE results, which are linear in the first section and become stiffer at around half of the static load capacity. This behaviour is caused by the wire-ring gap closure phenomenon, explained in Section 5.3.1. Up to this point, the analytical tool is accurate showing excellent compliance; however, a slight deviation can be observed. There are some potential root causes for this behaviour. For example, the stiffness constants were obtained from an approximate formula that can introduce a small error that stiffens the results. In addition to this, all the assumptions and simplifications made for the development of the analytical formulation can also introduce small errors. It is worth mentioning this phenomenon, but it is not significant enough to consider the compliance as not being very good.

Axial stiffness curves are similar and the static load capacity is the same in all cases. The stiffer behaviour that is seen at the beginning of the preloaded case is caused by the rollers that will lose contact further on. They are initially loaded because of the preload, and the axial force has to deal with it. Once the preload is overcome and the rollers lose contact, the trend is equivalent to the non-preloaded situation.

Regarding the radial and tilting moment load cases, there is a more significant difference between the local and global stiffness curves. Besides, the static load capacity is lower in these two load cases under global conditions. The causes of these phenomena are easily recognizable observing the next performance indicators results.
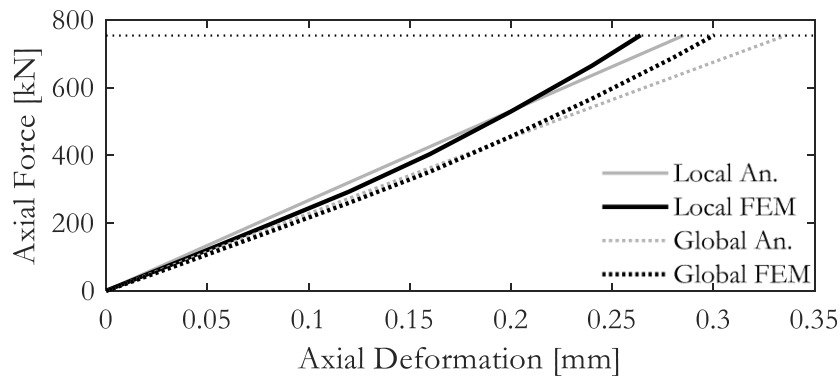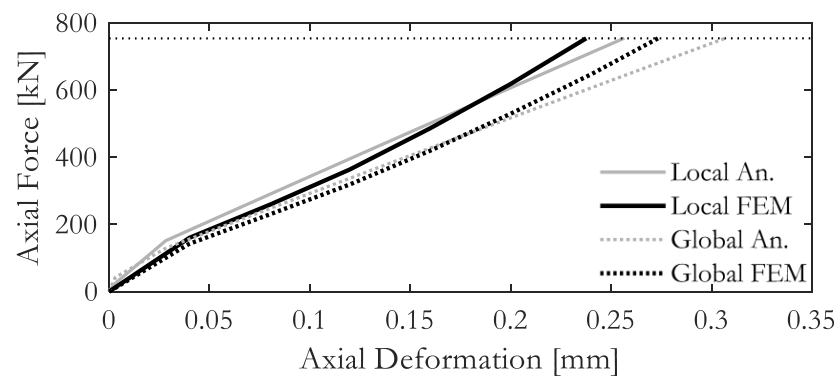
Figure 5.20 Axial load case stiffness curves comparison: (a) No roller preload; (b) 20 [μm] roller preload.
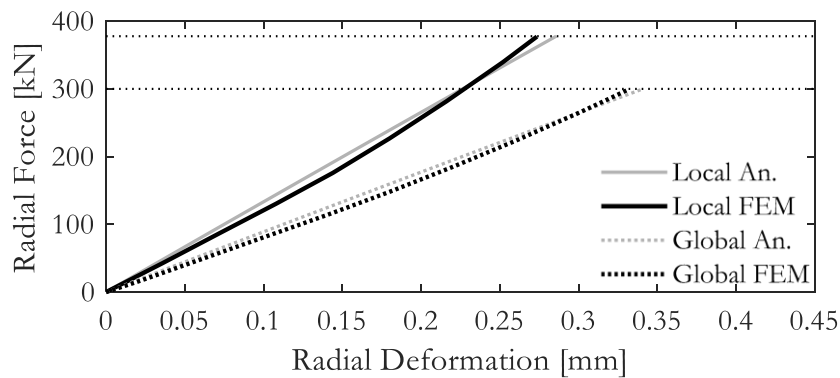

Figure 5.21 Radial load case stiffness curves comparison.
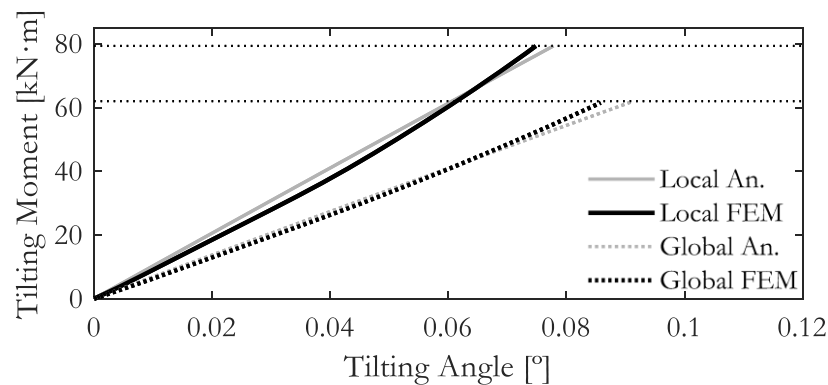

Figure 5.22 Tilting moment load case stiffness curves comparison.

After comparing the stiffness curves, it was deemed appropriate to compare the normal contact force and contact angle results. These results provide important information about the behavior of the bearing and are crucial to calculate the static load capacity of the bearing. The plots that represent these results can only display them at one load level; for this reason, Figure 5.23 to Figure 5.30 show the normal contact force and contact angle on all the rolling elements at 50% of the calculated static load capacity. The choice of this load level was based on its proximity to the gap closure phenomenon, which was the limit until the assumptions made are valid. Nevertheless, similar results are obtained for 100% of the static load capacity.

Regarding the axial load, the four studied cases present almost perfect agreement. There is a small deviation of 0.2 degrees in the global condition cases, which can be considered negligible. The other two load cases, radial and tilting moment loads, also show very good correlation. The effect of the local and global behaviour conditions is more evident in these two cases, since type A and B rollers are loaded simultaneously. The imposed sector displacement must be distributed between contact and ring deformation. On the one hand, the contribution of the ring deformation is small for type A rollers, so the contact deformation must absorb the external imposed displacement. On the other hand, the flexibility of the rings absorbs a significant proportion of the external imposed displacement in the case of type B rollers. Since the stiffness of the contact is higher than the stiffness provided by the rings (in the global models), it is reasonable that type A rollers transmit more force than type B rollers. This difference in the force level between type A and B rollers increases the gap between the local and global stiffness curves. However, this phenomenon is not so evident in the axial load case, since only type A rollers are loaded. There is also a fact that confirms the correct representation of the stiffness and physical phenomena of the system. The loads are applied as external imposed displacements and it was proven that the load distribution was obtained properly. Achieving these results is more difficult with imposed displacements than with applied forces, where it is easier to obtain the proper load distribution regardless of the deformations.
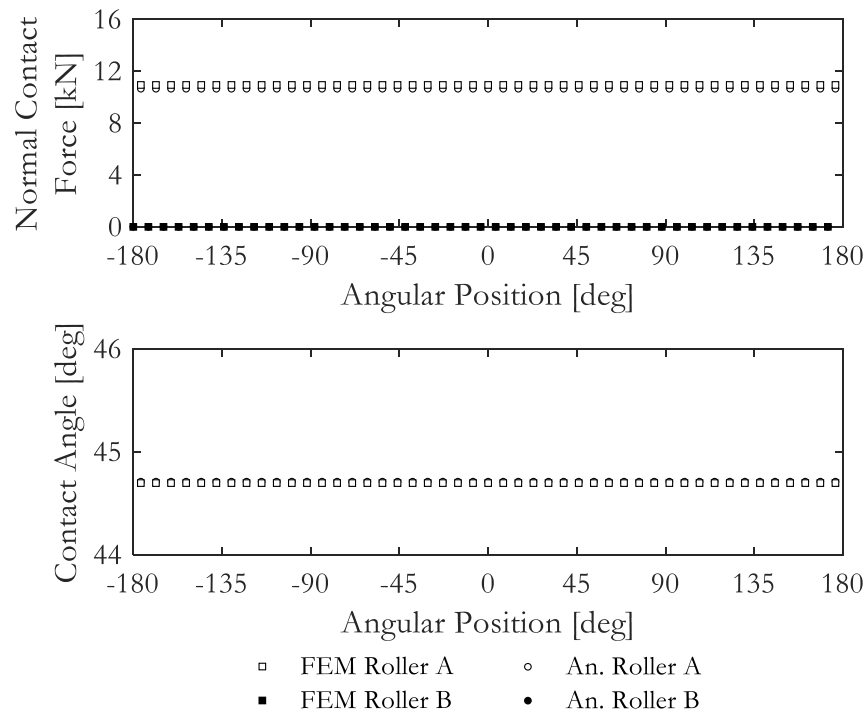
Figure 5.23 Axial load case for 50% of the C_{0a} with local models: normal contact force and angle.
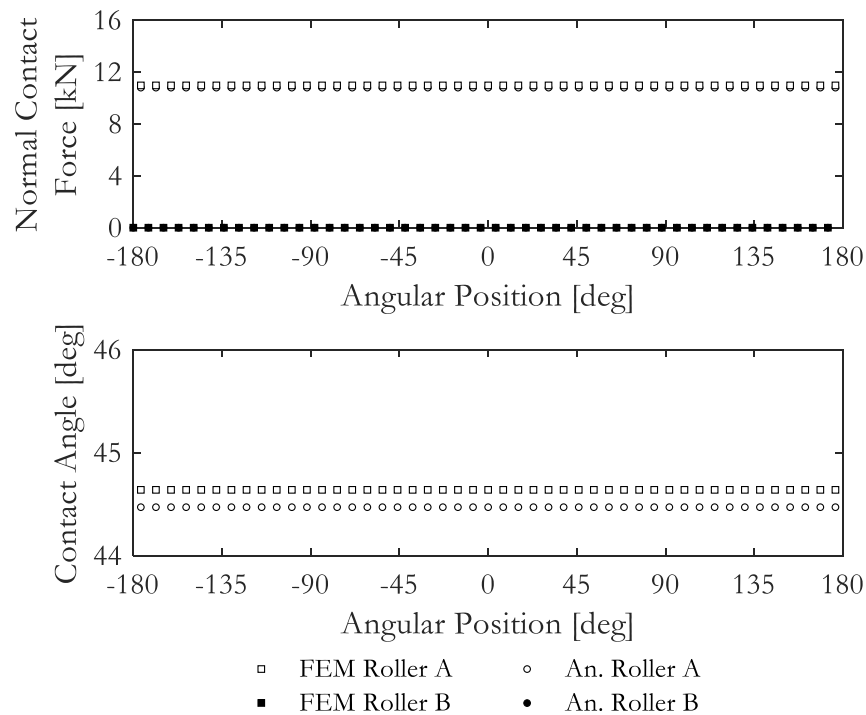

Figure 5.24 Axial load case for 50% of the C_{0a} with global models: normal contact force and angle.

Figure 5.25 Axial load case (20 [μm] preload) for 50% of the $\boldsymbol{C_{0a}}$ with local models: normal contact force and angle.

Figure 5.26 Axial load case (20 [μm] preload) for 50% of the $\boldsymbol{C_{0a}}$ with global models: normal contact force and angle.
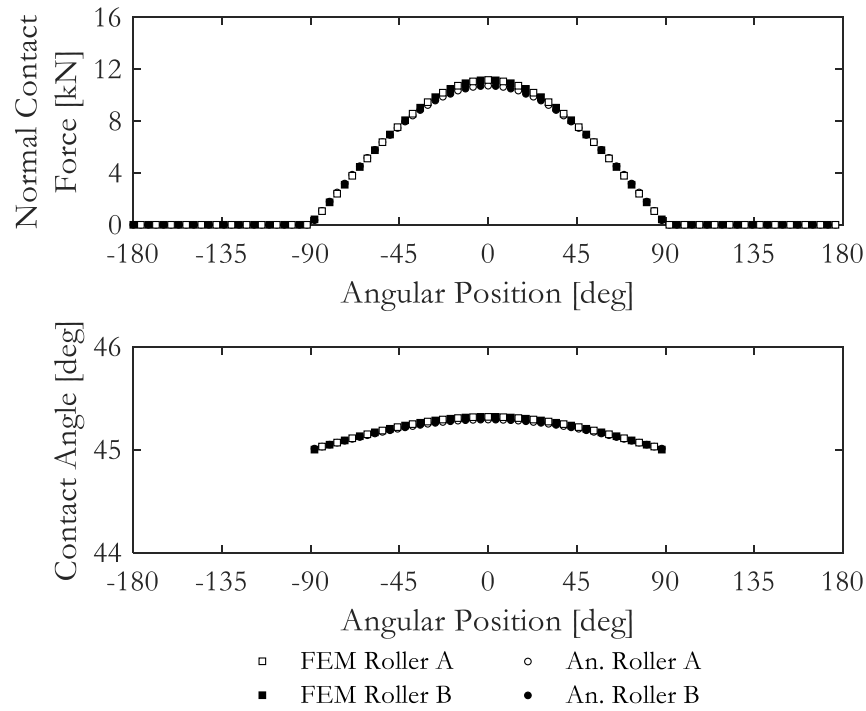
Figure 5.27 Radial load case for 50% of the C_{0a} with local models: normal contact force and angle.
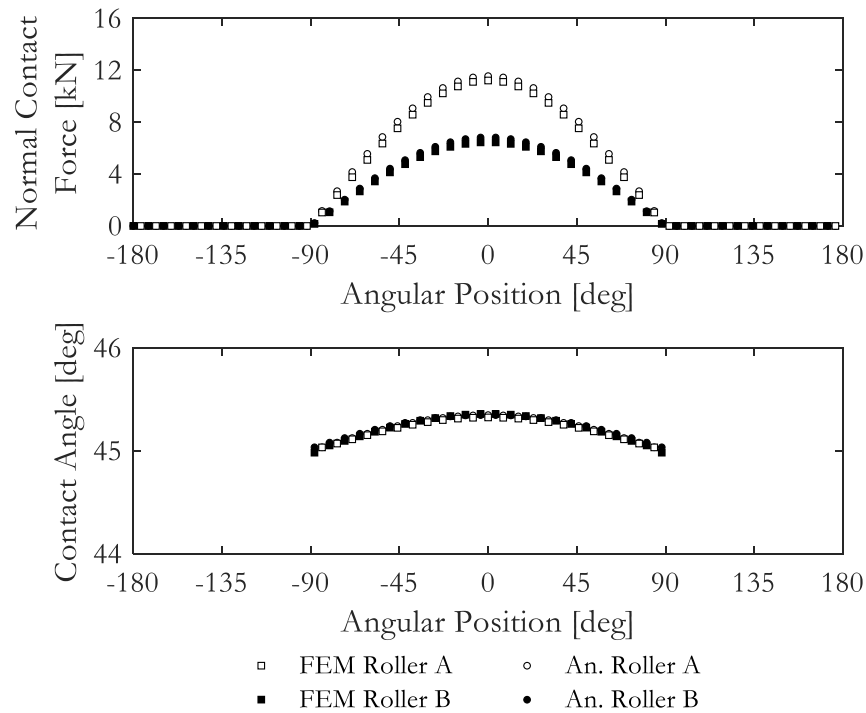
Figure 5.28 Radial load case for 50% of the C_{0a} with global models: normal contact force and angle.
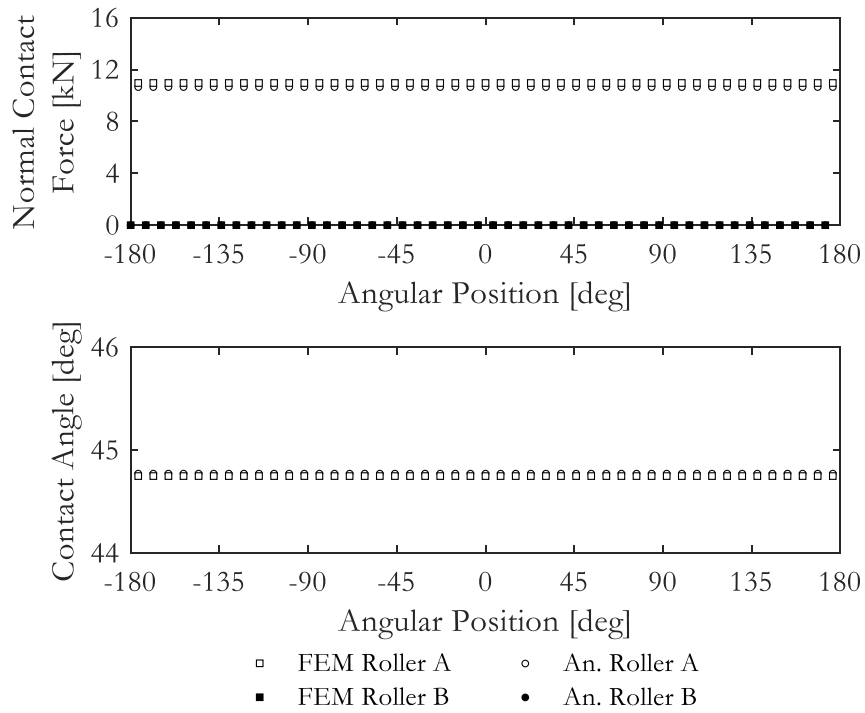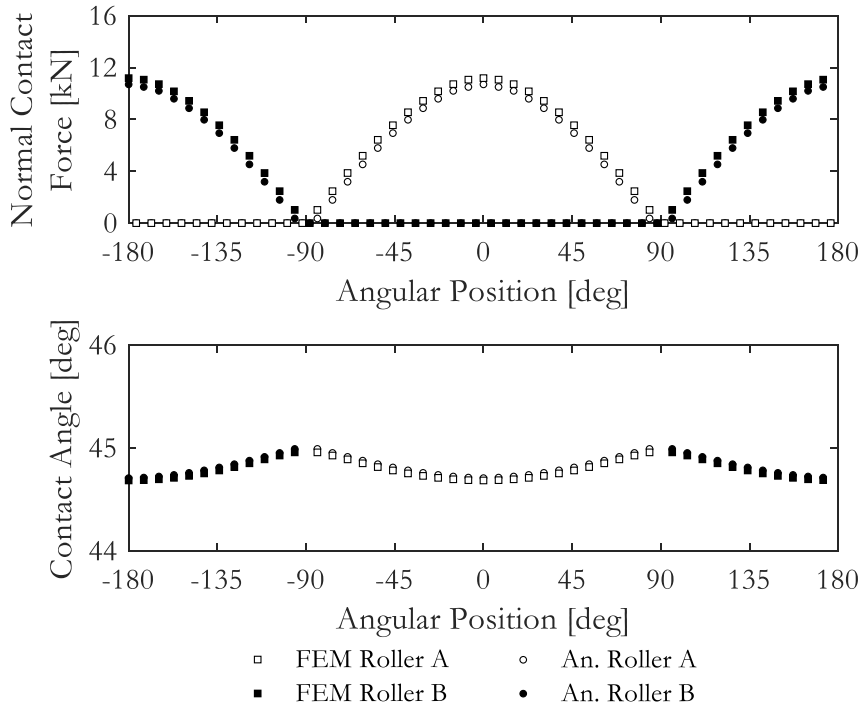
Figure 5.29 Tilting moment load case for 50% of the C_{0a} with local models: normal contact force and angle.

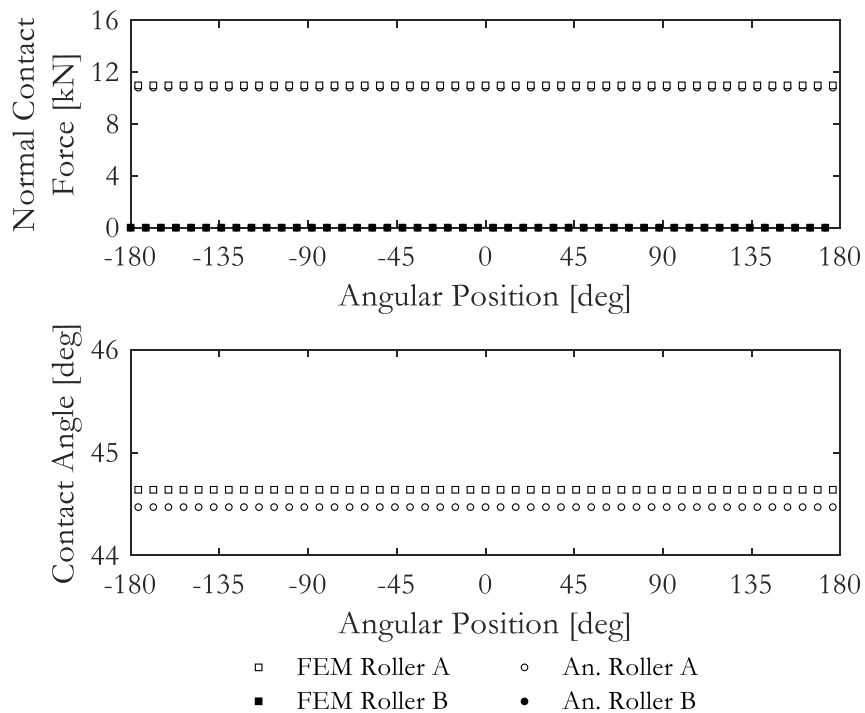

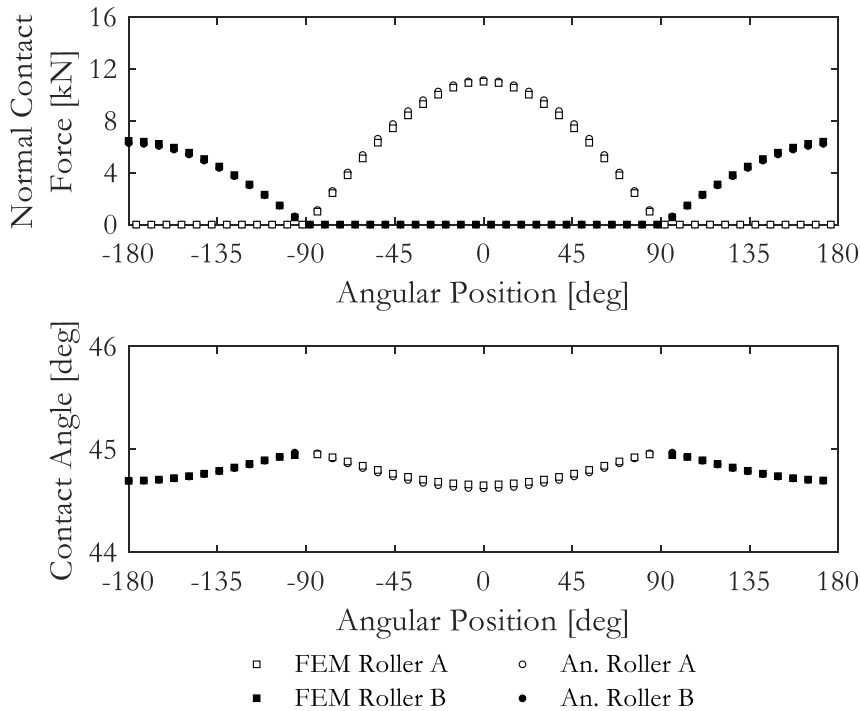**Figure 5.30** Tilting moment load case for 50% of the C_{0a} with global models: normal contact force and angle.

It can be seen how the maximum normal contact force is the same in all the studied cases with both local and global conditions. This is obvious, since the maximum allowable contact load is defined by the contact geometry, and all the plots were obtained for 50% of the static load capacity. Nevertheless, the static

load capacity is different depending on the boundary conditions. The lower load level of type B rollers under global conditions reduces the force transmitted by the bearing when the static load capacity is reached. Table 5.6 gathers the values of the static load capacity calculated with the ISO-76 standard [24,25] and with the analytical tool. In line with the comments made in this section, the static load capacity obtained with the analytical tool is almost the same for the axial load case in both local and global conditions. However, there is a significant difference when it comes to the radial and tilting moment load case.

The results of the standard can only be compared with the analytical tool results with local conditions, since the assumptions made for its calculation are similar. As a result, it can be stated that the standard is conservative for static load capacity calculation. Nonetheless, it must be mentioned this is not the case for the global conditions, where the static load capacity for tilting moment loads is smaller.

Table 5.6 Static load capacity comparison.

	ISO-76 Standard	**An. Tool Local**	**An. Tool Global**
C_{0a} [kN]	694.72	753.59	751.79
C_{0r} [kN]	277.89	377.70	299.93
C_{0m} [kN·m]	72.95	79.32	61.99

The comparison of the static load capacity is relevant, but no evidence has been provided to this point that confirms that the static load capacity is calculated properly with the analytical tool. For this reason, Figure 5.31 to Figure 5.34 represent the FE pressure lines along the major axis of the most loaded contact when the static load capacity is reached. Each pressure point in the plots corresponds to the pressure on one contact element, which was obtained as the average of the element nodal pressures (with the ETABLE command in Ansys®).

The pressure peaks at the edges of the raceway are probably the first things that can be noticed at first glance. The roller-wire contact is always truncated on the major axis, and large non-realistic pressure peaks appear because of the edge effects and the linear material assumption. These pressure peaks can be avoided to a great extent by applying a wire edge geometry correction such as

the one suggested by Gunia and Smolnicki [159] and commented in the literature review section. Besides this, a small roller crowning could also be applied to reduce this phenomenon even more.

Pressure lines are not uniform, they are slightly tilted. The tangential friction forces that appear in the roller-wire contact are the reason for this behaviour. It is worth mentioning that the tilt is in one or another direction depending on the predominant sector imposed displacement, since the pressure lines tilt in one direction for the axial and tilting moment load case and in the opposite for the radial load case.

If the pressure peaks are not taken into account, the pressure along the contact does not reach the maximum allowable pressure of 4000 [MPa]. For this reason, it can be said that the analytical simulation tool obtains excellent results, but slightly underestimates the static load capacity for all the studied load cases. This means that the analytical model is slightly conservative but still more accurate than the current methodologies. The formula used in the analytical algorithm to obtain the pressure (Equation (1.23)) considers a cylinder-plane contact with uniform applied load, with no tilt and no edge effects. Therefore, a perfect match was not expected.
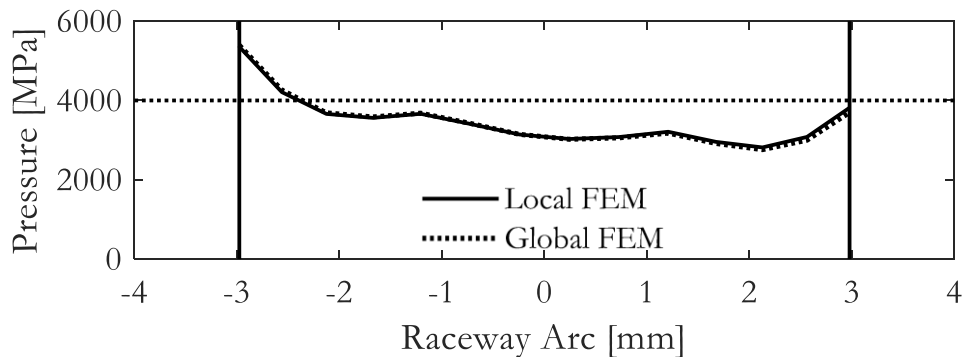

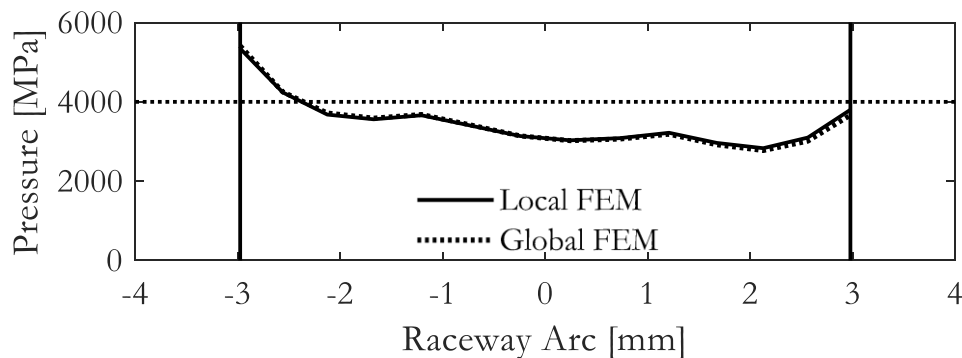**Figure 5.31** Axial load case roller-wire contact major axis pressure lines.

Figure 5.32 Axial load case (with 20 [μm] roller preload) roller-wire contact major axis pressure lines.
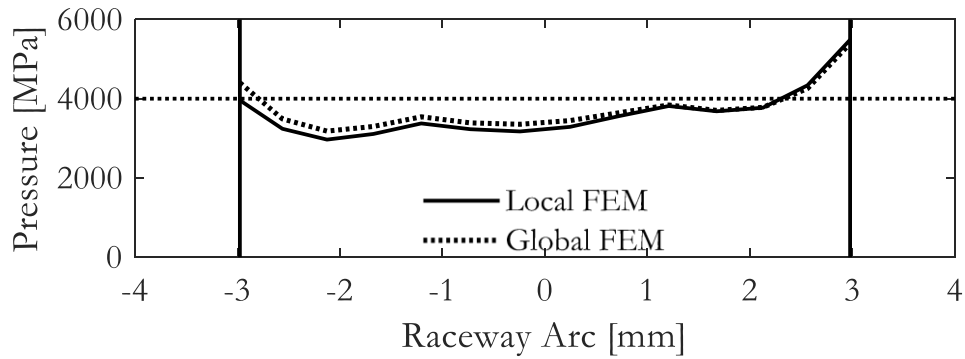
Figure 5.33 Radial load case roller-wire contact major axis pressure lines.
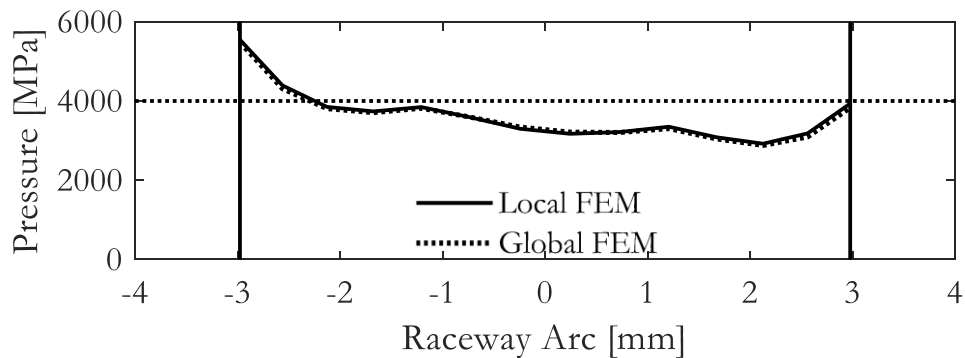

Figure 5.34 Tilting moment load case roller-wire contact major axis pressure lines.

This point concludes the validation process of the analytical simulation tool. The performance indicators results comparison between the analytical tool and FE models tally in all of the study cases. For this reason, it can be asserted that the analytical calculation can be used to obtain the bearing stiffness curves and the static load capacity, and also to solve the load distribution problem accurately.

5.6 Results

Up to this point, the performance of the analytical simulation tool was only tested with pure load cases. For this reason, the purpose of this section consists in showing its complete calculation potential by means of a more complex calculation example.

For the sake of simplicity and coherence, the reference bearing geometry presented in the previous section is also used here. The geometrical and operational data of Table 5.5 are enough to calculate the stiffness curves and the static load capacity of the bearing. Figure 5.35, Figure 5.36 and Figure 5.37 show the force-deformation results of the bearing until the static load capacity, where both local and global boundary conditions results are shown. The axial curves are the same ones that were presented in the previous section. However,

the radial and tilting moment curves are new, since non-preloaded results were provided then. It can also be seen that, in these load cases, the preload produces the same behaviour previously shown for the axial load case.
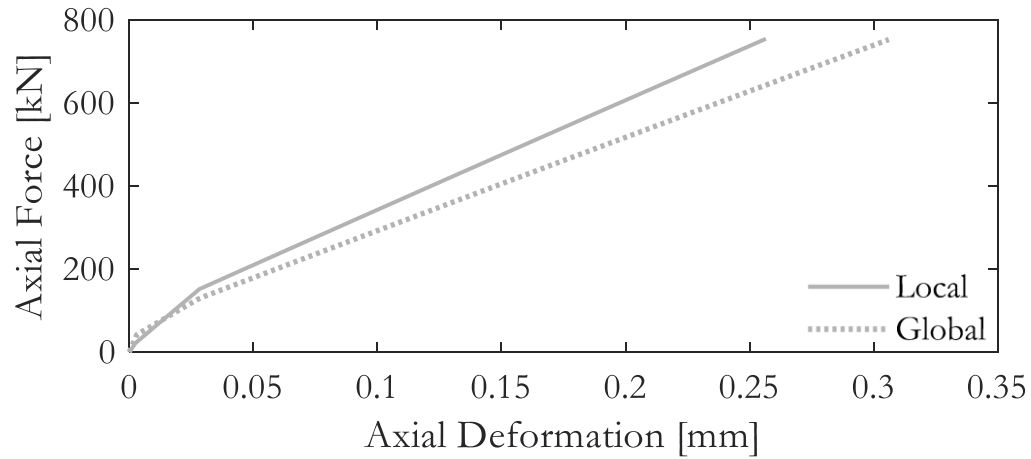
Figure 5.35 Axial stiffness curves.
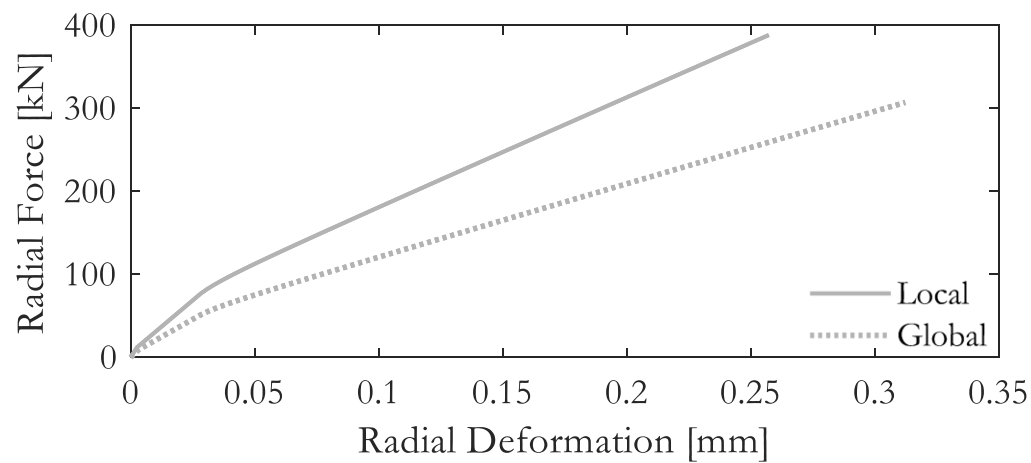
Figure 5.36 Radial stiffness curves.
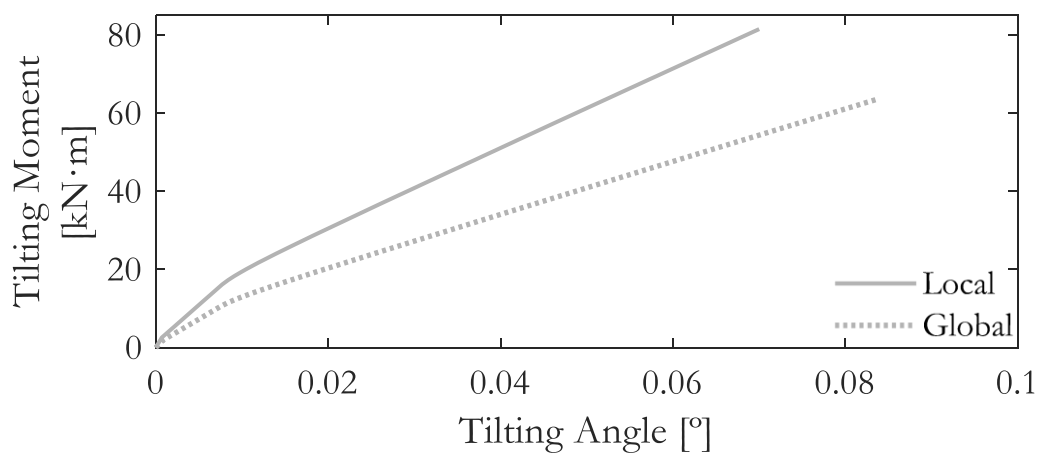
Figure 5.37 Tilting stiffness curves.

The static load capacity values calculated with the simulation tool are compiled and compared with the values obtained with the ISO-76 [24,25] formulae in Table 5.7. It can be noticed that the values are very similar to the ones shown in Table 5.6. Slightly higher values were obtained in this case as a result of the introduction of preloaded rollers. However, the values calculated with the standard are the same, since the preload cannot be considered.

Table 5.7 Calculated static load capacity.

	ISO-76 Standard	An. Tool Local	An. Tool Global
C_{0a} [kN]	694.72	754.35	752.57
C_{0r} [kN]	277.89	388.18	306.97
C_{0m} [kN·m]	72.95	81.51	63.45

To solve the load distribution problem, it is necessary to introduce the load values that act on the bearing. Table 5.8 shows the values and orientation of the applied forces selected for this simulation. In this table, a drawing of the loads orientation is represented together with an indication of the nomenclature of the normal contact forces.

Table 5.8 Load values and orientations for the load distribution problem.

F_A [kN]	F_R [kN]	θ_R [°]	M_t [kN·m]	θ_t [°]
30	130	30	20	110
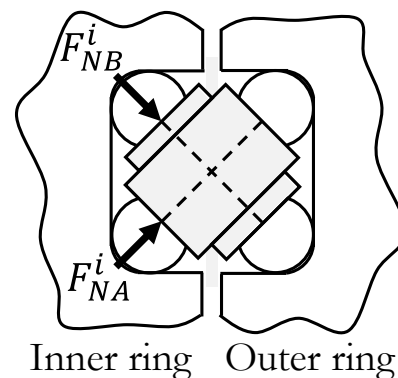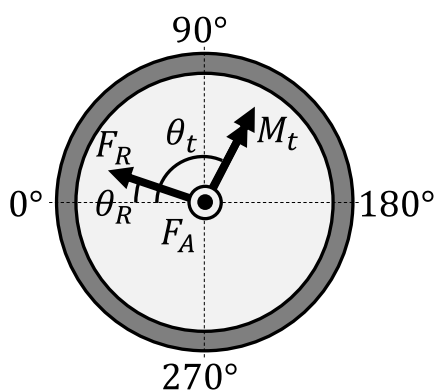
The load distribution problem can be solved considering local or global boundary conditions. Surprisingly, very similar results are obtained in terms of contact results. This does not mean that the boundary conditions have no effect, since the deformation of the rings is very different. However, the applied forces are the same, and in order to reach the equilibrium, the loads are distributed almost identically. For this reason, only results with the global boundary conditions are presented in this section.

The rollers contact status is the first result that the analytical simulation tool obtains. Figure 5.38 represents the applied loads and the contact status of the rollers at the end of the simulation.
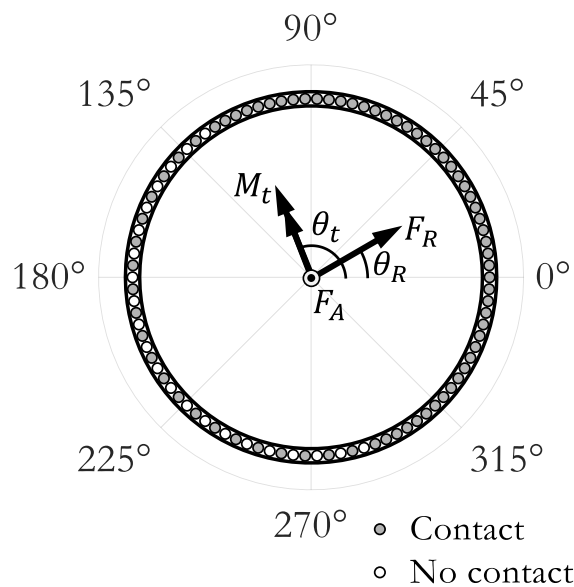
Figure 5.38 Contact status.

Figure 5.39 shows the normal contact force distributions at the end of the simulation. In this plot, the effect of each load in the load distribution is better appreciated. Axial force compresses type A rollers and separates type B rollers, but this load is relatively low. On the other side, the higher radial load compresses all the rollers between $\theta_R + 90°$ and $\theta_R - 90°$, with the maximum peak being at θ_R. At this point, type A rollers in the vicinity of θ_R should be the most loaded rollers. Nevertheless, the applied tilting moment has a significant effect. In this case, tilting moment between θ_t and $\theta_t - 180°$ induces a tension axial force, and a compression axial force between θ_t and $\theta_t + 180°$. This compresses type B rollers and unload type A rollers in the θ_t and $\theta_t - 180°$ section; the opposite behaviour occurs in the section between θ_t and $\theta_t + 180°$. The effect of all the applied loads explains the final load distribution.

Figure 5.40 represents the contact angle for each rolling element. From this plot, information about the sector predominant imposed displacement can be deduced. Radial displacement is predominant on all type B rollers and on type A rollers between 297 and 107 [°], since the contact angle variations are positive. Negative contact variations means that the axial displacement is predominant, which is the case for the other half of type A rollers. Some type B rollers do not appear on this plot because they lose the contact and there is no point in representing a contact angle value.

Figure 5.39 Normal contact force results.
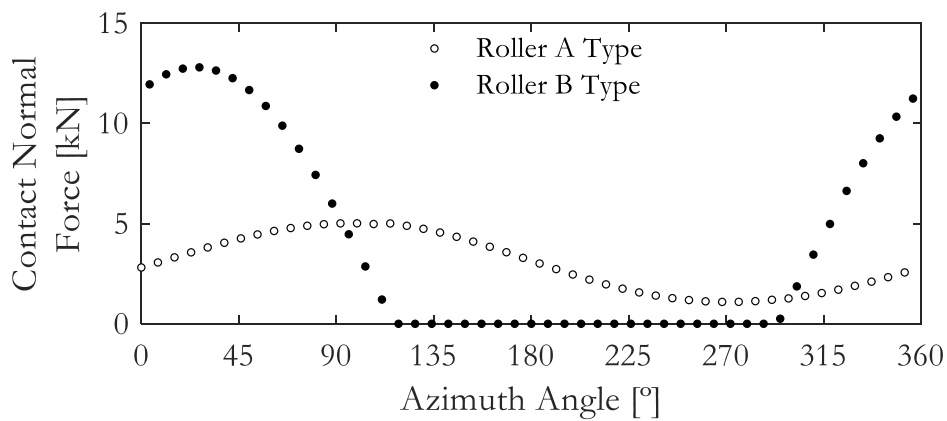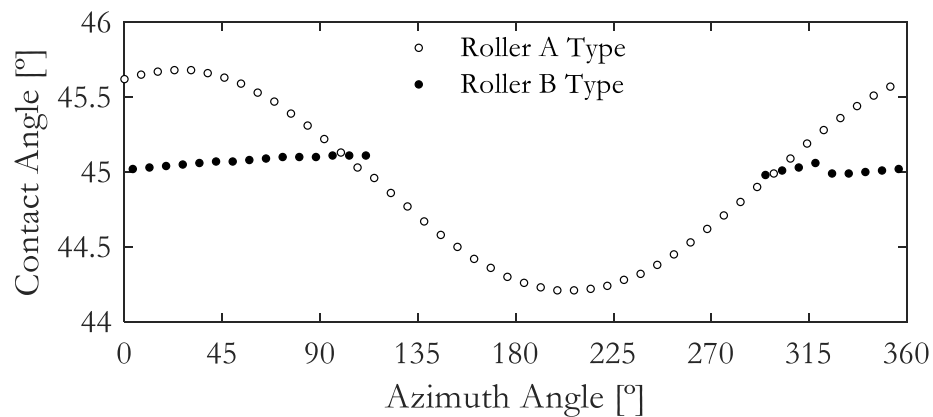
Figure 5.40 Contact angle results.

Finally, the normal contact force on the most loaded roller reached the 59% of the maximum allowable contact force. As a result, a contact pressure of 3080 [MPa] was generated in that contact.

6 Experimental validation of crossed roller wire-race bearing models

6.1 Introduction

According to the previous chapters, it can be stated that the methodology of this Thesis is highly dependent on FE analyses. The physical phenomena that occur during the loading process were observed on FE results and the mechanical behaviour of the bearings was obtained by the same means. This way, the analytical models developed to represent the mechanical behaviour of the bearings under study were conceived after the evaluation of FE analyses results. Besides this, the accuracy of the analytical models was assessed via a results comparison with an equivalent FE model. With all this, it was deemed appropriate to evaluate the validity of the FE models used for the aforementioned purposes. This chapter presents the methodology and results of the experimental test campaign carried out to validate the FE models, and therefore, the analytical formulation, which was developed based on and validated by these FE models.

Some state-of-the-art test benches of different sizes were presented in Section 1.4.7. Usually, the most versatile test benches are large, complex and very expensive. For this reason, they belong to manufacturers [135,136] and powerful research centres [119,139–141,143] and are not generally available for more modest research organizations. However, less ambitious experimental tests can be carried out with simpler test benches [102,160]. In this case, the second option was considered to be most appropriate. Besides this, the objective of validating the FE models can be achieved with this strategy.

In the following sections, the methodology to carry out the setup of the test bench and the experimental test campaign are explained. Finally, the results obtained are presented and compared with the equivalent FE model results.

6.2 Methodology of the experimental test

In this section, the whole process followed to carry out the experimental tests is presented. First, the test bench used to perform the tests is introduced. Then, the selection process of the bearings to be tested is explained together with the design of the specific clamping tools. Finally, the experimental test campaign proposed for the validation of the FE models is presented.

6.2.1 Test bench

As has been mentioned, the adaptation of an available test bench is a good option to validate the FE models used in this Thesis. With that in mind, the Servosis ME 405-30 test bench, located in the E.I.B. of Bilbao, was found to be a good alternative. This machine was designed to perform tension-compression tests on different kinds of specimens, depending on the installed clamping tools. A picture of the test bench with its main components is provided in Figure 6.1. Regarding the test bench features, its mechanical transmission system formed by two spindles can apply a maximum load of 300 [kN]. The distance between the columns allows to test a bearing with an external diameter of up to 600 [mm]. In terms of control, the PCD2K software was developed specifically by the manufacturer for these kinds of benches. This software allows for the tests to be performed by the introduction of loads or displacements, depending on the convenience. The load cell placed in the middle of the machine bridge provides the reaction force in real time and the encoder that measure the deformations have a resolution of 10 [µm].

Considering these characteristics and after some preliminary calculations, this test bench was considered to be appropriate for performing bearing axial compression tests. Nevertheless, this strategy presents a relevant drawback; it is necessary to design and manufacture specific clamping tools for the bearings under study. Besides this, external measurement devices must be arranged for two reasons. Firstly, bearing deformations are very small and the machine measuring system does not have enough resolution. Secondly, the machine measures the deformation of the whole kinematic chain.

It is true that the bearing FE models used in this thesis are also subjected to radial and tilting moment loads. However, performing these kinds of tests would require a specific bearing test bench like the ones mentioned in the introduction. Besides this, the purpose of the experimental tests consist of the validation of the FE models, and that can be made with the evaluation of the axial load case. Of course, an extended validation including additional load cases would be interesting, but not necessary.

1. Controller
2. Motor and transmission
3. Spindles
4. Load cell
5. Clamping tolos
6. Manual control

Figure 6.1 Servosis ME 405-30 test bench.

6.2.2 Test specimens

The design of the bearings under study is an important task, since they must be able to provide relevant results and also meet the characteristics of the test bench. An experimental test campaign is expensive and tedious, so everything must be planned in order to obtain the maximum return. In this sense, two specimens of two different bearing designs were considered to be tested so as to obtain more diverse results. Both bearing designs must be similar, since the clamping tools will be the same for both of them; but they must be also different enough to obtain conclusions. For this reason, both bearings have the same external ring geometry and the only difference between them lies in the geometry of the wire-roller-wire subset and the rings housing. To this end,

several FE analysis were performed until both bearing geometries were different enough but within the design space considered for the development of the analytical model. The geometry of the rings was obtained, as is usual in this thesis, with the standard ring geometry [15]. Of course, the geometry of the rings was determined with the larger housing bearing (bearings 3 and 4 in Table 6.1). Finally, this table also shows the geometrical data of the other bearing geometry to be tested. To provide a more visual representation of the bearing designs, the cross-section of both alternatives are shown in Figure 6.2. It is worth also mentioning the layout of the assembly bolts, which were arranged in such a way that the tightening process was easily performed from the top side.

Table 6.1 Test bearings geometrical data.

D_{pw} [mm]	D_w [mm]	λ [mm]	Rf	α_0 [°]	H [mm]	N_R	C_{0a} [kN]	Label
400	14	8	0.8	45	19	72	652.6	Bearings 1-2
400	16	10	0.4	45	25.56	62	660.3	Bearings 3-4

(a)   (b)
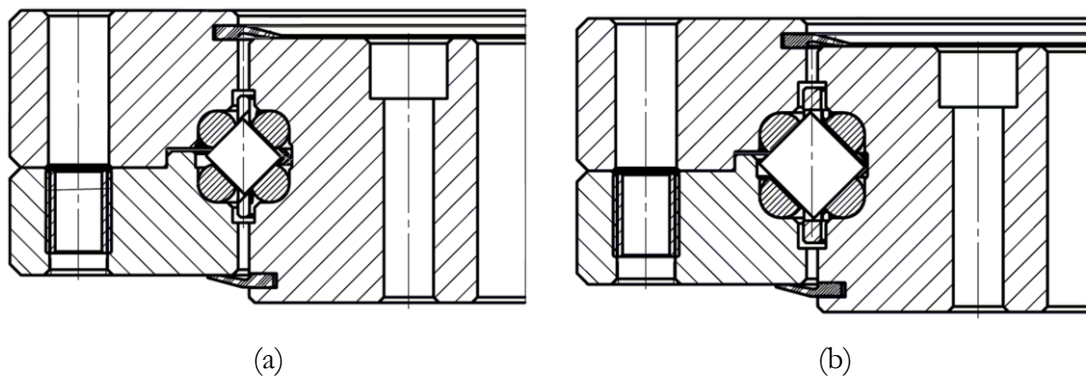
Figure 6.2 Bearing designs cross-section: (a) Bearings 1-2; (b) Bearings 3-4.

6.2.3 Clamping tools and test assembly

As has been mentioned, specific clamping tools had to be designed and built to test the aforementioned bearings. The development of the clamping tools may seem a simple task, but they should be as light and stiff as possible. Light tools simplify the assembly process and the stiffness avoids measurement errors. Besides this, any misalignment between the tools can result in non-desired loads. With all this in mind, some FE analyses were carried out to obtain

the final result of Figure 6.3. The whole test assembly is depicted in this figure. The lower tool is made of one piece, which is connected to the test machine by means of a male-female joint locked with a pin. This connection is relevant since the load is transmitted through the pin. The upper tool is similar but more complex; it was made of two parts and an axial spherical bearing. The installation of an axial spherical bearing aims to reduce problems caused by lack of parallelism and prevent the introduction of undesirable tilting moments. The three parts that compose the clamping tools were manufactured in AISI 1042 steel finished with a bluing treatment. Since weight is a relevant issue, both upper and lower clamping tools weigh 64 and 48 [kg] respectively. All the drawings of the clamping tools can be found in Appendix C. In order to allow the assembly-disassembly process and lift the whole tool, a retention bolt connected both parts. Additional handles and eyebolts were added to simplify the assembly of the tools.
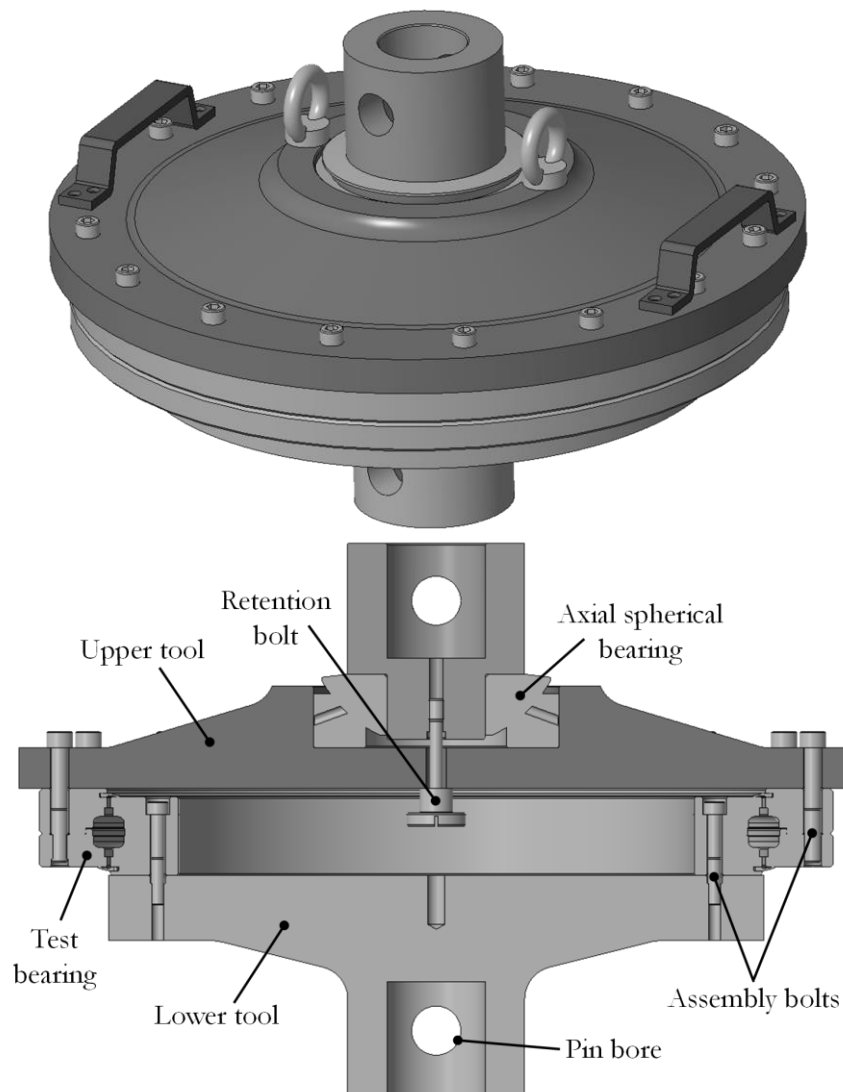
Figure 6.3 Bearing test assembly.

Regarding the necessary additional measuring equipment to record only the deformation of the bearing, four Mitutoyo IP42 543-470B dial indicators were applied every 90 degrees, as shown in Figure 6.3. These dial indicators had a micrometric resolution and a maximum permissible error of ± 3 [μm] (certificates of inspection can be found in Appendix D). Finally, the whole test assembly is shown in Figure 6.4.
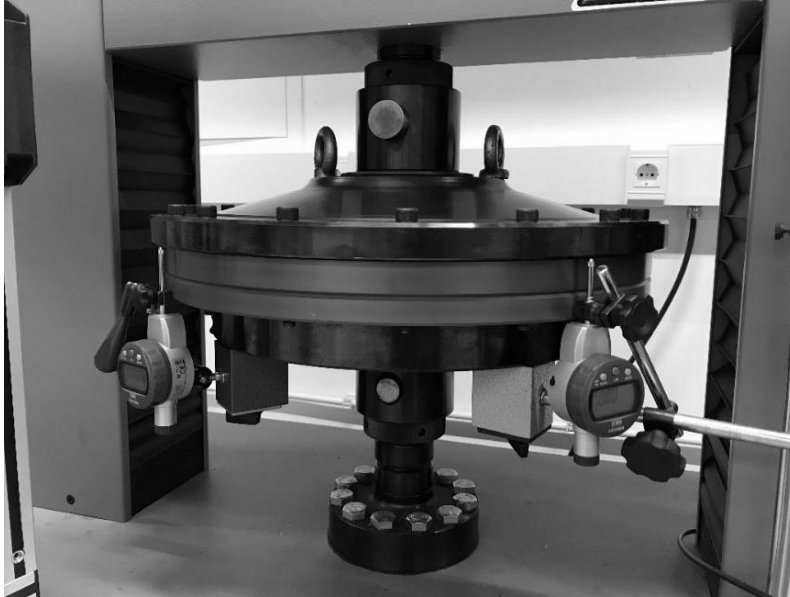
(a)
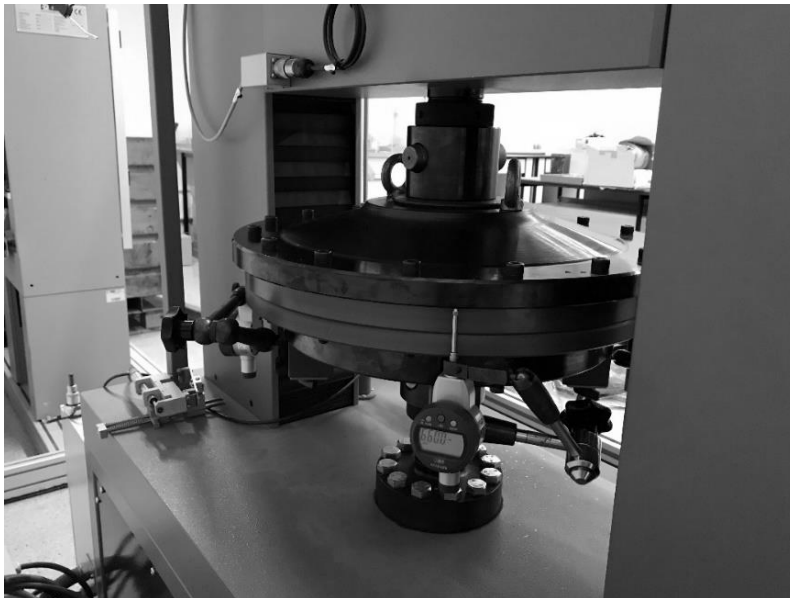
(b)

Figure 6.4 Test assembly: (a) Front view; (b) Rear view.

6.2.4 Experimental test campaign

Once the bearings and the components of the test assembly are ready, it is time to define the tests to be performed. First, it is important to study if the bolt preload affects the FE models and analytical models. For this reason, there were two groups of tests: with no bolt preload and with bolt preload. No bolt preload tests consisted of bolts tightened with a wrench until the eventual tool-bearing gaps were removed. Conversely, the same tests were performed but applying a bolt preload equivalent to 50% of the maximum allowable preload. Bolt preload was applied with a manual torque wrench (Figure 6.5), so the value of the torque to be applied had to be calculated. To do this, Equation (6.1) was used, where $T_{max.}$ is the maximum allowable torque, K is the friction coefficient, σ_{yp} is the yield stress, $A_{eq.}$ is the equivalent stress area and d_n is the nominal bolt diameter.

$$T_{max.} = K \cdot (\sigma_{yp} \cdot A_{eq.}) \cdot d_n \tag{6.1}$$

The friction coefficient of the bolt (K_f) can be calculated with Equation (6.2); where μ and μ' are the friction coefficients between threads and between the bolt head and the surface, λ_b is the helix angle and α_b is the thread angle.

$$K_f = 0.5 \cdot \frac{\mu + tg(\lambda_b) \cdot cos(\alpha_b)}{cos(\alpha) - \mu \cdot tg(\lambda_b)} + 0.625 \cdot \mu' \tag{6.2}$$

Bolts data are gathered in Table 6.2, where the M8 bolts correspond to the inner ring and the M10 bolts to the outer ring. The friction coefficient was low since the bolts were lubricated with WD-40 oil before each assembly. T_b is the bolt preload to be applied for each bolt type.

Table 6.2 Bolt data.

	Grade	d_n	$A_{eq.}$	σ_{yp}	μ	μ'	K_f	T_b
		[mm]	[mm²]	[MPa]				[N·m]
M8	8.8	8	36.6	640	0.1	0.1	0.145	27.28
M10	8.8	10	58	640	0.1	0.1	0.144	53.66

Inner ring bolts were tightened as shown in Figure 6.5, but the outer ring bolts were tightened while the bearing was supporting a load of 10 [kN]. This

procedure was established to allow the upper clamping tool to accommodate the spherical bearing and recover the centred position before bolt tightening.
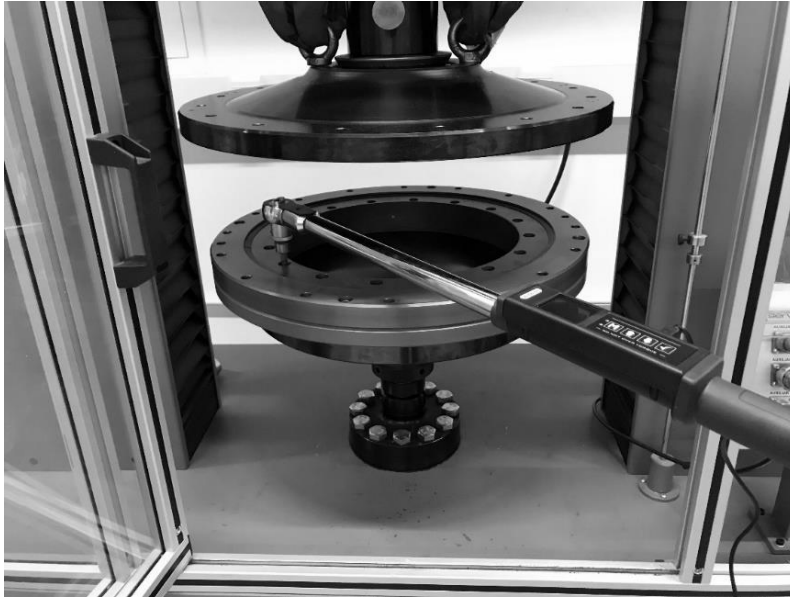

Figure 6.5 Bolt tightening with the torque wrench.

Regarding the sources of uncertainty related with the assembly process, it is important to control irregular or low bolt preload (non-preloaded bolts case) in conjunction with bearing misalignment. In order to control these phenomena, each bearing is removed and reassembled in a different position before each test. To evaluate this, it was considered enough to perform three tests for each bearing and tightening methodology; this makes a total of six assemblies per bearing.

Repeatability for each assembly is another phenomenon that has been taken into consideration. For this purpose, each loading process is repeated four times for each assembly. The first loading process aims to accommodate the bearing for the test and the other three to assess the repeatability of the results. The first loading process retrieved non-realistic results in all cases, so it was discarded. This way, possible measuring or loading errors can be easily discriminated. Each loading process consists of introducing a compressive load in steps, reading the deformations on the dial indicators. The maximum load was established at 200 [kN], since it was not desirable to reach the maximum load of the test bench. Besides this, these tests were conceived to be non-destructive, and greater loads may generate excessive permanent deformations on the races. However, it is a relevant load value considering that the axial static load capacity of both bearing designs is around 650 [kN] (calculated with the methodology proposed in Chapter 5). Besides this, according to manufacturers,

these kind of bearings do not usually exceed 20% of the static load capacity during operation.

At this point, a brief summary together with Figure 6.6 may help to understand the experimental test campaign. There are two bearing designs and two specimens per design. The same tests must be performed with and without bolt preloading. Three tests were planned for each bearing and preload case, where the bearing is reassembled on the test rig for each test. Each test consists of four loading processes. In summary, each bearing is assembled 6 times and subjected to 24 loading processes, making a total of 24 assemblies and 92 loading processes.
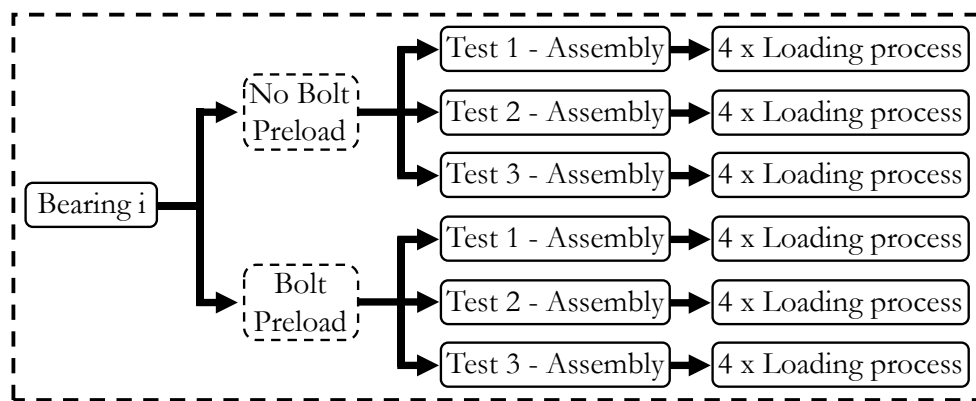

Figure 6.6 Experimental test campaign for one bearing specimen.

6.3 Results and FE models validation

The results of the experimental test campaign are presented in this section. It was considered appropriate to gather only the most relevant results in such a way that everything is clear and understandable. However, all the results obtained from the experimental test campaign are included in Appendix B.

6.3.1 Effect of the bearing assembly

First of all, it is worth mentioning the effect that the assembly has on the bearing load distribution. For example, Figure 6.7 shows the measurements of the dial indicators for Bearing 2 at the 4th loading process of tests 1 and 2 for the bolt preload case. On the one hand, it can be seen how the deformations of the first plot are even and only a compressive force is acting. On the other hand, the deformations on the second plot indicate that a tilting moment load was introduced in combination with the axial load. This behaviour is most probably caused by misalignment between the bearing and the clamping tools.

(a)

(b)
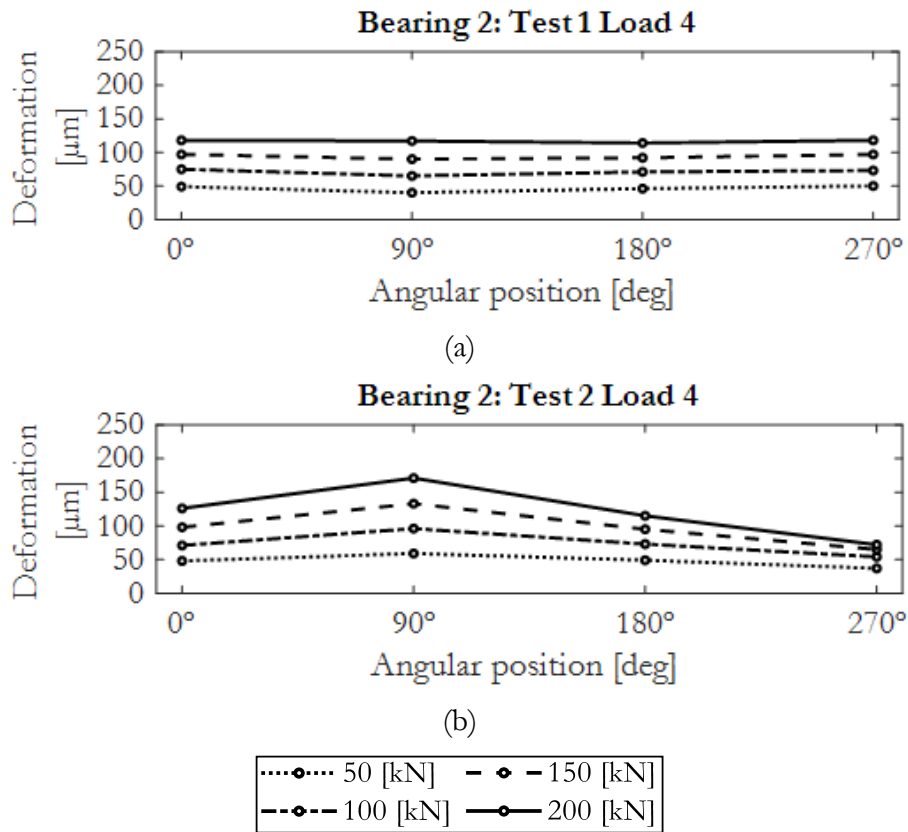
Figure 6.7 Bearing deformation according to the dial indicators measurements: (a) Bolt preload-Bearing 2-Test 1-4th loading process; (b) Bolt preload-Bearing 2-Test 2-4th loading process.

There can be two types of misalignment that generate an undesirable radial or tilting moment loads. One source of misalignment is related with the bearing and the lower clamping tool. The lower clamping tool is threaded, so the bolts have to go through the inner ring bolt holes. Of course, the bearing bolt hole diameter is greater than the bolt external diameter to allow for assembly. As a result, this gap allows a ±1 [mm] radial displacement when all the bolts are in place but not tightened, as can be seen in Figure 6.8.
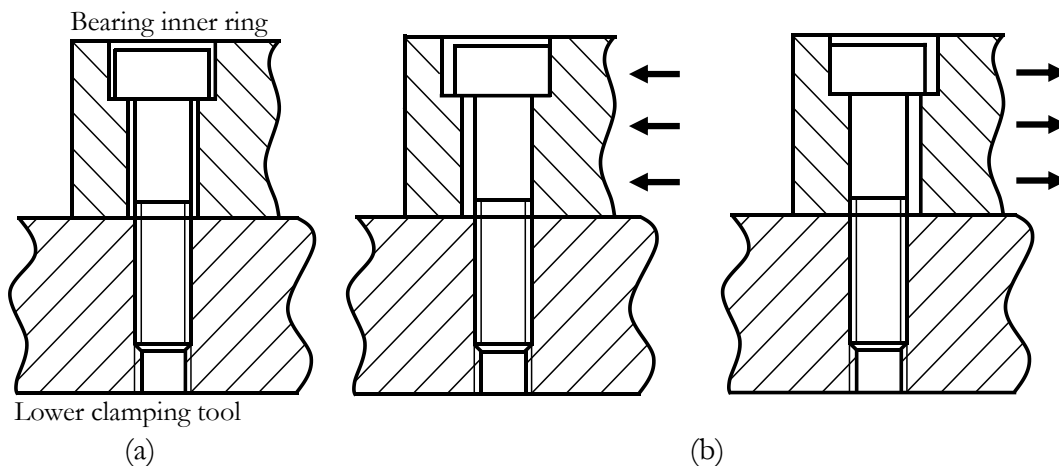
Figure 6.8 Bearing arrangement: (a) No misalignment; (b) Misalignment.

The same phenomenon occurs with the outer bearing ring and the upper clamping tool. In this case, the thread is in the bearing outer ring and the upper clamping tool is the part that can become misaligned in the way shown in Figure 6.9. These two sources of misalignment make it very difficult to obtain the perfect bearing assembly. Besides this, the misalignment of the axial spherical bearing induces an undesired radial load and the eccentricity of the axial load also generates a tilting moment.
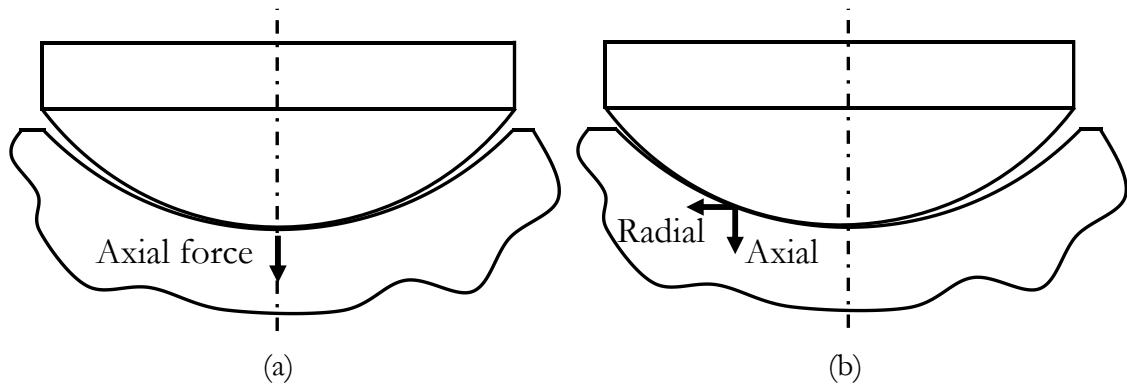
Figure 6.9 Upper clamping tool arrangement: (a) No misalignment; (b) Misalignment.

Despite the fact that the tilting moment generated by misalignment influences the bearing deformation, Figure 6.10 shows that the stiffness curves calculated with the average deformation are almost the same for the previous example cases. Accordingly, it can be said that the tilting moment arising as a result of misalignment does not have a significant effect on the axial stiffness results.
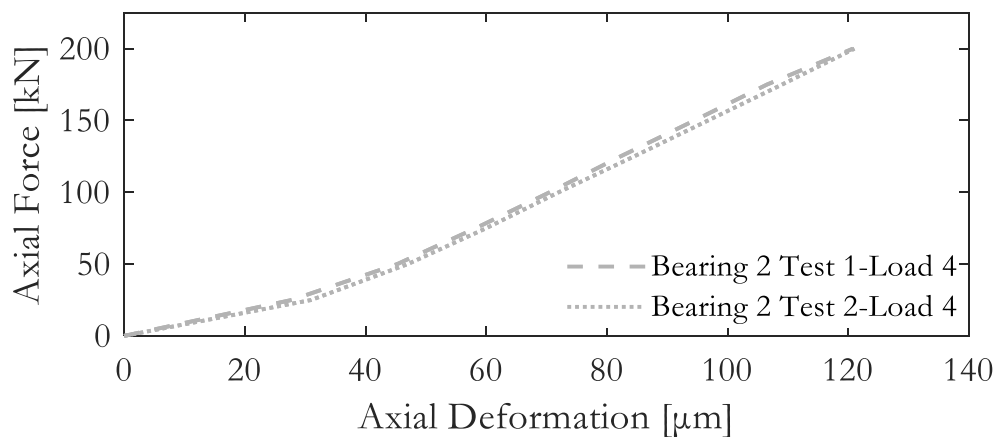
Figure 6.10 Axial stiffness curves obtained with the average deformations.

6.3.2 Repeatability of the tests

As has been indicated, each test consisted of four loading processes. Figure 6.11 and Figure 6.12 show the results of the complete bearing 2 test 1 and test 2.
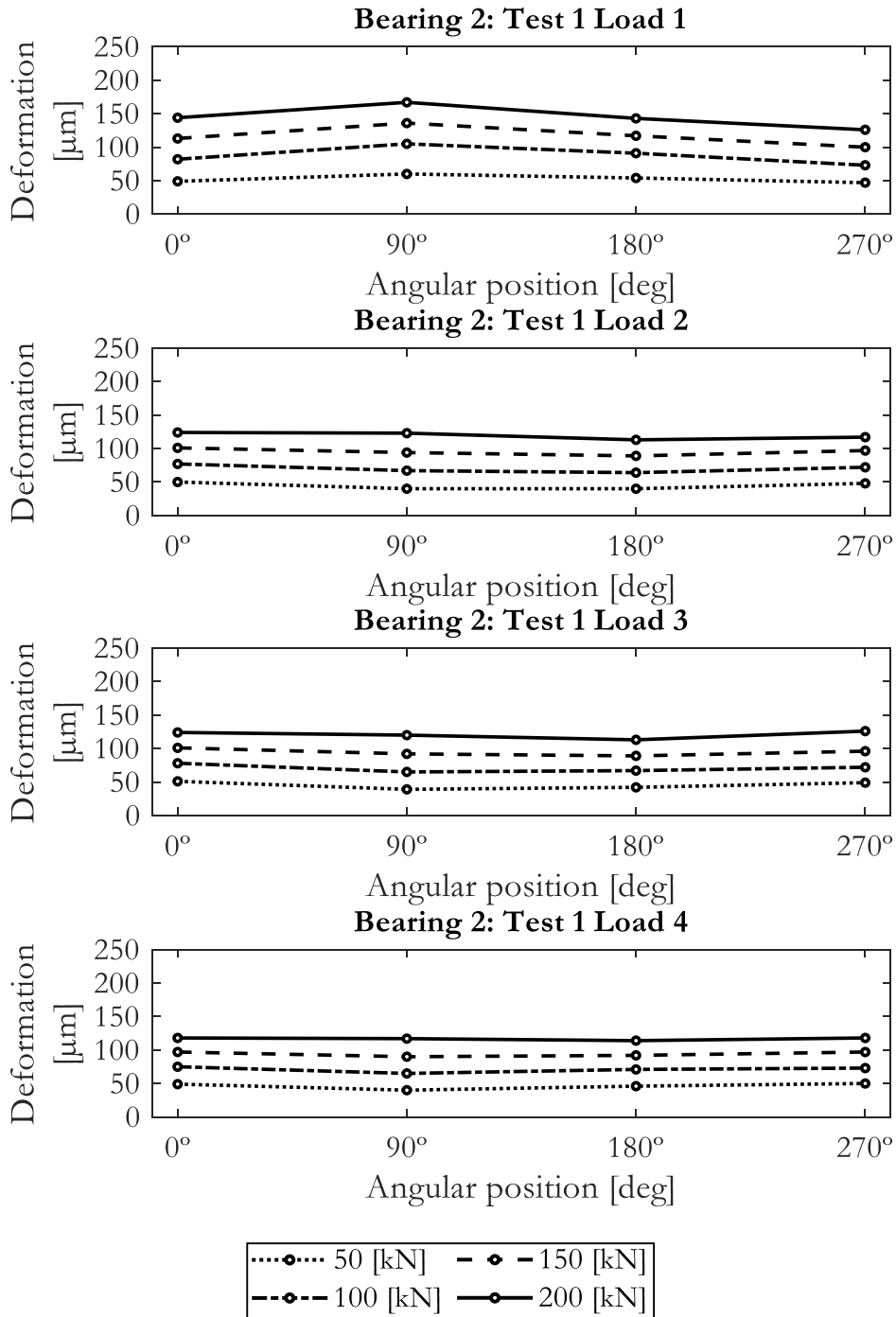
**Figure 6.11** Bearing deformation according to the dial indicators measurements: Bolt preload-Bearing 2-Test 1.
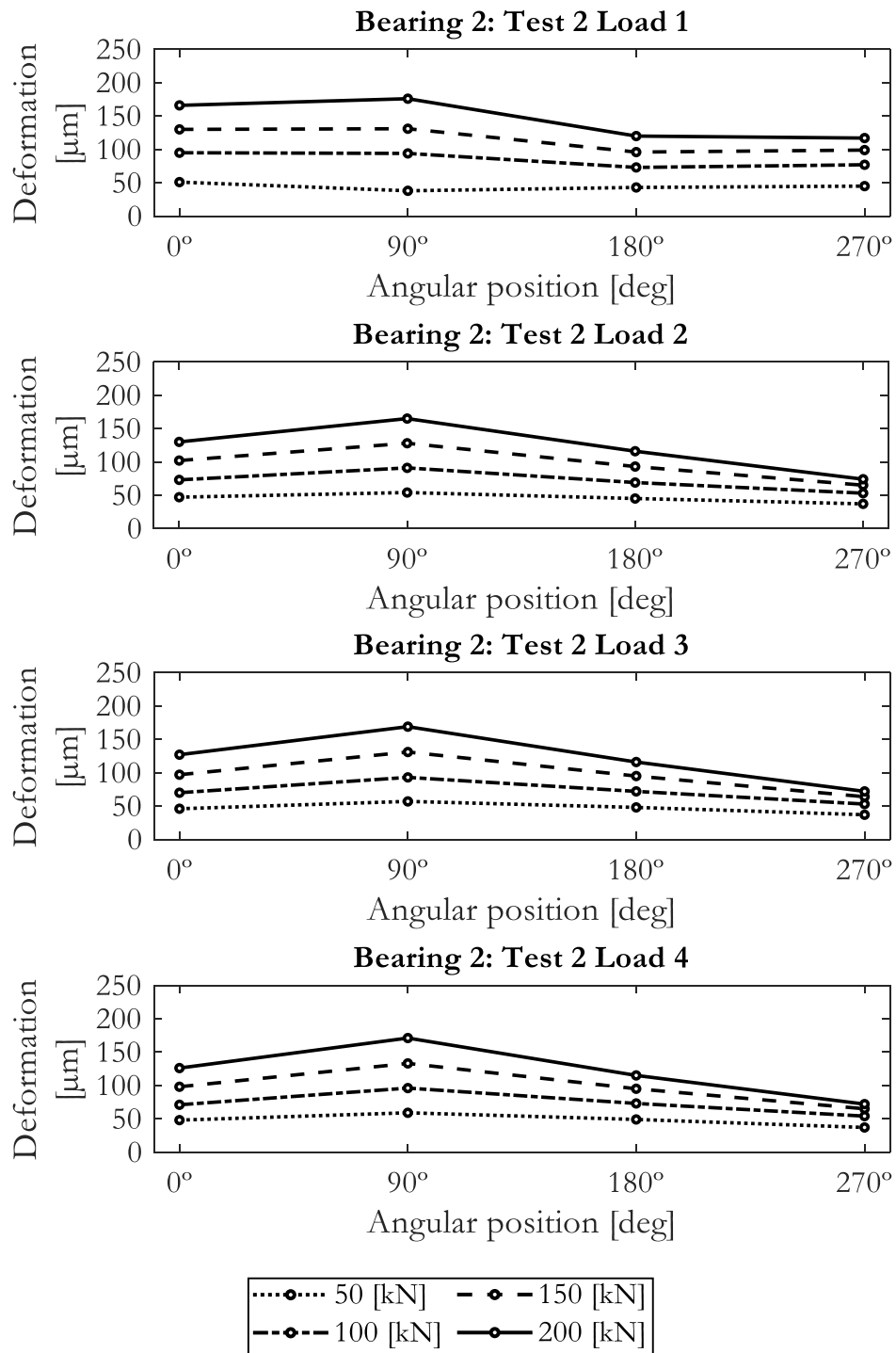
Figure 6.12 Bearing deformation according to the dial indicators measurements: Bolt preload-Bearing 2-Test 2.

It can be seen that in both cases the first loading process differs from the following three. This behaviour was caused by the settling of the axial spherical bearing. The other three loading processes showed excellent repeatability.

6.3.3 Experimental test results

The purpose of this section is to analyse the results of the experimental tests and obtain conclusions of the structural behaviour of the bearings. Because of the type of test that was carried out, only stiffness results can be compared. However, relevant conclusions can be drawn. As has been indicated, there are two specimens per bearing design and they were tested multiple times to check the influence of the assembly process and the repeatability. Figure 6.13 and Figure 6.14 shows all the obtained experimental stiffness curves with the exception of the first loading process of each test, because of the axial spherical bearing settlement. Each stiffness curve was obtained with the average measurements of the dial indicators for every load level.

Figure 6.13 Bearings 1 and 2 experimental results.

Bearings 3 and 4 Axial Stiffness Results (No Bolt Preload)
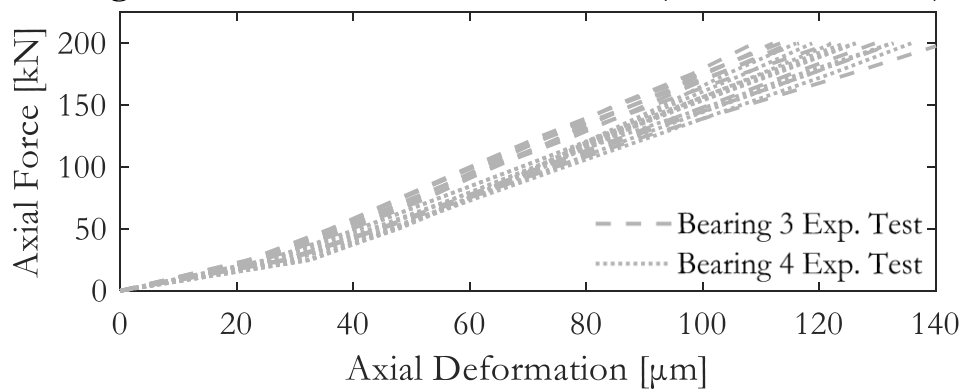
Bearings 3 and 4 Axial Stiffness Results (Bolt Preload)
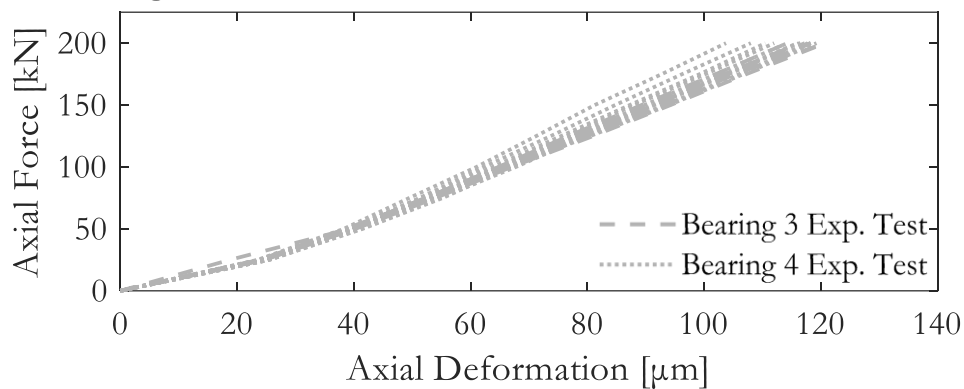
Figure 6.14 Bearings 3 and 4 experimental results.

Regarding the repeatability of the experimental results, a slight dispersion among the stiffness curves is observed. This is something to be expected and unavoidable, since there are several factors of uncertainty, including the human factor. However, the repeatability is much better in the tests where the bolt preload is controlled.

The non-linear behaviour shown in all the curves was not expected, since the FE results always show a linear behaviour all along this load range. An extensive investigation of this behaviour was not carried out, but it can be related to the manufacturing errors. Due to these errors, some rollers could be more loaded than others at the beginning of the loading process. It is not until a higher load level is reached that all the rollers make contact and the linear behaviour starts.

Also of relevance is the stiffness difference between bearings 1 and 2. Extensive research on the cause of this difference was not carried out. However, there could be some circumstances that might promote this behaviour. Deficient lubrication may impede correct wire-twisting, which results in increased stiffness and higher contact pressure on one wire race edge (Figure 6.15a). Manufacturing errors can also influence structural behaviour, as

shown in Figure 6.15b. The wire housing radius (R_{wh}), which is the radius difference between the wire and the ring accommodation is usually fixed to 100 [μm] to allow some lubrication. On the one hand, the wire-ring contacts behaviour is stiffer if this gap is small or does not even exist. On the other hand, the behaviour is more flexible if the gap is bigger.

Pressure peak

Correct lubrication
Correct wire twist

Incorrect lubrication
Deficient wire twist

(a)

Stiffer wire-ring contact
(Deficient machining)

More flexible wire-ring contact
(Excessive machining)

(b)
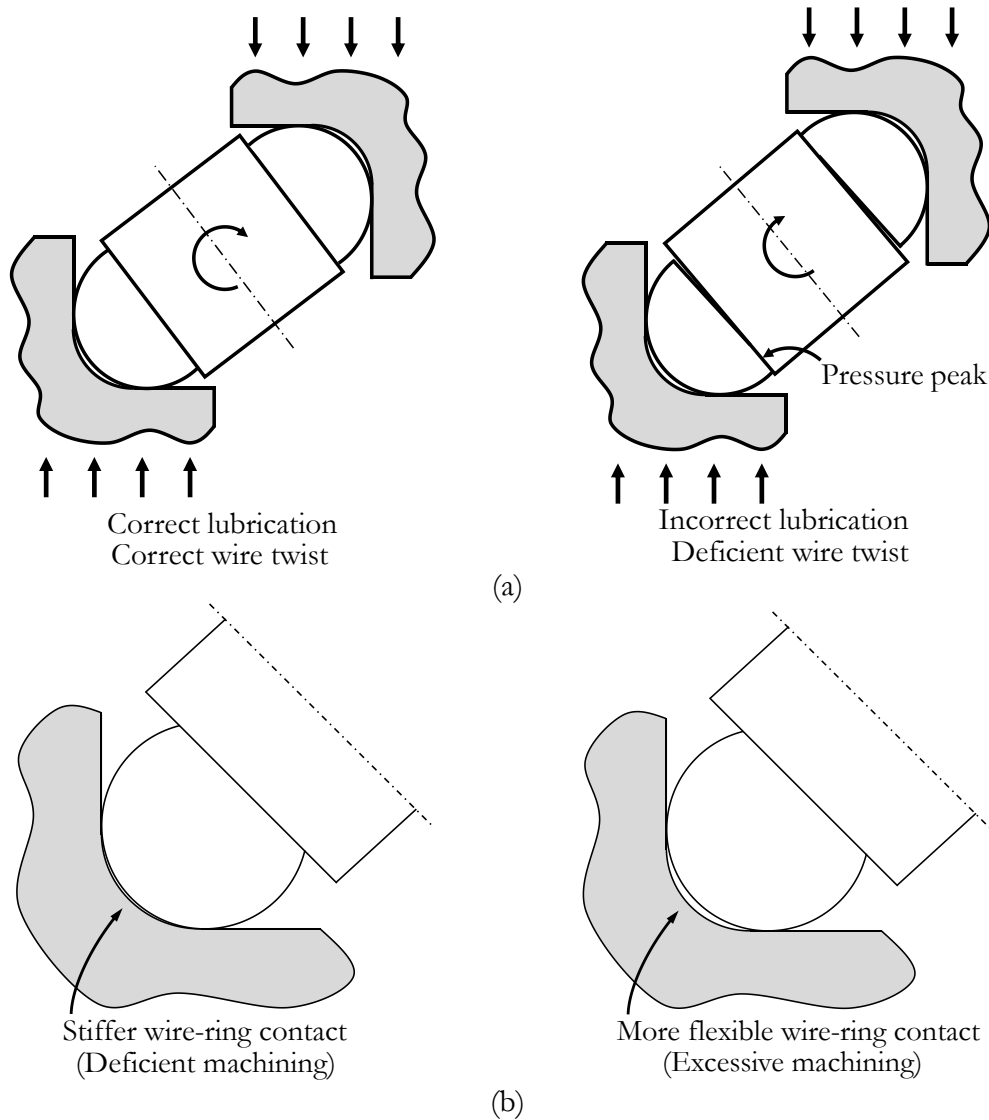
Figure 6.15 Effect on the bearing stiffness: (a) Correct wire-ring lubrication; (b) Correct ring machining.

Another potential effect of the bolt preload is related with the stiffness results. This has been left for the end of the section since it is significant enough to add new stiffness plots; Figure 6.16 shows the average stiffness curves comparison for each bearing with and without bolt preload. After reviewing the results, it can be said that an adequate bolt preload has a relevant effect on the stiffness behaviour in comparison with low and non-controlled bolt preload. Therefore, the lack of bolt preload not only leads to more scattered results but also to a more flexible structural behaviour.
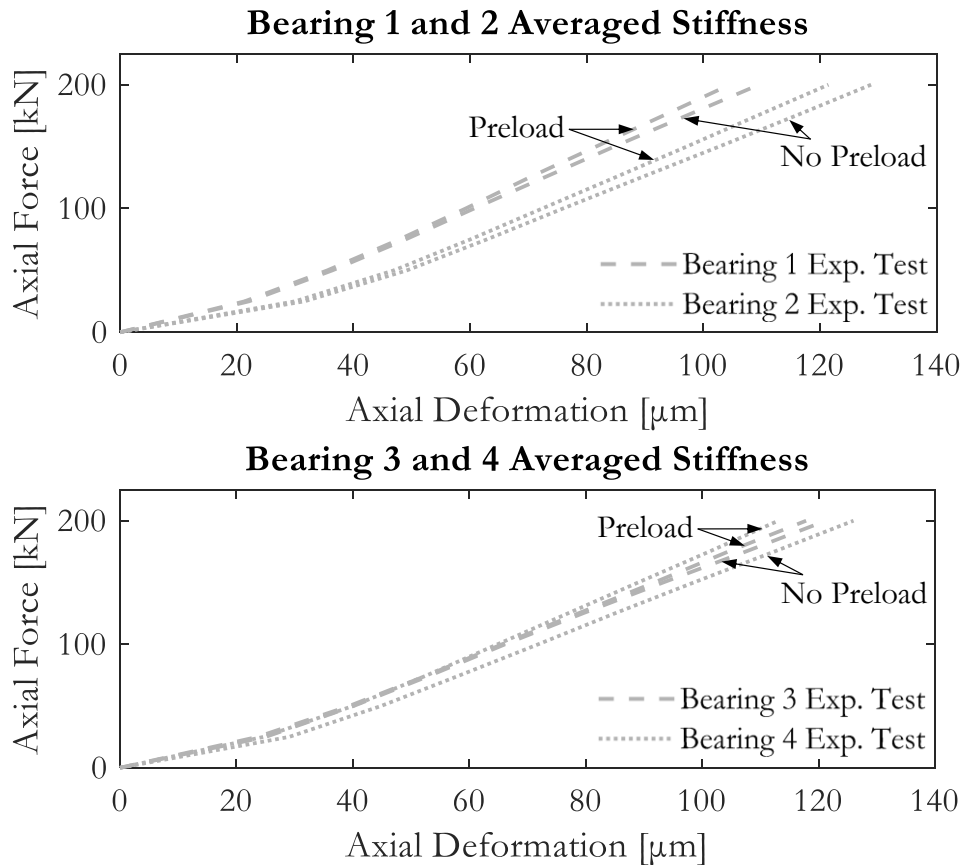
Figure 6.16 Averaged stiffness results for preloaded and non-preloaded tests.

6.3.4 FE models validation

Finally, the validation of the FE models developed in this thesis consists of an axial stiffness results comparison. No specific FE models were developed ad-hoc for the validation. Instead of this, the multiparametric FE model introduced in the previous section (Figure 5.18b) was used. That model takes advantage of the cyclic symmetry of the bearing geometry and a mesh sensibility analysis was performed to assess the best accuracy-computational cost ratio. Bolts were not modelled, since it is assumed that the bolted joint has been designed correctly.

Regarding the comparison, there are different alternatives by which to carry it out. There are two specimens per bearing design and they were tested multiple times to check the influence of the assembly and the repeatability. One alternative consisted in compiling all the results to obtain the equivalent stiffness behaviour. However, experimental results showed some dispersion and it was considered to be more illustrative to show the FE stiffness result over the area formed by all the experimental results obtained with each bearing.

Figure 6.17 and Figure 6.18 show the stiffness comparison between the experimental tests and the FE results without and with bolt preload. The area that represents experimental test results considered all the obtained experimental results with the exception of the first loading process of each test, because of the axial spherical bearing settling.

Regarding the results comparison, the FE results are inside the area created by all the experimental results. Accordingly, it can be said that the FE models used in this thesis are experimentally validated and they can be used to study the mechanical behaviour of the crossed roller wire-race bearings. Additionally, they can also be used to evaluate the accuracy of the analytical models developed in this Thesis. Based on all of this, it is also fair to say that better results could have been obtained with a preliminary study of the friction coefficients of the roller-wire and wire-ring contacts, an exhaustive measurement of the microgeometry and a more sophisticated system to avoid misalignment. As has been mentioned above, manufacturing errors could be the root cause of the non-linear behaviour reported by the tests. Considering these manufacturing errors in the modelling could lead to better correlation with the test and a promising future research line.

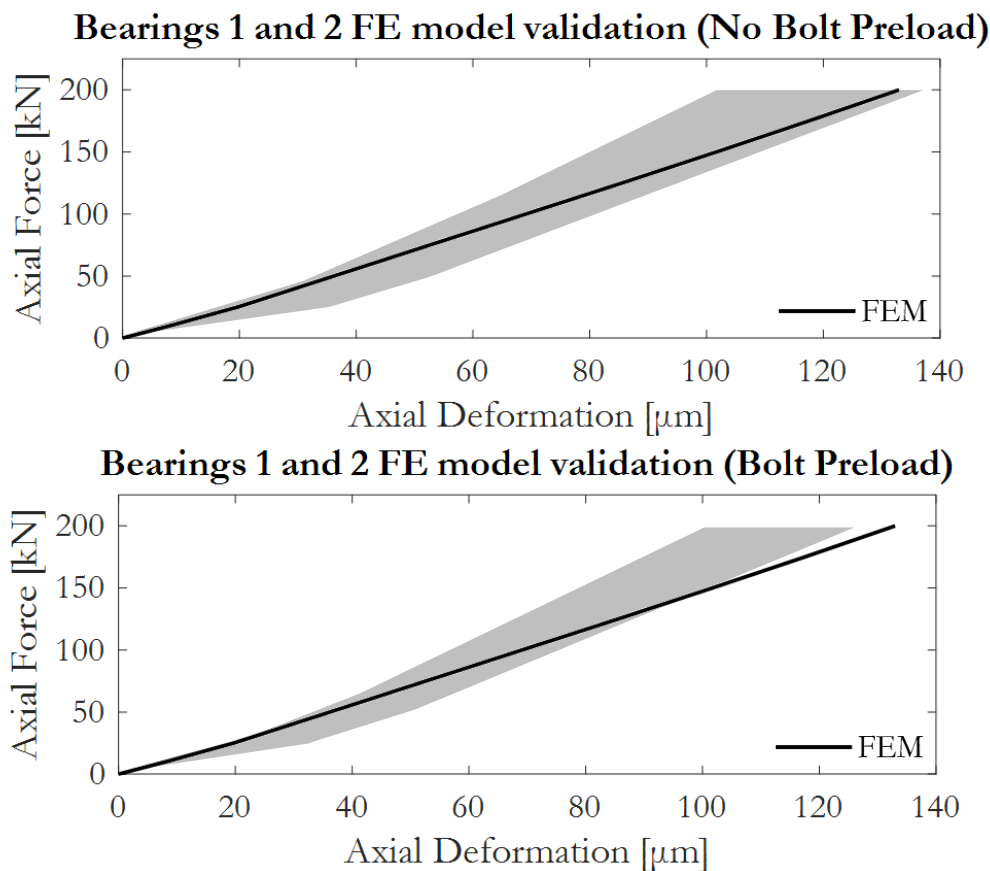**Figure 6.17** Bearings 1 and 2 FE model experimental validation.

Bearings 3 and 4 FE model validation (No Bolt Preload)

Bearings 3 and 4 FE model validation (Bolt Preload)
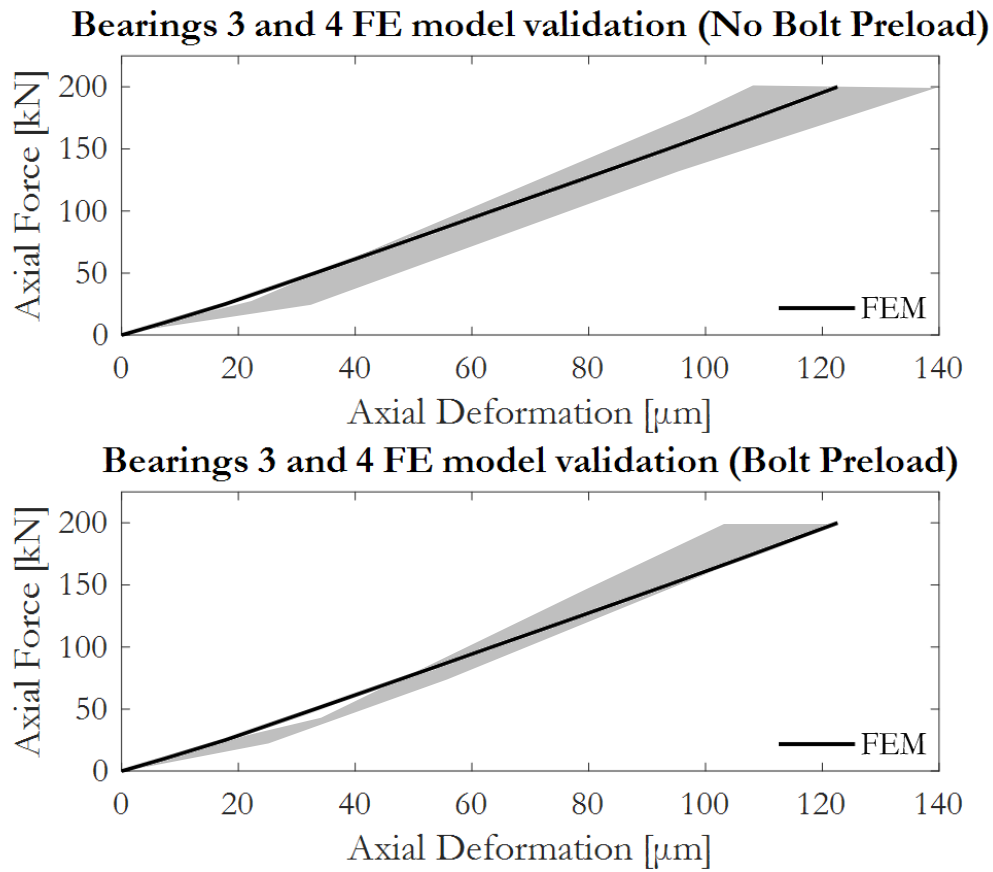
Figure 6.18 Bearings 3 and 4 FE model experimental validation.

7 Efficient strategies for the Finite Element modelling of wire-race bearings

7.1 Introduction

The Finite Element Method is a simulation tool that has contributed to the improvement of the machine element design and research over the years. There is a wide spectrum of applications where the FE assists the researchers and designers, but FE models can be complex and computationally heavy. For this reason, there is a constant pursuit of efficient FE modelling strategies that help to reduce the computational cost and convergence problems. A literature review of the current slewing bearing FE modelling strategies was made in Section 1.4.6. However, no efficient FE modelling strategies have ever been proposed for wire-race bearings. It is true that the research force in the case of slewing bearings is higher, but wire-race bearings FE models present more complexity and size to face. Based on this, it was considered relevant to develop efficient FE strategies to fill that gap.

This section is divided into two parts, one for each wire-race bearing type studied in this thesis: four-point contact ball and crossed roller wire-race slewing bearings. In each part, explanations about the proposed efficient FE strategies are provided and one application example is carried out to illustrate the application process. However, this is not enough, since the validity of the proposed FE models must be assessed. To this end, the results of the proposed efficient FE models are compared with the results of reference FE models.

7.2 Ball wire-race bearings

The structural behaviour of four-point contact ball wire-race slewing bearings was studied in previous sections. The wire twisting phenomenon, the limited wire-raceway area and the different materials implied difficulties in establishing an analytical calculation method. The same problems arise when it comes to making simplifications in a FE model. For these reasons, it seems reasonable, as a first approach, to implement a FE simplification that currently works for conventional slewing bearings. With this in mind, the FE simplification proposed by Daidié et al. [126] was found to be a good alternative. The content of this work is properly explained in Section 1.4.6, so there is no reason for providing any additional explanations. If it is proven that this FE simplification is suitable for wire-race slewing bearings, a more complex FE simplification that includes the wires can be proposed as future work.

Daidié et al. developed a simplified mechanism for conventional slewing bearings, where the osculation ratio is usually high. However, in the case of wire-race slewing bearings the osculation ratio can be either low or high. This may not appear to be problem at first glance, but the formulae used for the definition of the mechanism depends on the value of the osculation ratio. This does not imply any significant problems, but additional formulae must be considered from the work developed by Houpert [47] for low osculation ratio values. These ranges were defined as $0.886 < s < 0.992$ for low osculation ratio values and $0.886 < s < 0.992$ for high osculation ratio values. Houpert defined the formulae in a general form, where two constants ($Cte1, Cte2$) must be set depending on the osculation ratio range. However, these formulae cannot be applied directly and two equations must be derived from this work to create the simplified FE mechanism. All the derived equations and all the different values of $Cte1$ and $Cte2$ are gathered in Appendix A.

The first one (Equation (7.1)) represents the contact interference δ, where s is the osculation ratio, Q is the contact force and D_w is the ball diameter.

$$\delta = Cte1 \cdot (1 - s)^{-Cte2} \cdot \frac{Q^{2/3}}{D_w^{1/3}} \tag{7.1}$$

This equation is the first step for the definition of the traction-only non-linear spring stiffness behaviour, but it cannot be directly implemented. This equation must be rearranged in the form of Equation (7.2), where K_c is the stiffness of

the contact. However, Equation (7.3) retrieves the stiffness of one contact, and the non-linear spring used in the simplified FE mechanism represents the stiffness of both ball-raceway contacts. Finally, the stiffness of the spring (k_B) can be obtained with Equation (7.4).

$$Q = k_B \cdot \delta^{3/2} \tag{7.2}$$

$$k_B = Cte1 \cdot (1-s)^{3/2 \cdot Cte2} \cdot D_w^{1/2} \tag{7.3}$$

$$K_s = 0.5^{3/2} \cdot k_B \tag{7.4}$$

The second equation represents the major and minor contact ellipse semi-axes (a, b). These parameters are necessary to define the rigid shell surface that transmits the contact force to the ring. Both semi-axes can be obtained with the same expression, which is represented in Equation (7.5). One more time, the selection of the constants defines the semi-axis to calculate and the osculation ratio range.

$$a = b = Cte1 \cdot (1-s)^{-Cte2} \cdot D_w^{1/3} \cdot Q^{1/3} \tag{7.5}$$

Once the formulation to define the mechanism has been introduced, the method by which to implement the simplified mechanism in the FE model can be explained. To this end, the implementation does not differ particularly much from the one proposed by Daidié et al. [126]. The only difference lies in the fact that the raceway is located on the wires and not on the rings. For this reason, the rigid surface that transmits the ball-raceway contact force must be placed on the wire.

Figure 7.1a shows a drawing of one diagonal of the FE simplified mechanism. Black lines represent the rigid beams, which are linked by the traction only non-linear spring element. Two wire-raceway surfaces are coloured in light grey and the rigid surfaces in dark grey. In the case under study, the bearing is a four-point contact wire-race bearing, which means that the ball has four contact points. For this reason, the complete mechanism of Figure 7.1b is composed of two diagonals.

(a)   (b)
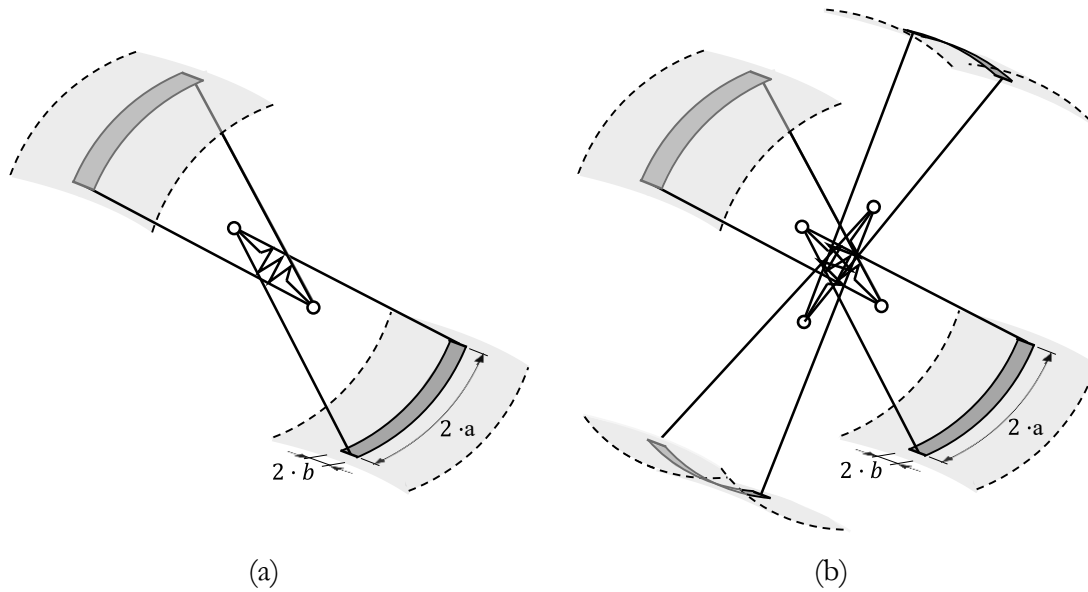
Figure 7.1 Ball wire-race bearing simplified FE mechanism: (a) 1 Diagonal; (b) 2 Diagonals

With the simplified FE mechanism described, the next step consists in implementing it on a FE model. In addition, it is also necessary to validate the accuracy of the simplification. To this end, two multiparametric FE models were created, one with the FE simplification implemented and another one to serve as a reference model. A results comparison of both FE models should illustrate whether the simplification is valid or not as an efficient FE modelling strategy. As has been mentioned, the formulae for the FE simplification depends on the osculation ratio, so both high and low osculation ratio alternatives must be validated. This makes it necessary to perform two analyses with each bearing FE model, with the geometrical data shown in Figure 7.2 and its numerical values figuring in Table 7.1.

Figure 7.2 Four-point contact wire-race bearing cross-section.

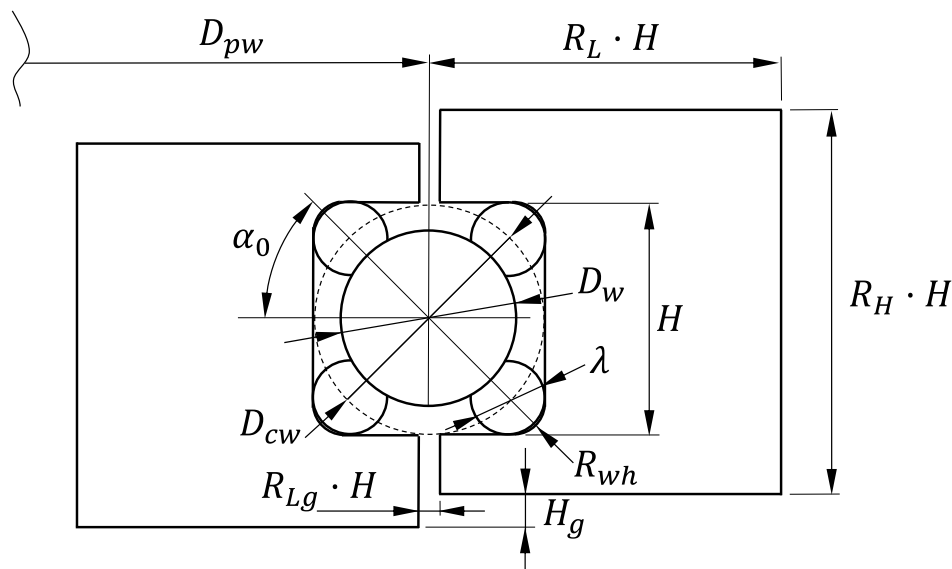Once again, the geometry of the rings depends on the size of the housing (H) and is defined according to the coefficients proposed by Heras et al. [15]. In order to complete Table 7.1, the axial static load capacity calculated with the methodology proposed in [13] is also included.

Table 7.1 Geometrical values and static load capacity.

D_w	D_{pw}	Rf	α_0	λ	s	C_{0a}
[mm]	[mm]		[°]	[mm]		[kN]
16	420	0.5	45	7	0.87	674.2
16	420	0.5	45	7	0.943	1213.1

N_b	R_{wh}	R_L	R_H	R_{Lg}	H_g
					[mm]
82	3.9	1.9	2.15	0.1	3
82	3.9	1.9	2.15	0.1	3

Axial load case was considered to be the best option for the validation of the FE strategy because of its simplicity. The FE simplification proposed by Daidié has been proven to work correctly for any kind of loads in conventional slewing bearings. Therefore, it can be assumed that once this strategy is validated for wire-race slewing bearings under the axial load case, it will also be valid for other load cases. As has been explained in previous chapters, the geometry and the load case are cyclic symmetric, so only half a sector can be modelled. Figure 7.3 shows the reference and the efficient FE model, where the mesh of the shared volumes is identical. Wire-ring contacts and the ball-wire contact in the reference FE model were defined as frictional with Augmented Lagrange formulation, a friction coefficient of $\mu = 0.1$, a maximum penetration tolerance of 1 [μm] and updating the contact stiffness in each iteration. The bonded contact defined to connect the contact ring partition with the rest of the ring was defined with a maximum penetration tolerance of 3 [μm].

Regarding the boundary conditions, symmetry boundary conditions were applied on all the symmetry faces of both FE models. Axial load is applied by means of imposed displacements on the surfaces that are in contact with the

surrounding structures, while the displacements in the other directions are constrained. Axial displacement is exerted until the static load capacity is reached.

The reference FE model does not require additional explanations; however, some comments must be made regarding the efficient FE model. COMBIN39 element (in Ansys®) was used to represent the traction-only non-linear spring element, where the stiffness curve defined by Equation (7.4) was introduced as an element real constant. The rigid beams of the mechanism were modelled with MPC184 elements. These elements were also used to model the rigid surface that transmit the load to the raceway. A net of rigid beams was built on the raceway surface instead of using a rigid shell.
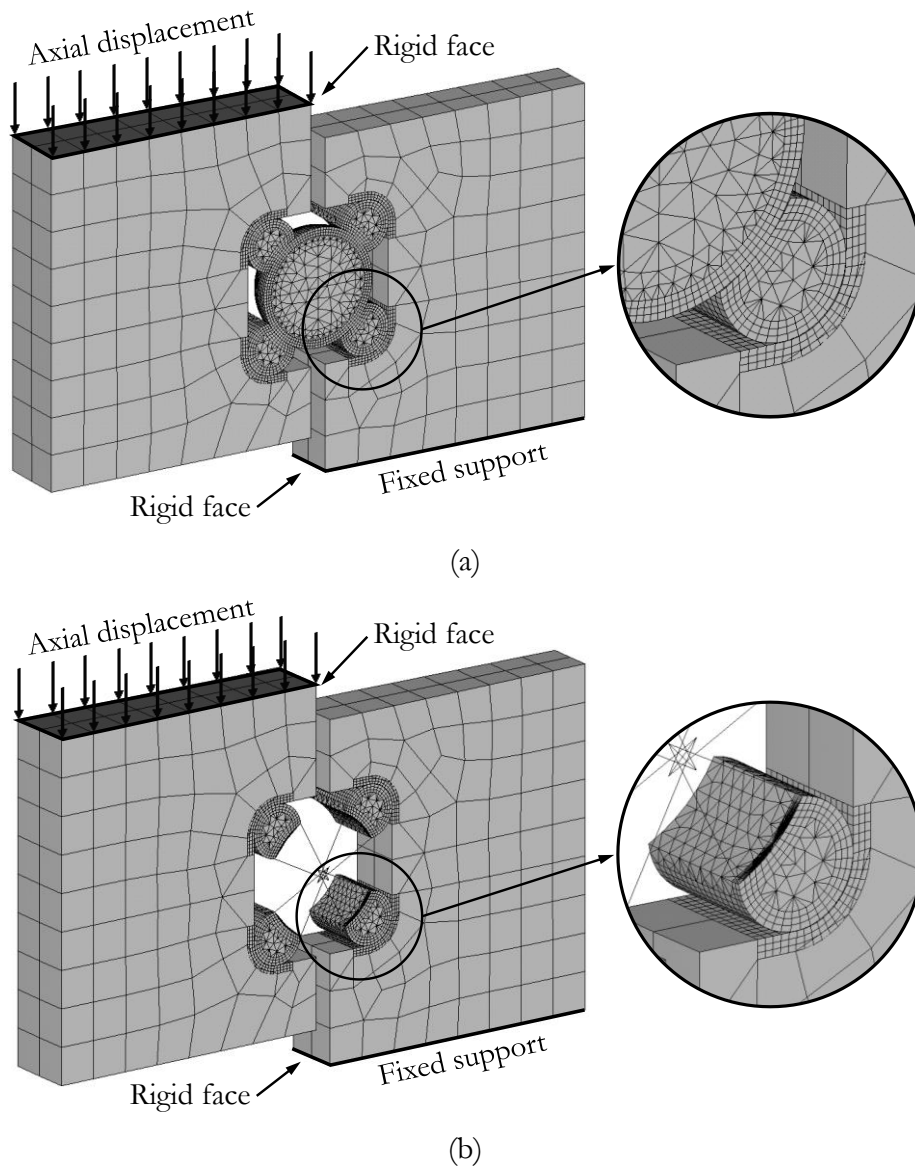

(a)

(b)

Figure 7.3 Axial FE models: (a) Reference model (400,000 DoF); (b) Efficient model (235,000 DoF).

Finally, the size of both FE models must be compared, since the purpose of the study consists in obtaining an efficient FE modelling strategy. The reference FE model has around 400,000 DoF, while the efficient FE model with the same mesh has around 235,000 DoF. This means that 40% of DoF savings are achieved. Slightly better efficiency could have been obtained if the wire raceway had been meshed with coarser elements. This was not carried out in order to perform the comparison with the same mesh for both models. In addition to the DoF reduction, the suppression of the ball-wire contacts non-linearity improves the convergence of the model and prevents severe convergence problems caused by the loss of contact.

Based on the above, the results of the validation can now be presented. Once again, the stiffness, the contact force and the contact angle are the performance indicators used to compare the behaviour of both models. Figure 7.4 shows the axial stiffness curves obtained in each analysis, where a significant deviation can be seen between the reference and the efficient FE model. Figure 7.5 and Figure 7.6 represent the evolution of the contact force and contact angle, where the same deviation occurs.
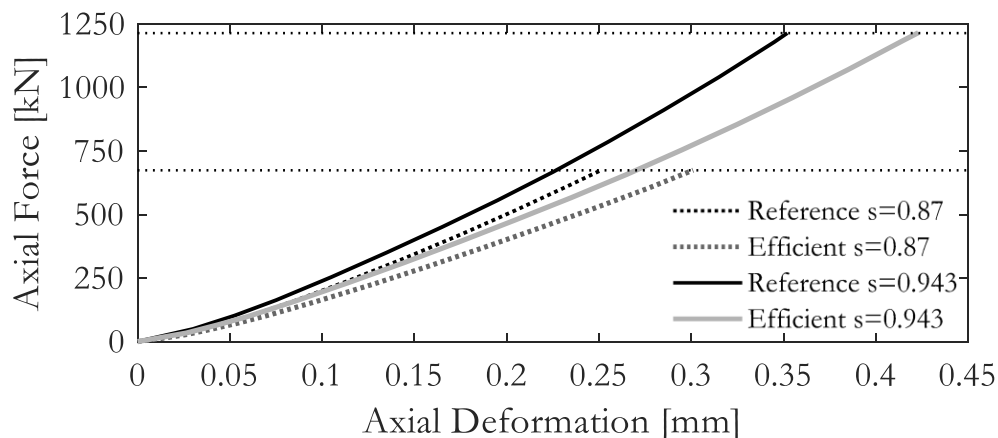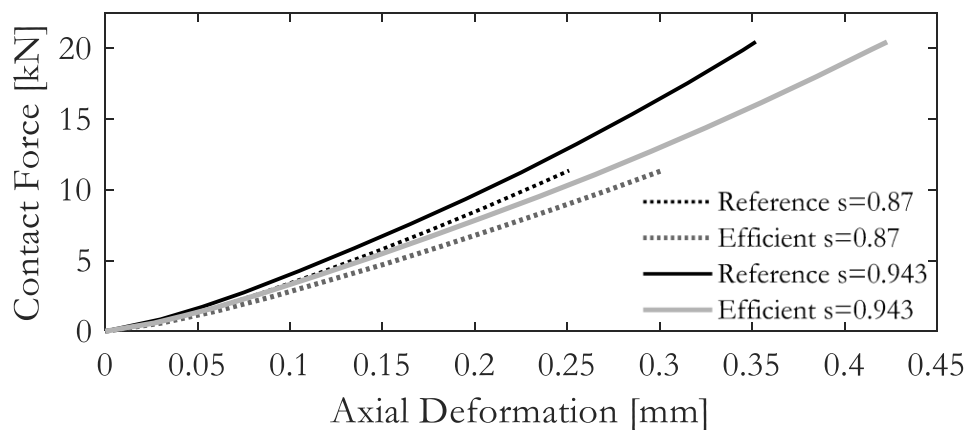

Figure 7.4 Axial stiffness results.

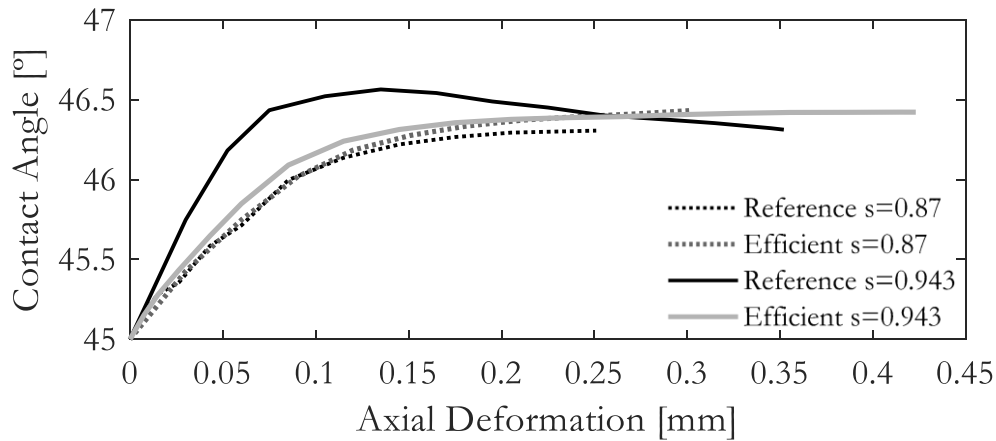**Figure 7.5** Contact force results.

Figure 7.6 Contact angle results.

According to the stiffness results, the FE model with the simplification applied is far more flexible than the reference FE model. The formulation introduced in the non-linear springs to represent the stiffness of the contacts is reliable, so the source of error can only come from the connection of the mechanism with the raceway. Figure 7.7 shows the equivalent elastic strain in one wire of the efficient FE model with $s = 0.943$. It can be seen how the rigid surface of the mechanism penetrates the wire, generating an indentation that should not occur. This mechanism was designed to represent the contact deformation with the non-linear spring element. Therefore, the contact zone must be properly stiffened or the deformation of the raceway would add extra flexibility to the component; which occurs here.
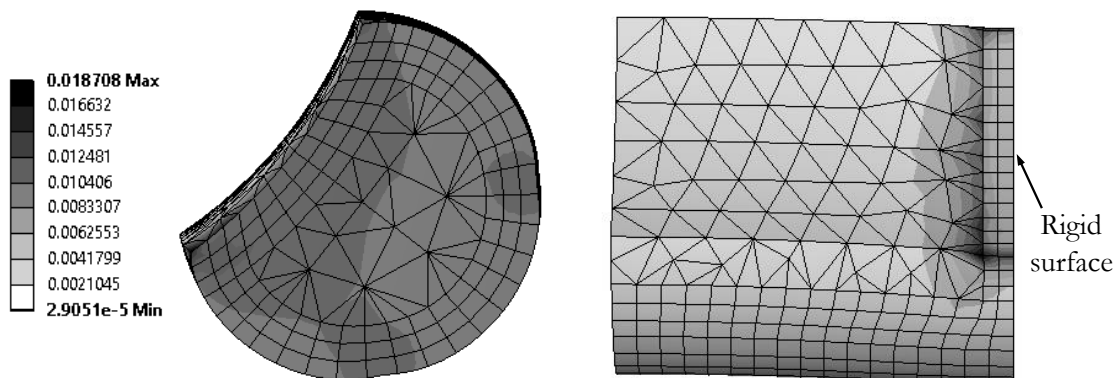
Figure 7.7 Equivalent elastic strain in a wire of the efficient FE model ($s = 0.943$).

The source of error has now been clearly identified, and for this reason, it is worth attempting to modify the model in such a way that the problem can be solved. If the raceway contact zone was not properly stiffened, the first attempt should focus on addressing this issue. To this end, a very rigid material ($E = 2 \cdot 10^5$ [GPa]) is defined and assigned to a certain volume of the wire. This volume cannot be defined either randomly or very precisely. For this reason,

the volume of Figure 7.8 was considered enough to contain the local effects of the raceway deformation. This volume goes from the raceway to the wire centre and from the symmetry plane to half the length of the wire. This improvement does not interfere with the wire-ring contact, and also allows a wire twisting differential between sectors.
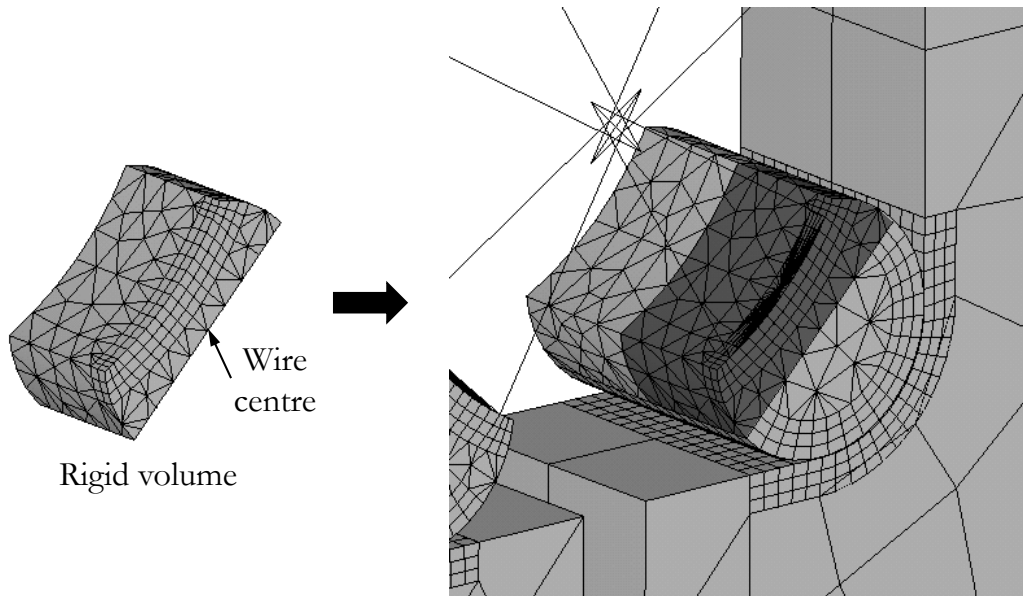
Figure 7.8 Wire rigid material volume.

Regarding the stiffness and contact force results of Figure 7.9 and Figure 7.10, a significant part of the error is corrected with the improvement. Figure 7.11 shows the contact angle results comparison, which shows good correlation for the $s = 0.87$ case and a slight deviation for the $s = 0.943$ case. This difference comes from the lack of wire twisting at the beginning of the loading process in the reference FE model. However, the deviation is not significant enough to affect the overall behaviour of the component.
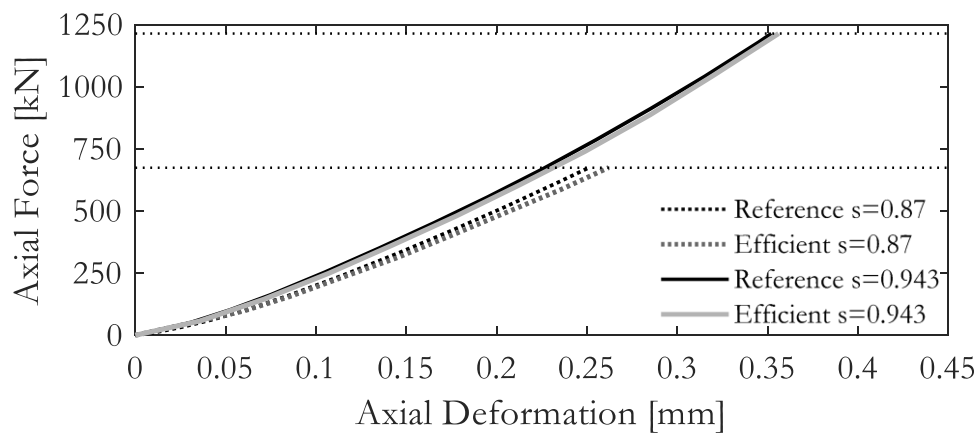
Figure 7.9 Axial stiffness results.
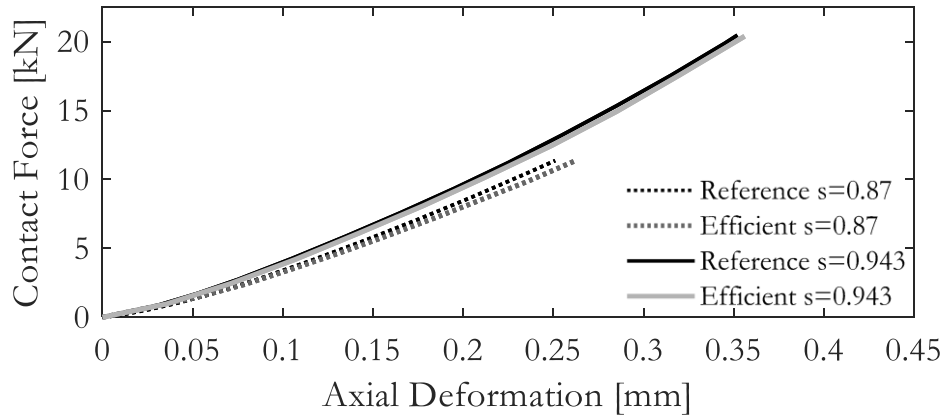
Figure 7.10 Contact force results.
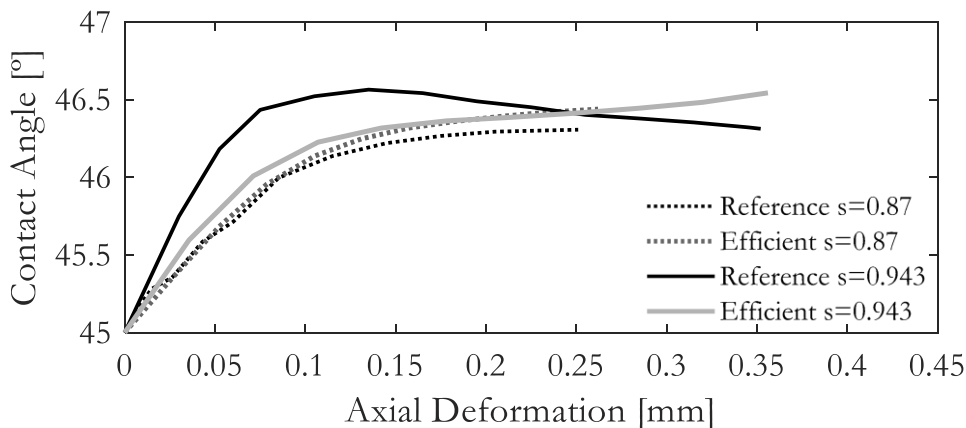
Figure 7.11 Contact angle results.

In order to evaluate whether the FE simplification introduces an error, Table 7.2 gathers the relative errors in terms of axial deformation at the end of the loading process. The direct application of the FE simplification proposed by Daidié et al. [126] is not a good alternative, since more flexible behaviour is obtained. However, if a volume portion of the raceway is stiffened, very good results can be achieved.

Table 7.2 Stiffness error introduced by the FE simplifications.

Error [%]	Initial efficient FE model	Improved efficient FE model
$s = 0.87$	20.0	4.5
$s = 0.943$	20.1	1.0

The proposed FE modelling strategy must be accurate but also efficient. For this reason, it is also very important to compare the computational cost of each

reference and efficient FE models. All the analyses were performed on a workstation with an Intel® Xeon® E5-2697 v3 @ 2.6GHz processor with 14 physical cores (28 logical), a RAM of 128GB and solid state disks (SSD). Table 7.3 compiles the CP and elapsed time of each simulation, where the elapsed time is greater than the CP time in all simulations. This means that the analyses are in I/O bound, which means that the lack of RAM memory is slowing down the solution process. However, it can also be seen how the efficient FE model involves a smaller computational cost than the reference FE model. With this, the efficiency of the FE modelling strategy is assessed and confirmed.

Table 7.3 CPU and elapsed time of the FE analyses.

[s]	Time	Reference FE model	Improved efficient FE model
$s = 0.87$	CP	788.45	480.2
	Elapsed	1268.0	797.0
$s = 0.943$	CP	914.8	567.2
	Elapsed	1462.0	1109

With all of this, it can be said that the improved efficient FE simplification proposed in this section is an accurate and efficient FE modelling alternative for four-point contact wire-race slewing bearings. It is worth recalling that a more efficient FE model can be obtained with a less refined mesh in the roller-wire contact area.

7.3 Crossed roller wire-race bearings

In this section, two efficient FE modelling strategies are proposed for crossed roller wire-race bearings. Unlike the strategy described in the previous section, in this case, both rolling elements and wires are removed and replaced with an equivalent mechanism. This substantial simplification was possible because of the previous development of an analytical formulation that represents the structural behaviour of these components. In contrast, the implementation process is much more complex. For this reason, the theoretical background of both alternatives is described separately first. Then, explanations regarding its

implementation in a FE model are provided. Finally, the validation process used to assess the accuracy of the efficient FE modelling strategies is introduced.

7.3.1 User-defined matrix element strategy

As has been mentioned, the efficient FE modelling strategy proposed in this section is based on the crossed roller wire-race bearing analytical formulation presented in Chapter 5. This analytical formulation represented the structural behaviour of one bearing sector for local or global conditions and was implemented in an analytical simulation tool. In this case, the purpose is to implement the analytical formulation in a FE model. Figure 7.12 summarizes the whole process, where the previous and current work is represented. The top part shows the concepts introduced in Chapter 5, where the analytical formulation was proposed, the stiffness constants (k_1, k_2, k_3) calculated and its performance validated via FE results comparison. The lower part of the figure shows the contribution of this section, where the analytical formulation is implemented in a FE model and validated.
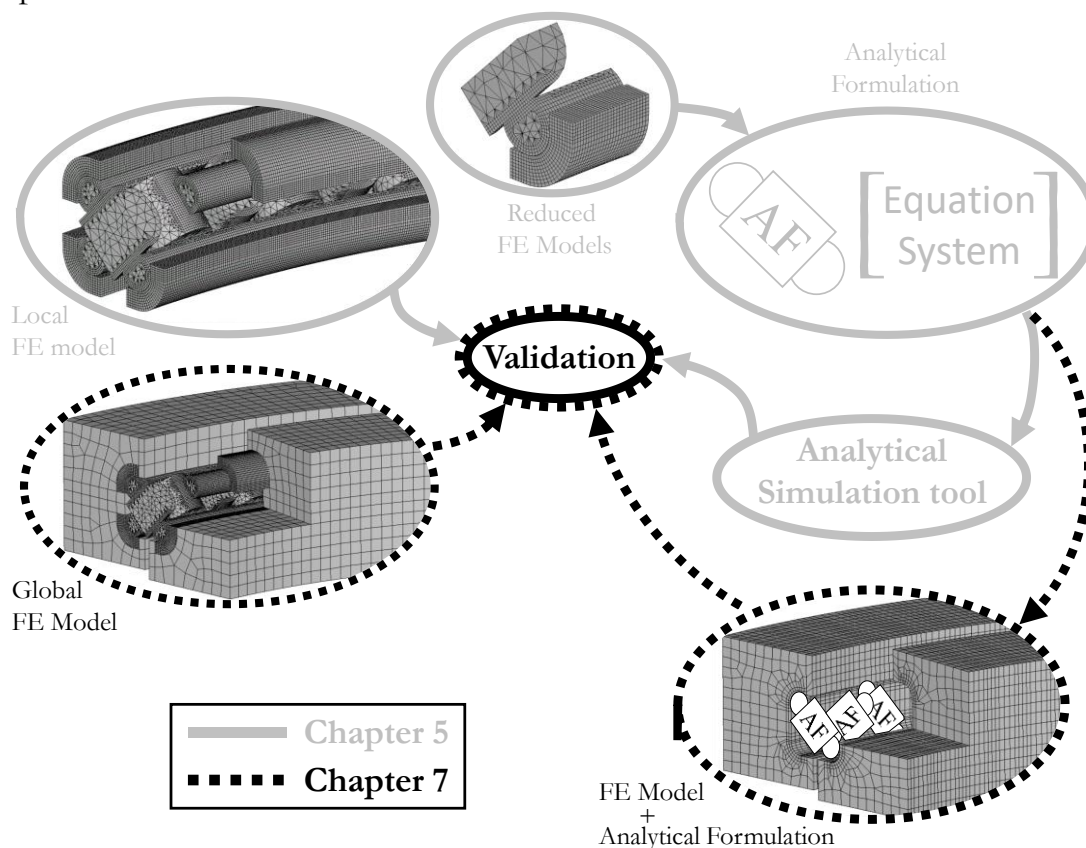

Figure 7.12 Summary of the user-defined matrix FE strategy.

For the sake of clarity, explanations will be made on the basis of type A rollers. Additional explanations will be provided with respect to the type B rollers at the end of the section. The process for the implementation of the

analytical formulation in a FE model starts with the set of equations that it is composed of. Equations (5.1) to (5.6) were conceived to represent the structural behaviour of one type A roller bearing sector i. Wire-ring friction forces vary depending on the prevailing axial (Δ_A^i) or radial (Δ_R^i) relative displacement between rings. To deal with this, a plus-minus ($\pm, \mp$) sign strategy was used, where the upper signs correspond to prevailing Δ_A^i and the lower signs to prevailing Δ_R^i. This way, both equation systems for each case can be represented in a single set.

At first glance, it seems complicated to implement the previous set of equations in a FE model. However, if the equation system is arranged in a matrix form, the resulting matrix can be considered as a kind of stiffness matrix that relates the forces and deformations of the wire-roller-wire set. With this in mind, the MATRIX27 element (in Ansys®) allows for the introduction of a linear user-defined matrix that links forces and displacements between two points with six degrees of freedom. This element could meet the requirements to represent the relationships defined in the analytical formulation if the set of equations is reduced to the degrees of freedom δ_{x1}, δ_{y1}, δ_{z1}, δ_{x2}, δ_{y2} and δ_{z2} shown in Figure 7.13. However, this is not straightforward due to two main issues: the equation system is non-linear and it is not related with the degrees of freedom of the MATRIX27. These problems can be solved by means of mathematical operations, which will be explained in detail below.
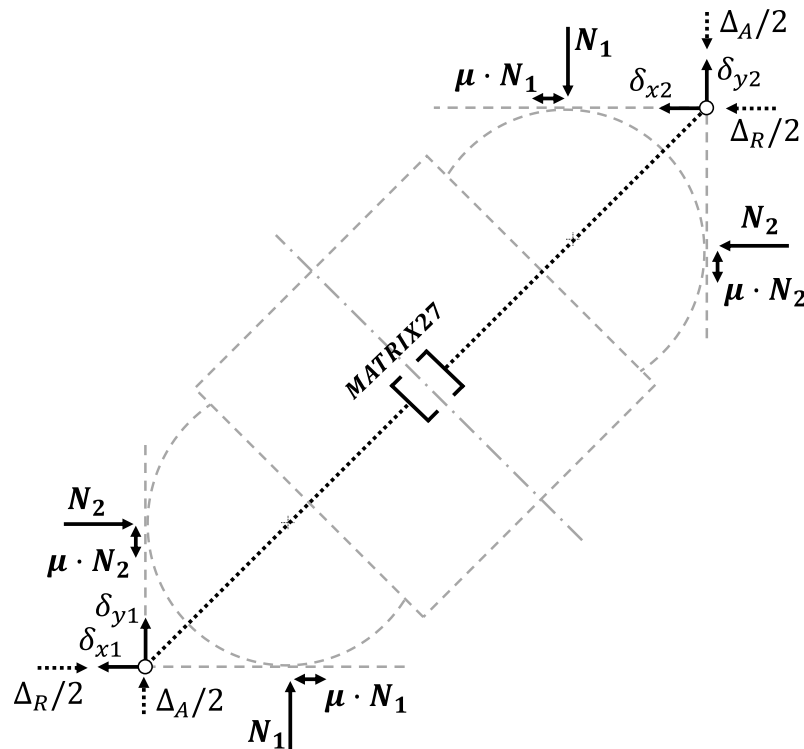

Figure 7.13 Degrees of freedom of the MATRIX27 element.

The first mathematical operation intends to transform the non-linear system of equations into a linear one. To this end, the first step consists in introducing Equations (5.1) and (5.2) in Equations (5.3) to (5.6). This reduces the complexity of the mathematical operation by reducing the size of the system to Equations (7.6) to (7.9).

$$f_1(\Delta_1, \Delta_2, \Delta_3, \alpha) = (k_2 \cdot \Delta_2 \pm \mu \cdot k_1 \cdot \Delta_1) \cdot cos(\alpha)$$
$$+(k_1 \cdot \Delta_1 \mp \mu \cdot k_2 \cdot \Delta_2) \cdot sin(\alpha) - k_3 \cdot \Delta_3$$

(7.6)

$$f_2(\Delta_1, \Delta_2, \Delta_3, \alpha) = -D_{CW}/2 \cdot cos(\alpha_0) + \Delta_R/2 - \Delta_2$$
$$+(D_{CW}/2 - \Delta_3) \cdot cos(\alpha)$$

(7.7)

$$f_3(\Delta_1, \Delta_2, \Delta_3, \alpha) = -D_{CW}/2 \cdot sin(\alpha_0) + \Delta_A/2 - \Delta_1$$
$$+(D_{CW}/2 - \Delta_3) \cdot sin(\alpha)$$

(7.8)

$$f_4(\Delta_1, \Delta_2, \Delta_3, \alpha) = k_2 \cdot \Delta_2 \cdot \left((D_{CW}/2 - \Delta_3) \cdot sin(\alpha)\right)$$
$$\pm \mu \cdot k_1 \cdot \Delta_1 \cdot \left(((\lambda/2 - \Delta_1) + (D_{CW}/2 - \Delta_3) \cdot sin(\alpha))\right)$$
$$\pm \mu \cdot k_2 \cdot \Delta_2 \cdot \left((\lambda/2 - \Delta_2) + (D_{CW}/2 - \Delta_3) \cdot cos(\alpha)\right)$$
$$-k_1 \cdot \Delta_1 \cdot \left((D_{CW}/2 - \Delta_3) \cdot cos(\alpha)\right)$$

(7.9)

Then, first order Taylor series can be applied at the initial point $(\Delta_1, \Delta_2, \Delta_3, \Delta_\alpha) = (0,0,0,0)$, where $\Delta_\alpha = \alpha - \alpha_0$. If the terms are rearranged:

$$\begin{bmatrix} a & b & c & 0 \\ 0 & -1 & d & e \\ -1 & 0 & f & g \\ h & i & 0 & 0 \end{bmatrix} \cdot \begin{Bmatrix} \Delta_1 \\ \Delta_2 \\ \Delta_3 \\ \Delta_\alpha \end{Bmatrix} = \begin{Bmatrix} 0 \\ j \\ k \\ 0 \end{Bmatrix}$$

(7.10)

$$a = \pm \mu \cdot k_1 \cdot cos(\alpha_0) + k_1 \cdot sin(\alpha_0)$$
$$b = k_2 \cdot cos(\alpha_0) \mp \mu \cdot k_2 \cdot sin(\alpha_0)$$
$$c = -k_3$$
$$d = -cos(\alpha_0)$$
$$e = -(D_{CW}/2) \cdot sin(\alpha_0)$$
$$f = -sin(\alpha_0)$$

(7.11)

$$g = (D_{CW}/2) \cdot cos(\alpha_0)$$
$$h = \pm \mu \cdot k_1 \cdot \lambda/2 \pm \mu \cdot k_1 \cdot D_{CW}/2 \cdot sin(\alpha_0) - k_1 \cdot D_{CW}/2 \cdot cos(\alpha_0)$$
$$i = k_2 \cdot D_{CW}/2 \cdot sin(\alpha_0) \pm \mu \cdot k_2 \cdot \lambda/2 \pm \mu \cdot k_2 \cdot D_{CW}/2 \cdot cos(\alpha_0)$$
$$j = -\Delta_R/2$$
$$k = -\Delta_A/2$$

This mathematical operation could introduce an error if the calculation point is far from the initial point. However, for small deformations this error can be considered negligible. To demonstrate this assumption, results obtained with the non-linear and linear equation systems were compared and no error was found.

With the analytical formulation transformed into a linear equation system, the next stage consists of applying a change of variables. This operation aims to relate the latter equation system with the degrees of freedom of the MATRIX27 element (δ_{x1}, δ_{y1}, δ_{x2}, δ_{y2}). At this point, the variables of the system are ($\Delta_1, \Delta_2, \Delta_3, \Delta_\alpha$) and there is no direct relationship between them and (δ_{x1}, δ_{y1}, δ_{x2}, δ_{y2}). For this reason, it is necessary to solve the equation system to obtain the expressions of $\Delta_1, \Delta_2, \Delta_3, \Delta_\alpha$. Applying the Cramer rule to the equation system:

$$\Delta_1 = \frac{Det.1}{Det.} \qquad \Delta_2 = \frac{Det.2}{Det.} \qquad \Delta_3 = \frac{Det.3}{Det.} \qquad \Delta_\alpha = \frac{Det.4}{Det.} \qquad (7.12)$$

Where:

$$Det. = \begin{vmatrix} a & b & c & 0 \\ 0 & -1 & d & e \\ -1 & 0 & f & g \\ h & i & 0 & 0 \end{vmatrix} \qquad Det.1 = \begin{vmatrix} 0 & b & c & 0 \\ j & -1 & d & e \\ k & 0 & f & g \\ 0 & i & 0 & 0 \end{vmatrix}$$

$$Det.2 = \begin{vmatrix} a & 0 & c & 0 \\ 0 & j & d & e \\ -1 & k & f & g \\ h & 0 & 0 & 0 \end{vmatrix} \qquad Det.3 = \begin{vmatrix} a & b & 0 & 0 \\ 0 & -1 & j & e \\ -1 & 0 & k & g \\ h & i & 0 & 0 \end{vmatrix} \qquad (7.13)$$

$$Det.4 = \begin{vmatrix} a & b & c & 0 \\ 0 & -1 & d & j \\ -1 & 0 & f & k \\ h & i & 0 & 0 \end{vmatrix}$$

So:

$$Det. = (-1) \cdot h \cdot (b \cdot d \cdot g - b \cdot e \cdot f + c \cdot g) +$$
$$+ (1) \cdot i \cdot (-c \cdot e + a \cdot d \cdot g - a \cdot e \cdot f)$$

$$Det.1 = j \cdot (-c \cdot g \cdot i) + k \cdot (i \cdot c \cdot e)$$
$$= Det.1j \cdot j + Det.1k \cdot k \qquad (7.14)$$

$$Det.2 = j \cdot (c \cdot g \cdot h) + k \cdot (-h \cdot c \cdot e) =$$
$$= Det.2j \cdot j + Det.2k \cdot k$$

$$Det.3 = j \cdot (a \cdot g \cdot i - b \cdot g \cdot h) + k \cdot (-a \cdot e \cdot i + b \cdot e \cdot h) =$$
$$= Det.3j \cdot j + Det.3k \cdot k$$

$$Det.4 = j \cdot (h \cdot b \cdot f - i \cdot a \cdot f - i \cdot c) +$$
$$+k \cdot (-h \cdot b \cdot d - h \cdot c + i \cdot a \cdot d) =$$
$$= Det.4j \cdot j + Det.4k \cdot k$$

(7.14)

According to Figure 7.13, the following change of variables can be applied:

$$j = -\frac{\Delta_R}{2} = -\frac{1}{2} \cdot (\delta_{x2} - \delta_{x1}) \tag{7.15}$$

$$k = -\frac{\Delta_A}{2} = -\frac{1}{2} \cdot (\delta_{y1} - \delta_{y2}) \tag{7.16}$$

Where $\delta_{x1}, \delta_{y1}, \delta_{x2}$ and δ_{y2} are the degrees of freedom of the MATRIX27 element. Thus, Equations (5.1) and (5.2) can be rewritten as:

$$N_1^i = k_1 \cdot \Delta_1 = k_1 \cdot \frac{Det.1}{Det.}$$
$$= k_1 \cdot \frac{Det.1j \cdot \left(-1/2 \cdot (\delta_{x2} - \delta_{x1})\right) + Det.1k \cdot \left(-1/2 \cdot (\delta_{y1} - \delta_{y2})\right)}{Det.}$$

(7.17)

$$N_2^i = k_2 \cdot \Delta_2 = k_2 \cdot \frac{Det.2}{Det.}$$
$$= k_2 \cdot \frac{Det.2j \cdot \left(-1/2 \cdot (\delta_{x2} - \delta_{x1})\right) + Det.2k \cdot \left(-1/2 \cdot (\delta_{y1} - \delta_{y2})\right)}{Det.}$$

(7.18)

Once again, according to Figure 7.13:

$$F_{x1} = -N_2 \mp \mu \cdot N_1 \tag{7.19}$$

$$F_{y1} = N_1 \mp \mu \cdot N_2 \tag{7.20}$$

$$F_{x2} = N_2 \pm \mu \cdot N_1 \tag{7.21}$$

$$F_{y2} = -N_1 \pm \mu \cdot N_2 \tag{7.22}$$

Introducing Equations (7.17) and (7.18) into Equations (7.19) to (7.22):

$$F_{x1} = -k_2 \cdot \frac{Det.\,2j \cdot \left(-\frac{1}{2} \cdot (\delta_{x2} - \delta_{x1})\right) + Det.\,2k \cdot \left(-\frac{1}{2} \cdot (\delta_{y1} - \delta_{y2})\right)}{Det.}$$

$$\mp \mu \cdot k_1 \cdot \frac{Det.\,1j \cdot \left(-\frac{1}{2} \cdot (\delta_{x2} - \delta_{x1})\right) + Det.\,1k \cdot \left(-\frac{1}{2} \cdot (\delta_{y1} - \delta_{y2})\right)}{Det.}$$

(7.23)

$$F_{y1} = k_1 \cdot \frac{Det.\,1j \cdot \left(-\frac{1}{2} \cdot (\delta_{x2} - \delta_{x1})\right) + Det.\,1k \cdot \left(-\frac{1}{2} \cdot (\delta_{y1} - \delta_{y2})\right)}{Det.}$$

$$\mp \mu \cdot k_2 \cdot \frac{Det.\,2j \cdot \left(-\frac{1}{2} \cdot (\delta_{x2} - \delta_{x1})\right) + Det.\,2k \cdot \left(-\frac{1}{2} \cdot (\delta_{y1} - \delta_{y2})\right)}{Det.}$$

(7.24)

$$F_{x2} = k_2 \cdot \frac{Det.\,2j \cdot \left(-\frac{1}{2} \cdot (\delta_{x2} - \delta_{x1})\right) + Det.\,2k \cdot \left(-\frac{1}{2} \cdot (\delta_{y1} - \delta_{y2})\right)}{Det.}$$

$$\pm \mu \cdot k_1 \cdot \frac{Det.\,1j \cdot \left(-\frac{1}{2} \cdot (\delta_{x2} - \delta_{x1})\right) + Det.\,1k \cdot \left(-\frac{1}{2} \cdot (\delta_{y1} - \delta_{y2})\right)}{Det.}$$

(7.25)

$$F_{y2} = -k_1 \cdot \frac{Det.\,1j \cdot \left(-\frac{1}{2} \cdot (\delta_{x2} - \delta_{x1})\right) + Det.\,1k \cdot \left(-\frac{1}{2} \cdot (\delta_{y1} - \delta_{y2})\right)}{Det.}$$

$$\pm \mu \cdot k_2 \cdot \frac{Det.\,2j \cdot \left(-\frac{1}{2} \cdot (\delta_{x2} - \delta_{x1})\right) + Det.\,2k \cdot \left(-\frac{1}{2} \cdot (\delta_{y1} - \delta_{y2})\right)}{Det.}$$

(7.26)

Finally, the terms of the previous equations are developed and rearranged into Equation (7.27). The matrix of coefficients of this equation system is the user-defined matrix that will be introduced in the MATRIX27 element.

$$\begin{Bmatrix} F_{x1} \\ F_{y1} \\ F_{z1} \\ M_{x1} \\ M_{y1} \\ M_{z1} \\ F_{x2} \\ F_{y2} \\ F_{z2} \\ M_{x2} \\ M_{y2} \\ M_{z2} \end{Bmatrix} = \begin{bmatrix} k_{11} & k_{12} & 0 & 0 & 0 & 0 & k_{13} & k_{14} & 0 & 0 & 0 & 0 \\ k_{21} & k_{22} & 0 & 0 & 0 & 0 & k_{23} & k_{24} & 0 & 0 & 0 & 0 \\ 0 & 0 & 0 & 0 & 0 & 0 & 0 & 0 & 0 & 0 & 0 & 0 \\ 0 & 0 & 0 & 0 & 0 & 0 & 0 & 0 & 0 & 0 & 0 & 0 \\ 0 & 0 & 0 & 0 & 0 & 0 & 0 & 0 & 0 & 0 & 0 & 0 \\ 0 & 0 & 0 & 0 & 0 & 0 & 0 & 0 & 0 & 0 & 0 & 0 \\ k_{31} & k_{32} & 0 & 0 & 0 & 0 & k_{33} & k_{34} & 0 & 0 & 0 & 0 \\ k_{41} & k_{42} & 0 & 0 & 0 & 0 & k_{43} & k_{44} & 0 & 0 & 0 & 0 \\ 0 & 0 & 0 & 0 & 0 & 0 & 0 & 0 & 0 & 0 & 0 & 0 \\ 0 & 0 & 0 & 0 & 0 & 0 & 0 & 0 & 0 & 0 & 0 & 0 \\ 0 & 0 & 0 & 0 & 0 & 0 & 0 & 0 & 0 & 0 & 0 & 0 \\ 0 & 0 & 0 & 0 & 0 & 0 & 0 & 0 & 0 & 0 & 0 & 0 \end{bmatrix} \cdot \begin{Bmatrix} \Delta_{x1} \\ \Delta_{y1} \\ \Delta_{z1} \\ \theta_{x1} \\ \theta_{y1} \\ \theta_{z1} \\ \Delta_{x2} \\ \Delta_{y2} \\ \Delta_{z2} \\ \theta_{x2} \\ \theta_{y2} \\ \theta_{z2} \end{Bmatrix}$$

(7.27)

$$k_{11} = \frac{1}{Det.} \cdot \frac{1}{2} \cdot (-k_2 \cdot Det.\,2j \mp \mu \cdot k_1 \cdot Det.\,1j)$$

$$k_{12} = \frac{1}{Det.} \cdot \frac{1}{2} \cdot (k_2 \cdot Det.\,2k \pm \mu \cdot k_1 \cdot Det.\,1k)$$

$$k_{13} = \frac{1}{Det.} \cdot \frac{1}{2} \cdot (k_2 \cdot Det.\,2j \pm \mu \cdot k_1 \cdot Det.\,1j)$$

$$k_{14} = \frac{1}{Det.} \cdot \frac{1}{2} \cdot (-k_2 \cdot Det.\,2k \mp \mu \cdot k_1 \cdot Det.\,1k)$$

$$k_{21} = \frac{1}{Det.} \cdot \frac{1}{2} \cdot (k_1 \cdot Det.\,1j \mp \mu \cdot k_2 \cdot Det.\,2j)$$

$$k_{22} = \frac{1}{Det.} \cdot \frac{1}{2} \cdot (-k_1 \cdot Det.\,1k \pm \mu \cdot k_2 \cdot Det.\,2k)$$

$$k_{23} = \frac{1}{Det.} \cdot \frac{1}{2} \cdot (-k_1 \cdot Det.\,1j \pm \mu \cdot k_2 \cdot Det.\,2j)$$

$$k_{24} = \frac{1}{Det.} \cdot \frac{1}{2} \cdot (k_1 \cdot Det.\,1k \mp \mu \cdot k_2 \cdot Det.\,2k)$$

$$k_{31} = \frac{1}{Det.} \cdot \frac{1}{2} \cdot (-k_2 \cdot Det.\,2j \mp \mu \cdot k_1 \cdot Det.\,1j)$$

$$k_{32} = \frac{1}{Det.} \cdot \frac{1}{2} \cdot (k_2 \cdot Det.\,2k \pm \mu \cdot k_1 \cdot Det.\,1k)$$

$$k_{33} = \frac{1}{Det.} \cdot \frac{1}{2} \cdot (k_2 \cdot Det.\,2j \pm \mu \cdot k_1 \cdot Det.\,1j)$$

$$k_{34} = \frac{1}{Det.} \cdot \frac{1}{2} \cdot (-k_2 \cdot Det.\,2k \mp \mu \cdot k_1 \cdot Det.\,1k)$$

$$k_{41} = \frac{1}{Det.} \cdot \frac{1}{2} \cdot (-k_1 \cdot Det.\,1j \pm \mu \cdot k_2 \cdot Det.\,2j)$$

$$k_{42} = \frac{1}{Det.} \cdot \frac{1}{2} \cdot (k_1 \cdot Det.\,1k \mp \mu \cdot k_2 \cdot Det.\,2k)$$

$$k_{43} = \frac{1}{Det.} \cdot \frac{1}{2} \cdot (k_1 \cdot Det.\,1j \mp \mu \cdot k_2 \cdot Det.\,2j)$$

$$k_{44} = \frac{1}{Det.} \cdot \frac{1}{2} \cdot (-k_1 \cdot Det.\,1k \pm \mu \cdot k_2 \cdot Det.\,2k)$$

(7.28)

As was explained at the beginning of the section, there are not so many differences between type A and type B roller analytical formulations. For this reason, all the mathematical operations have been developed for the type A roller. However, the user-defined matrix of the MATRIX27 element for type B roller must also be provided. The components of this user-defined matrix are

identical to the type A roller user-defined matrix with the exception of k_{12}, k_{14}, $k_{21}, k_{23}, k_{32}, k_{34}, k_{41}$ and k_{43}, whose signs change.

7.3.2 Non-linear spring element strategy

The second crossed roller wire-race bearing efficient FE modelling strategy consists of a simple compression-only, non-linear spring mechanism. As shown in Figure 7.14, the spring replaces the wires and the roller and represents the deformation of the set under different axial or radial imposed displacements. Despite the fact that the spring replicates the compatibility of deformations properly, friction forces are not considered.
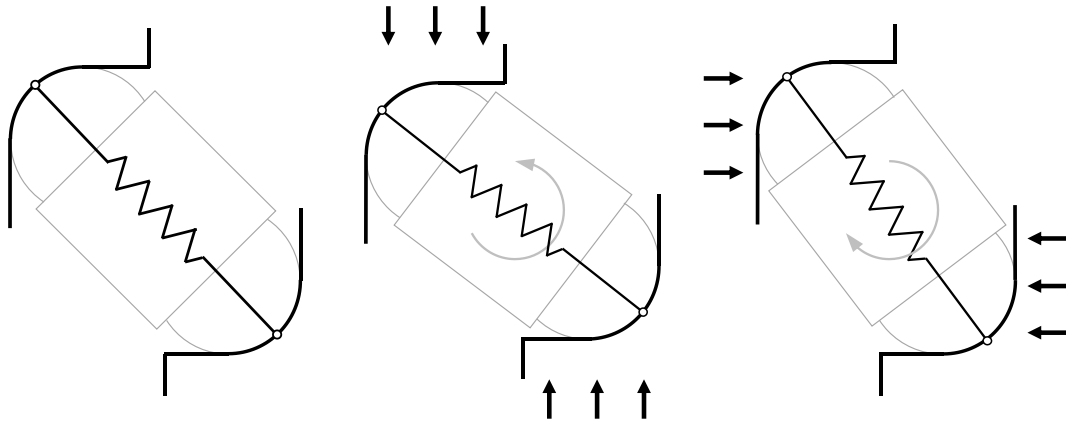

Figure 7.14 Schema of the spring based alternative model.

The stiffness of the equivalent spring (k_{cbn}) is obtained analytically from an equation based on the geometrical relationships of k_1, k_2 and k_3 (Figure 7.15a). To this end, it is first necessary to combine the stiffness of k_1 and k_2 into a k_p. This operation is defined in Equation (7.29), which represents the projection of k_1 and k_2 on the roller-wire contact normal line, defined by the initial contact angle α_0. Hereafter, the serial combination of k_p with k_3 (Figure 7.15b) results in the stiffness of the equivalent spring k_{cbn}, which can be calculated with Equation (7.30) and is represented in Figure 7.15c.
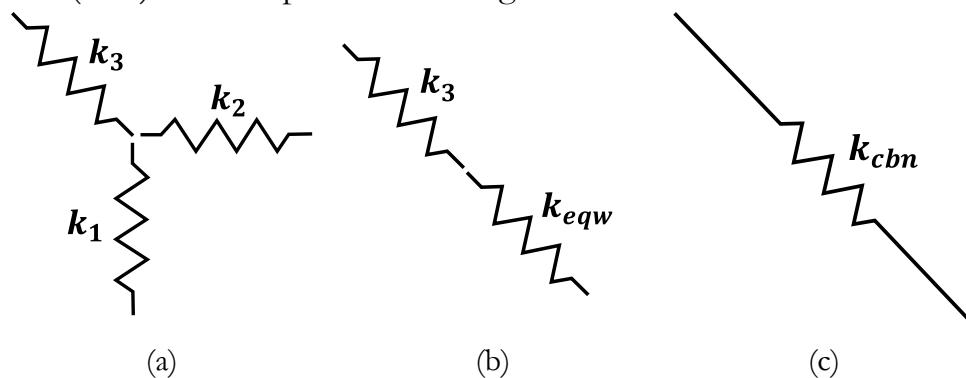

(a)   (b)   (c)

Figure 7.15 Geometrical relationships to obtain the stiffness of the spring: (a) $\boldsymbol{k_1, k_2}$ and $\boldsymbol{k_3}$ representation; (c) Serial combination; (c) Non-linear spring element stiffness $\boldsymbol{k_{cbn}}$.

$$F_{eqw} = \sqrt{\left(k_2^2 \cdot cos^2(\alpha_0) + k_1^2 \cdot sin^2(\alpha_0)\right)} \cdot \delta_{eqw} = k_{eqw} \cdot \delta_{eqw} \qquad (7.29)$$

$$k_{cbn} = \frac{k_3 \cdot k_{eqw}}{k_3 + k_{eqw}} = \frac{k_3 \cdot \sqrt{\left(k_2^2 \cdot cos^2(\alpha_0) + k_1^2 \cdot sin^2(\alpha_0)\right)}}{k_3 + \sqrt{\left(k_2^2 \cdot cos^2(\alpha_0) + k_1^2 \cdot sin^2(\alpha_0)\right)}} \qquad (7.30)$$

Despite the equivalent spring stiffness being linear, the spring element must be non-linear because of the compression only behaviour. This made necessary the election of the COMBIN39 non-linear spring element (in Ansys®).

7.3.3 Implementation in a FE model

The MATRIX27 and the COMBIN39 elements were conceived to represent the behaviour of the wire-roller-wire set, but they must be properly linked to the bearing rings to fulfil their role. To that end, it was considered appropriate to study the contact FE results of a loaded wire-ring contact. On the one hand, Figure 7.16a shows how the contact happens to be along two parallel lines. Accordingly, two rigid surfaces should be created to transmit the force from the equivalent mechanism to the ring surface. On the other hand, the pressure distribution of Figure 7.16b indicates that the central zones, which are closer to the roller-wire contact, are more loaded.
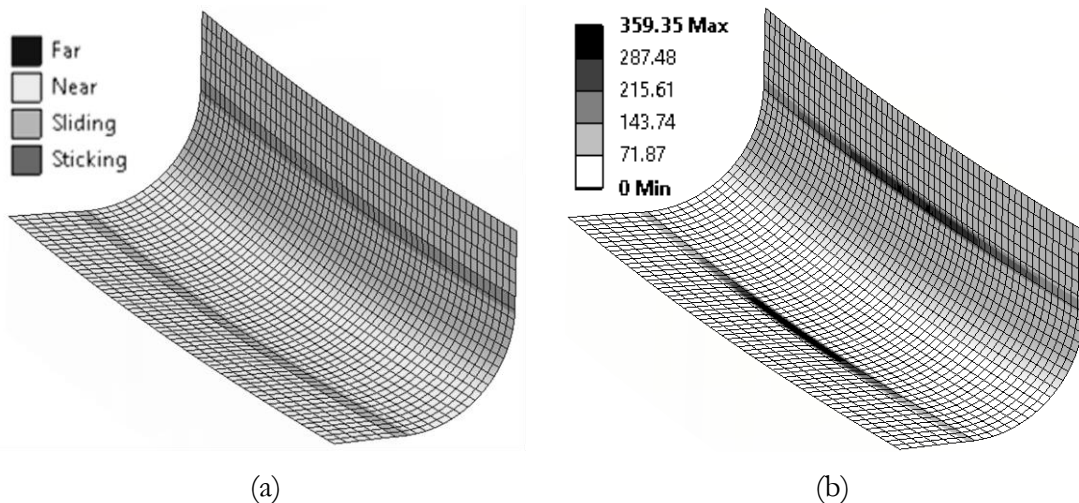

Figure 7.16 Wire-ring FE contact results: (a) Contact Status; (b) Contact pressure [MPa].

According to the contact results, the conception of the mechanism was not simple. However, the final simplified FE mechanism is shown in Figure 7.17. MATRIX27 and COMBIN39 nodes are linked through rigid beams to two rigid surfaces modelled with shell elements. In turn, a no separation frictionless

contact is defined between the rigid shells and ring surfaces to join them without adding any circumferential stiffness to the ring. Because of this, the displacement and rotation degrees of freedom in the circumferential direction must be also constrained on the nodes of the MATRIX27/COMBIN39 elements. This forces the mechanism to work on the radial plane and prevents rigid body motion.
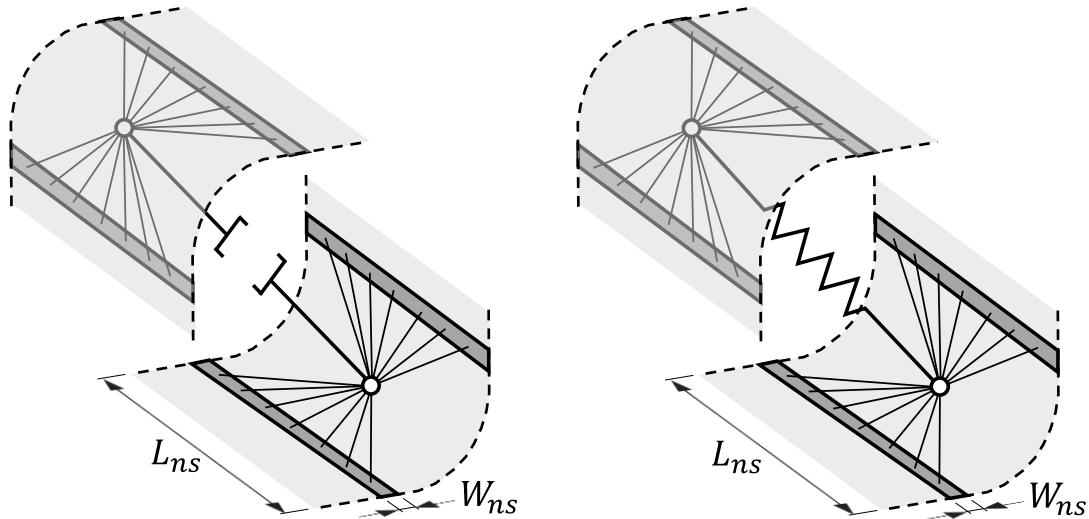

Figure 7.17 MATRIX27 and COMBIN39 simplified FE mechanism.

Regarding the dimensions of the contact surface, L_{ns} is the arc length that corresponds to the angle formed by two rolling elements ($2 \cdot 360°/N_R$). The contact surface width W_{ns} can be defined as the approximated wire-ring contact width when the static load capacity is reached. To obtain this value, the formulas for line-contact calculations proposed by Houpert [47] can be used. First, it is necessary to obtain the roller-wire normal contact force with Eq. (7.31), where L is the length of the roller-wire contact and P_{max} is the maximum allowable contact pressure (4000 [MPa]).

$$Q = 2 \cdot \pi \cdot L \cdot \frac{D_w}{2} \cdot \frac{P_{max}^2}{E} \tag{7.31}$$

Secondly, the projection of this force onto the corresponding direction (e.g. the vertical axis in the next formula) is applied to one of the wire-ring line contacts to obtain the contact semi-width (*b*) with (1.18).

Finally, authors recommend defining W_{ns} as two times (*b*). This statement is not trivial, since a wider rigid surface also stiffens the contact area and avoids the need to define a rigid volume underneath (unlike the case presented in the previous section). Besides this, each rigid volume of each sector would be

linked, creating slender rigid rings inside the bearing rings that would add unrealistic stiffness to the component.

As mentioned, the MATRIX27 formulation considers the friction forces in the contacts, while the COMBIN39 does not. Therefore, greater accuracy is expected using MATRIX27. However, it has been explained that the direction of these friction forces depends on the prevailing relative displacement between rings, and unfortunately this aspect cannot be reproduced by a unique user-defined matrix. For this reason, two different matrices must be created: one for prevailing axial displacement and another for prevailing radial displacement. Therefore, depending on the relative displacement of the sector, one of the two matrices should be introduced for each roller. In addition to this, it must be recalled that the sign criterion is different for rollers A and B, as explained in Chapter 5. Thus, a total of four different user-defined matrices are required for the analysis of a bearing, two for each roller type. Obviously, the procedure to select the proper matrix must be based on previous FE or analytical calculations to obtain the approximate relative displacements. The suggested procedure consists of a combination of both MATRIX27 and COMBIN39 strategies. First, a FE simulation with the COMBIN39 element obtains the predominant relative displacement between rings for each sector with notable accuracy. Second, the proper MATRIX27 user-defined matrix is introduced in each sector based on the previous results. Accordingly, two FE simulations are required, but this procedure has better convergence and is more efficient than a detailed solid-meshed FE model.

7.3.4 FE Validation

Once the efficient FE modelling strategies have been described, their accuracy must be assessed. To this end, two efficient FE models are built, one for the MATRIX27 alternative and another for the COMBIN39. Then, the results of the efficient FE models and of the reference FE model are compared for three pure load cases (axial, radial and tilting moment). The reasons for the election of these load cases have been explained in previous sections. Bearing geometrical data (Figure 7.18) for the validation are gathered in Table 7.4, where the rings are dimensioned following the standard geometry proposed in [15], but dependent on the housing H rather than on the rolling element diameter D_w.

Table 7.4 Reference bearing geometry data.

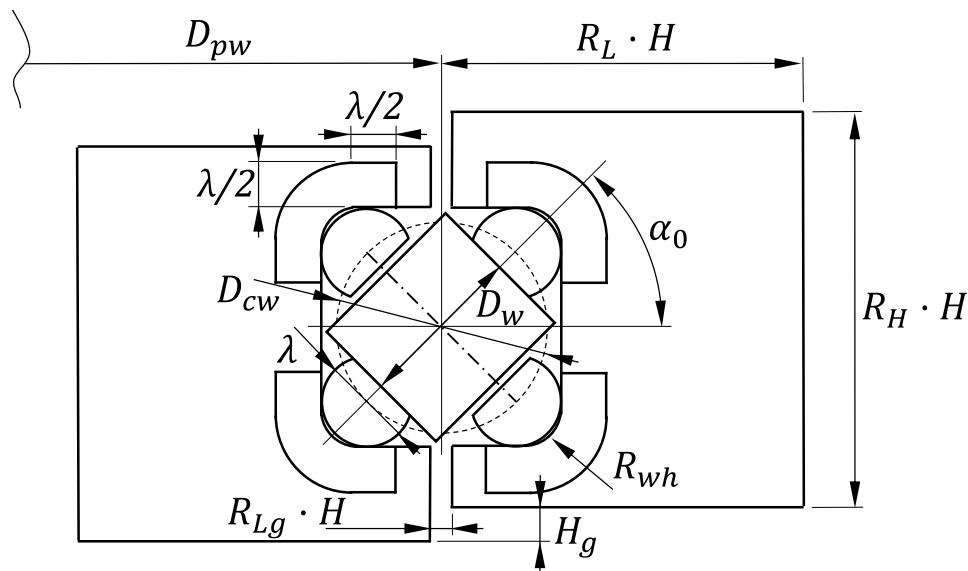| D_w	D_{pw}	Rf	α_0	λ	N_R	R_{wh}	R_L	R_H	R_{Lg}	H_g
[mm]	[mm]		[°]	[mm]						[mm]
14	420	0.5	45	8	94	3.9	1.9	2.15	0.1	3

Figure 7.18 Bearing geometrical parameters.

Figure 7.19a shows an efficient FE model for the radial and tilting moment load case, where the wires and rollers have been replaced with the simplified FE mechanisms. Besides this, mesh refinements are not required, which also reduces the size of the mesh and the computational cost. Rings were modelled with linear elastic aluminium (E =71 [GPa]), and a penetration tolerance of 1 [µm] was defined for the no-separation shell-ring contacts. Boundary conditions represent rigid supporting structures, while loads are applied as a relative displacement between rings using a remote node on the bearing centre. Symmetry boundary conditions were applied to symmetry planes and the circumferential displacement was constrained for the nodes of the MATRIX27 or COMBIN39 elements.

Figure 7.19b shows the reference FE model described in Section 5.5. For further information about this FE model, the reader may go back to that chapter.

The mesh comparison between FE models can be observed in Figure 7.19c. Despite the evident differences in the mesh, the most relevant data for the comparison of two FE models is the number of DoF. In this sense, the efficient

FE models retrieve 2,054,625 DoF while the reference FE model has 26,914,527 DoF. The disparity in the number of DoF gives an idea of the efficiency of the proposed FE modelling strategies. Moreover, the suppression of the non-linearities generated by the frictional contacts improves the convergence and consequently the solution process.
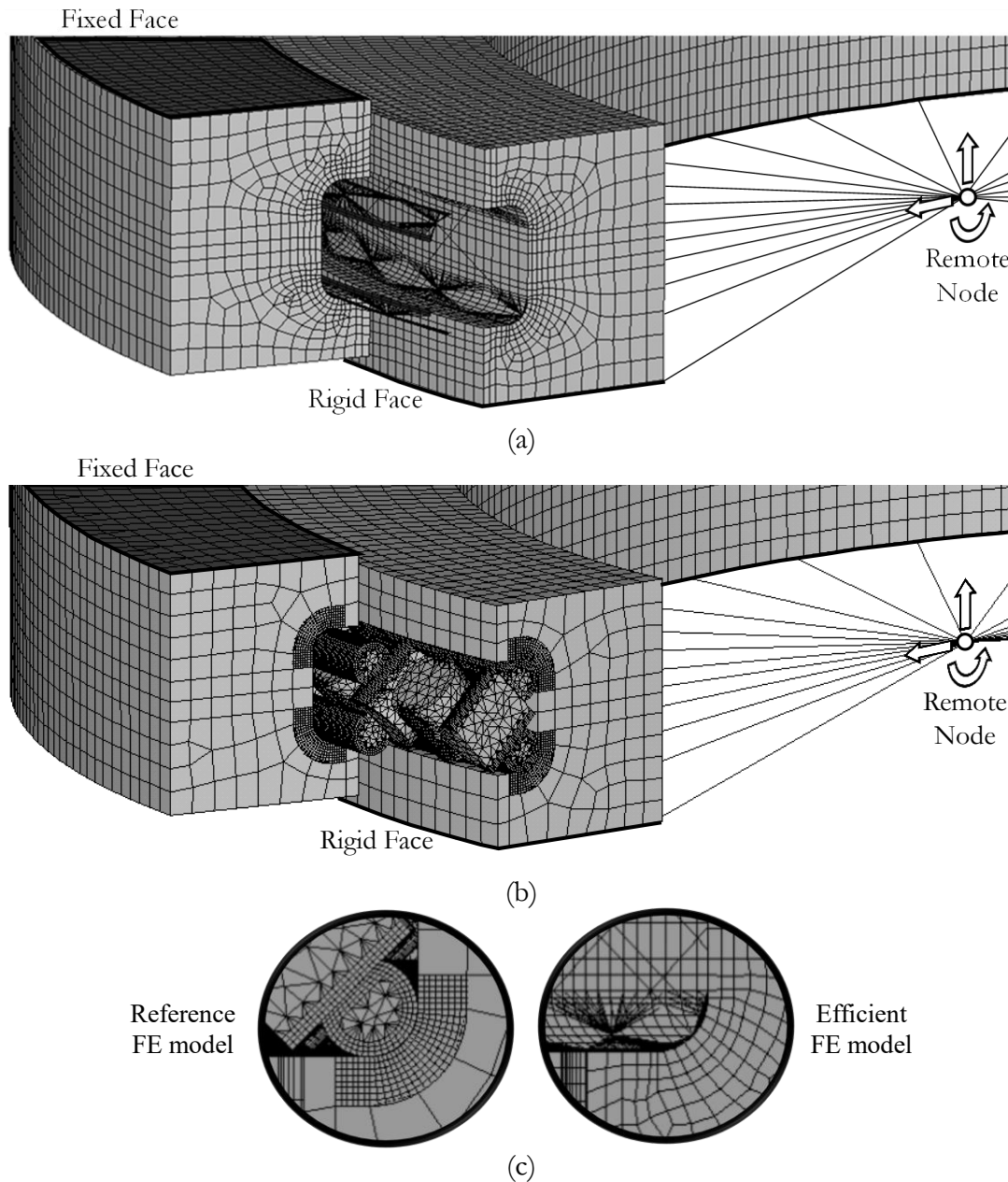

Figure 7.19 Validation FE models: (a) Efficient FE model; (b) Reference FE model; (c) Mesh comparison.

Having performed the FE analyses, it is time to compare the results to assess the validity of the proposed FE modelling strategy. The first performance indicator to be evaluated is the bearing stiffness. Figure 7.20 shows the bearing stiffness curves for each FE model under the three pure load cases. The upper grey area represents load values over 40% of the bearing static load capacity.

For the case under study, beyond that load, a stiffer behaviour is observed in the reference model. This is caused by the wire-ring gap closure phenomenon explained in Section 5.3.1, which is not considered in the efficient models formulation or in the calculation of the stiffness constants k_1, k_2 and k_3.

The stiffness behaviour is quite similar for the three load cases. Below 40% of the static load capacity, the MATRIX27 alternative obtains almost perfect results, whereas the COMBIN39 shows a slight deviation. As mentioned, the gap closure phenomenon leads to a higher accuracy loss as the load magnitude increases, especially for the COMBIN39 model. Table 7.5 lists a summary of the errors with respect to the reference curve at different values of the static load capacity (C_0).
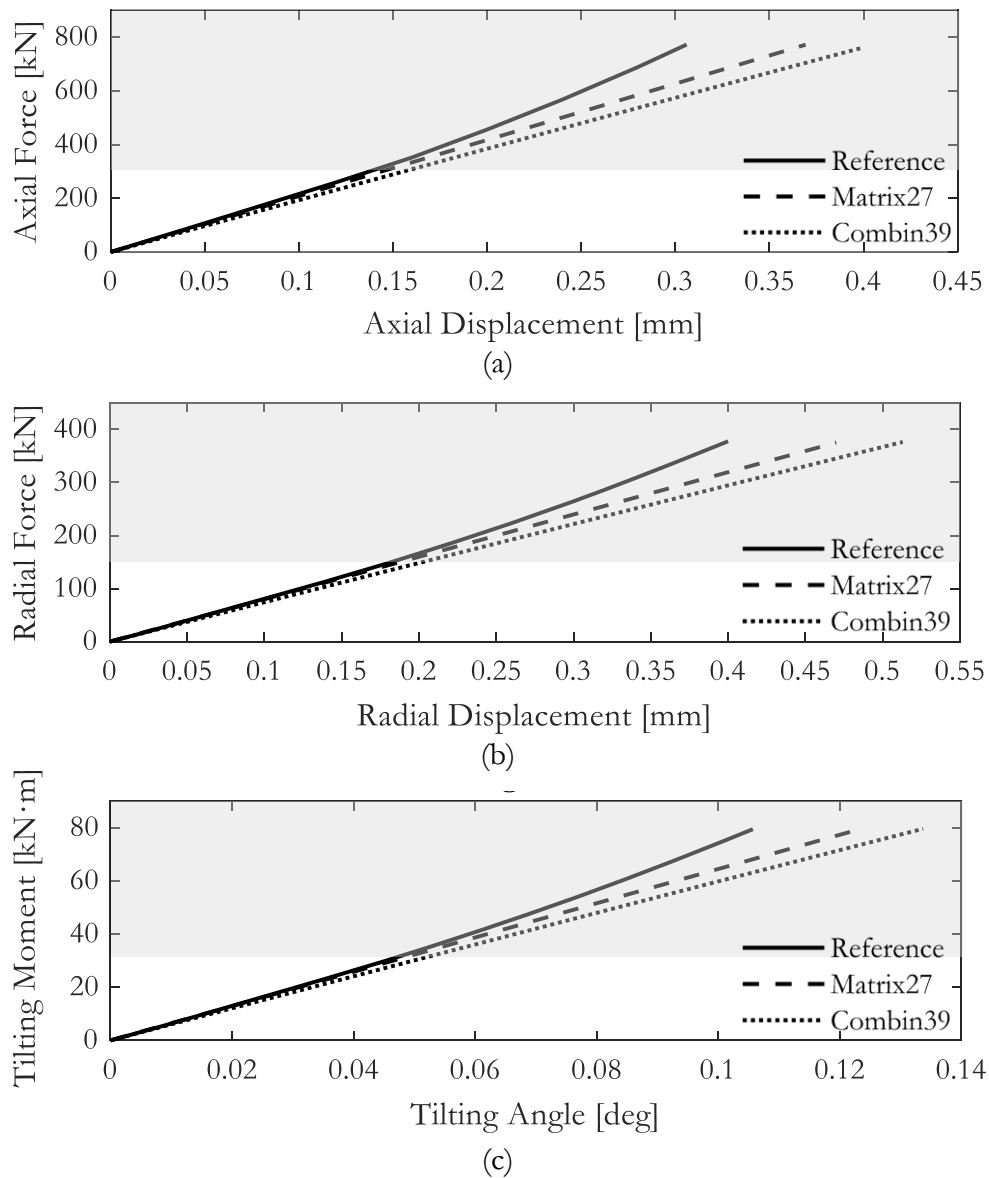

Figure 7.20 Bearing stiffness curves comparison: (a) Axial load case; (b) Radial load case; (c) Tilting moment load case.

Table 7.5 Error in stiffness curves.

[%]	MATRIX27			COMBIN39		
	30% C_0	40% C_0	50% C_0	30% C_0	40% C_0	50% C_0
Axial	3.8	4.8	6.8	12.1	13.4	15.9
Radial	1.5	3.1	5.4	9.3	11.1	13.8
Tilting	1.65	2.98	5	8.85	10.4	12.7

Regarding the other three performance indicators, roller-wire contact results are shown in Figure 7.21, Figure 7.22 and Figure 7.23 for the axial, radial and tilting moment load cases respectively. The results in these plots were obtained for the same load value at 40% of static load capacity, since it is the approximate limit of validity of the assumptions made for the development of the FE models. In all cases, normal contact load values are similar. In terms of contact angle, almost no difference exists. With regard to the tangential contact force, the MATRIX27 alternative provides acceptable results, where the deviation is caused by the simplifications made for representation of the contacts. On the other hand, the tangential behaviour is not considered in the COMBIN39 model. Therefore, it can be concluded that the omission of the tangential forces is the source of the difference in stiffness results shown in Figure 7.20.
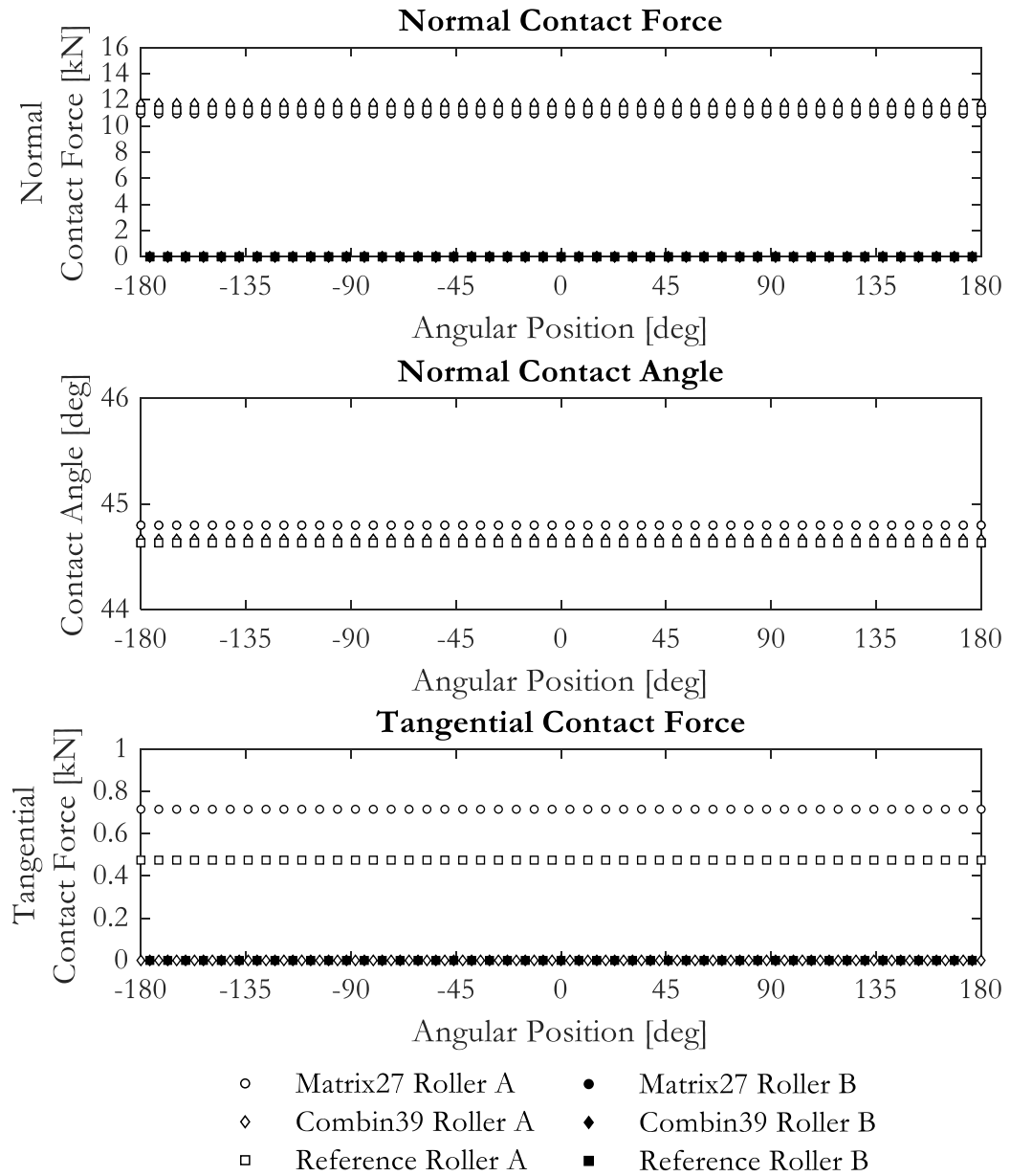
Normal Contact Force

Normal Contact Angle

Tangential Contact Force

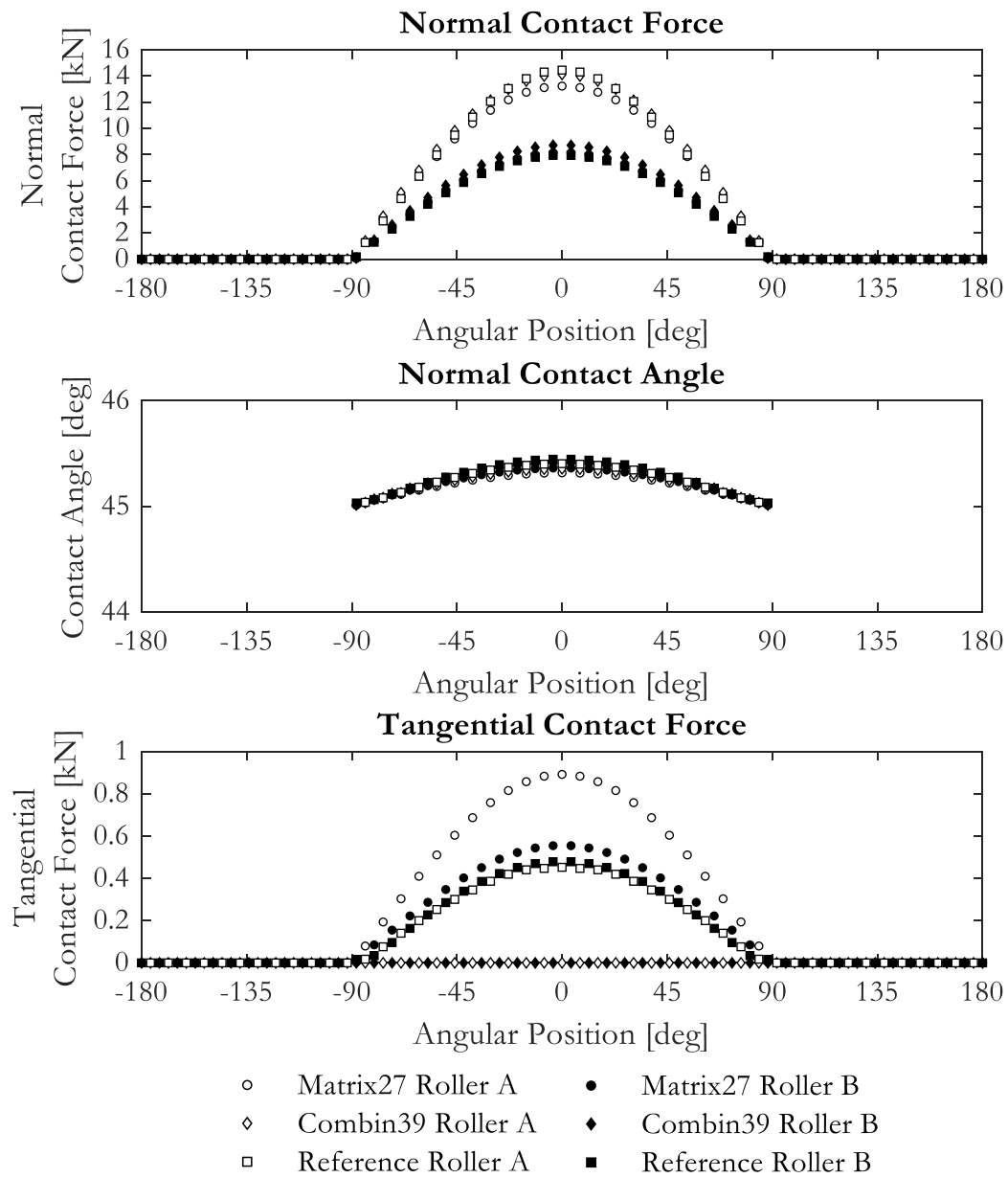| ○ | Matrix27 Roller A | ● | Matrix27 Roller B |
| ◇ | Combin39 Roller A | ◆ | Combin39 Roller B |
| □ | Reference Roller A | ■ | Reference Roller B |

Figure 7.21 Axial load case contact results.
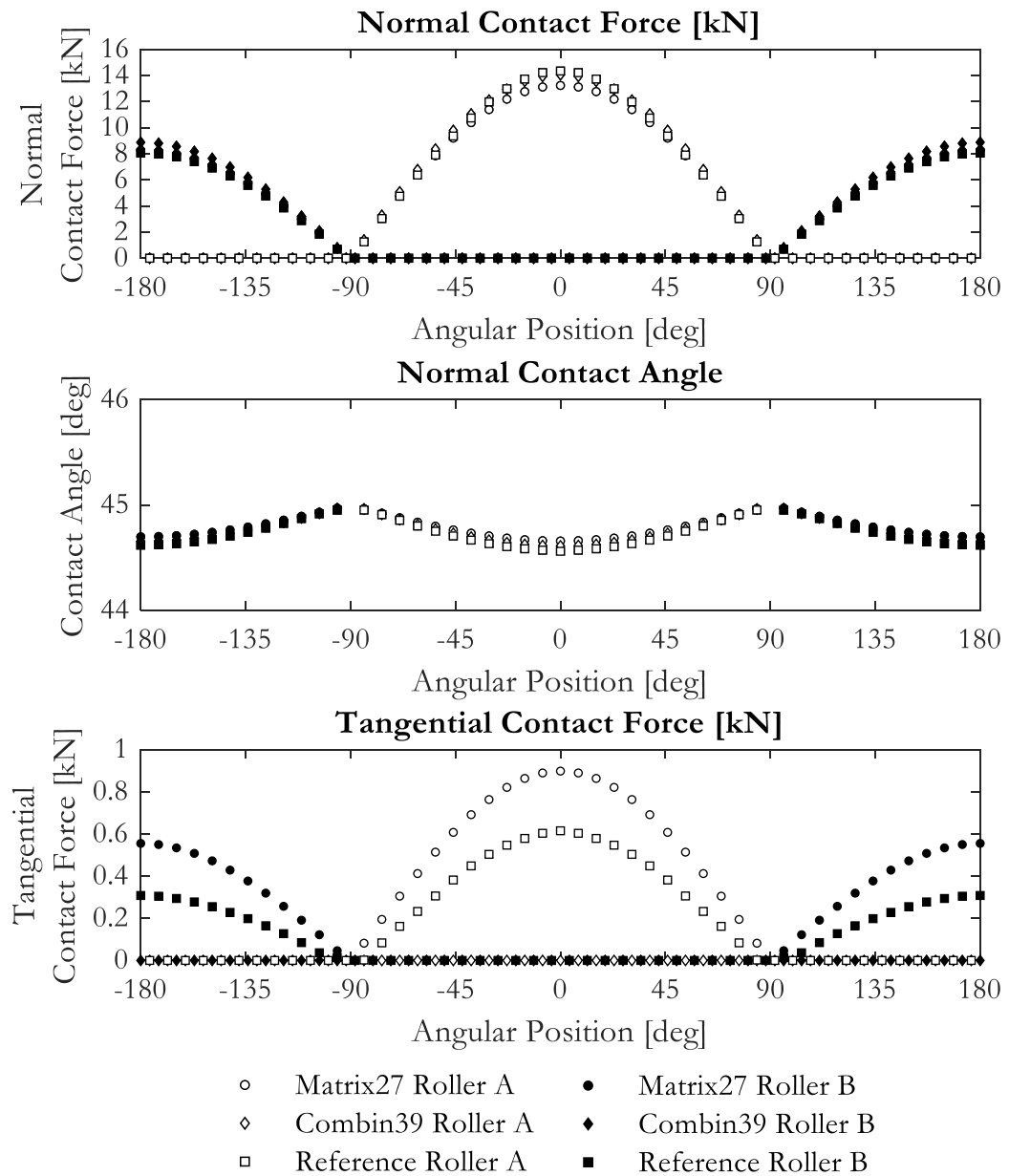
Figure 7.22 Radial load case contact results.

Figure 7.23 Tilting moment load case contact results.

Based on the above, it can be concluded that the MATRIX27 and the COMBIN39 efficient FE modelling strategies are accurate until a significant percentage of the static load capacity. In the majority of applications, bearing operating conditions fall within this region. Even if the design conditions are close to the static load capacity, the accuracy of the proposed FE models is good enough to perform initial calculations.

It is also worth also recalling that stress analysts can take advantage of both proposed approaches. The COMBIN39 FE strategy can provide useful results for fast simulations in initial design stages. Besides this, this approach can also be used as a first iteration of a more accurate simulation, obtaining the relative

displacements between rings that are required to perform a FE simulation according the MATRIX27 FE strategy.

Finally, once the FE analyses for the validation have been performed and the results compared, the true efficiency of the FE modelling strategies is evaluated. All the analyses were performed on a workstation with an Intel® Xeon® E5-2697 v3 @ 2.6GHz processor with 14 physical cores (28 logical), a RAM of 128GB and solid state disks (SSD). Table 7.6 presents the CP and elapsed time for each simulation, where the phenomenon presented in the previous sections happens to occur again (analyses in I/O bound). This phenomenon is more evident in the reference FE model for radial and tilting moment loads, since it has 27M. DoF. Regarding the efficiency of the proposed FE modelling strategies, the COMBIN39 FE model was 100 times faster for the tilting moment load case in comparison with the reference FE model. MATRIX27 FE model is almost as efficient, but it is worth remembering that the implementation of this strategy for combined load cases requires a previous analysis with the COMBIN39 FE model. Even considering this, the computational cost savings are exceptional. It is also worth mentioning that the relationship between the computational cost and the number of DoF is exponential. This means that the savings are more significant as the size of the FE model increases.

Table 7.6 CPU and elapsed time of the FE analyses.

[s]	Time	Reference FE model	MATRIX27 efficient FE model	COMBIN39 efficient FE model
Axial load	CP	2264	198	205
	Elapsed	2275	678	753
Radial load	CP	40113	3365	3776
	Elapsed	100936	4768	4302
Tilting moment	CP	30489	1651	1271
	Elapsed	164889	1976	1554

8 Influence of geometrical parameters on the structural behaviour: design guidelines for wire-race bearings

8.1 Introduction

Due to the lack of works regarding wire-race bearings, some insight becomes necessary when an engineer faces the design problem. Therefore, knowing the effects of design parameters on the performance of the bearings is a necessary step to optimize the design. To this regard, a study of the effects of several geometrical parameters on the performance under axial load is presented in this chapter. The results were obtained by means of FE simulations within a DoE for both four-point contact and crossed roller wire-race bearings. It can be considered that the conclusions obtained from this study are also valid for other load cases. Besides this, radial and tilting moment FE analyses are quite costly in terms of computational cost. If these load cases would have been considered, such an exhaustive study could have not been carried out.

First, the foundations of the study must be established, which means that the geometrical parameters under analysis have to be defined. After this, the boundaries of the study, i.e. the design space, must be defined according to bearing catalogues, since it is only of interest to study real bearing designs and see what happens slightly further beyond; there is no point in studying unrealistic geometries. Once the geometrical parameters are defined with their maximum and minimum range values, the DoE must be planned and carried out, where each Design Point will imply one FE analysis. Finally, the FE results are processed in such a way that the physical phenomena can be clearly observed and the main and crossed effects evaluated, so a set of design guidelines can be properly established.

8.2 Design parameters definition

For the sake of clarity, four-point contact and crossed roller wire-race bearings will be referred to as ball and roller bearings from now on, since this change in the nomenclature simplifies the understanding of the text.

As can be seen in Figure 8.1, there are many parameters that define the bearing geometry, and there is no sense in studying them all. For this reason, only the design parameters relating to the geometry of the contact areas were considered for this study. Bearing mean diameter (D_{pw}) and the initial contact angle (α_0) remained constant because their effects are already known from studies on conventional slewing bearings. Besides this, D_{pw} is usually dependant on the application and cannot be modified. In the case of roller bearings, the length of the rollers was also not considered as a design parameter. Roller length does not affect the roller-raceway contact area, because it is always larger than the raceway width on wire-race bearings. R is the radius of the ring groove where the wire is placed, and its value is usually λ minus 0.1 [mm] [4]. Regarding the number of rolling elements, a fill factor of 100% [15] was established. This means that the number of rolling elements is the maximum allowable.

In order to obtain generalist results, the parameters of the DoE were defined as non-dimensional or dependant on the rolling element diameter. This means that it could be assumed that the conclusions obtained from a certain D_w are also valid for smaller or higher D_w values. However, results may change with the scale, so the first design parameter to be considered is the rolling element diameter.

The wire diameter is also another geometrical parameter that is essential for the definition of the bearing geometry and its influence must be evaluated. However, as was explained in the previous paragraph, it has to be dependant on D_w. For this reason, the non-dimensional parameter λ_r was defined as the second design parameter, where $\lambda_r = \lambda/D_w$.

In order to evaluate the influence of the raceway size, the non-dimensional parameter Rf (Eq. (5.11)) was selected as the third design parameter. This parameter was introduced in Chapter 5, in such a way that $Rf = 0$ means that no material is machined (wire-rolling element non-conformal contact) and $Rf = 1$ means that half of the wire section is removed ($D_w = D_{cw}$).

$$Rf = 1 + \frac{1}{\lambda/D_w} - \frac{1}{\lambda/D_{cw}} \qquad (5.11)$$

Apart from the three design parameters defined above (D_w, λ_r, Rf), the osculation ratio (s) is a crucial parameter for the definition of the ball-raceway contact. For this reason, it must be included as an additional design parameter for the ball bearings.

Regarding the dimensions of the rings, the size of their cross-section is usually related to the rolling element diameter. For this reason, it was considered unappropriate to keep a constant rings cross-section for all the study cases. The solution to this problem was found on the standard bearing ring geometry proposed by Heras et al. [15], which is dependant on the size of the housing (H) and has already been used in previous chapters. Table 8.1 compiles the constant geometry parameters and the coefficients that define the geometry of the rings. Regarding the mean bearing diameter, a generalist value was used, as well as standard values for the ring geometry parameters.
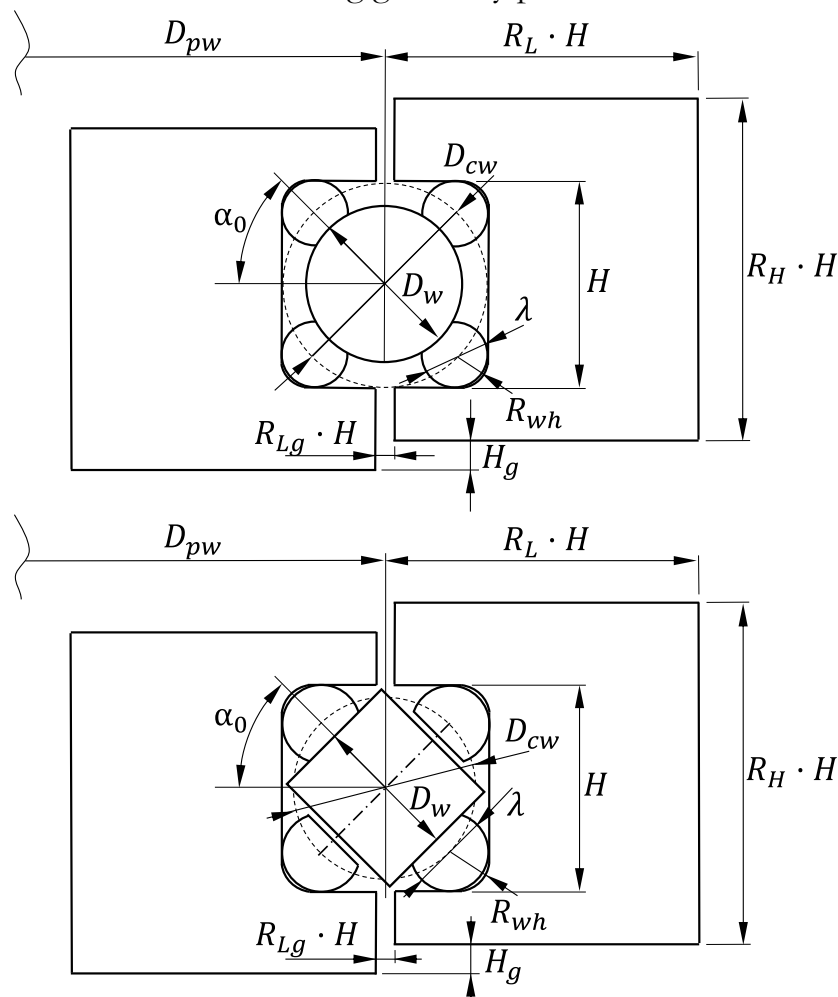
Figure 8.1 Four-point contact and crossed roller wire-race bearing cross-section.

Table 8.1 Ring coefficients and constant geometry parameters.

D_{pw}	α_0	Fill Factor	R_L	R_H	R_{Lg}	H_g
[mm]	[°]	[%]				[mm]
420	45	100	1.9	2.15	0.1	3

8.3 Design of Experiments

A 2 level full factorial design was considered to assess overall main and crossed effects, from which Pareto charts are built. Besides this, some additional design points were added to account for non-linearities and to simplify postprocessing. With all this, the DoE consisted of a total of 25 design points for ball bearings and 15 for roller bearings. The ranges of the geometrical parameters that appear in the matrices of experiments were defined from values found in commercial catalogues.
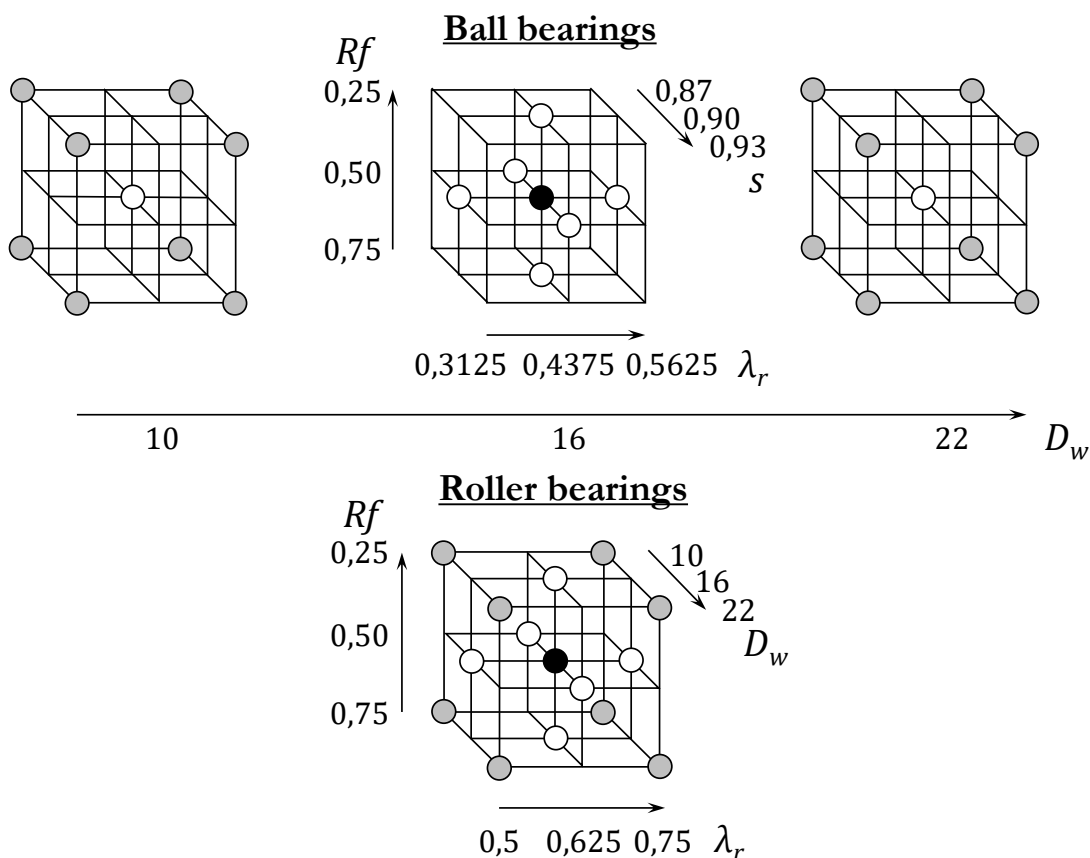
Figure 8.2 Matrices of experiments.

Figure 8.2 shows the matrices of experiments built for both bearing types, where a color code indicates the purpose of each design point. Grey points are

those regarding the 2 level full factorial design. Each black point corresponds to the reference bearing geometry and acts as a midpoint to account for possible non-linearities in main effects. White design points represent geometries where the main effects can be independently analyzed and observed.

8.4 Finite Element models

One multiparametric FE model for each bearing type was built in Ansys® to carry out the simulations of the DoE campaign. As previously mentioned, the study was limited to axial load case, so both load and symmetry are cyclic symmetric. This means only a half sector model with half a ball is enough for ball bearings, and a half sector model with two roller halves is enough for roller bearings. As usual, structural steel ($E = 200$ [GPa]) was assigned for rolling elements and wires, and aluminium ($E = 71$ [GPa]) for the rings. Chamfers or eventual roller crowning were not considered in the FE models, and neither were wire edge fillets, since there is no standard geometry for the wires so far. To this respect, Gunia and Smolnicki [159] proposed a wire-edge geometry correction. As mentioned in the literature review, this geometry correction reduced the stress concentrations due to edge effects, but the behaviour of the rest of the contact did not change significantly. This reduction of the stress concentration has important implications in bearing fatigue life, but does not affect the global behaviour of the contact; therefore nor does the response of the bearing in terms of load distribution or global deflections. Consequently, the FE model will predict when the contact reaches the limits of the raceway for the ball case, for example, but cannot calculate the real stress peaks. These areas are quite local and good results can be obtained at a certain distance from them.

Figure 8.3 shows the FE models developed for the study. It can be seen that the mesh is not exactly the same as the ones performed for other models presented in previous chapters. Nonetheless, it has been proven via mesh sensitivity analysis that all the FE models are equivalent in terms of accuracy regarding the evaluated performance indicators. In the current FE models some partitions were carried out on the geometry that allow meshing of different volumes of the same component with different mesh sizes and a continuous mesh. The DoF of the model changes from one case to another depending on the value of the geometrical parameters, but the total number is always around 1,500,000 DoF for both bearing types. Contacts are grease lubricated, so they were defined as frictional with a coefficient of friction of 0.1 [102,163,164]. The

Augmented Lagrange formulation was selected, letting the program automatically control the normal contact stiffness and updating it each iteration in order to achieve a maximum mesh penetration of 1 [μm].

While boundary conditions usually depend on the application or the surrounding structures, this work intends to be generalist and aims to study the local behaviour of the component. In this sense, rigid boundary conditions were imposed to the external faces of the rings and an external axial displacement was applied to those faces until the static load capacity was reached. This way, the effect of the parameters under study can be evaluated supressing the effect of the flexibility of the rings or the boundary conditions. The FE model is also more constrained, which improves the convergence and obtains better results to isolate the target effects defined in the study. Static load capacity values were calculated using the method developed in [13] for ball bearings and in [9] for roller bearings. Symmetry boundary conditions were also applied to the cyclic symmetric faces.

(a)

(b)
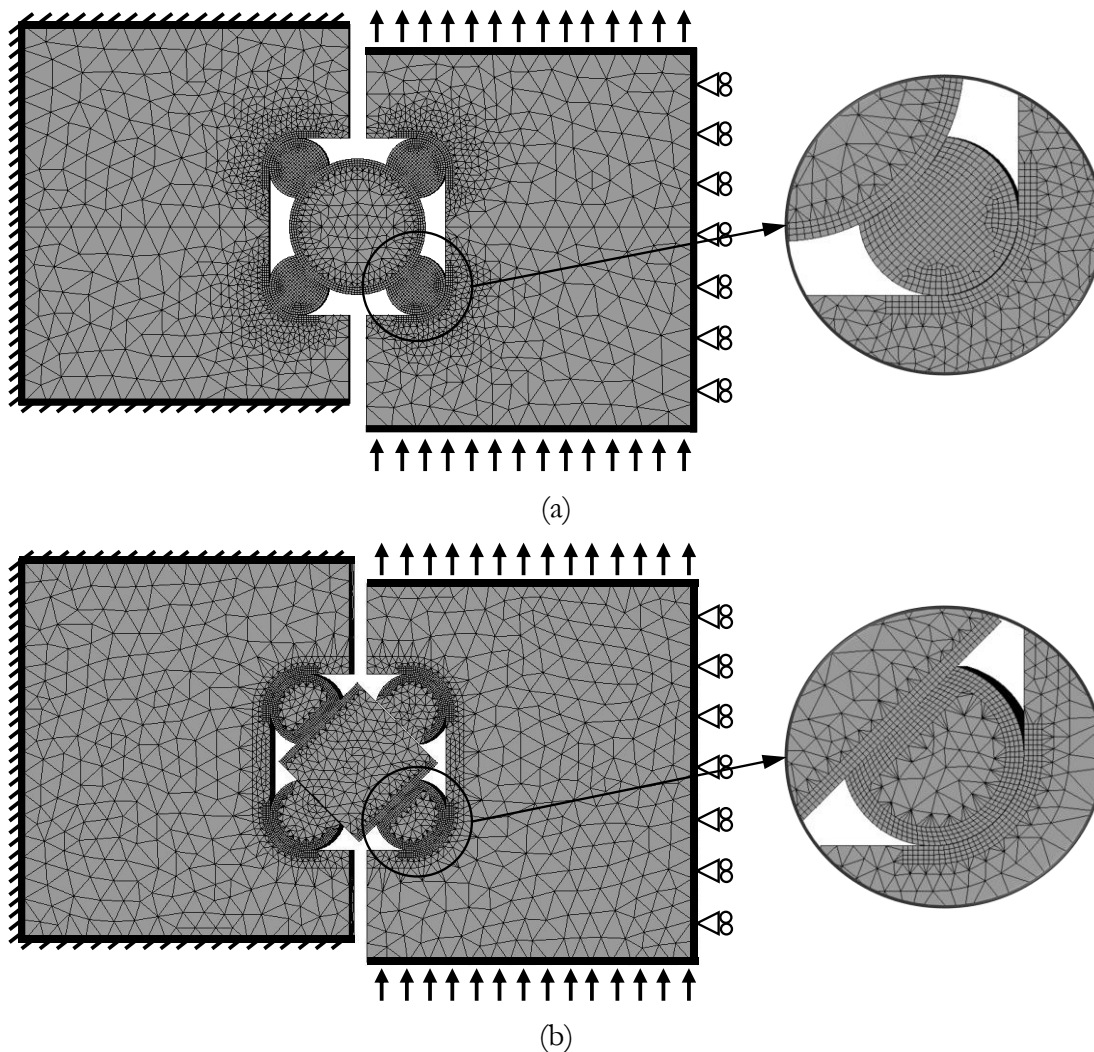
Figure 8.3 FE models: (a) Ball bearing (b) Roller bearing.

8.5 Results

With the FE analyses of the DoE campaign having been performed, it is time to process the results and evaluate the main and crossed effects. In order to assess the influence of the geometrical design parameters in the performance of the bearing, some performance indicators must be used. These performance indicators properly represent the structural behavior of the bearing and its capacity to support external loads. The selected indicators are the static load capacity, the bearing axial stiffness, the wire twist, the contact angle and the pressure contours along the contact major semi-axis. These performance indicators have been used throughout this document, so there is no need to define them. However, it is worth listing them. The first performance indicator is the static load capacity, which is calculated with the formulae proposed in the ISO-76 standard (Equation (1.1) and (1.2)) [24,25]. Contrarily, the other performance indicators were obtained from the FE simulations. Axial stiffness is the key performance indicator that represents the structural behaviour of the component. In order to evaluate the wire-roller-wire set, the contact angle and wire twist were also defined as performance indicators. Finally, pressure contours along the contact major semi-axis were obtained to evaluate the behaviour of the contact.

Since the study consists of two types of bearing, the results of each bearing type will be presented in separate sections. Each section starts with explanations about the relative weight of the main effects of each design parameter and the crossed effects among them on the overall values of the performance indicators. Crossed effects can have a significant effect on the performance indicators; a study of those crossed effects is necessary to ensure whether the conclusions obtained from the analysis of the main effects are sufficient or not. Then, those main effects are analysed for each performance indicator and finally, a brief summary of the main effects is provided.

8.5.1 Ball Bearings

Main and crossed effects

Figure 8.4 shows a summary of the main and crossed effects of the design parameters on the overall values of the performance indicators, where the summation of main and crossed effects equals 100%. It can be seen that crossed effects do not have a significant effect on the axial static load capacity and the stiffness, with a cumulative effect of 12% and 20% respectively. The summation

of the crossed effects for the wire twist amounts to 27%, which is also relatively low. Regarding the contact angle variation, the cumulative weight of the crossed effects rises up to 41%; this reveals a diffuse effect of the design parameters and this can be due, in part, to the inherent difficulty of establishing a proper overall value to represent the contact angle variation.
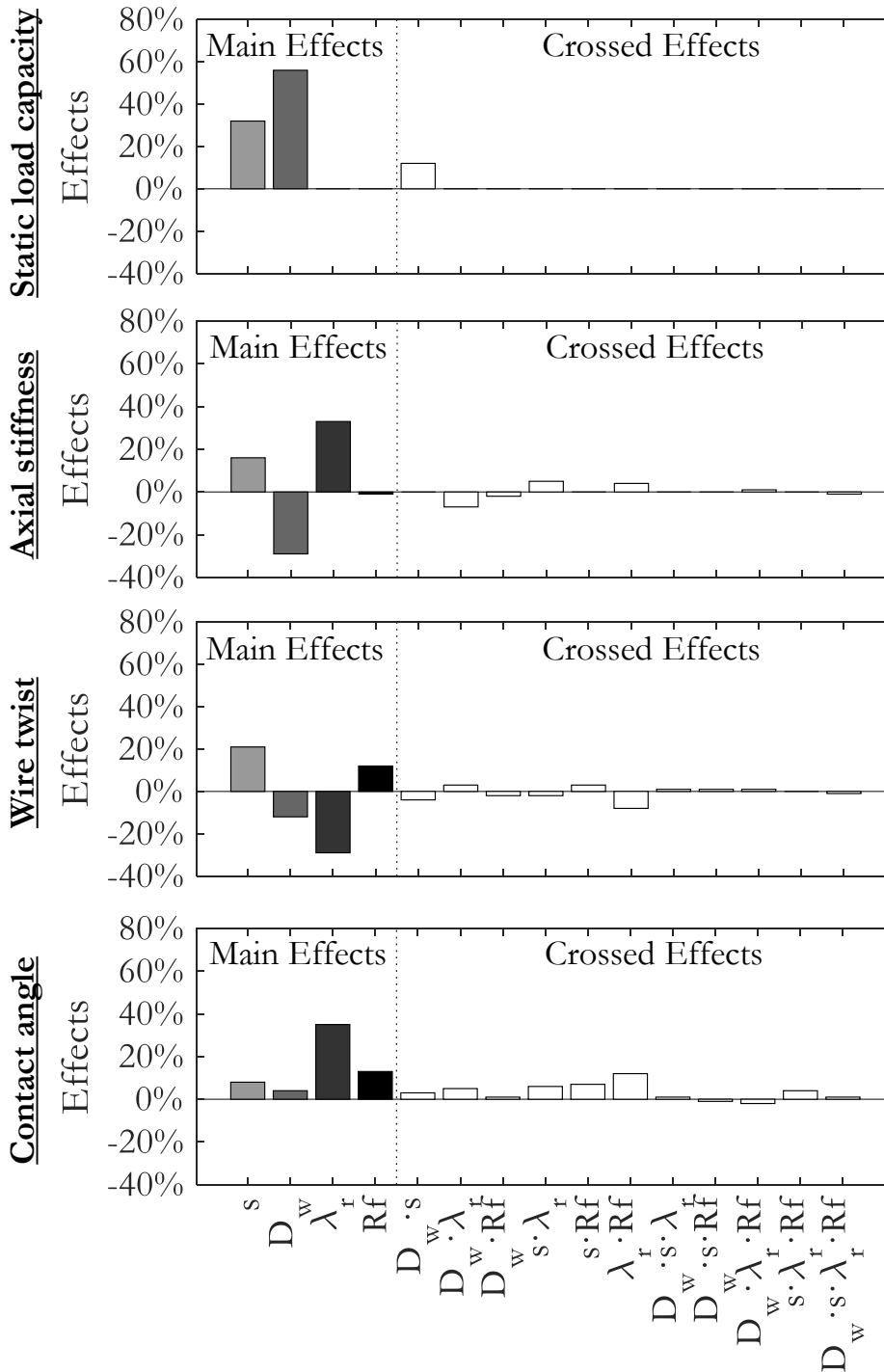

Figure 8.4 Ball bearing main and crossed effects.

Axial Static Load Capacity

In this section, the axial static load capacity according to the ISO-76 standard [24,25] is compared. The effect of the contact ellipse truncation cannot be calculated with this method but will be evaluated later. The axial static load capacity is a parameter that can be altered by changes in the osculation ratio (s) or in ball diameter D_w as can be seen in Figure 8.5. A more conformal contact can support more load before reaching the maximum allowable contact pressure. The same happens with a bigger ball diameter, but we must take account of the fact that a larger diameter involves a lower number of rolling elements. λ_r and Rf do not apparently affect the capacity, because they do not modify the geometry of the contact.

s	0.87	0.90	0.93
D_w	10	16	22
λ_r	0.3125	0.4375	0.5625
Rf	0.25	0.5	0.75
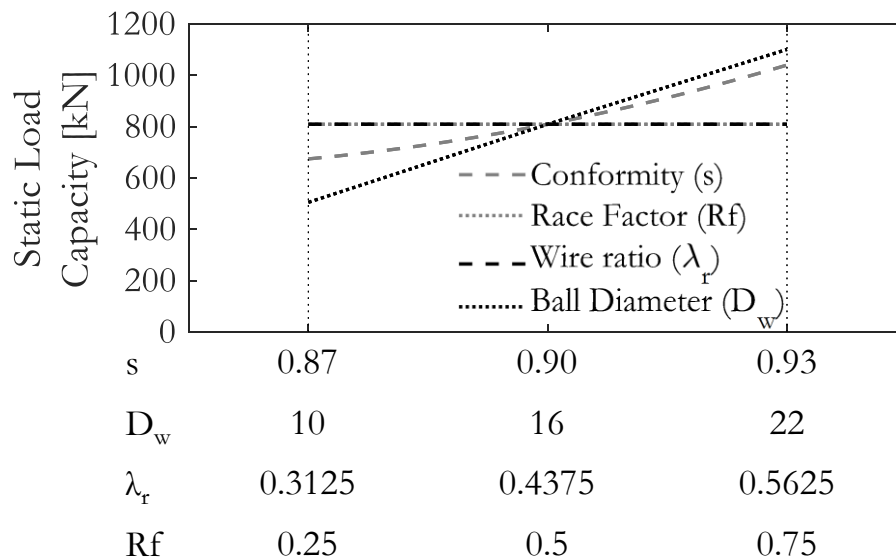
Figure 8.5 Ball bearing axial static load capacity.

Axial Stiffness

Figure 8.6 shows the stiffness curves for the different cases. As could be predicted, stiffness slightly increases with the osculation ratio, since a more conformal contact is stiffer. Rf does not affect the stiffness as it does not change the contact geometry. A higher λ_r involves a larger wire diameter, which makes the wire-ring contact stiffer. Finally, an increase in D_w results in a more flexible bearing. This effect comes from the reduction of the number of rolling elements. A contact with a larger ball is stiffer, but fewer contacts have to support higher contact forces for the same external applied force.
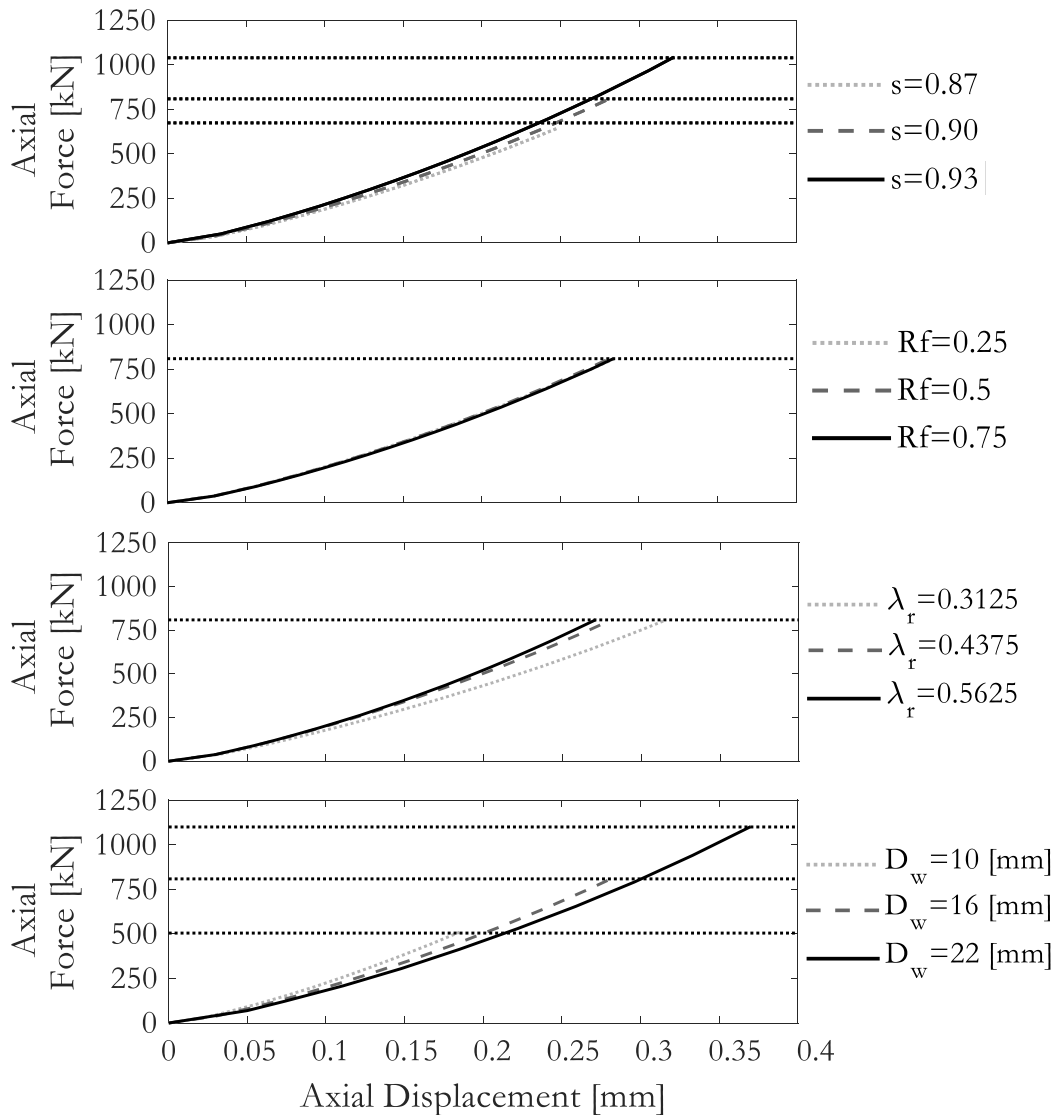
Figure 8.6 Ball bearing stiffness results.

Wire Twist

Figure 8.7 shows that larger osculation ratios result in wire twisting starting earlier, because in a less conformal contact the ball would not climb over the raceway as much. The race factor almost does not affect wire twist; however a slight difference can be seen near C_{0a}. This phenomenon happens because larger Rf values involve larger raceways, stimulating ball climbing and therefore a more off-centre contact ellipse that generates more wire twisting moment. The effect of increasing λ_r and D_w is the same since both of them modify the size of the housing (H). The smaller the size, the larger the wire twist for the same external applied displacement (Δ_{axial}) and vice versa, as can be seen in Figure 8.8, where (θ) is an angle related with the wire twist. Besides this, it has been proven that the wire twist varies proportionally with the inverse of D_w.
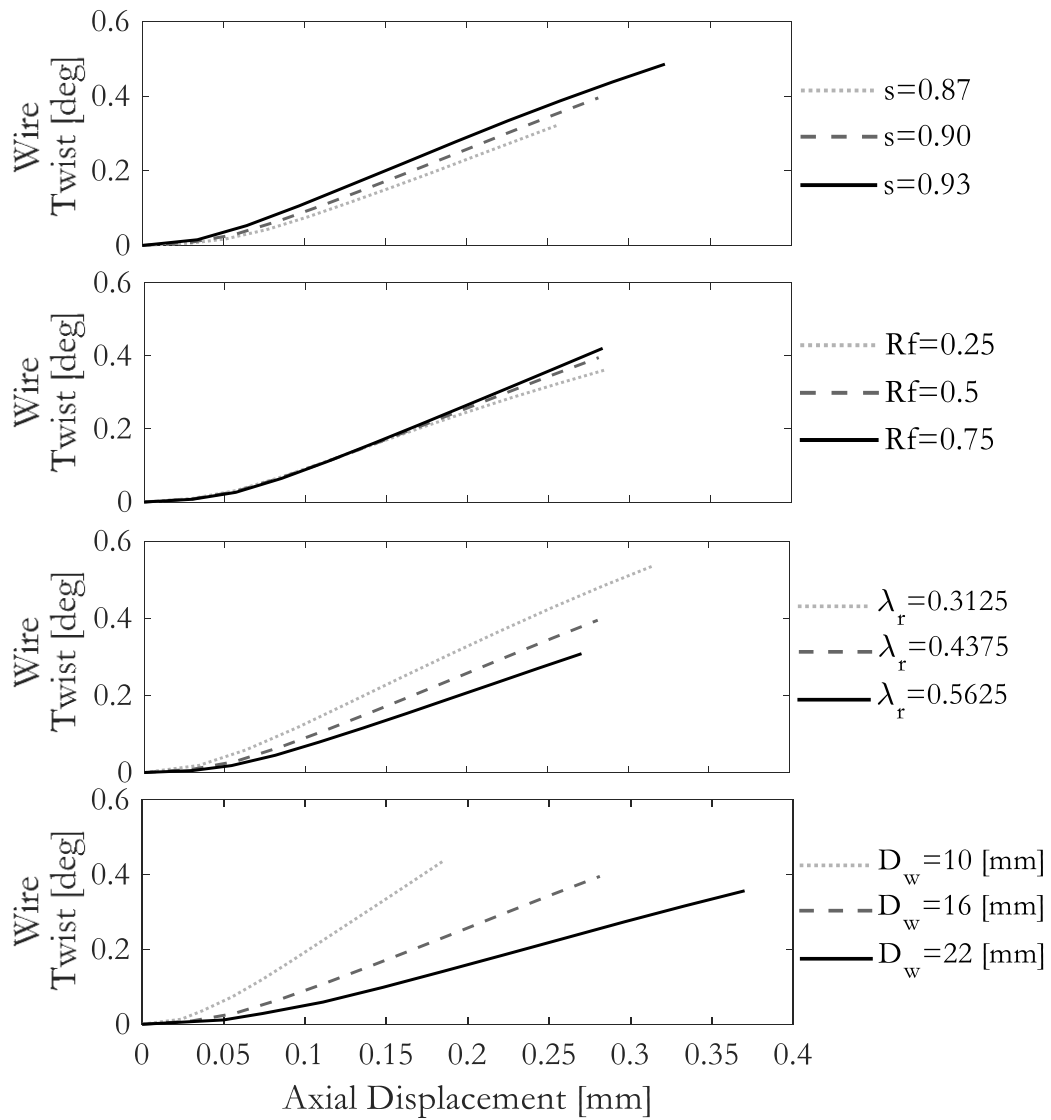
Figure 8.7 Ball bearing wire twist results.
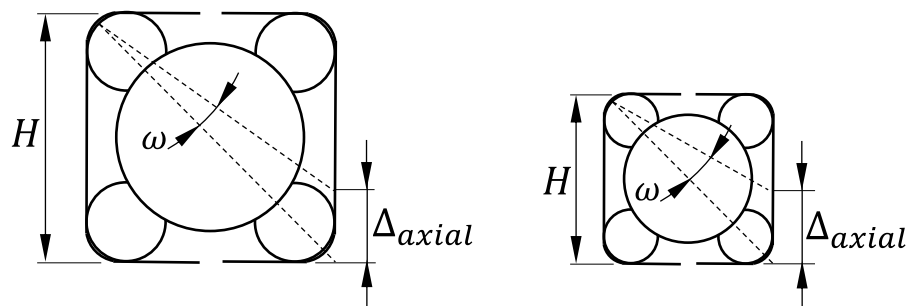
Figure 8.8 Effect of an external applied displacement in wire twist.

Contact angle

The contact angle is related to wire twist and to ball climbing phenomenon, as it can be derived from the plots in Figure 8.7 and Figure 8.9. As previously mentioned, larger osculation ratios result in the ball starting to climb over the raceway early followed by later stabilization because of the action of the wire

twist. Lower osculation ratios are less likely to climb over the raceway and for this reason the evolution of the curves is not as aggressive. The variation with Rf is similar at the beginning with a later deviation because of the wire twist. The increasing wire twist with the reduction of λ_r keeps the contact ellipse centred on the raceway, which results in a fairly constant contact angle. D_w seems to have almost no effect on the contact angle. Nevertheless, for smaller values, the ball tends to start climbing faster and the contact angle rises, which is later counterbalanced by the wire twist.
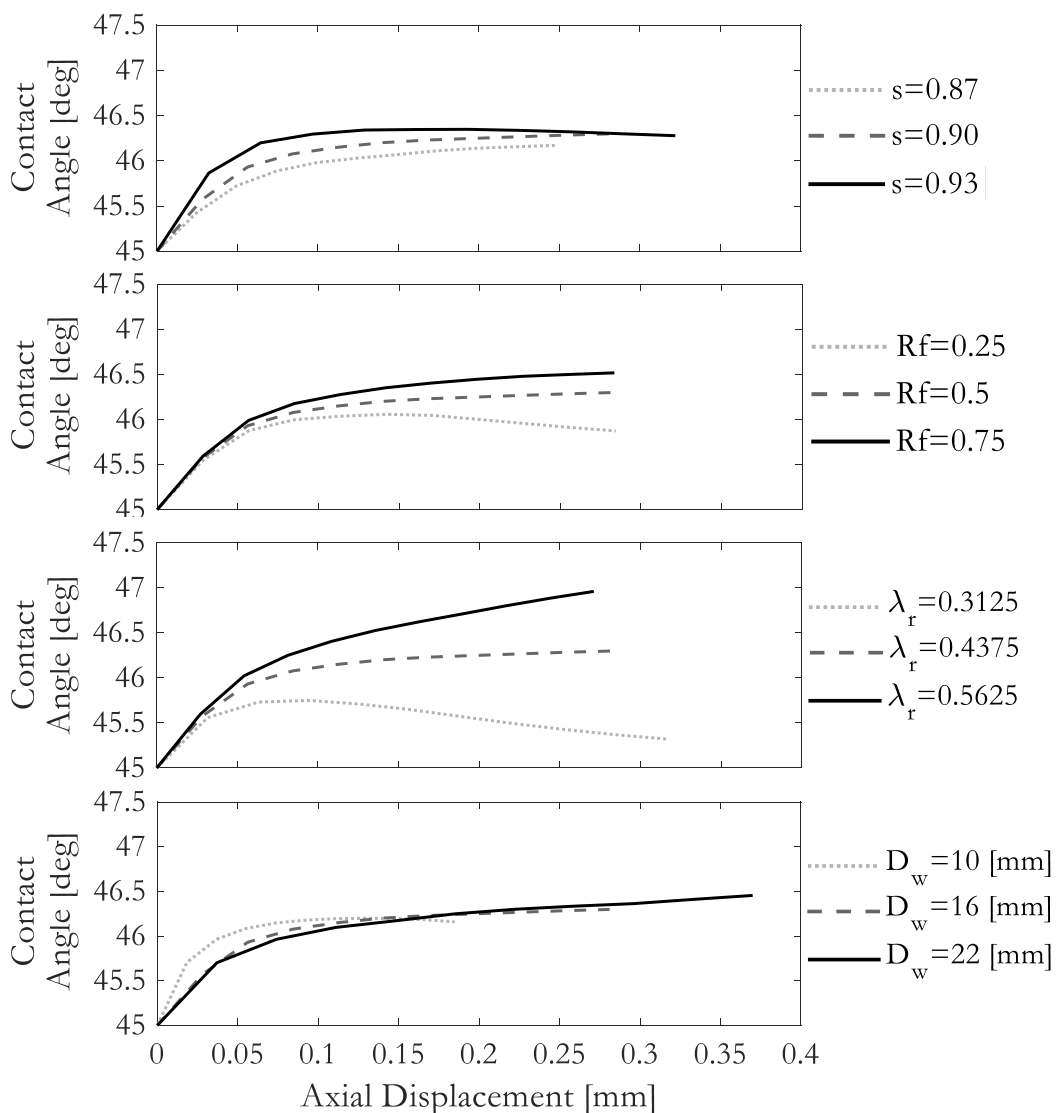
Figure 8.9 Ball-wire contact angle results.

Contact pressure contours

Pressure contours along the contact major semi-axis are relevant since they indicate whether the maximum allowable load pressure has been exceeded or if the contact ellipse has reached the raceway boundaries causing truncation. Note

that, in this case, truncation happens to be in the lesser loaded zone of the ellipse. For this reason, the pressure peaks are not as acute as could be expected on the edges. The osculation ratio appears to generate the expected behaviour, i.e., a more concentrated contact occurs with lower osculation ratio values. The effect of reducing the raceway with large values of Rf or small values of λ_r increases the risk of suffering ellipse truncation as can be observed in Figure 8.10b and Figure 8.10c. As a result of varying the values of D_w, it can be stated that the behaviour of the contact ellipse is identical but scaled. Another conclusion that can be drawn from these graphs is that the static load capacity calculated in [13] appears to be a good estimate, and that truncation can be a problem with certain small values of s, Rf or λ_r.
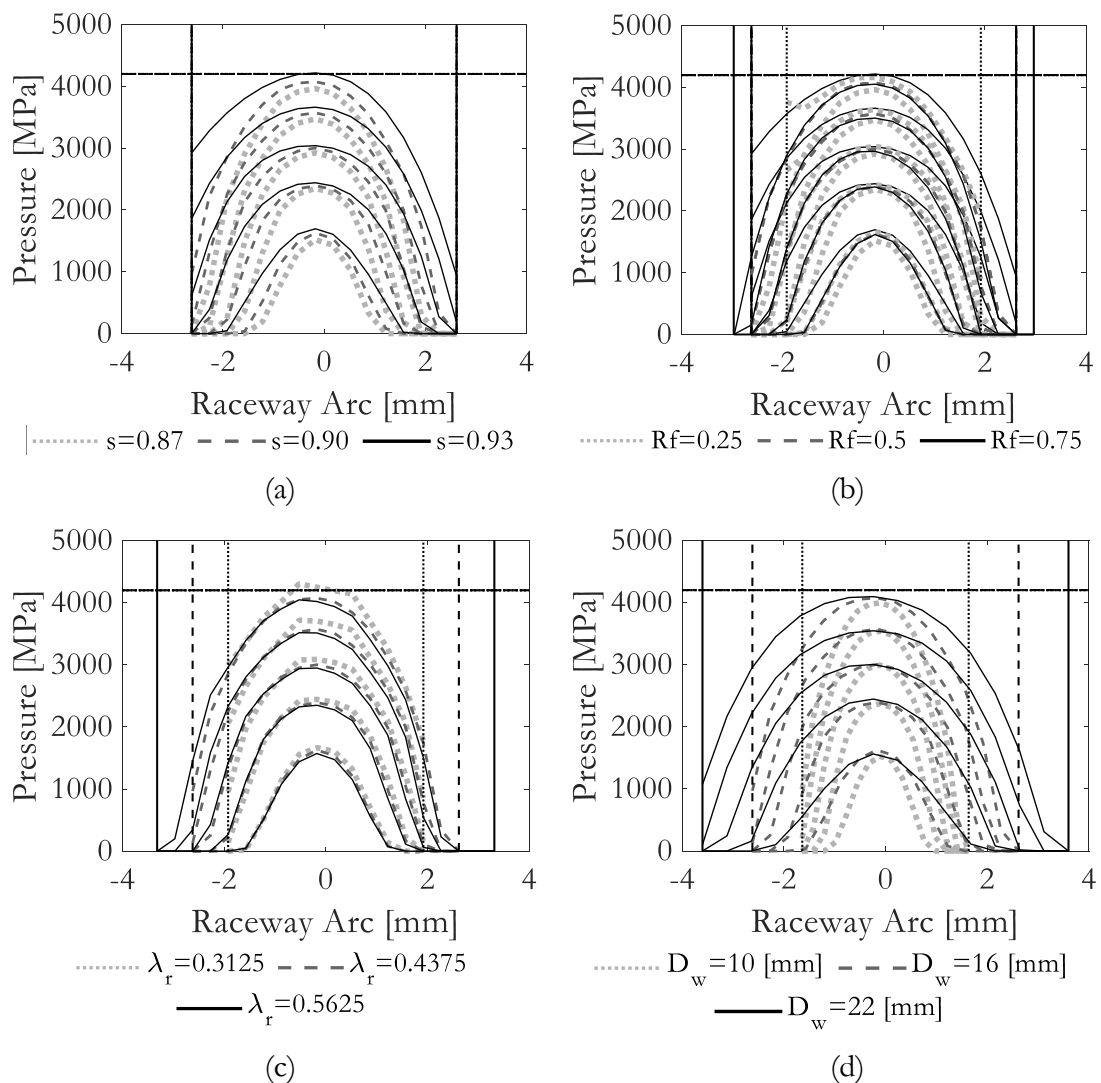
Figure 8.10 Ball bearing contact pressure results: (a) Osculation ratio (b) $\boldsymbol{Rf}$ (c) $\boldsymbol{\lambda_r}$; (d) Ball diameter.

8.5.2 Roller Bearings

Main and crossed effects

Figure 8.11 shows a summary of the main and crossed effects of each geometrical parameter in the overall values of the performance indicators, where the summation of main and crossed effects equals 100%. The summation of crossed effects is equal to or less than 20% for all performance parameters, specifically 20% for axial static load capacity, 11% for stiffness, 14% for wire twist and 17% for contact angle. For this reason, it can be said that the effect caused by crossed effects is low.
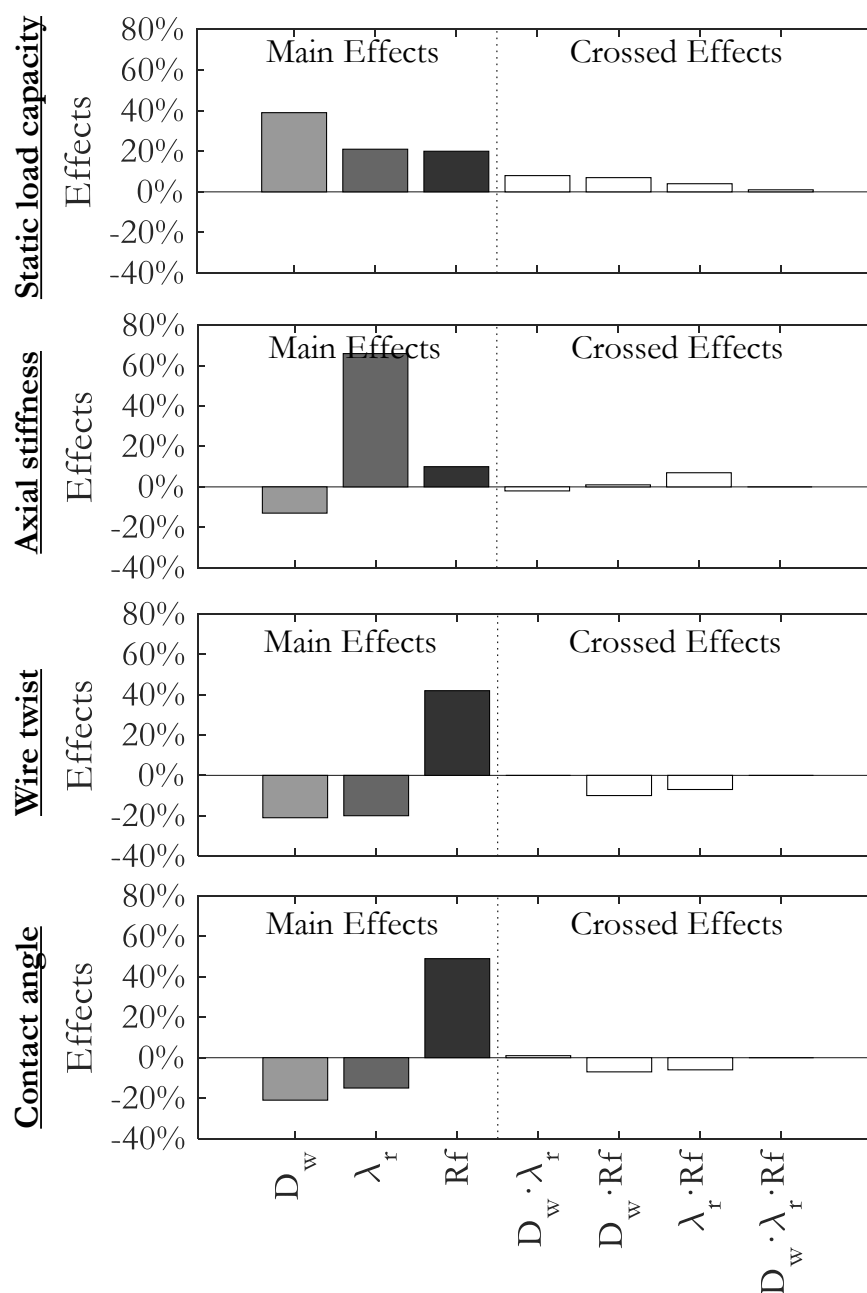
Figure 8.11 Roller bearing main and crossed effects.

Axial Static Load Capacity

This indicator depends on the contact geometry and is affected by all the studied parameters, because all of them modify the contact length. Rf and λ_r have less of an effect on C_{0a} compared with D_w, as shown in Figure 8.12.

Regarding the effect of varying D_w on the static load capacity, another important fact must be pointed out. In the DoE arranged for this study, the chosen design parameters were D_w, λ_r and Rf. But if the chosen parameters had been D_w, λ and Rf, a strange phenomenon would have occurred. A variation in D_w with constant λ and Rf does not have any effect on the static load capacity, so it cannot be considered as a valid strategy to increase the static load capacity. To prove this, the formula proposed in the ISO-76 standard [24,25] to obtain the static load capacity for conventional bearings can be analysed:

$$C_{0a} = 220 \cdot \left(1 - \frac{D_w \cdot cos(\alpha)}{D_{pw}}\right) \cdot N_R \cdot L \cdot D_w \cdot sin(\alpha) \qquad (1.2)$$

In the proposed situation, if λ and Rf remained constant, so would the contact length. Additionally, for slewing bearings the term in brackets is close to one, and D_w is inversely proportional to the number of rollers (N_R) with a constant fill ratio. This implies that an increase in one of them would result in a reduction in the other, maintaining the static load capacity constant.
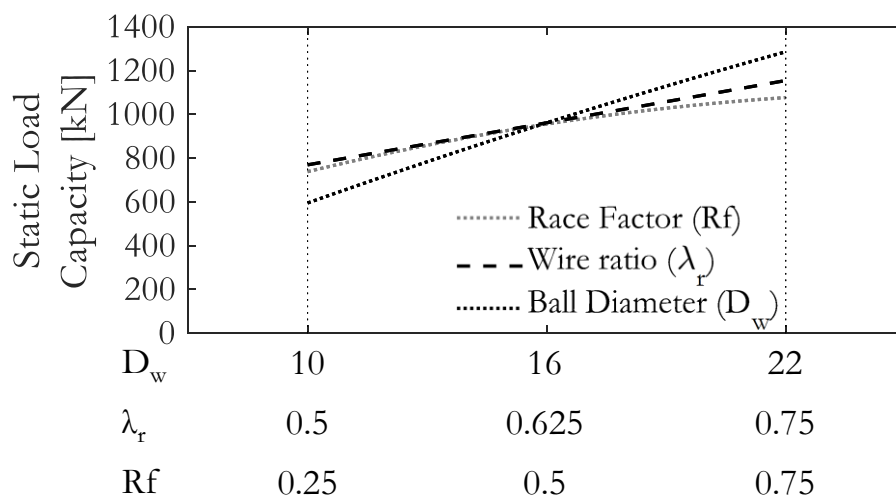
Figure 8.12 Roller bearing static load capacity.

Axial stiffness

Axial stiffness is affected by contact geometry: a roller raceway contact with a larger contact length is stiffer than another with a shorter one, as can be seen when Rf or λ increases. In terms of Rf, this phenomenon is non-linear since the relationship between Rf and the raceway length is also non-linear. For this reason, the $Rf = 0.25$ curve is more flexible than the other two, where the contact length is similar. Roller diameter seems to have little effect on axial stiffness; the effect of a more rigid contact with higher D_w is compensated for with less rollers.
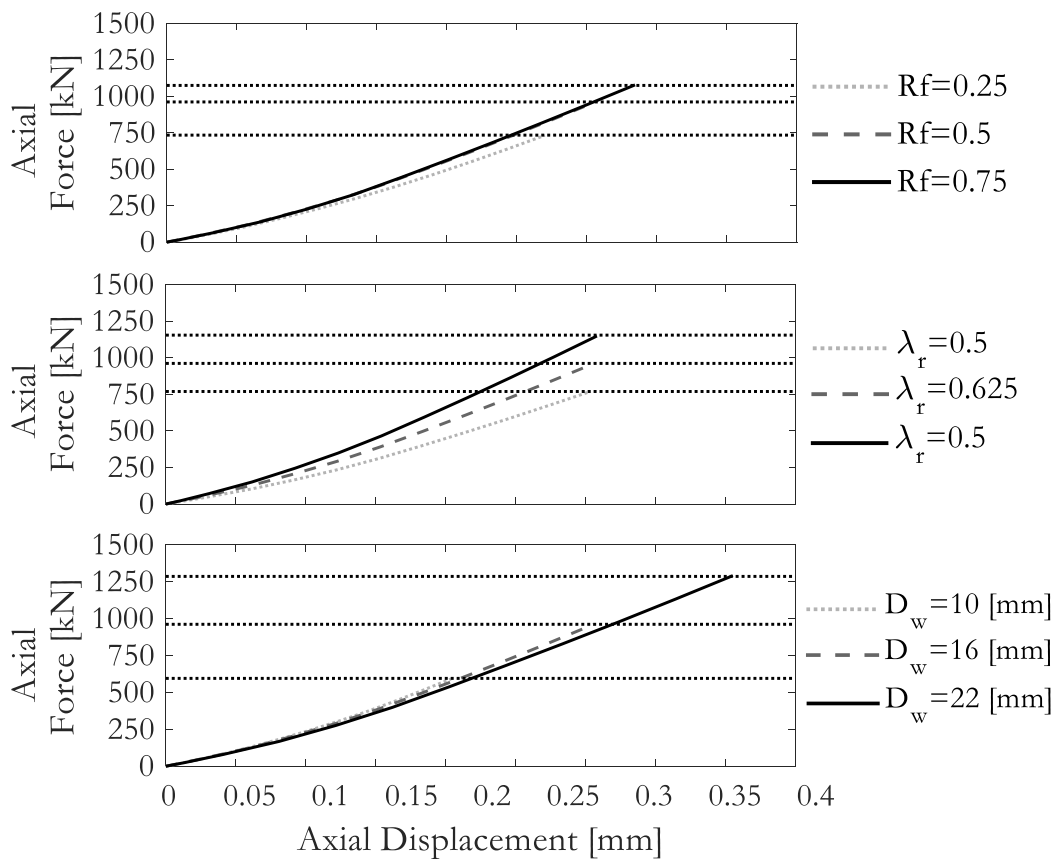
Figure 8.13 Roller bearing stiffness results.

Wire twist

Just as was the case with the ball bearings, if the wire-roller-wire set is smaller, for the same applied external displacement the set can twist more. This phenomenon can be seen in Figure 8.14, where every graph shows how wire twist is greater when the roller-wires set is smaller.
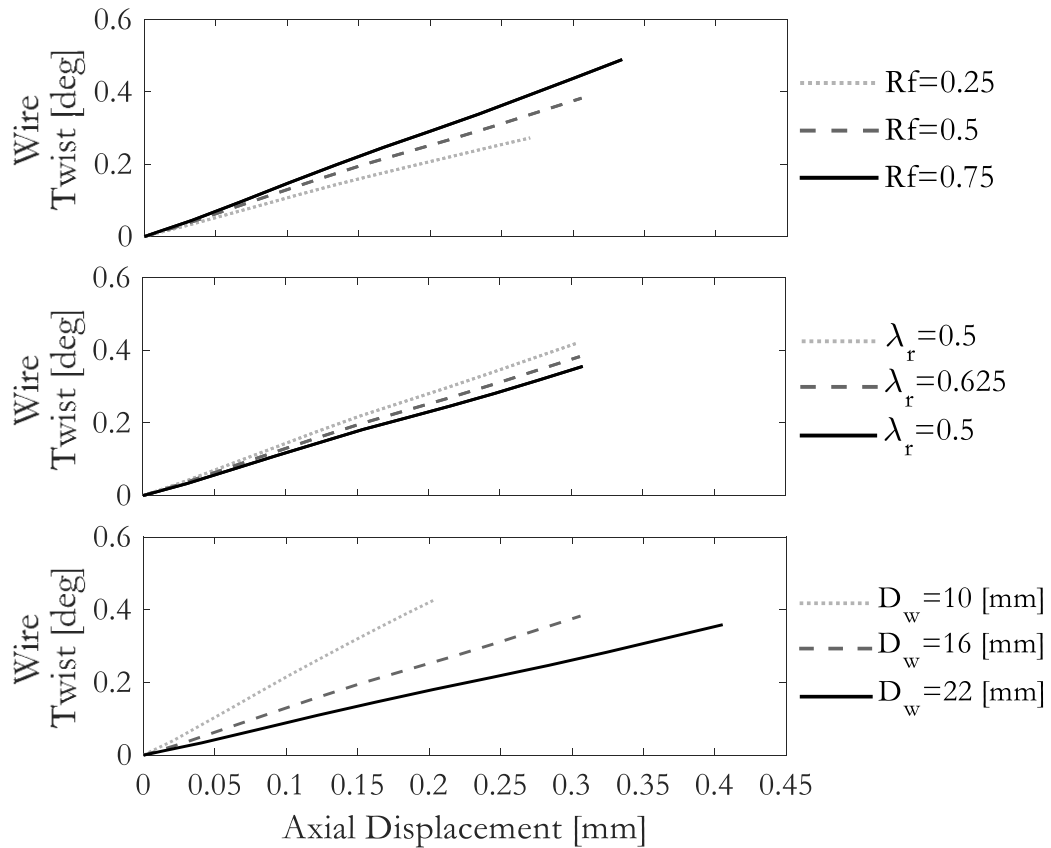
Figure 8.14 Roller bearing wire twist results.

Contact angle

The contact angle variation shown in Figure 8.15 is so closely related to wire twist, that the wire twist values are almost the same as the contact angle variation values. This small deviation comes from the deformation of the roller-wire contact.
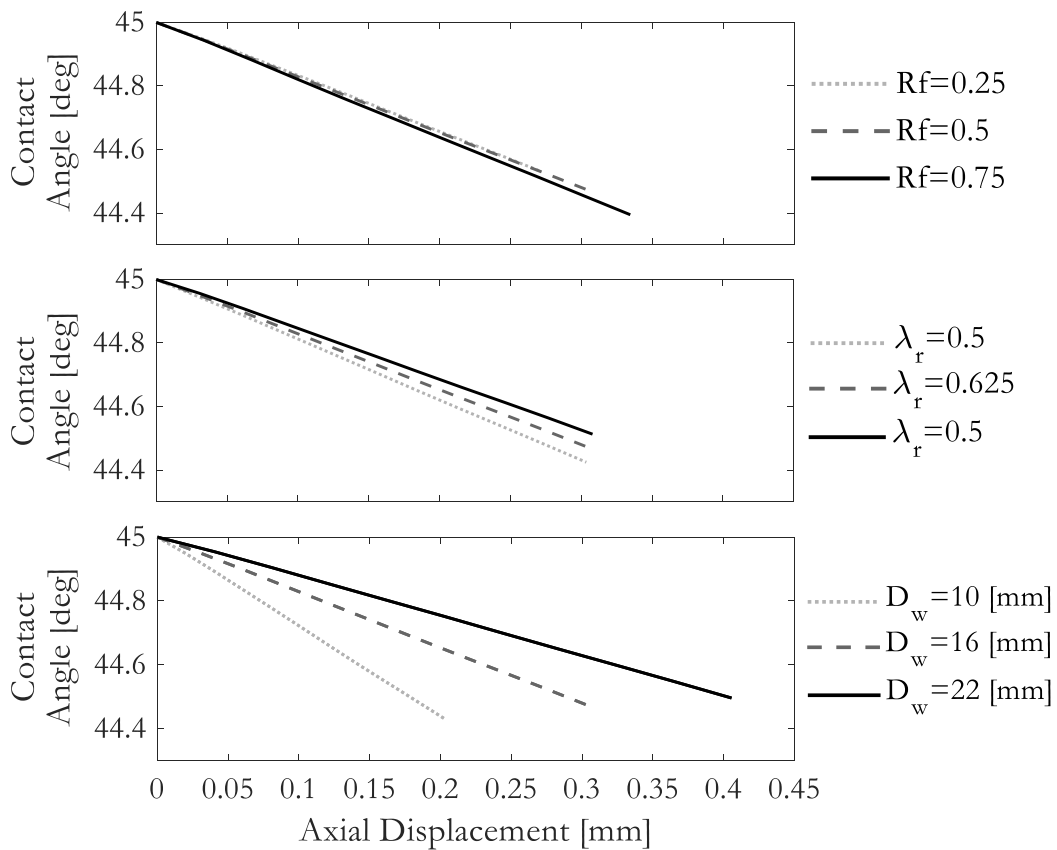
Figure 8.15 Roller contact angle results.

Contact pressure contours

This section presents the pressure lines along the longitudinal axis of the contact patch during the loading process. On roller bearings, the contact is always truncated in the direction of the major semi-axis. In this sense, even though very large non-realistic pressure peaks appear in Figure 8.16 due to linear material assumption, this does not imply that these peaks do not exist. Indeed, the free edges of the wire exert some pressure peaks in the location of the wire edges. However, these pressure peaks can be avoided to a great extent with edge filleting and slight crowning.

Regarding the results, identical behaviour is observed in all cases, where friction generates a tangential force on roller-wire contact that tilts the pressure lines. As a result, the maximum pressure reaches and surpasses the maximum allowable limit. The appearance of this kind of phenomena can be expected but not predicted using the analytical model in [9], since it assumes that the contact angle remains constant at 45 [°] and that the contact force is evenly distributed.
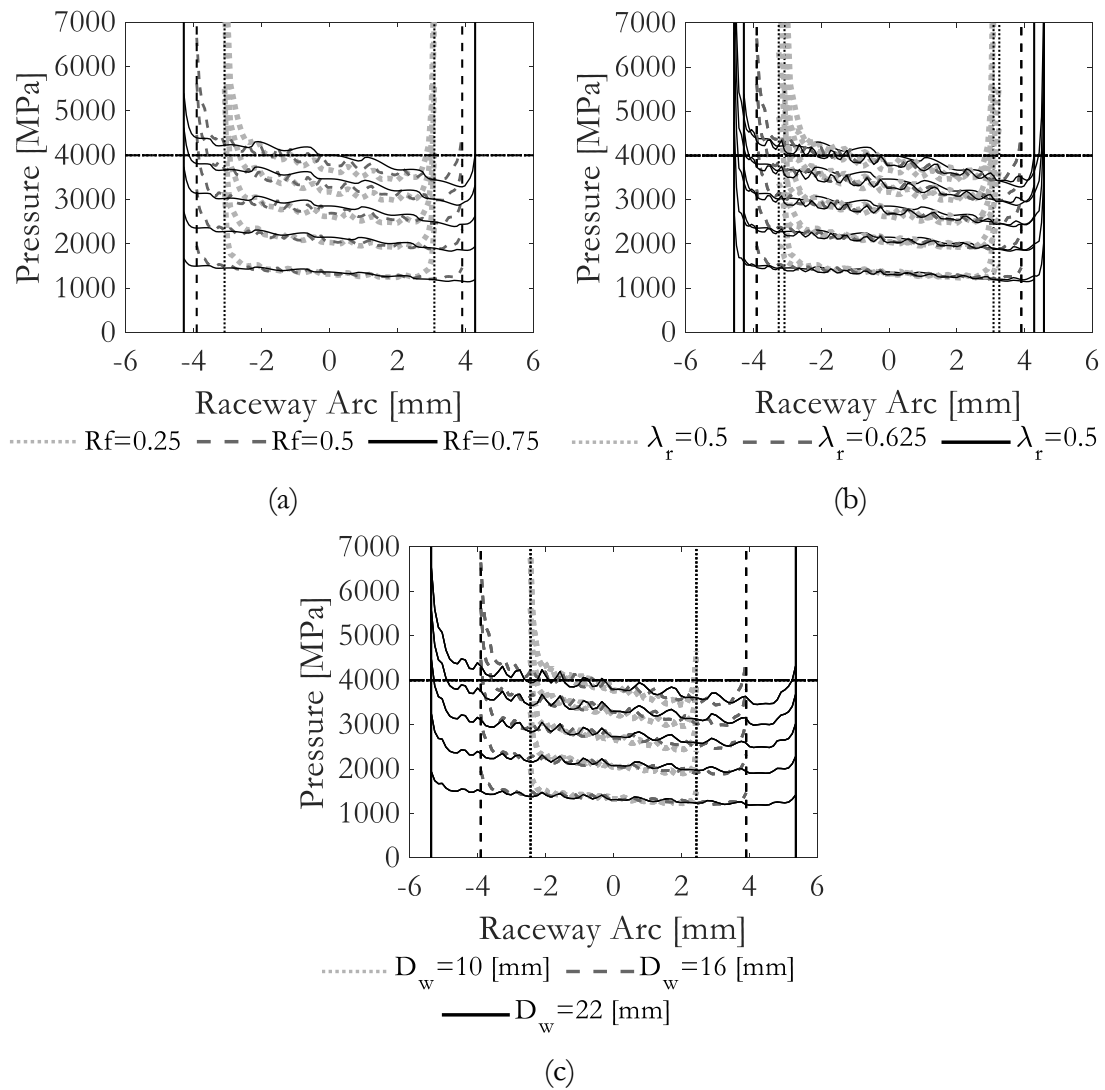
Figure 8.16 Roller bearing contact pressure results: (a) Rf; (b) λ_r; (c) Roller diameter.

8.5.3 Results summary

All the results presented in this section are compiled in Figure 8.17 and Figure 8.18 for ball and roller bearings respectively. These plots compare the overall performance indicators of the reference case with the ones where a single parameter was increased or decreased, providing a graphical presentation of how much the variation of a geometrical design parameter affects the overall value of each performance indicator.

Ball bearings

On ball bearings, axial static load capacity is only affected by the osculation ratio and ball diameter, with a significant variation. Overall stiffness constant retrieved a slight increase with high values of s and λ_r and low values of D_w. The overall contact angle seems to increase with all studied parameters,

especially with λ_r. Overall wire twist is not affected as much by studied parameters. Contact angle variation is not so closely related to wire twist since the ball climbing phenomenon has a significant contribution. In addition to this, non-linearities are observed for some design parameters on some performance indicators and the most evident ones are: the effect of s on the axial load capacity, the effect of λ_r on the stiffness, and the effect of s and Rf on the contact angle.
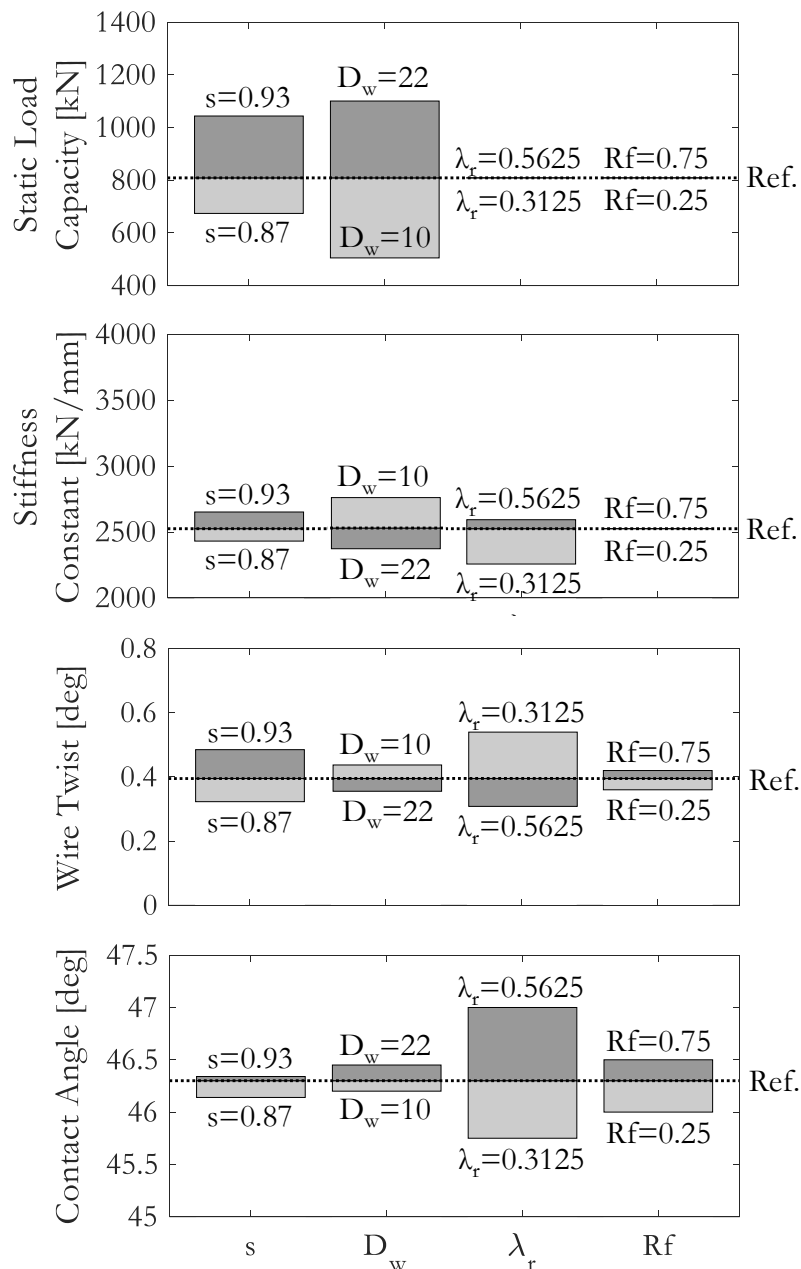
Figure 8.17 Effect of the design parameters on ball bearing performance.

Roller bearings

Axial static load capacity suffers important variations with all geometrical parameters because of the contact length increase or decrease. On the one hand, stiffness does not change significantly with roller diameter. The effect of increasing the contact length is compensated with the reduction in the roller number. On the other hand, λ_r and Rf directly affect the roller-wire and wire-ring contact geometry, which contribute to the stiffness fluctuations. Variations in contact angle and wire twist are closely related with a small deviation caused by roller-wire contact deformation. In addition to this, non-linearities are observed for some design parameters on some performance indicators, with the most evident being the effect of Rf on the axial load capacity and the stiffness, and the effect of D_w on the wire twist.
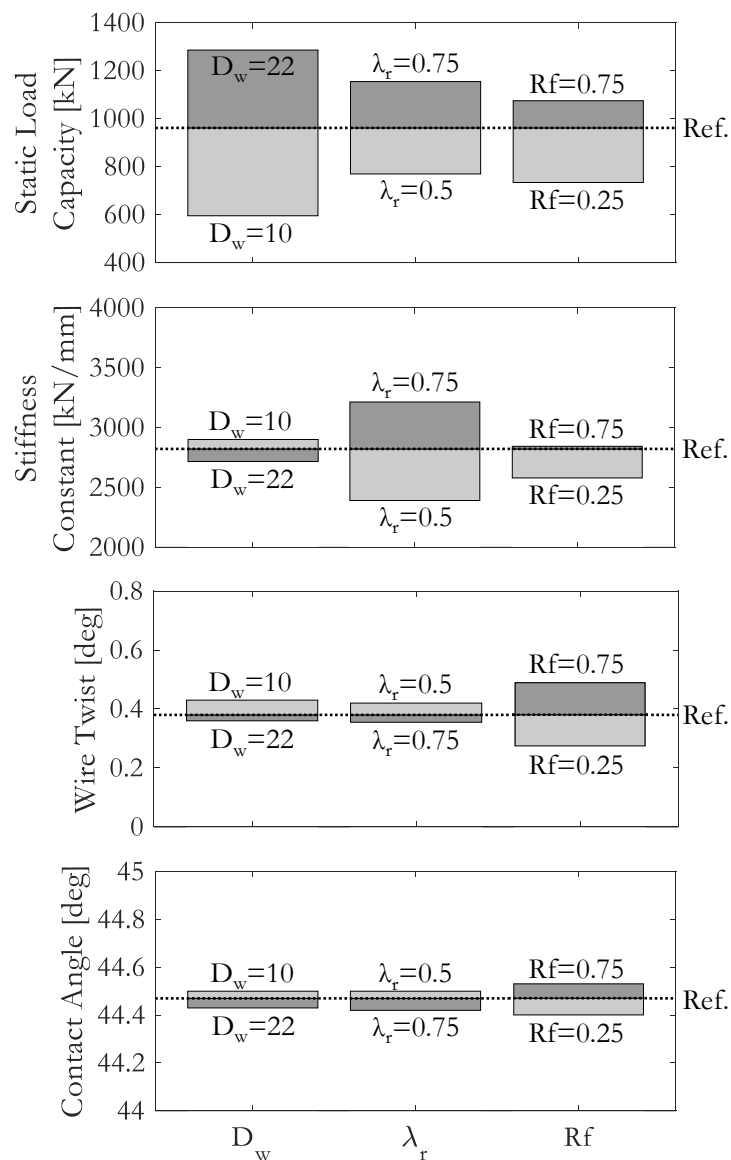
Figure 8.18 Effect of the design parameters on roller bearing performance.

9 Conclusions and future work

9.1 Conclusions

The main conclusions drawn from the research work carried out in this Doctoral Thesis are presented in this final section. Keeping in line with the document, the conclusions are listed following the same order as the previous chapters.

- The study of the static structural response of four-point contact slewing bearings revealed that the wire twisting phenomenon, i.e. the rotation of the wire cross-section under external load, has a significant effect on bearing performance. This phenomenon keeps the ball-raceway contact centred on the wire raceway so that contact truncation is avoided. For this reason, adequate lubrication of the wire-ring contact is crucial. Incorrect lubrication of this contact may impede wire twisting and will lead to contact truncation. Attention must be also paid to the osculation ratio, since high osculation ratio values combined with small raceways can also result in truncation problems. Regarding the comparison with conventional slewing bearings, the additional contacts and the aluminium rings reduce the stiffness of the component. Besides this, eventual truncation problems can arise if the osculation ratio is high and the boundary conditions are flexible enough.

- An engineering formula was developed to obtain the twisting stiffness of the race-shaped wire that can be found in four-point contact wire-race bearings. The proposed formula was elaborated based on an evidence-based deformation assumption at a differential level for the section of the wire. After the integration and mapping process, the formula was tuned as a function of the principal wire geometrical parameters. Finally, the accuracy of the proposed formula was assessed by comparisons with equivalent FE results.

- A four-point contact wire-race slewing bearing analytical formulation to perform structural calculations under axial, tilting moment loads or a combination of both under rigid rings boundary conditions was proposed. This formulation was based on representing the physical phenomena that occur in one sector of the bearing under this type of loading. The stiffness and the status of the contacts were also key aspects to take into consideration. In this regard, the limitations in terms of representing the wire-ring contact status lead to only consider the axially loaded sector situation. As a result, a non-linear system of equations is reached, which represents the structural response of one sector of the bearing with one rolling element. The response of the whole bearing is obtained from the summation of all sector results. Analytical and FE results were compared in order to validate the analytical formulation, obtaining good agreement between them.

- Another analytical formulation was proposed for crossed-roller wire-race slewing bearings. The analytical formulation development process is very similar to the previous one, also considering that each sector is independent of each other. However, in this case, axial and radial loads can be applied to the bearing sectors, which allows any combination of loads to be applied to the whole bearing. After defining some assumptions, an analytical formulation based on non-linear equations was developed to represent the structural behaviour of one bearing sector. The proposed approach works not only for the rigid rings assumption, but the flexibility of the rings can also be considered. As the final objective consisted of developing an analytical calculation tool, the formulation was implemented on a simulation algorithm. On the one hand, this algorithm can be used to calculate the stiffness and the static load capacity of any bearing geometry within a certain design space. On the other hand, the load distribution problem can be also solved. However, an optimization process had to be carried out in the calculation process. Finally, a validation by means of a FE results comparison was successfully performed.

- The EF models, in whose results the basis of the developed analytical approaches rests on, were experimentally validated. FE models were used to study the behaviour of the wire-race bearings and to validate the accuracy of the analytical models. Because of this, their accuracy had to be proven. To this end, an experimental test campaign was

carried out on a tension-compression test bench for four specimens of two bearing designs. Axial stiffness results showed that a lack of bolt preload during the assembly process increased the scatter and lead to more flexible behaviour. Slight non-linear behaviour was also observed at the beginning of the loading process, which could be caused by manufacturing errors. Finally, the experimental and the FE results for both bearing designs were very much in line with each other.

- In spite of the versatility and accuracy of the FE models, the related computational cost is high and convergence problems are likely to arise. In order to address these drawbacks, several wire-race bearing FE modelling strategies were proposed and validated via a results comparison with reference FE models. Regarding four-point contact wire-race bearings, the efficient strategy proposed by Daidié for conventional slewing bearings was implemented. This strategy consisted of replacing the balls with a mechanism composed of rigid beams and a non-linear spring that simulates the stiffness of the contacts. After some modifications, it gave excellent results with improved efficiency. Moreover, two other efficient FE modelling strategies were proposed for crossed roller wire-race bearings. The first one consisted of implementing the analytical formulation developed in this thesis in a FE model by means of user-defined elements, which replace the wires and the rollers. The second alternative consisted of replacing these elements by non-linear springs. Both alternatives showed good agreement and excellent efficiency, with the most beneficial case being 100 times less time consuming than the reference FE models. It is also worth mentioning that the first alternative is slightly more accurate but more tedious to implement.

- Finally, some design guidelines for four-point contact and crossed-roller wire-race bearings were proposed. Firstly, a DoE based on FE analyses of both bearing configurations under axial load was performed. Then, main and crossed effects of the design parameters were evaluated and the design guidelines were consequently deduced. In the case of four-point contact wire-race bearings, static load capacity is only affected by contact geometry parameters such as the osculation ratio and the ball diameter. It rises as any of the two parameters increases. Axial stiffness does not change significantly with any parameter. Contact angle variation increases with all the parameters,

but more abruptly with the wire diameter. Wire twist increases with the osculation ratio and the size of the raceway, while it decreases with the ball and wire diameter. Regarding crossed roller wire-race bearings, it increases as all parameters do. Axial stiffness is mainly affected by the wire diameter. It increases as the wire diameter increases. Contact angle variation and wire twist increase in line with the size of the raceway and slightly decrease with the roller and wire diameter.

9.2 Future work

As a result of the work conducted in this Doctoral Thesis, various research lines were left open as possible future work. Some of these alternatives are proposed in the following points:

- Comparing the structural behaviour of crossed roller wire-race bearings with the equivalent conventional slewing bearings.

- Developing the current four-point contact wire-race slewing bearing analytical model so radial loads can be applied. The performance of the ball wire-race slewing bearing analytical model could be improved if the flexibility of the rings is considered. In addition to this, a simulation algorithm could be built in order to create an analytical simulation tool. Also to this regard, other four-point contact wire-race slewing bearing analytical model alternatives could be studied. Some ideas are proposed in Figure 9.1, where the tangential behaviour of the wire-ring contacts can be included or the wire structural behaviour better represented.
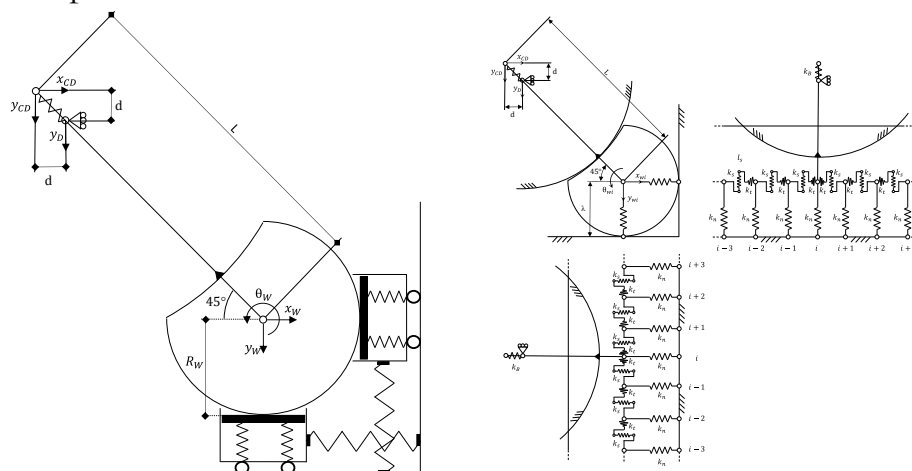
Figure 9.1 Proposed alternatives for future ball wire-race bearings analytical models.

- Studying the effect of the manufacturing errors on the performance of the bearing. The manufacturing errors could also be included in the analytical models for bearing calculations.

- A more efficient FE modelling strategy could be developed for ball wire-race slewing bearings if the wire-ring contacts are included in the simplification, as has been done for crossed roller wire-race bearings.

- Studying the wire edge effects thoroughly and developing some wire edge corrections for crossed-roller wire race bearings.

9.3 Derived research publications

As a result of the research work presented in this Doctoral Thesis, the following research articles were published in high impact factors scientific journals:

- Martín, I. Heras, J. Aguirrebeitia, M. Abasolo, I. Coria, Static structural behaviour of wire bearings under axial load: Comparison with conventional bearings and study of design and operational parameters, Mech. Mach. Theory. 132 (2019) 98–107.
  DOI: 10.1016/j.mechmachtheory.2018.10.016

- J. Aguirrebeitia, I. Martín, I. Heras, M. Abasolo, I. Coria, Wire twisting stiffness modelling with application in wire race ball bearings. Derivation of analytical formula and finite element validation, Mech. Mach. Theory. 140 (2019).
  DOI: 10.1016/j.mechmachtheory.2019.05.012

- Martín, I. Heras, I. Coria, M. Abasolo, J. Aguirrebeitia, Structural modeling of crossed roller wire race bearings: Analytical submodel for the roller-wire-ring set, Tribol. Int. (2020) 106420.
  DOI: 10.1016/j.triboint.2020.106420

- Martín, I. Heras, J. Aguirrebeitia, L.M. Macareno, Influence of the geometrical design on ball and crossed roller wire race bearing behavior under axial load, Tribol. Int. 156 (2021).
  DOI: 10.1016/j.triboint.2020.106817

- Martín, J. Aguirrebeitia, I. Heras, M. Abasolo, Efficient Finite Element modelling of crossed roller wire race slewing bearings, Tribol. Int. 161 (2021).
  DOI: 10.1016/j.triboint.2021.107098

Furthermore, other advances in the scope of wire-race slewing bearings were presented in national and international congresses:

- J. Aguirrebeitia, M. Abasolo, I. Heras, I. Coria, I. Martín, Limitaciones en la aplicación de procedimientos de cálculo y selección de rodamientos con pista de rodadura alámbrica, XXII Congreso Nacional de Ingeniería Mecánica, 19-21 September 2018, Madrid, Spain, 1358-1364. ISSN: 0212-5072

- I. Martín, I. Heras, J. Aguirrebeitia, M. Abasolo, I. Coria, Analytical Model for the Estimation of Axial Stiffness and Contact Results in Wire Race Ball Bearings, in: T. Uhl (Ed.), Adv. Mech. Mach. Sci. Proc. 15th IFToMM World Congr. Mech. Mach. Sci., Springer International Publishing, Cham, 2019: pp. 3873–3882.
  DOI: 10.1007/978-3-030-20131-9_384

- I. Martín, I. Heras, I. Coria, M. Abasolo, J. Aguirrebeitia, Herramienta de cálculo para rodamientos de alambre de rodillos cruzados: Algoritmo de resolución e implementación. XXIII Congreso Nacional de Ingeniería Mecánica. 20-22 de October 2021, Jaén, Spain. ISSN: 0212-5072.

References

[1]   Franke GmbH, Wire Race Bearings for Lightweight Design. Aluminum, 3D-Printing and Carbon CFRP, (2017).

[2]   SKF Group/Kaydon Corporation, WireRace and inserted raceway bearings for weight savings and consistent friction torque brochure, (2018).

[3]   Rothe Erde GmbH, Rothe Erde wire-race bearings. The proven bearing concept., n.d.

[4]   KMF Kunststoff-Metall-Formteile GmbH, Wire ball bearing catalogue, (n.d.).

[5]   Franke GmbH, Brochure: Why Wire-Race Bearings?, (2013).

[6]   Franke GmbH, Light Bearings for Innovation, 2018.

[7]   ADM Research group of the University of the Basque Country webpage, (n.d.). https://www.ehu.eus/en/web/mechanical-design/about-us.

[8]   J. Aguirrebeitia, R. Avilés, I. Fernández de Bustos, M. Abasolo, Calculation of General Static Load-Carrying Capacity for the Design of Four-Contact-Point Slewing Bearings, J. Mech. Des. 132 (2010) 064501. https://doi.org/10.1115/1.4001600.

[9]   J. Aguirrebeitia, M. Abasolo, R. Avilés, I. Fernández de Bustos, General Static Load Capacity in Slewing Bearings. Unified Theoretical Approach for Crossed Roller Bearings and Four Contact Point Angular Ball Bearings ., 13th World Congr. Mech. Mach. Sci. 19-25 June. (2011) 19–25.

[10]   J. Aguirrebeitia, M. Abasolo, R. Avilés, I. Fernández de Bustos, General static load-carrying capacity for the design and selection of four contact point slewing bearings: Finite element calculations and theoretical model validation, Finite Elem. Anal. Des. 55 (2012) 23–30. https://doi.org/10.1016/j.finel.2012.02.002.

[11]   J. Aguirrebeitia, J. Plaza, M. Abasolo, J. Vallejo, General static load-carrying capacity of four-contact-point slewing bearings for wind turbine generator actuation systems, Wind Energy. (2013). https://doi.org/10.1007/s00393-017-0297-1.

[12]   J. Aguirrebeitia, M. Abasolo, R. Avilés, I. Fernández de Bustos, Theoretical calculation of general static load-carrying capacity for the design and selection of three row roller slewing bearings, Mech. Mach. Theory. 48 (2012) 52–61. https://doi.org/10.1016/j.mechmachtheory.2011.09.003.

[13]   J. Aguirrebeitia, J. Plaza, M. Abasolo, J. Vallejo, Effect of the preload in the general static load-carrying capacity of four-contact-point slewing bearings for wind turbine generators: theoretical model and finite element calculations, Wind Energy. 17 (2014) 1605–1621. https://doi.org/10.1002/we.1656.

[14]   M. Abasolo, I. Coria, J. Plaza, J. Aguirrebeitia, New selection curves for four contact point slewing bearings, Proc. Inst. Mech. Eng. Part C J. Mech. Eng. Sci. 230 (2016) 1715–1725. https://doi.org/10.1177/0954406215583522.

[15]   I. Heras, J. Aguirrebeitia, M. Abasolo, I. Coria, An engineering approach for the estimation of slewing bearing stiffness in wind turbine generators, Wind Energy. 22 (2019) 376–391. https://doi.org/10.1002/we.2292.

[16]   I. Heras, J. Aguirrebeitia, M. Abasolo, Friction torque in four contact point slewing bearings: Effect of manufacturing errors and ring stiffness, Mech. Mach. Theory. 112 (2017) 145–154. https://doi.org/10.1016/j.mechmachtheory.2017.02.009.

[17]   I. Heras, J. Aguirrebeitia, M. Abasolo, J. Plaza, Friction torque in four-point contact slewing bearings: Applicability and limitations of current analytical formulations, Tribol. Int. 115 (2017) 59–69. https://doi.org/10.1016/j.triboint.2017.05.011.

[18]   I. Heras, J. Aguirrebeitia, M. Abasolo, I. Coria, I. Escanciano, Load distribution and friction torque in four-point contact slewing bearings considering manufacturing errors and ring flexibility, Mech. Mach. Theory. 137 (2019) 23–36. https://doi.org/10.1016/j.mechmachtheory.2019.03.008.

[19]   J. Plaza, M. Abasolo, I. Coria, J. Aguirrebeitia, I. Fernández de Bustos, A new finite element approach for the analysis of slewing bearings in wind turbine generators using superelement techniques, Meccanica. 50 (2015) 1623–1633. https://doi.org/10.1007/s11012-015-0110-7.

[20]   N. Akturk, M. Uneeb, R. Gohar, The Effects of Number of Balls and Preload on Vibrations Associated With Ball Bearings, J. Tribol. 119 (1997) 747–753. https://doi.org/10.1115/1.2833880.

[21]   J. Aguirrebeitia, J. Plaza, M. Abasolo, J. Vallejo, Effect of the preload in the general static load-carrying capacity of four-contact-point slewing bearings for wind turbine generators: Theoretical model and finite element calculations, Wind Energy. 17 (2014) 1605–1621. https://doi.org/10.1002/we.1656.

[22]   H. Basener, Race wire bearing, 4568205, 1986.

[23]   SKF, Slewing bearings catalogue, (2015).

[24]   ISO 76:2006. Rolling bearings - Static load ratings, 2006.

[25]   ISO/TR 10657:1991. Explanatory notes on ISO 76, 1991.

[26]   J. Lai, P. Ovize, H. Kuijpers, A. Bacchettto, S. Ioannides, J. Beswick, S.W. Dean, Case Depth and Static Capacity of Surface Induction-Hardened Rings, J. ASTM Int. 6 (2009) 102630. https://doi.org/10.1520/JAI102630.

[27]   P. Göncz, M. Ulbin, S. Glodež, Computational assessment of the allowable static contact loading of a roller-slewing bearing's case-hardened raceway, Int. J. Mech. Sci. 94–95 (2015) 174–184. https://doi.org/10.1016/j.ijmecsci.2015.03.006.

[28]   Franke GmbH, Wire Race Bearings as Roller Bearings Catalogue, (2019).

[29]   Kaydon, Kaydon WireX Brochure, (2015).

[30]   ISO/TS 16281:2008. Rolling bearings - Methods for calculating the modified reference rating life for universally loaded bearings, 2008.

[31]   T.A. Harris, M.N. Kotzalas, Essential Concepts of Bearing Technology, 2006.

[32]   G. Chen, J. Wen, Load performance of large-scale rolling bearings with supporting structure in wind turbines, J. Tribol. 134 (2012). https://doi.org/10.1115/1.4007349.

[33]   Liebherr, Slewing Bearings Product Catalogue, 2017.

[34]   NSK, Technical Report CAT. No. E728g, (2013).

[35]   The Timken Company, Timken engineering manual, (2019).

[36]   Schaeffler Technologies AG & Co., Slewing rings Catalogue 404, (2012).

[37] ISO 281: 2007. Rolling bearings - Dynamic load ratings and rating life, 2007.

[38] ISO/TR 1281-1:2008. Rolling bearings - Explanatory notes on ISO 281. Part 1: Basic dynamic load rating and basic rating life, 2008.

[39] ISO/TR 1281-2:2008. Rolling bearings - Explanatory notes on ISO 281. Part 2: Modified rating life calculation, based on a systems approach to fatigue stresses, 2008.

[40] T.A. Harris, M.N. Kotzalas, Advanced Concepts of Bearing Technology,: Rolling Bearing Analysis, CRC Press, 2006.

[41] T.A. Harris, J.H. Rumbarger, C.P. Butterfield, Wind Turbine Design Guideline DG03: Yaw and Pitch Rolling Bearing Life. NREL/TP-500-42362, 2009.

[42] E. V Zaretsky, Rolling bearing life prediction, theory, and application, 2013.

[43] H. Hertz, On the Contact of Elastic Solids, Misc. Pap. (1896) 146–162.

[44] H. Hertz, On the Contact of Rigid Elastic Solids and on Hardness, Micellaneous Pap. (1896) 163–183.

[45] R. Pandiyarajan, M.S. Starvin, K.C. Ganesh, Contact Stress Distribution of Large Diameter Ball Bearing Using Hertzian Elliptical Contact Theory, Procedia Eng. 38 (2012) 264–269. https://doi.org/10.1016/j.proeng.2012.06.034.

[46] D.E. Brewe, B.J. Hamrock, Simplified solution for elliptical-contact deformation between two elastic solids, J. Tribol. (1977). https://doi.org/10.1115/1.3453245.

[47] L. Houpert, An Engineering Approach to Hertzian Contact Elasticity - Part I, Trans. ASME. 123 (2001). https://doi.org/10.1115/1.1308043.

[48] L. Houpert, An Engineering Approach to Non-Hertzian Contact Elasticity - Part II, Trans. ASME. 123 (2001) 589–594. https://doi.org/10.1115/1.1308042.

[49] K.L. Johnson, One Hundred Years of Hertz Contact, Proc. Inst. Mech. Eng. (1982). https://doi.org/10.1243/pime_proc_1982_196_039_02.

[50] J. Prescott, Applied Elasticity, Longmans, Green and Company, 1924. https://books.google.es/books?id=yXdBAAAAIAAJ.

[51] H.R. Thomas, V.A. Hoersch, Stresses due to the pressure of one elastic solid upon another with special reference to railroad rails, 1930.

[52] G. Lundberg, Elastische Berührung zweier Halbräume, Forsch. Auf Dem Gebiete Des Ingenieurwesens. (1939). https://doi.org/10.1007/BF02584950.

[53] G. Lundberg, Cylinder compressed between two planes bodies, 1949.

[54] P. Eschmann, L. Hasbargen, Ball and Roller Bearings: Their Theory, Design, and Application, Heyden, 1958. https://books.google.es/books?id=PdtSAAAAMAAJ.

[55] A. Palmgren, Ball and Roller Bearing Engineering, 3rd ed., Burbank, Philadelphia, 1959.

[56] M.J. Puttock, E.G. Thwaite, Elastic Compression of Spheres and Cylinders at Point and Line Contact, Natl. Stand. Lab. Tech. Pap. (1969).

[57] B.N. Norden, On the compression of a cylinder in contact with a plane surface, Interag. Rep. (1973).

[58] J.H. Tripp, L.R. Center., Hertzian contact in two and three dimensions, (1985) 24 p. file://catalog.hathitrust.org/Record/011425404.

[59] K.L. Johnson, Contact Mechanics, (1989). https://doi.org/10.1201/b17588-12.

[60] B.J. Hamrock, Fundamentals Fluid Film Lubrication of, Nasa Publ. 1255. (1991).

[61] M. Najjari, R. Guilbault, Modeling the edge contact effect of finite contact lines on subsurface stresses, Tribol. Int. (2014). https://doi.org/10.1016/j.triboint.2014.04.024.

[62] Q. Li, V.L. Popov, Normal line contact of finite-length cylinders, Facta Univ. Ser. Mech. Eng. (2017). https://doi.org/10.22190/FUME170222003L.

[63] G. Lundberg, Elastic Contact Between Two Semi-infinite Bodies, Forsch. Auf Den Gebiete Des Ingenieurwes. 10 (1961) 165–174.

[64] P.M. Johns, R. Gohar, Roller bearings under radial and eccentric loads, Tribol. Int. 14 (1981) 131–136. https://doi.org/10.1016/0301-679X(81)90058-X.

[65] H. Fujiwara, T. Kobayashi, T. Kawase, K. Yamauchi, Optimized logarithmic roller crowning design of cylindrical roller bearings and its experimental demonstration, Tribol. Trans. 53 (2010) 909–916. https://doi.org/10.1080/10402004.2010.510619.

[66] L. Tudose, C. Tudose, Roller profiling to increase rolling bearing

performances, IOP Conf. Ser. Mater. Sci. Eng. 393 (2018). https://doi.org/10.1088/1757-899X/393/1/012002.

[67] R. Stribeck, Kugellager für beliebige belastungen, Zeitschrift Des Vereines Dtsch. Ingenieure. (1901) 45(3): 73--9 (pt I) & 45(4): 118--125 (pt II).

[68] R. Stribeck, Die wesentlischen eigenschaften der gleit- un rollenlager, Zeitschrift Des Vereines Dtsch. Ingenieure. (1902) 46(37):1341--1348 (pt I) & 46(38): 1432--1438 (pt.

[69] R. Stribeck, Ball bearings for various loads, Trans. ASME. 29 (1907) 420–463.

[70] H. Sjoväll, The load distribution within ball and roller bearings under given external radial and axial load, Tek. Tidskr. Mek. (1933) h.9.

[71] A.B. Jones, Analysis of stresses and deflections., New Depart. Eng. Data. 2 (1946).

[72] A.B. Jones, A general theory for elastically constrained ball and radial roller bearings under arbitrary load and speed conditions, J. Fluids Eng. Trans. ASME. 82 (1960) 309–320. https://doi.org/10.1115/1.3662587.

[73] J. Rumbarger, Thrust bearing with eccentric loads, Mach. Des. (1962).

[74] L. Houpert, A Uniform Analytical Approach for Ball and Roller Bearings Calculations, J. Tribol. (1997).

[75] S. Zupan, I. Prebil, Carrying angle and carrying capacity of a large single row ball bearing as a function of geometry parameters of the rolling contact and the supporting structure stiffness, Mech. Mach. Theory. 36 (2001) 1087–1103. https://doi.org/10.1016/S0094-114X(01)00044-1.

[76] J.I. Amasorrain, X. Sagartzazu, J. Damián, Load distribution in a four contact-point slewing bearing, Mech. Mach. Theory. 38 (2003) 479–496. https://doi.org/10.1016/S0094-114X(03)00003-X.

[77] M. Olave, X. Sagartzazu, J. Damian, A. Serna, Design of Four Contact-Point Slewing Bearing With a New Load Distribution Procedure to Account for Structural Stiffness, J. Mech. Des. 132 (2010) 21006. https://doi.org/10.1115/1.4000834.

[78] S. M S, M. K, The effect of manufacturing tolerances on the load carrying capacity of large diameter bearings, Sādhanā. 40 (2015) 1899–1911. https://doi.org/10.1007/s12046-015-0427-x.

[79] S. Aithal, N. Siva Prasad, M.S. Shunmugam, P. Chellapandi, Effect of manufacturing errors on load distribution in large diameter slewing

bearings of fast breeder reactor rotatable plugs, Proc. Inst. Mech. Eng. Part C J. Mech. Eng. Sci. 0 (2015) 1–12. https://doi.org/10.1177/0954406215579947.

[80] R. Potočnik, P. Göncz, S. Glodež, Static capacity of a large double row slewing ball bearing with predefined irregular geometry, Mech. Mach. Theory. 64 (2013) 67–79. https://doi.org/10.1016/j.mechmachtheory.2013.01.010.

[81] G. Lundberg, Die dynamische Tragfähigkeit der Wälzlager bei Berücksichtigung der Lagerluft, Forsch. Auf Dem Gebiete Des Ingenieurwesens. (1954). https://doi.org/10.1007/BF02558363.

[82] F.B. Oswald, E. V. Zaretsky, J. V. Poplawski, Effect of Internal Clearance on Load Distribution and Life of Radially Loaded Ball and Roller Bearings, Tribol. Trans. 55 (2012) 245–265. https://doi.org/10.1080/10402004.2011.639050.

[83] G. Chen, F. Mao, B. Wang, Effects of off-sized cylindrical rollers on the static load distribution in a cylinder roller bearing, Proc. Inst. Mech. Eng. Part J J. Eng. Tribol. 226 (2012) 687–696. https://doi.org/10.1177/1350650112441747.

[84] S. Yu, D. Wang, H. Dong, B. Wang, A new method for determining load distributions among rollers of bearing with manufacturing errors, Proc. Inst. Mech. Eng. Part C J. Mech. Eng. Sci. 227 (2013) 2402–2415. https://doi.org/10.1177/0954406213477778.

[85] R. Xiaoli, Z. Jia, R. Ge, Calculation of radial load distribution on ball and roller bearings with positive, negative and zero clearance, Int. J. Mech. Sci. 131–132 (2017) 1–7. https://doi.org/10.1016/j.ijmecsci.2017.06.042.

[86] A. Aschenbrenner, B. Schleich, S. Tremmel, S. Wartzack, A variational simulation framework for the analysis of load distribution and radial displacement of cylindrical roller bearings, Mech. Mach. Theory. 147 (2020). https://doi.org/10.1016/j.mechmachtheory.2019.103769.

[87] A.B. Jones, T.A. Harris, Analysis of a Rolling-Element Idler Gear Bearing Having a Deformable Outer-Race Structure, J. Basic Eng. 85 (1963) 273–278. http://dx.doi.org/10.1115/1.3656576.

[88] T.A. Harris, J.L. Broschard, Analysis of an Improved Planetary Gear-Transmission Bearing, J. Basic Eng. 86 (1964) 457–461. http://dx.doi.org/10.1115/1.3653139.

[89] L. Mignot, L. Bonnard, V. Abousleiman, Analysis of Load Distribution in Planet-Gear Bearings, AGMA Tech. Pap. 10FTM16. (2010).

[90] T. Lim, R. Singh, Vibration transmission through rolling element bearings, part I: Bearing stiffness formulation, J. Sound Vib. 139 (1990) 179–199.

[91] X. Hernot, M. Sartor, J. Guillot, Calculation of the Stiffness Matrix of Angular Contact Ball Bearings by Using the Analytical Approach, J. Mech. Des. 122 (2000) 83–90.

[92] H.-V. Liew, T. Lim, Analysis of time-varying rolling element bearing characteristics, J. Sound Vib. 283 (2005) 1163–1179.

[93] D. Noel, S. Le Loch, M. Ritou, B. Furet, Complete Analytical Expression of the Stiffness Matrix of Angular Contact Ball Bearings, J. Tribol. 135 (2013) 1–8.

[94] Y. Guo, R. Parker, Stiffness matrix calculation of rolling element bearings using a finite element/contact mechanics model, Mech. Mach. Theory. 51 (2012) 32–45.

[95] I. Heras, J. Aguirrebeitia, M. Abasolo, I. Coria, L. Martín, A straightforward way to calculate the stiffness of slewing bearings, in: Wind. 2019 Conf., 2019.

[96] Schaeffler Technologies AG & Co. KG, INA Slewing rings. Catalogue 404, (2012) 108. http://www.schaeffler.com/remotemedien/media/_shared_media/08_media_library/01_publications/schaeffler_2/catalogue_1/downloads_6/404_de_en_1.pdf.

[97] Thysennkrupp Rothe Erde GmbH, Rothe Erde Slewing Bearings, (2016) 242.

[98] A. Leblanc, D. Nelias, Ball Motion and Sliding Friction in a Four-Contact-Point Ball Bearing, J. Tribol. 129 (2007) 801–808. https://doi.org/10.1115/1.2768079.

[99] A. Leblanc, D. Nelias, Analysis of Ball Bearings with 2, 3 or 4 Contact Points, Tribol. Trans. 51 (2008) 372–380. https://doi.org/10.1080/10402000801888887.

[100] M.J. Todd, K.L. Johnson, A model for coulomb torque hysteresis in ball bearings, Int. J. Mech. Sci. 29 (1987) 339–354.

[101] S. Lacroix, D. Nelias, A. Leblanc, Four-Point Contact Ball Bearing Model With Deformable Rings, J. Tribol. 135 (2013) 1–8. https://doi.org/10.1115/1.4024103.

[102] A. Joshi, B. Kachhia, H. Kikkari, M. Sridhar, D. Nelias, Running Torque

of Slow Speed Two-Point and Four-Point Contact Bearings, Lubricants. 3 (2015) 181–196. https://doi.org/10.3390/lubricants3020181.

[103] D.C. Witte, Operating Torque of Tapered Roller Bearings, A S L E Trans. 16 (1973) 61–67. https://doi.org/10.1080/05698197308982705.

[104] S. Aihara, A new running torque formula for tapered roller bearings under axial load., J. Tribol. 109 (1987) 471–477. https://doi.org/https://doi.org/10.1115/1.3261475.

[105] R.S. Zhou, M.R. Hoeprich, Torque of Tapered Roller Bearings, J. Tribol. 113 (1991) 590–597. https://doi.org/10.1115/1.2920664.

[106] V.-C. Tong, S.-W. Hong, The effect of angular misalignment on the running torques of tapered roller bearings, Tribol. Int. 95 (2016) 76–85. https://doi.org/https://doi.org/10.1016/j.triboint.2015.11.005.

[107] C. Zhang, L. Gu, Y. Mao, L. Wang, Modeling the frictional torque of a dry-lubricated tapered roller bearing considering the roller skewing, Friction. 7 (2019) 551–563. https://doi.org/10.1007/s40544-018-0232-8.

[108] Y. Liu, W. Kang, Y. Zhu, K. Yan, J. Hong, Effects of Defect on Roller-Raceway Contact State and Friction Torque of Tapered Roller Bearings, J. Tribol. 142 (2020) 1–11. https://doi.org/10.1115/1.4047194.

[109] C.M.C.G. Fernandes, R.C. Martins, J.H.O. Seabra, Friction torque of cylindrical roller thrust bearings lubricated with wind turbine gear oils, Tribol. Int. 59 (2013) 121–128. https://doi.org/10.1016/j.triboint.2012.05.030.

[110] C.M.C.G. Fernandes, P.M.P. Amaro, R.C. Martins, J.H.O. Seabra, Torque loss in cylindrical roller thrust bearings lubricated with wind turbine gear oils at constant temperature, Tribol. Int. 67 (2013) 72–80. https://doi.org/10.1016/j.triboint.2013.06.016.

[111] D. Gonçalves, T. Cousseau, A. Gama, A. V. Campos, J.H.O. Seabra, Friction torque in thrust roller bearings lubricated with greases, their base oils and bleed-oils, Tribol. Int. 107 (2017) 306–319. https://doi.org/10.1016/j.triboint.2016.11.041.

[112] J.T. Sawicki, S. a. Johansson, J.H. Rumbarger, R.B. Sharpless, Fatigue Life Prediction for Large-Diameter Elastically Constrained Ball Bearings, J. Eng. Gas Turbines Power. 130 (2008) 22506. https://doi.org/10.1115/1.2772632.

[113] R. Potočnik, P. Göncz, J. Flašker, S. Glodež, Fatigue life of double row slewing ball bearing with irregular geometry, Procedia Eng. 2 (2010)

1877–1886. https://doi.org/10.1016/j.proeng.2010.03.202.

[114] I. Portugal, M. Olave, A. Zurutuza, A. López, M. Muñiz-Calvente, A. Fernández-Canteli, Methodology to evaluate fatigue damage under multiaxial random loading, Eng. Fract. Mech. (2017). https://doi.org/10.1016/j.engfracmech.2017.04.012.

[115] J. V. Poplawski, S.M. Peters, E. V. Zaretsky, Effect of roller profile on cylindrical roller bearing life prediction—part i: comparison of bearing life theories, 2001. https://doi.org/10.1080/10402000108982466.

[116] N.D. Londhe, N.K. Arakere, G. Subhash, Extended Hertz Theory of Contact Mechanics for Case-Hardened Steels With Implications for Bearing Fatigue Life, J. Tribol. 140 (2017) 21401. https://doi.org/10.1115/1.4037359.

[117] P. He, R. Liu, R. Hong, H. Wang, G. Yang, C. Lu, Hardened raceway calculation analysis of a three-row roller slewing bearing, Int. J. Mech. Sci. 137 (2018) 133–144. https://doi.org/10.1016/j.ijmecsci.2018.01.021.

[118] F. Schwack, F. Prigge, G. Poll, Finite element simulation and experimental analysis of false brinelling and fretting corrosion, Tribol. Int. 126 (2018) 352–362. https://doi.org/https://doi.org/10.1016/j.triboint.2018.05.013.

[119] P. He, R. Hong, H. Wang, C. Lu, Fatigue life analysis of slewing bearings in wind turbines, Int. J. Fatigue. 111 (2018) 233–242. https://doi.org/10.1016/j.ijfatigue.2018.02.024.

[120] Y.S. Su, S.R. Yu, S.X. Li, Y.N. He, Review of the damage mechanism in wind turbine gearbox bearings under rolling contact fatigue, Front. Mech. Eng. 14 (2019) 434–441. https://doi.org/10.1007/s11465-018-0474-1.

[121] M.U. Abdullah, Z.A. Khan, W. Kruhoeffer, Evaluation of Dark Etching Regions for Standard Bearing Steel under Accelerated Rolling Contact Fatigue, Tribol. Int. 152 (2020) 106579. https://doi.org/10.1016/j.triboint.2020.106579.

[122] M. Stammler, P. Thomas, A. Reuter, F. Schwack, G. Poll, Effect of load reduction mechanisms on loads and blade bearing movements of wind turbines, Wind Energy. 23 (2020) 274–290. https://doi.org/10.1002/we.2428.

[123] H. Golbach, Integrated Non-linear FE Module for Rolling Bearing Analysis, Proceeding NAFEMS World Congr. 2 (1999).

[124] T. Smolnicki, E. Rusiński, Superelement-Based Modeling of Load Distribution in Large-Size Slewing Bearings, J. Mech. Des. (2007).

https://doi.org/10.1115/1.2437784.

[125] T. Smolnicki, D. Derlukiewicz, M. Stańco, Evaluation of load distribution in the superstructure rotation joint of single-bucket caterpillar excavators, Autom. Constr. 17 (2008) 218–223. https://doi.org/10.1016/j.autcon.2007.05.003.

[126] A. Daidié, Z. Chaib, A. Ghosn, 3D Simplified Finite Elements Analysis of Load and Contact Angle in a Slewing Ball Bearing, J. Mech. Des. 130 (2008) 082601. https://doi.org/10.1115/1.2918915.

[127] S. Śpiewak, Methodology for calculating the complete static carrying capacity of twin slewing bearing, Mech. Mach. Theory. 101 (2016) 181–194. https://doi.org/10.1016/j.mechmachtheory.2016.03.017.

[128] O. Menck, M. Stammler, F. Schleich, Fatigue lifetime calculation of wind turbine blade bearings considering blade-dependent load distribution, Wind Energy Sci. 5 (2020) 1743–1754. https://doi.org/10.5194/wes-5-1743-2020.

[129] T.A. Harris, Rolling Bearing Analysis, John Wiley and Sons, 2001.

[130] L. Kania, Modelling of rollers in calculation of slewing bearing with the use of finite elements, Mech. Mach. Theory. 41 (2006) 1359–1376. https://doi.org/10.1016/j.mechmachtheory.2005.12.007.

[131] M. Stammler, S. Baust, A. Reuter, G. Poll, Load distribution in a roller-type rotor blade bearing, J. Phys. Conf. Ser. 1037 (2018). https://doi.org/10.1088/1742-6596/1037/4/042016.

[132] L. Molnár, K. Váradi, G. Bódai, P. Zwierczyk, L. Oroszváry, Simplified modeling for needle roller bearings to analyze engineering structures by FEM, Period. Polytech. Mech. Eng. 54 (2010) 27–33. https://doi.org/10.3311/pp.me.2010-1.05.

[133] E. Claesson, Modelling of roller bearings in ABAQUS, Chalmers University of Technology, Göteborg, Sweden, 2014.

[134] J. Aguirrebeitia, M. Abasolo, J. Plaza, I. Heras, FEM model for friction moment calculations in ball-raceway contacts for applications in four contact point slewing bearings, in: 14th World Congr. Mech. Mach. Sci. 25-30 Oct., Taipei, Taiwan, 2015. https://doi.org/10.6567/IFToMM.14TH.WC.OS18.018.

[135] Schaeffler Technologies GmbH & Co. KG, Bearing Solutions and Service for Wind Turbines Brochure, (2014).

[136] Liebherr-Components AG, System and Technology Expertise. Solutions

for Wind Energy Brochure, (2018).

[137] thyssennkrupp Rothe Erde GmbH, Official website, (n.d.). https://www.thyssenkrupp-rotheerde.com.

[138] Rollix, Official website, (n.d.). http://www.rollix.com.

[139] Windbox, Official website, (n.d.). http://www.clusterenergia.com/windbox.

[140] M. Stammler, F. Schwack, N. Bader, A. Reuter, G. Poll, Friction torque of wind-turbine pitch bearings – comparison of experimental results with available models, Wind Energy Sci. Discuss. 2017 (2017) 1–16. https://doi.org/10.5194/wes-2017-20.

[141] J.S. Nam, J.W. Han, Y.J. Park, Y.Y. Nam, G.H. Lee, Development of highly reproducible test rig for pitch and yaw bearings of wind turbine, J. Mech. Sci. Technol. 28 (2014) 705–712. https://doi.org/10.1007/s12206-013-1134-3.

[142] J.W. Han, J.S. Nam, Y.J. Park, G.H. Lee, Y.Y. Nam, An experimental study on the performance and fatigue life of pitch bearing for wind turbine, J. Mech. Sci. Technol. 29 (2015) 1963–1971. https://doi.org/10.1007/s12206-015-0417-2.

[143] M. Stammler, Endurance Test Strategies for Pitch Bearings of Wind Turbines, Gottfried Wilhelm Leibniz Universität Hannover, 2020.

[144] Y. Feng, X. Huang, J. Chen, H. Wang, R. Hong, Reliability-based residual life prediction of large-size low-speed slewing bearings, Mech. Mach. Theory. 81 (2014) 94–106. https://doi.org/10.1016/j.mechmachtheory.2014.06.013.

[145] Y. Pan, R. Hong, J. Chen, Z. Qin, Y. Feng, Incipient fault detection of wind turbine large-size slewing bearing based on circular domain, Meas. J. Int. Meas. Confed. 137 (2019) 130–142. https://doi.org/10.1016/j.measurement.2019.01.033.

[146] Z. Chaib, A. Daidié, D. Leray, Screw behavior in large diameter slewing bearing assemblies: numerical and experimental analyses, Int. J. Interact. Des. Manuf. 1 (2007) 21–31. https://doi.org/10.1007/s12008-007-0003-7.

[147] G. Chen, G. Wen, Z. Xiao, H. San, Experimental Study on Contact Force in a Slewing Bearing, J. Tribol. 140 (2018). https://doi.org/10.1115/1.4037356.

[148] S. Leupold, R. Schelenz, G. Jacobs, Investigation of the individual load

distribution of a blade bearing test rig by means of finite element simulation, J. Phys. Conf. Ser. 1618 (2020). https://doi.org/10.1088/1742-6596/1618/5/052056.

[149] Y. Hou, X. Wang, Measurement of load distribution in a cylindrical roller bearing with an instrumented housing: Finite element validation and experimental study, Tribol. Int. 155 (2021) 106785. https://doi.org/10.1016/j.triboint.2020.106785.

[150] X. Shan, T. Xie, W. Chen, A new method for determining the preload in a wire race ball bearing, Tribol. Int. 40 (2007) 869–875. https://doi.org/10.1016/j.triboint.2006.09.003.

[151] X. Shan, T. Xie, W. Chen, L. Wang, Modeling and simulation on the contact deformation distribution in a wire race ball bearing, 2009 IEEE Int. Conf. Robot. Biomimetics, ROBIO 2009. (2009) 2211–2214. https://doi.org/10.1109/ROBIO.2009.5420476.

[152] X.B. Shan, L.L. Wang, T. Xie, W.S. Chen, Mathematical Modeling and Experimental Verification of the Radial Stiffness for a Wire Race Ball Bearing, Appl. Mech. Mater. 120 (2011) 343–348. https://doi.org/10.4028/www.scientific.net/AMM.120.343.

[153] D.F. Zhong, J.B. Yuan, X.B. Shan, T. Xie, Theoretical and Experimental Study on Stiffness Characteristics of a Wire Race Ball Bearing, Adv. Mater. Res. (2012). https://doi.org/10.4028/www.scientific.net/AMR.569.461.

[154] X. Zhou, D. Li, R. Yu, Finite element analysis of the contact problem for a wire race ball bearing used in a rotating platform, Proc. - 3rd Int. Conf. Meas. Technol. Mechatronics Autom. ICMTMA 2011. 2 (2011) 221–224. https://doi.org/10.1109/ICMTMA.2011.343.

[155] R. Yu, X. Zhou, Optimization design of a wire race ball bearing for rotating platform based on MDO, 2014 Int. Conf. Adv. Eng. Technol. Res. ICAETR 2014. (2014) 2–5. https://doi.org/10.1109/ICAETR.2014.7012937.

[156] Y. Zhao, J. Yao, C. Tong, Optimization Design of Rectangular Cross-Sectional Wire Race Ball Bearing, Appl. Mech. Mater. 541–542 (2014) 553–558. https://doi.org/10.4028/www.scientific.net/AMM.541-542.553.

[157] D. Gunia, T. Smolnicki, The Analysis of the Stress Distribution in Contact Pairs Ball-Wire and Wire-Ring in Wire Raceway Slewing Bearing, in: E. Rusiński, D. Pietrusiak (Eds.), Proc. 13th Int. Sci. Conf., Springer International Publishing, Cham, 2017: pp. 185–195.

[158] D. Gunia, T. Smolnicki, The Influence of the Geometrical Parameters for Stress Distribution in Wire Raceway Slewing Bearing, Arch. Mech. Eng. 64 (2017). https://doi.org/10.1515/meceng-2017-0019.

[159] D. Gunia, T. Smolnicki, Comparison of Stress Distribution Between Geometrically Corrected Wire-Raceway Bearings and Non-corrected Wire-Raceway Bearings, in: E. Rusiński, D. Pietrusiak (Eds.), Proc. 14th Int. Sci. Conf. Comput. Aided Eng., Springer International Publishing, Cham, 2019: pp. 266–275.

[160] A. Dindar, M. Akkök, Ç. Mehmet, Experimental Determination and Analytical Model of Friction Torque of a Double Row Roller Slewing Bearing, J. Tribol. 139 (2017) 1–13. https://doi.org/10.1115/1.4033364.

[161] Franke GmbH, Wire Race Bearings Slim Bearings Bearing Assemblies Mounting and Maintenance Instructions, (2017).

[162] Iraundi S.A., Slewing bearings catalogue, (2016).

[163] D. Gonçalves, S. Pinho, B. Graça, A. V. Campos, J.H.O. Seabra, Friction torque in thrust ball bearings lubricated with polymer greases of different thickener content, Tribol. Int. (2016). https://doi.org/10.1016/j.triboint.2015.12.017.

[164] I. Heras, I. Coria, J. Aguirrebeitia, M. Abasolo, Par de fricción en rodamientos de vuelco de cuatro puntos de contacto: procedimiento de cálculo y resultados experimentales, in: XXII Congr. Nac. Ing. Mecánica, 19-21 Sept., Madrid, Spain, 2018.

[165] W.C.C. Young, R.G.G. Budynas, Roarks's Formulas for Stress and Strain, 2002. https://doi.org/10.1115/1.3423917.

Appendix A: Ball-raceway contact formulae summary

This appendix features a summary of the ball-raceway contact formulae proposed by Houpert in [74]. Some of these formulae have been modified in order to obtain simpler expressions. Additionally, the parameters have been also replaced to match to the ones used in this document.

Formulae

Interference (1 contact)

$$\delta = C_1' \cdot (1-s)^{-C_2} \cdot \frac{Q^{2/3}}{D_w^{1/3}} \qquad C_1' = C_1 \cdot 2^{1/3} \cdot \left(\frac{1-\nu^2}{E}\right)^{2/3}$$

$$\delta = C_1' \cdot (1-s)^{-C_2} \cdot D_w \cdot P_{max}^{\ 2} \qquad C_1' = C_1 \cdot 2^{-1} \cdot \left(\frac{1-\nu^2}{E}\right)^{2}$$

Contact Ellipse   a   b

$$\left.\begin{array}{l}a\\b\end{array}\right\} = C_1' \cdot (1-s)^{-C_2} \cdot D_w^{\ 1/3} \cdot Q^{1/3} \qquad C_1' = C_1 \cdot 2^{-1/3} \cdot \left(\frac{1-\nu^2}{E}\right)^{1/3}$$

Max. Pressure

$$P_{max} = C_1' \cdot (1-s)^{-C_2} \cdot \frac{Q^{1/3}}{D_w^{2/3}} \qquad C_1' = C_1 \cdot 2^{2/3} \cdot \left(\frac{E}{1-\nu^2}\right)^{2/3}$$

Stiffness

1 Contact

$$K = C_1' \cdot (1-s)^{3/2 \cdot C_2} \cdot D_w^{\ 1/2} \qquad C_1' = C_1^{-3/2} \cdot 2^{-1/2} \cdot \frac{E}{1-\nu^2}$$

Siendo

$$Q = K \cdot \delta^{3/2}$$

2 Contacts

$$C_1' = C_1^{-3/2} \cdot 2^{-2} \cdot \frac{E}{1-\nu^2}$$

	Low osculation ratio $0 < s < 0.886$			High osculation ratio $0.886 < s < 0.992$		
	C_1	C_1' E=200 [GPa]	C_2	C_1	C_1' E=200 [GPa]	C_2
Interference (1 contact)	1.3201	$4.567 \cdot 10^{-4}$	-0.1946	1.4586	$5.046 \cdot 10^{-4}$	-0.2414
	10.226	$1.058 \cdot 10^{-10}$	0.3652	14.965	$1.549 \cdot 10^{-10}$	0.1820
Contact Ellipse a	1.1552	$1.519 \cdot 10^{-2}$	0.4676	1.3085	$1.721 \cdot 10^{-2}$	0.4091
Contact Ellipse b	1.1502	$1.513 \cdot 10^{-2}$	-0.1876	1.1687	$1.537 \cdot 10^{-2}$	-0.1974
Max. Pressure	0.3593	$2.077 \cdot 10^{3}$	-0.2799	0.3122	$1.805 \cdot 10^{3}$	-0.2117
Stiffness 1 Contact	1.3201	$1.025 \cdot 10^{5}$	-0.1946	1.4586	$8.822 \cdot 10^{4}$	-0.2414
Stiffness 2 Contacts		$3.623 \cdot 10^{4}$			$3.119 \cdot 10^{4}$	

Appendix B: Experimental test results

This appendix features all the results of the experimental test campaign carried out in Chapter 6.

Bearing 1: Test 1 Load 1

Bearing 1: Test 1 Load 2

Bearing 1: Test 1 Load 3

Bearing 1: Test 1 Load 4
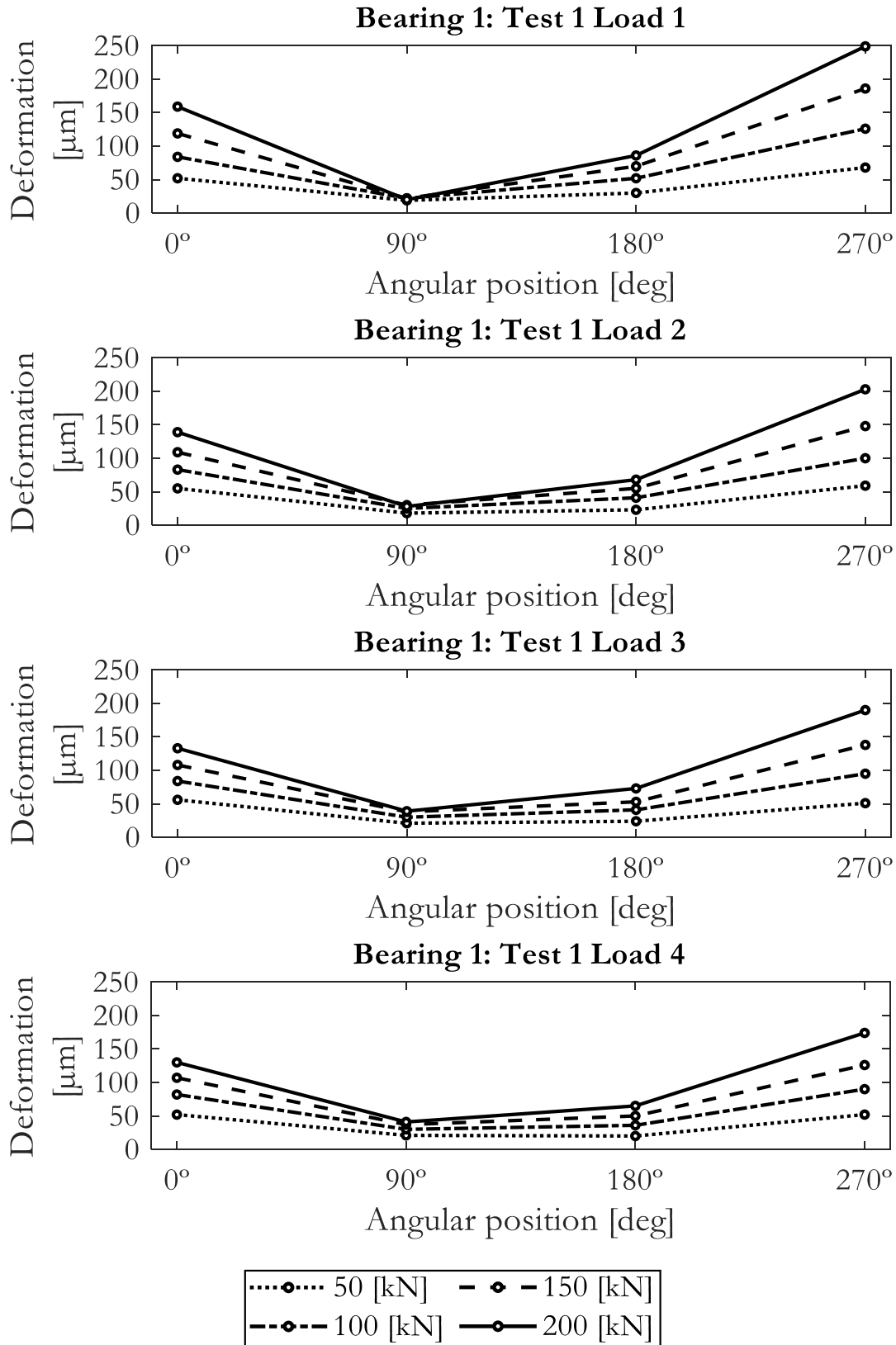
Figure B.1 Bearing 1: No bolt preload test 1.
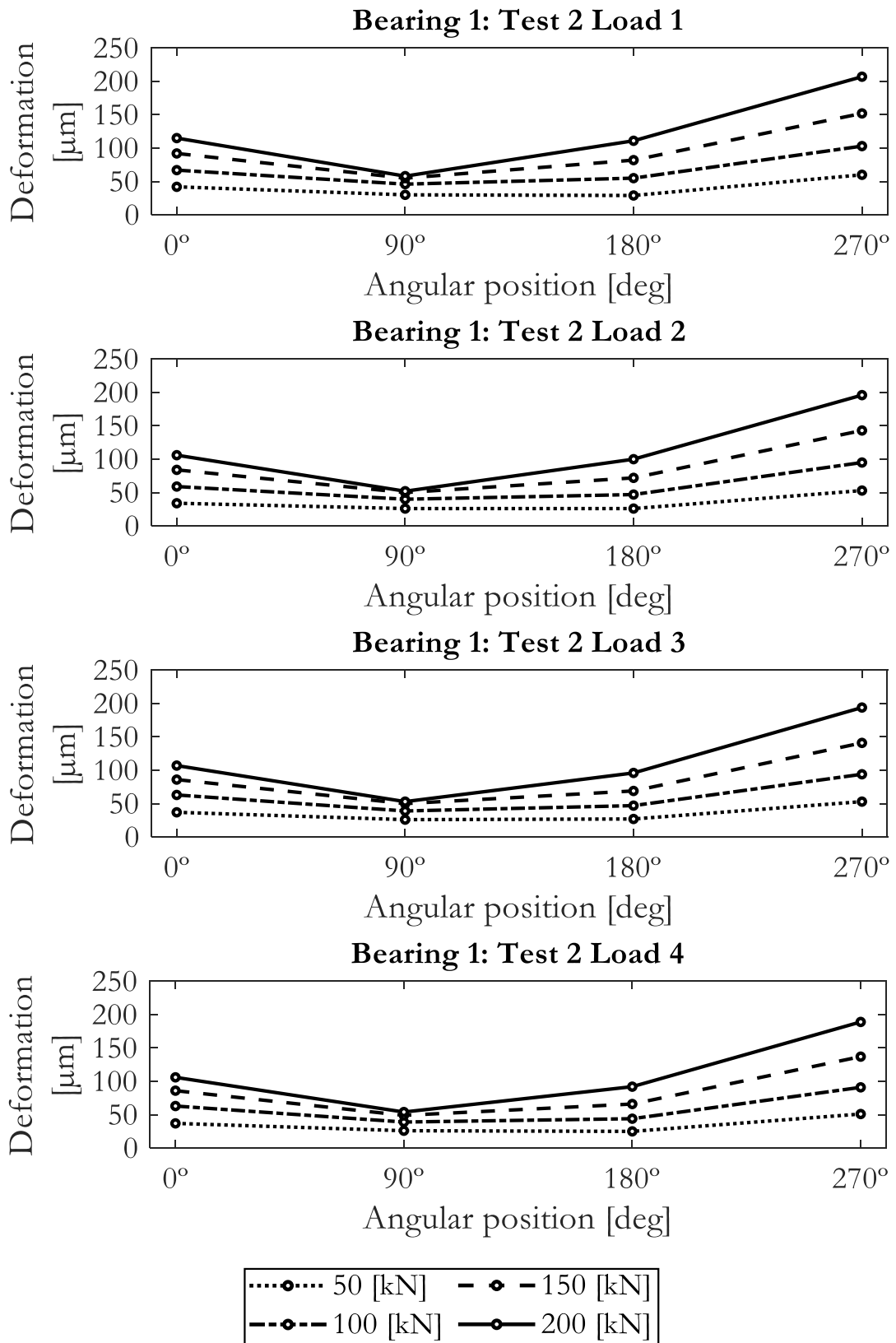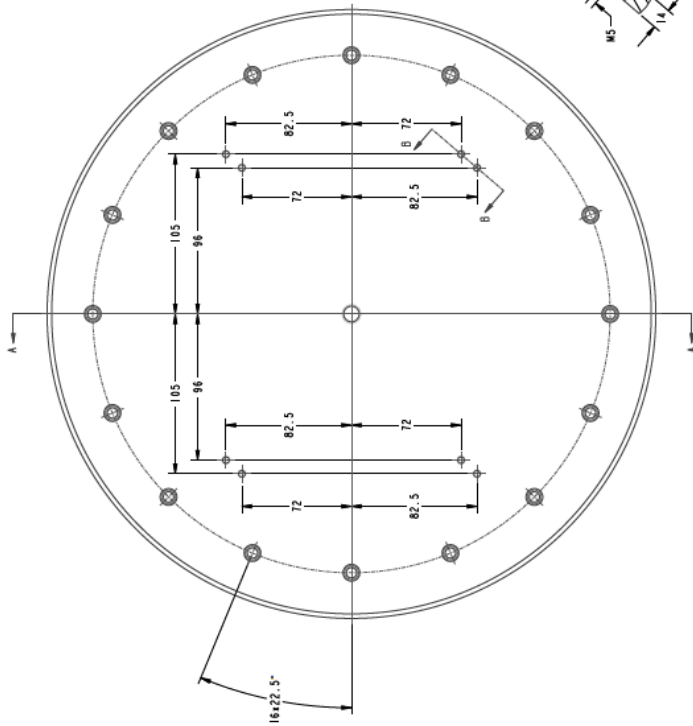
Figure B.2 Bearing 1: No bolt preload test 2.

Bearing 1: Test 3 Load 1

Bearing 1: Test 3 Load 2

Bearing 1: Test 3 Load 3

Bearing 1: Test 3 Load 4
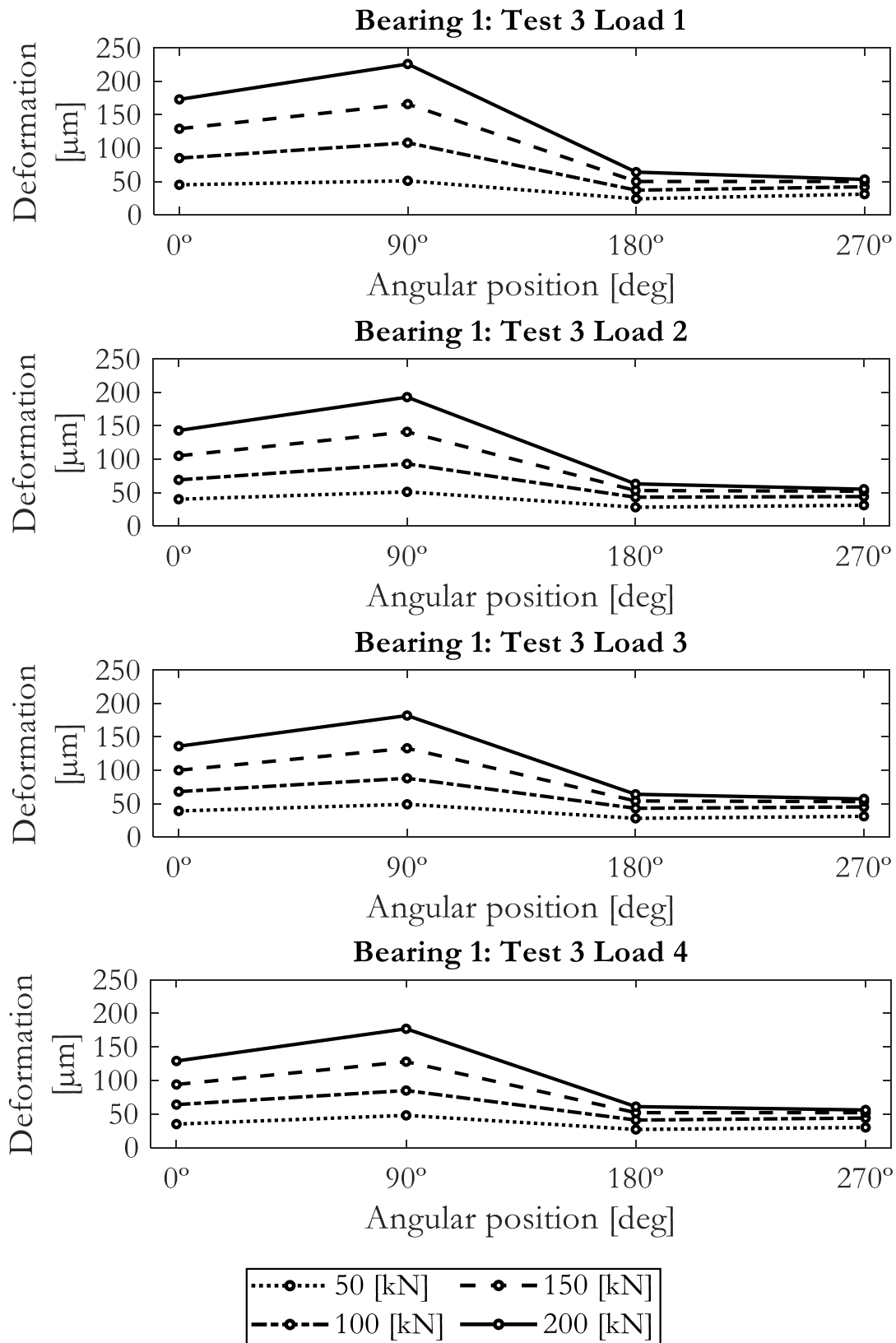
Figure B.3 Bearing 1: No bolt preload test 3.
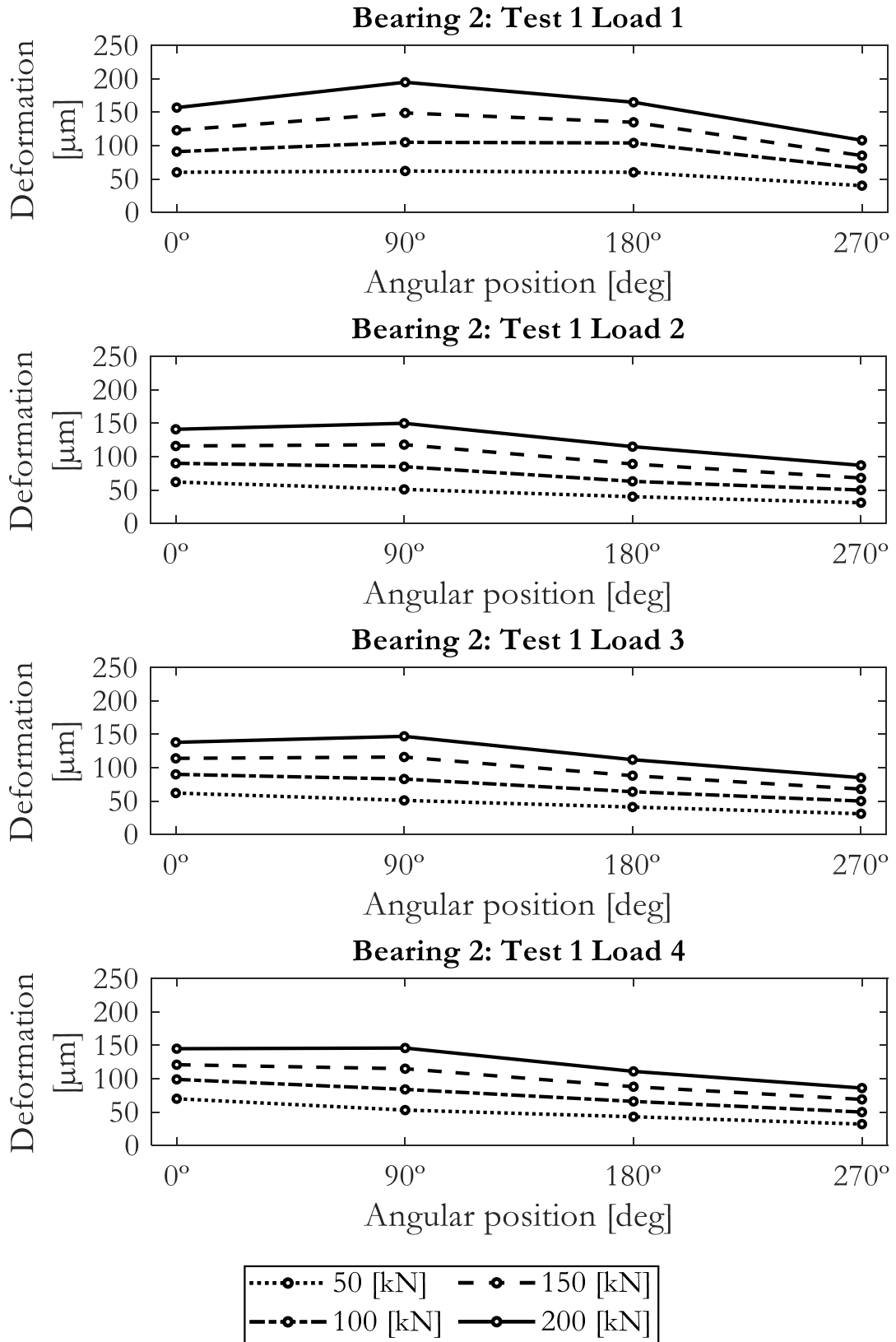
Figure B.4 Bearing 2: No bolt preload test 1.

Bearing 2: Test 2 Load 1

Bearing 2: Test 2 Load 2

Bearing 2: Test 2 Load 3

Bearing 2: Test 2 Load 4
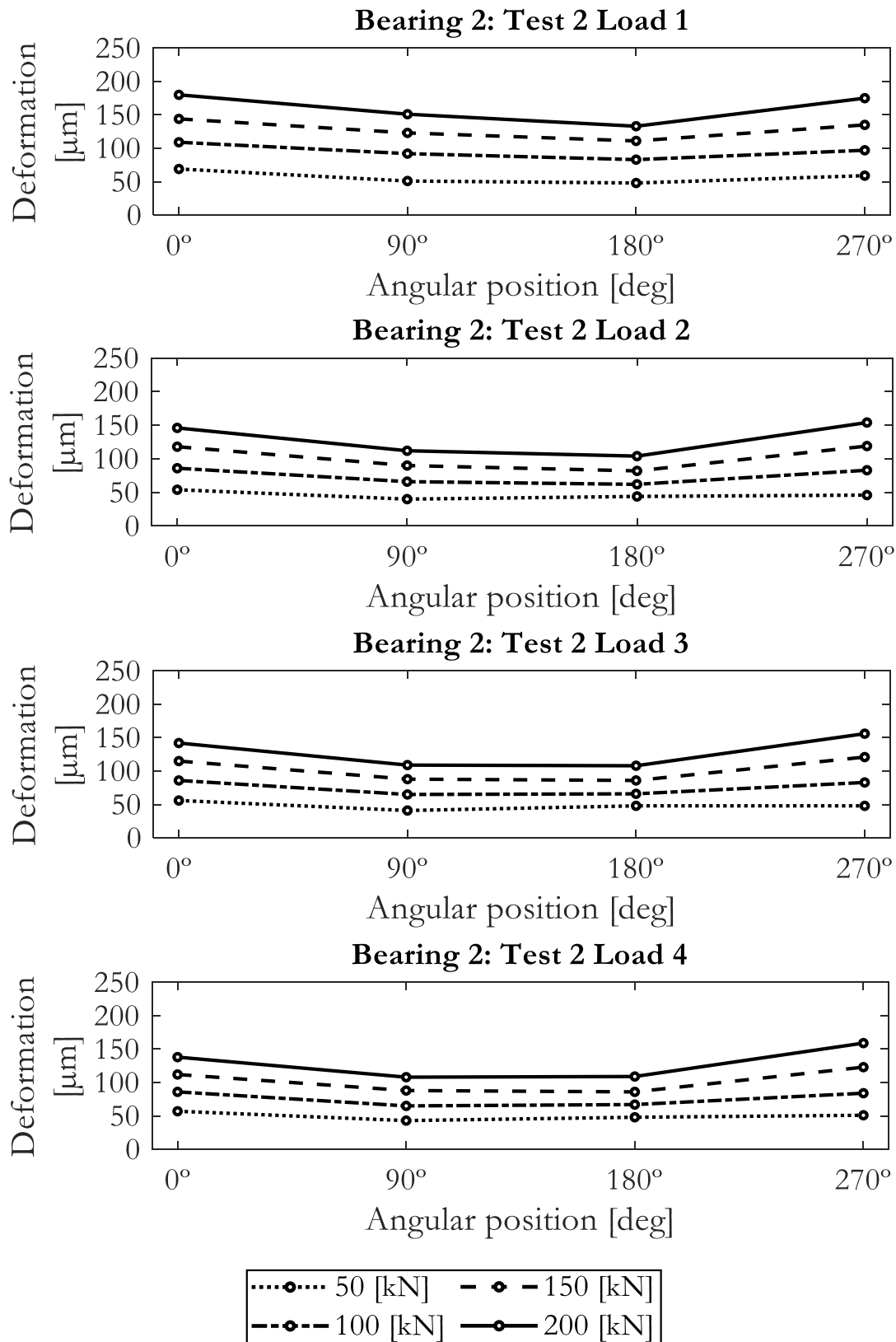
Figure B.5 Bearing 2: No bolt preload test 2.
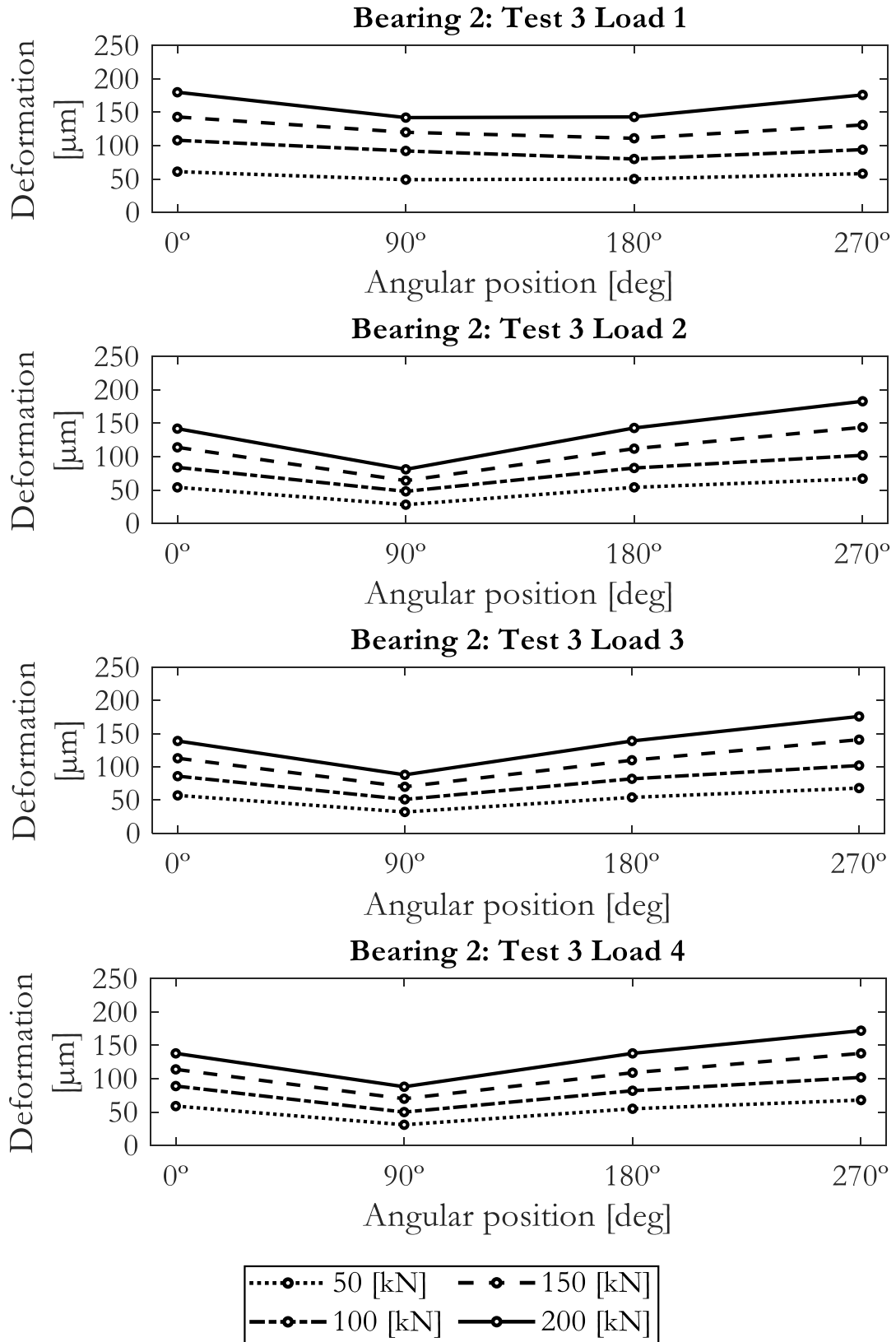
Figure B.6 Bearing 2: No bolt preload test 3.

Bearing 3: Test 1 Load 2

Bearing 3: Test 1 Load 3

Bearing 3: Test 1 Load 4
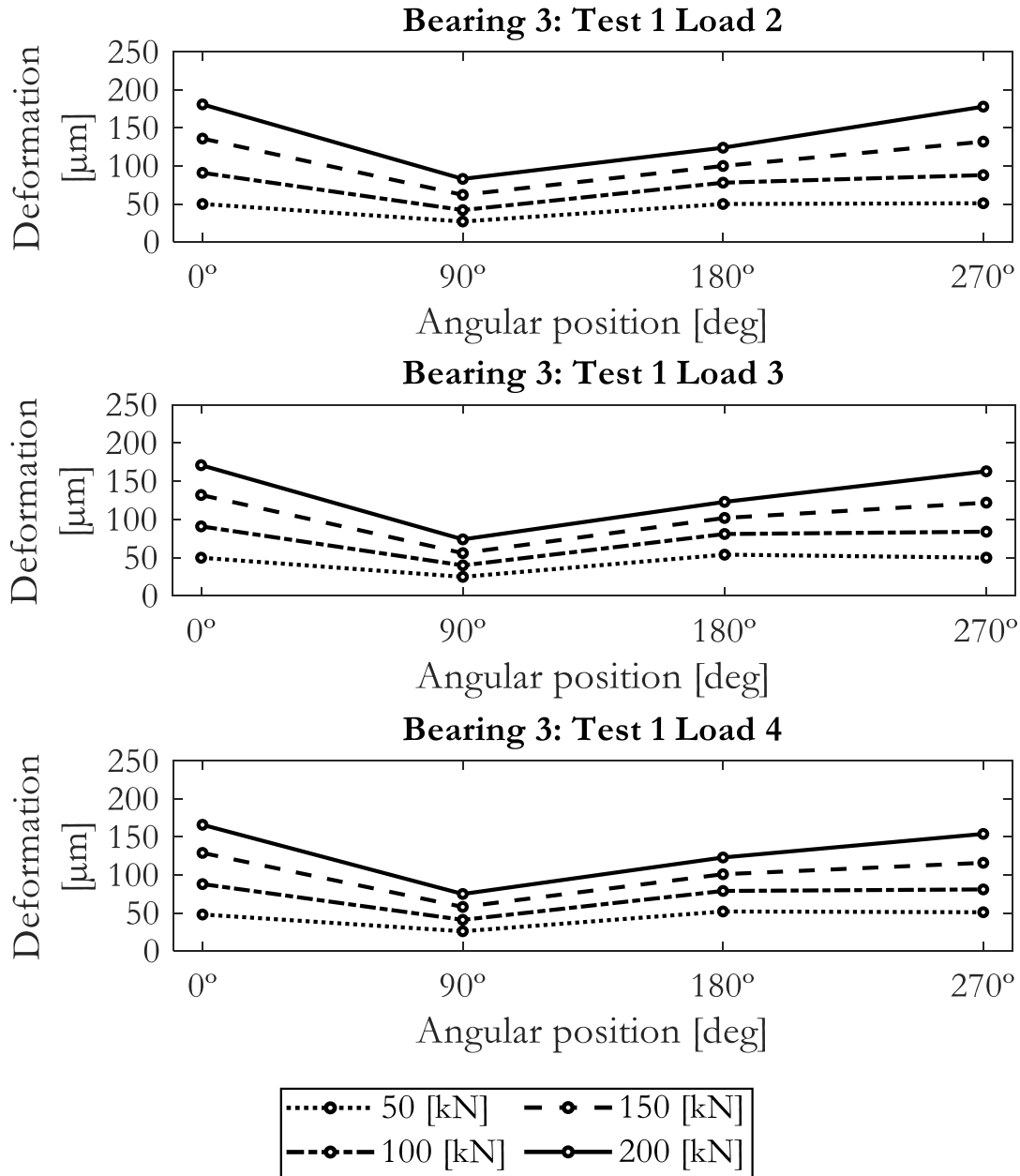
Figure B.7 Bearing 3: No bolt preload test 1.
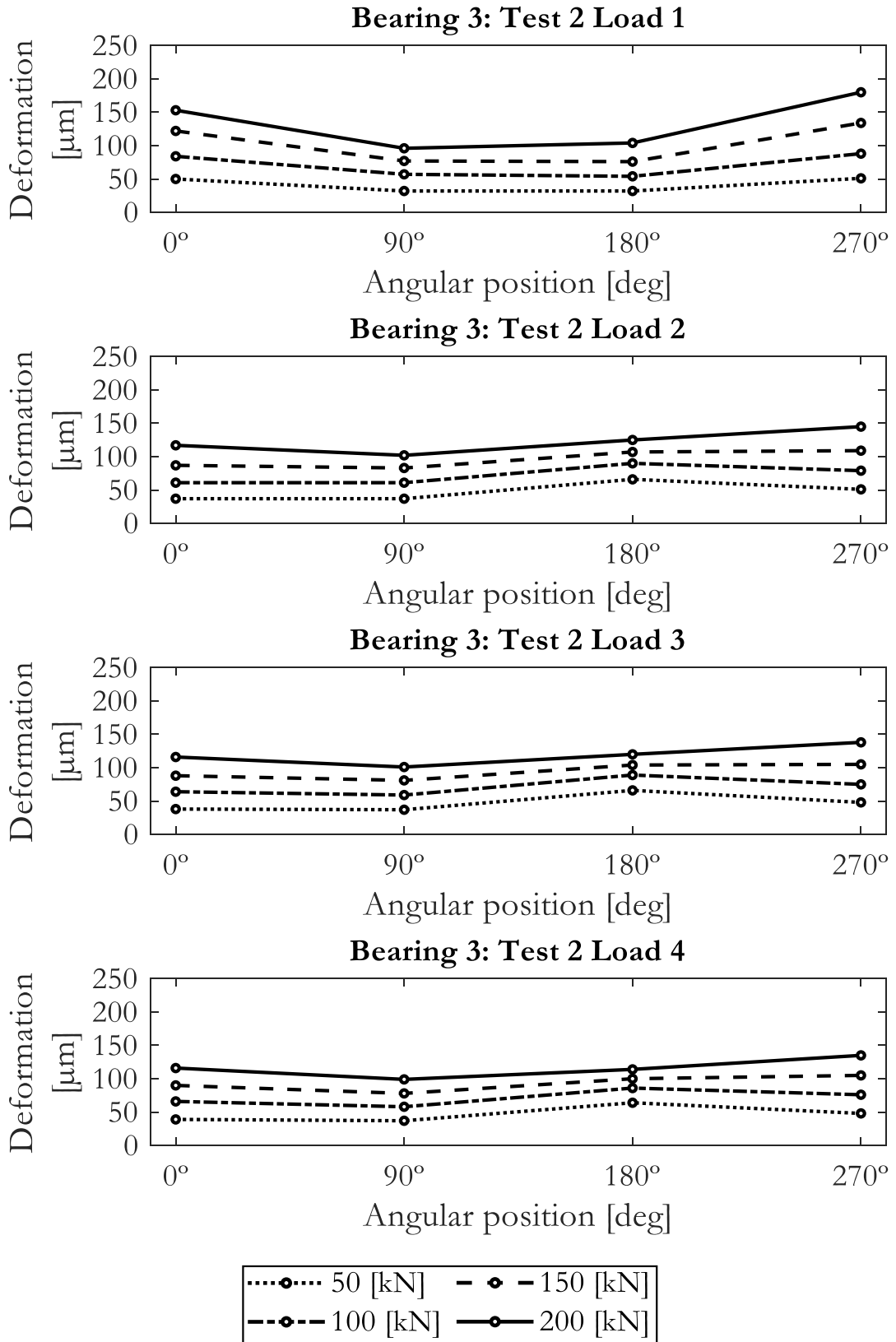
Figure B.8 Bearing 3: No bolt preload test 2.

Bearing 3: Test 3 Load 1

Bearing 3: Test 3 Load 2

Bearing 3: Test 3 Load 3

Bearing 3: Test 3 Load 4
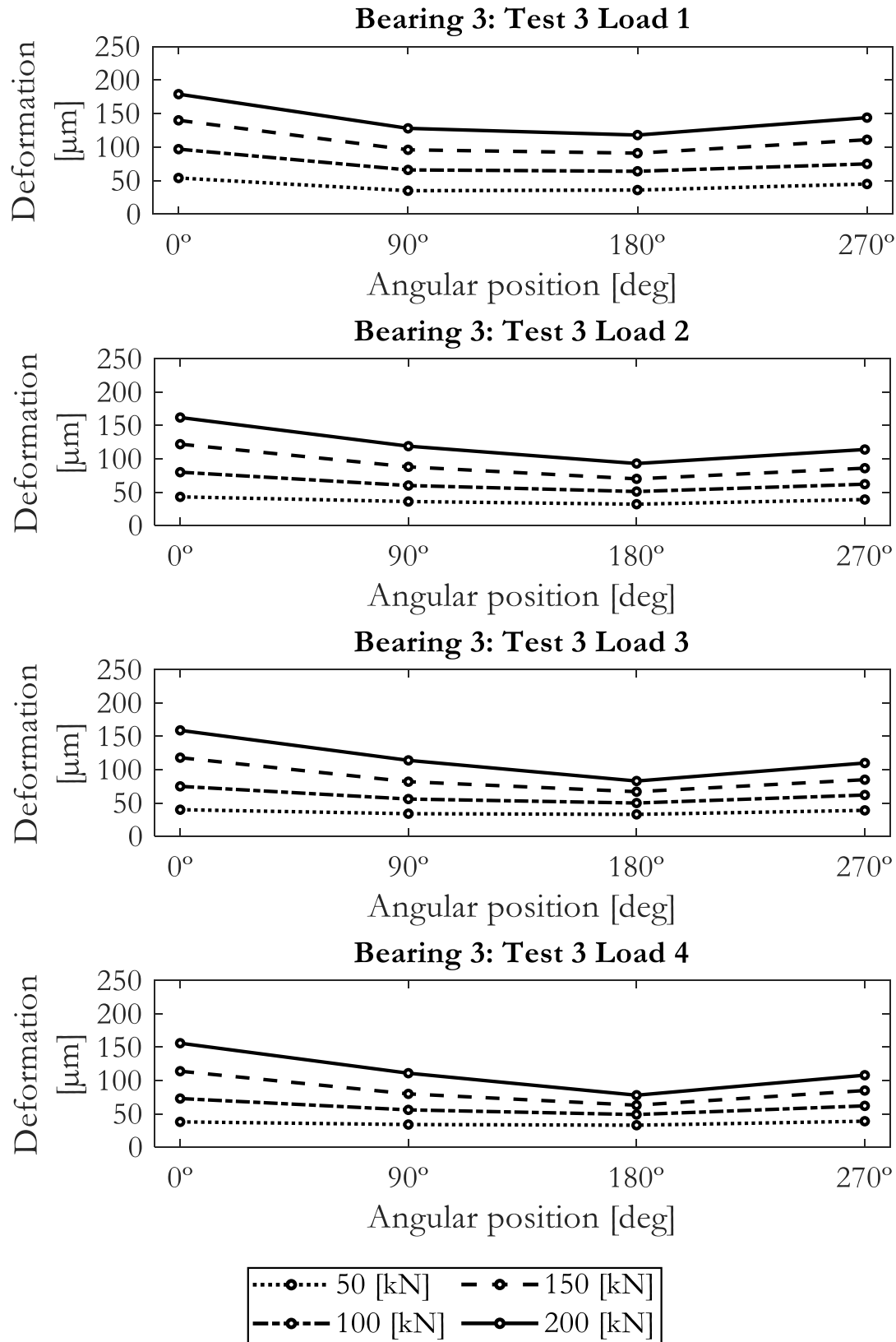
Figure B.9 Bearing 3: No bolt preload test 3.
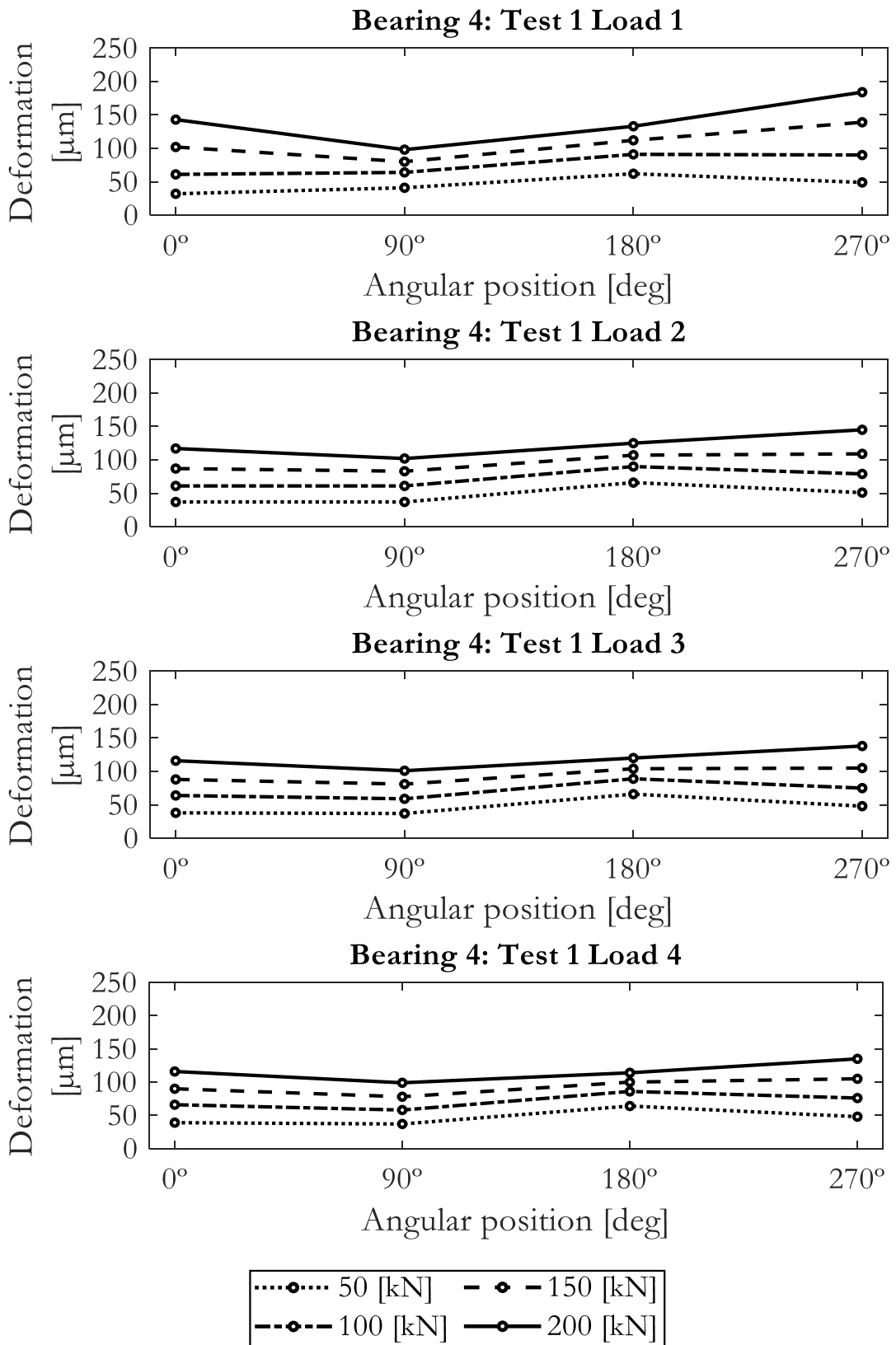
Figure B.10 Bearing 4: No bolt preload test 1.
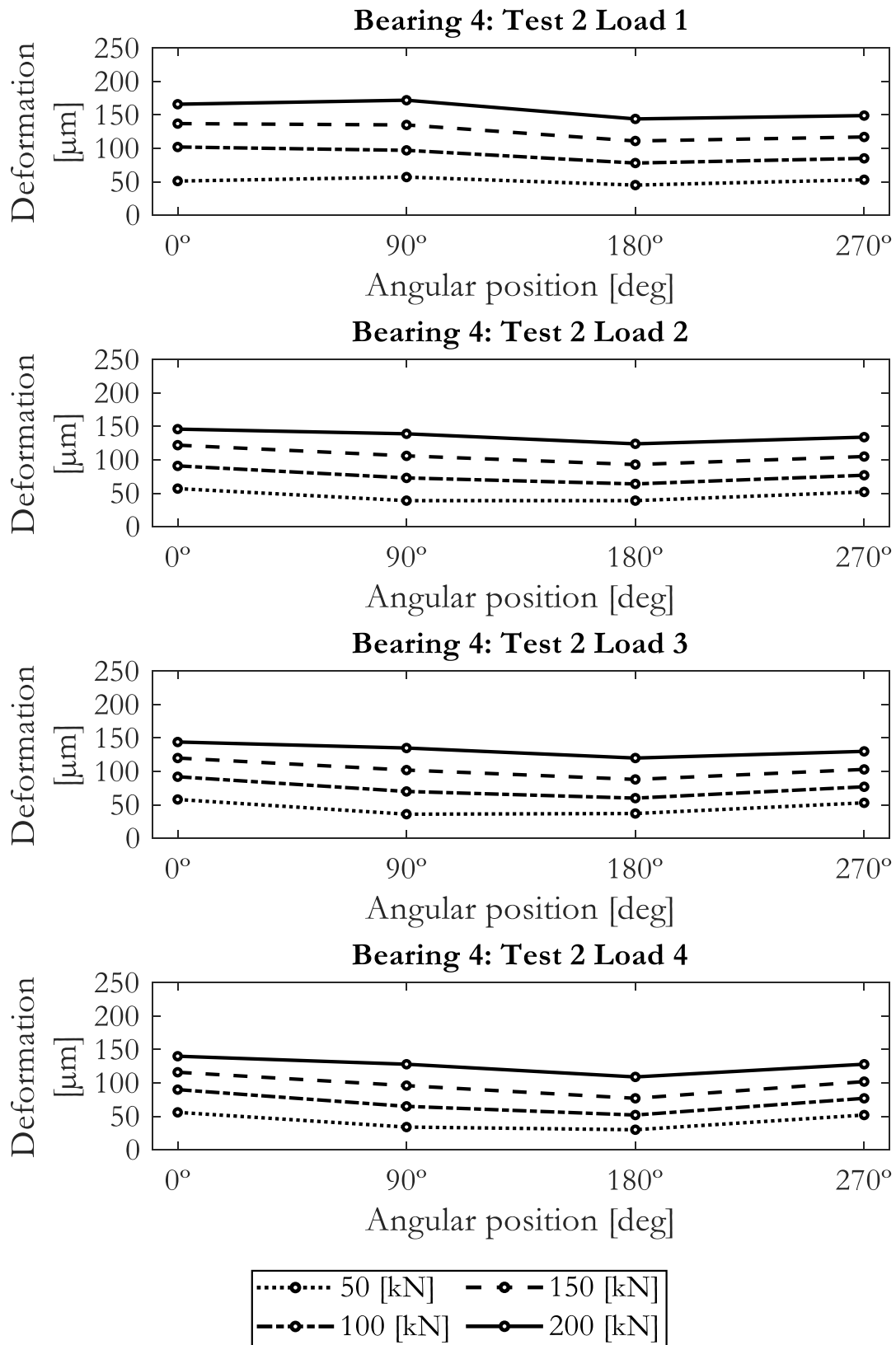
Figure B.11 Bearing 4: No bolt preload test 2.
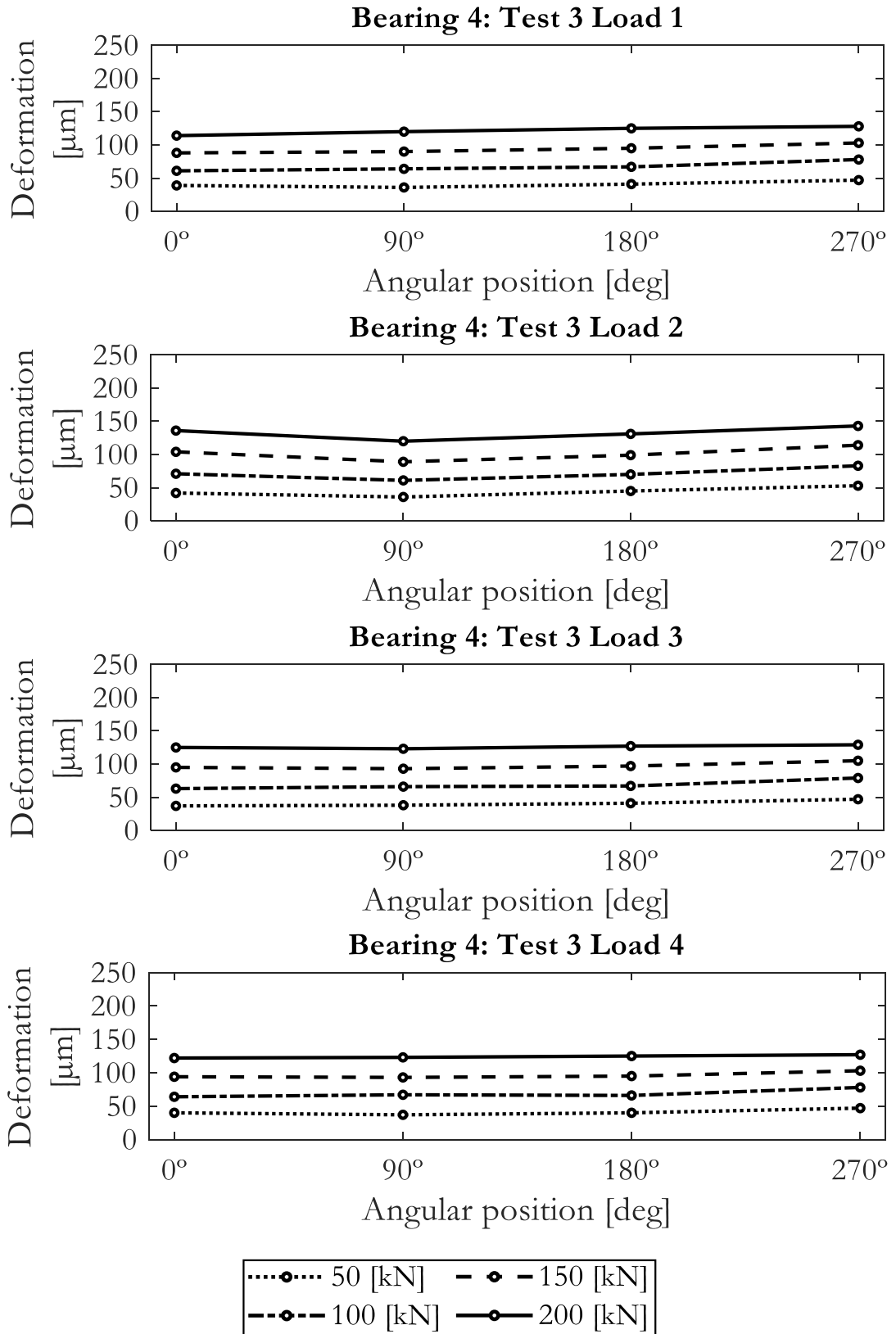
Figure B.12 Bearing 4: No bolt preload test 3.
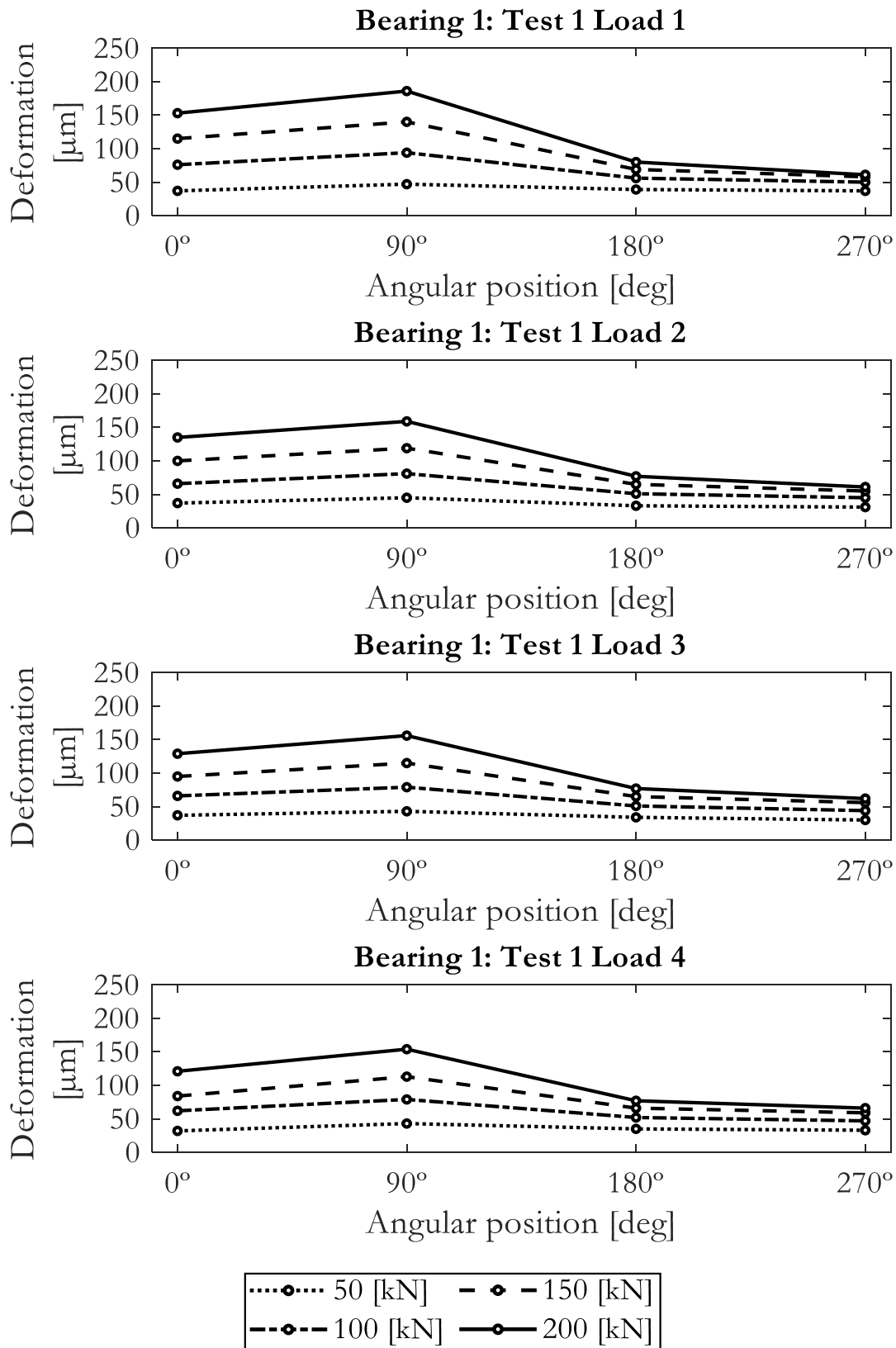
Figure B.13 Bearing 1: Bolt preload test 1.
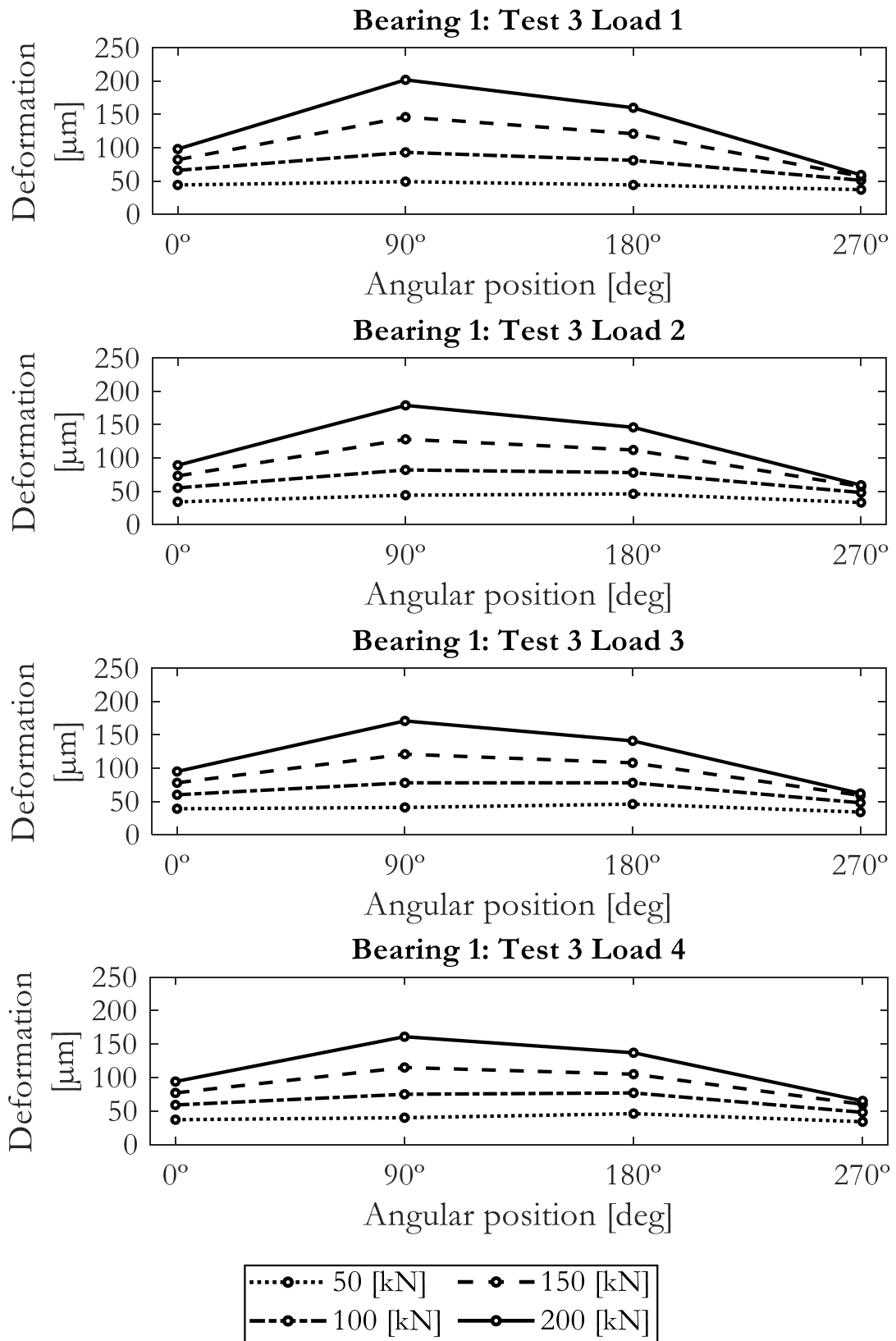
Figure B.14 Bearing 1: Bolt preload test 2.
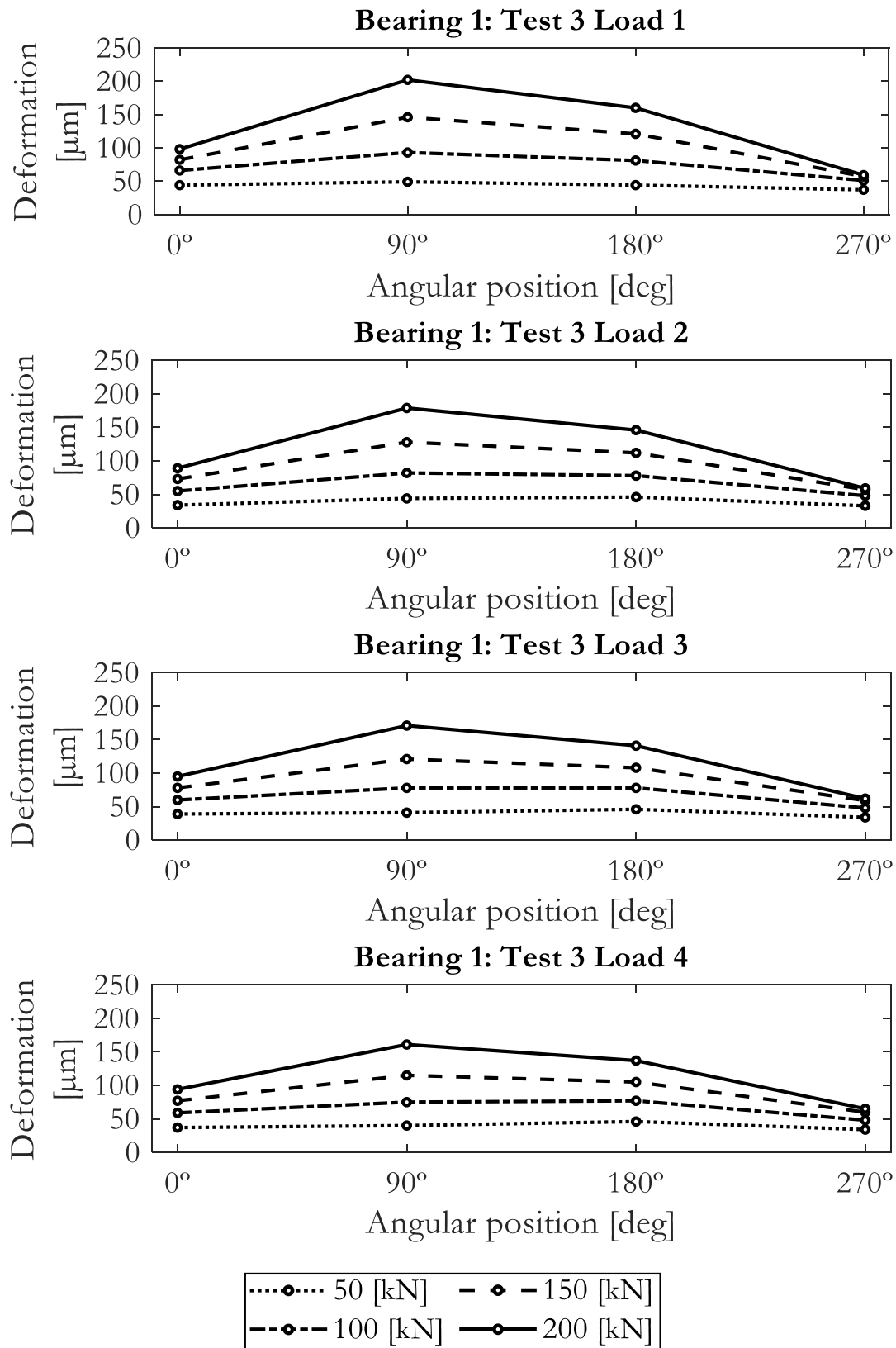
Figure B.15 Bearing 1: Bolt preload test 3.
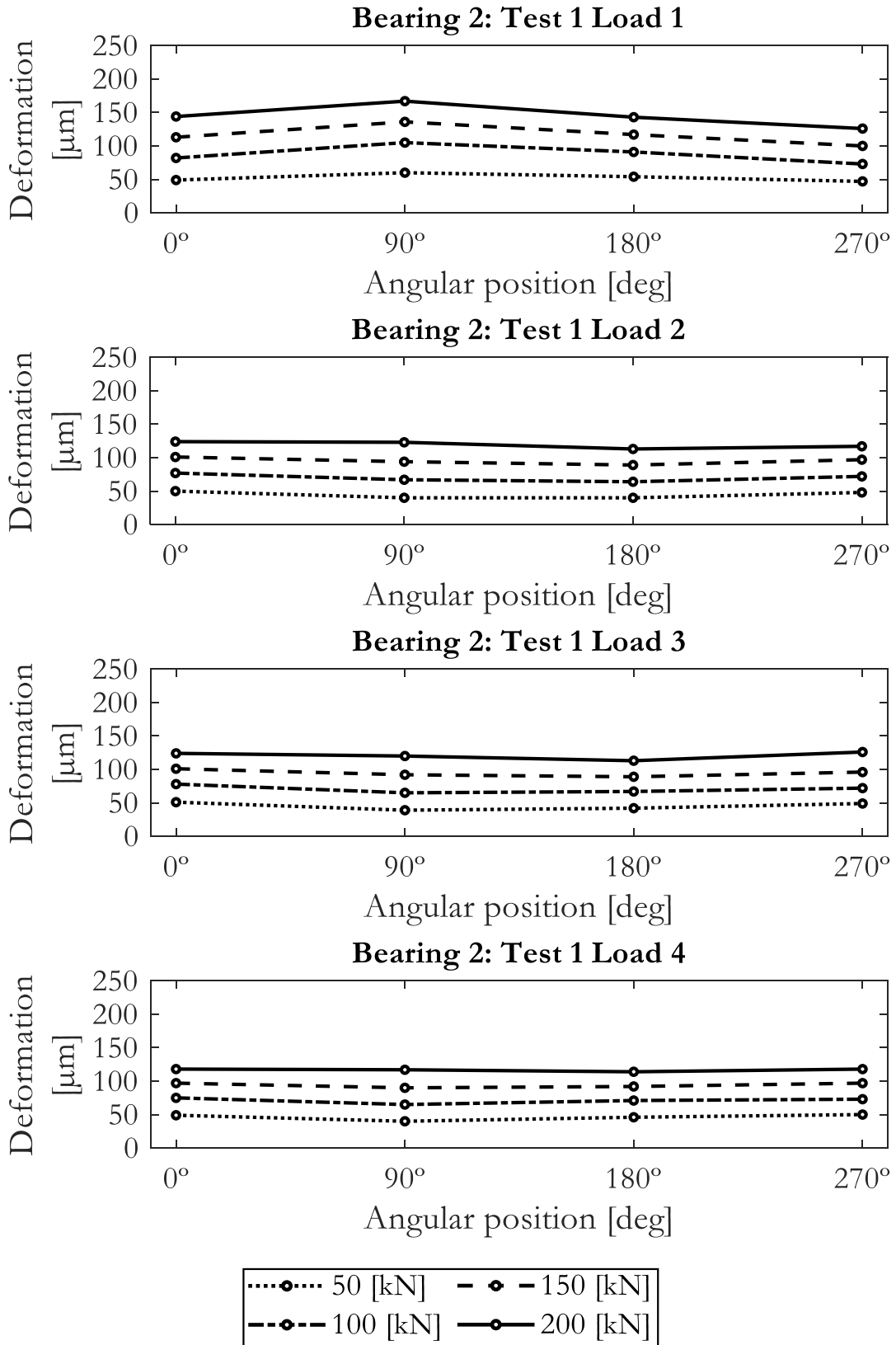
Figure B.16 Bearing 2: Bolt preload test 1.
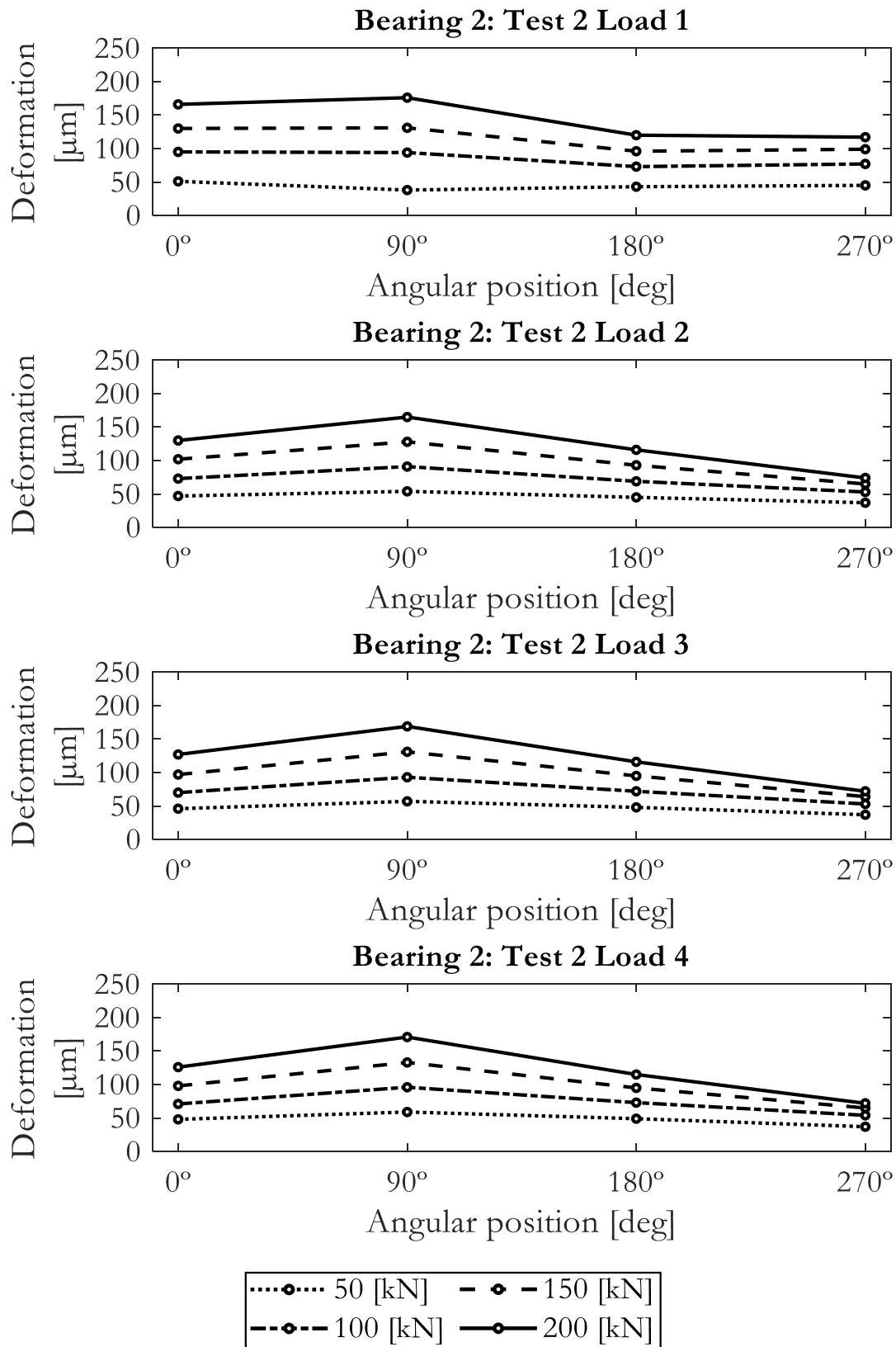
Figure B.17 Bearing 2: Bolt preload test 2.
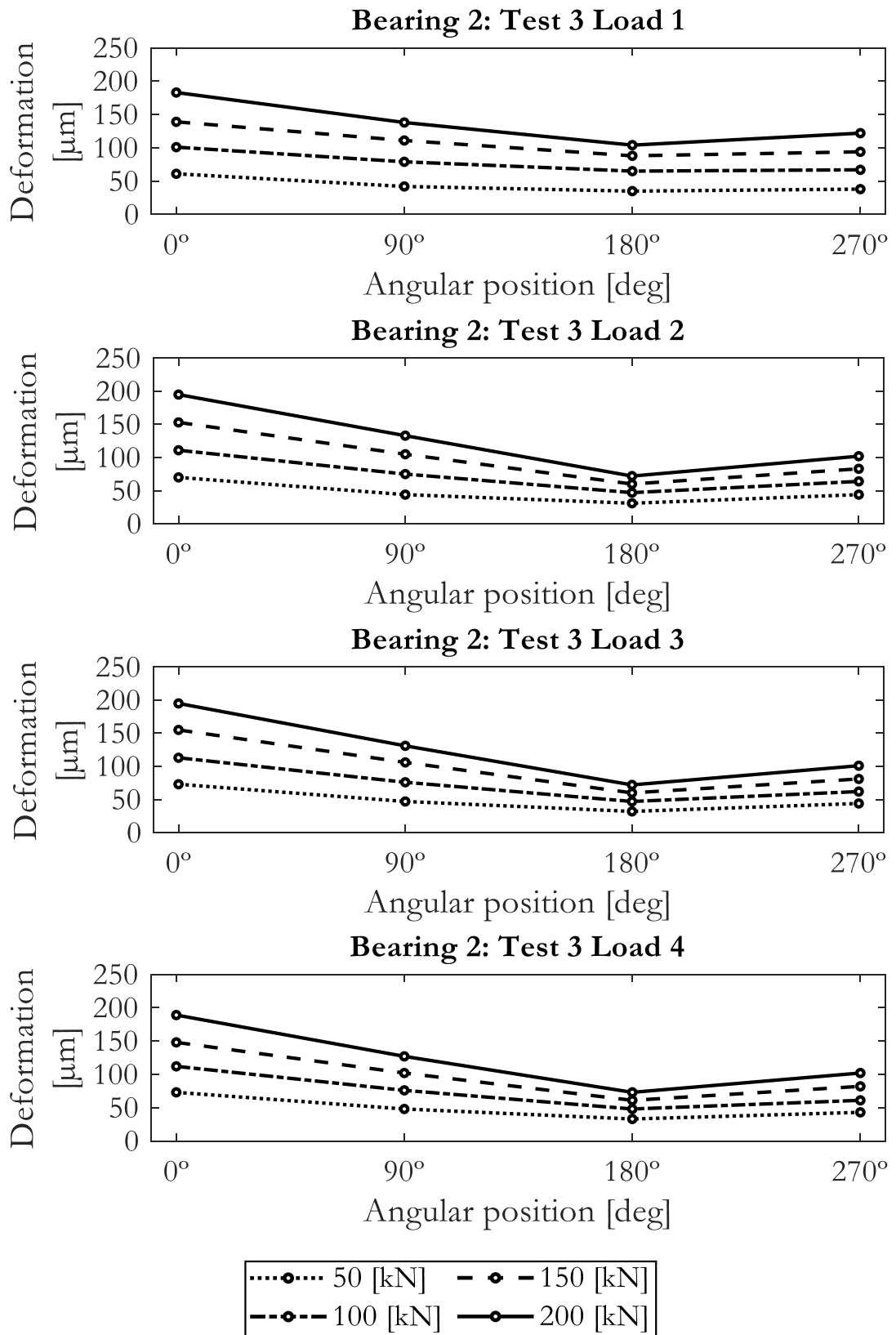
Figure B.18 Bearing 2: Bolt preload test 3.
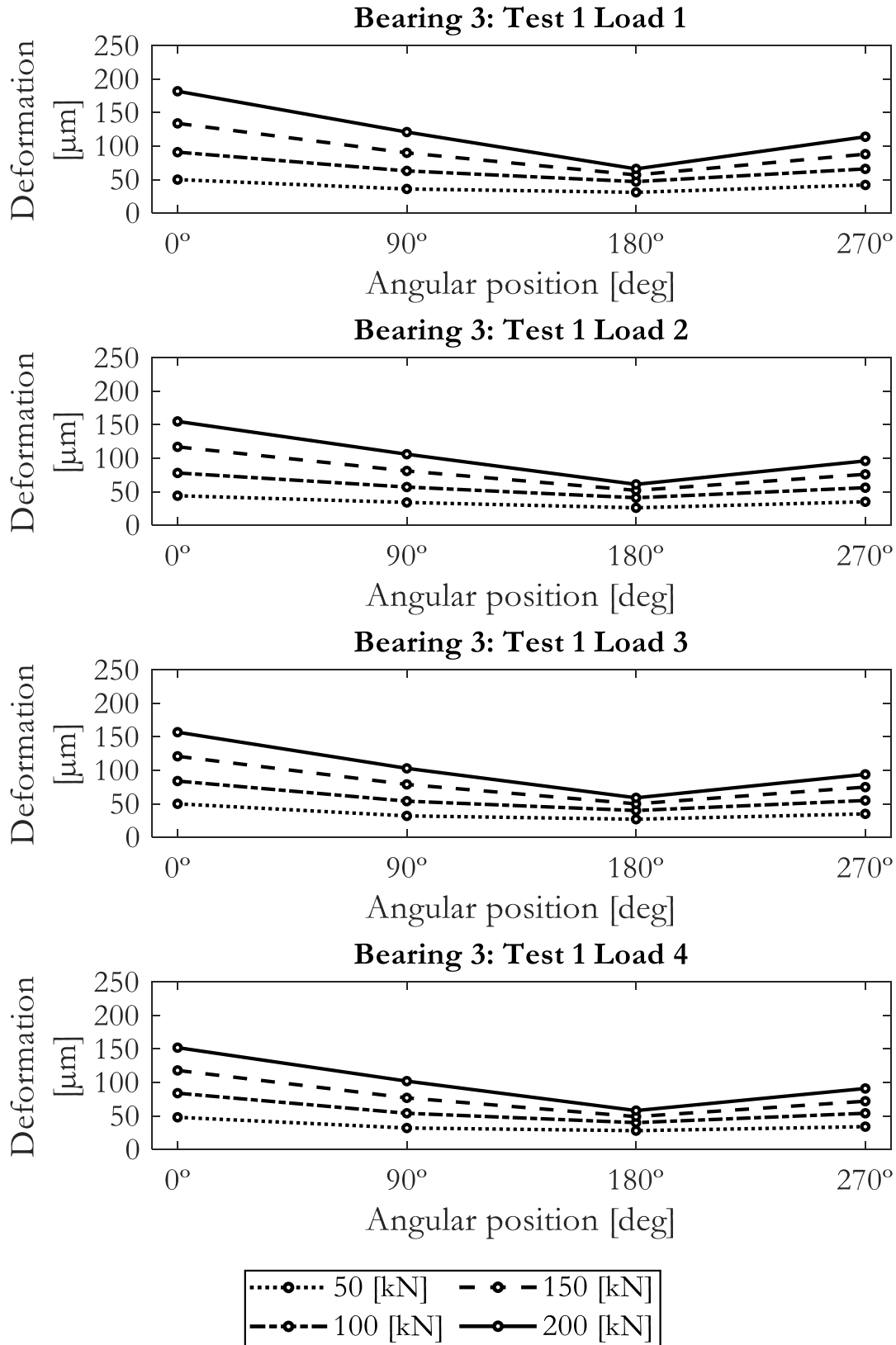
Figure B.19 Bearing 3: Bolt preload test 1.
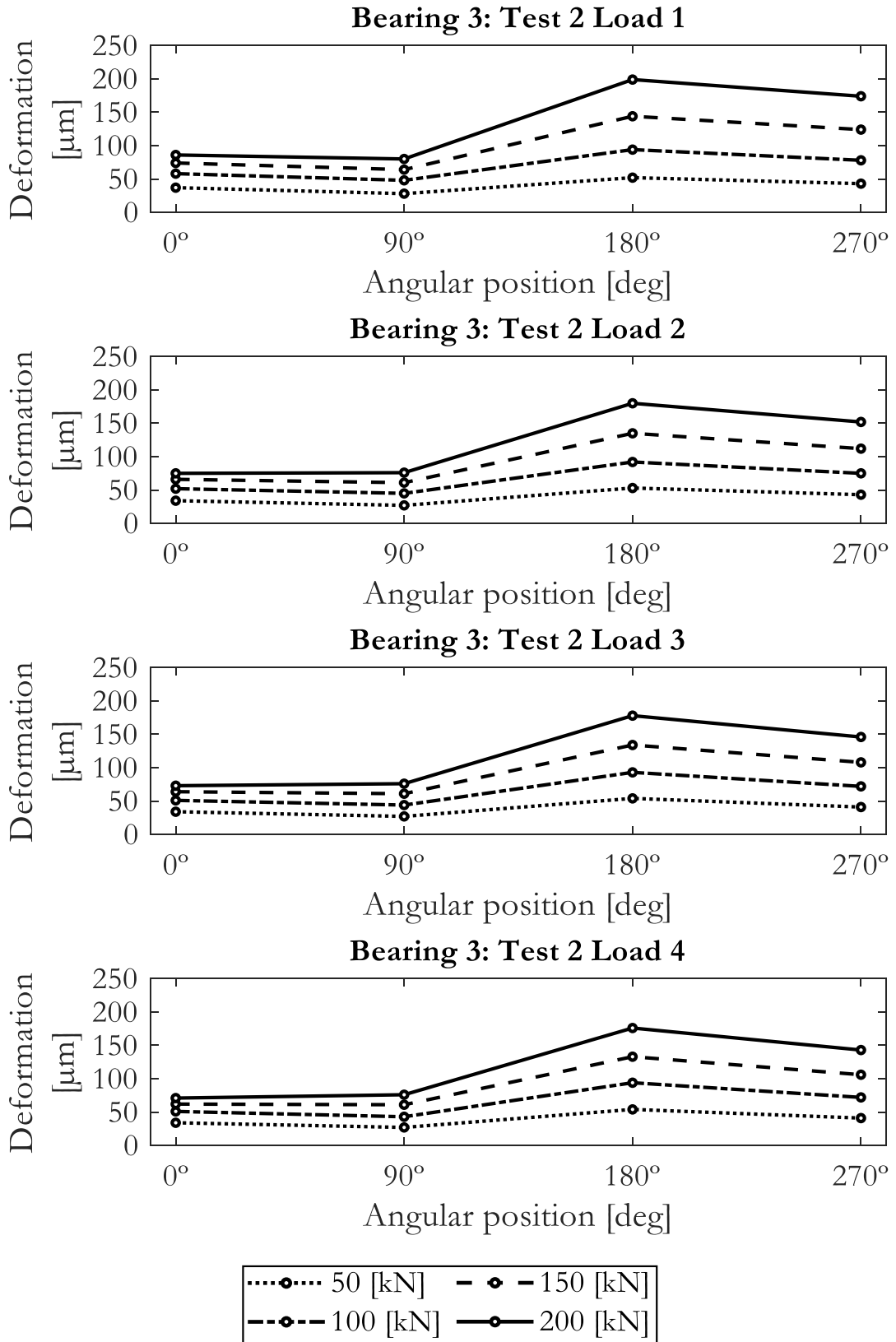
Figure B.20 Bearing 3: Bolt preload test 2.
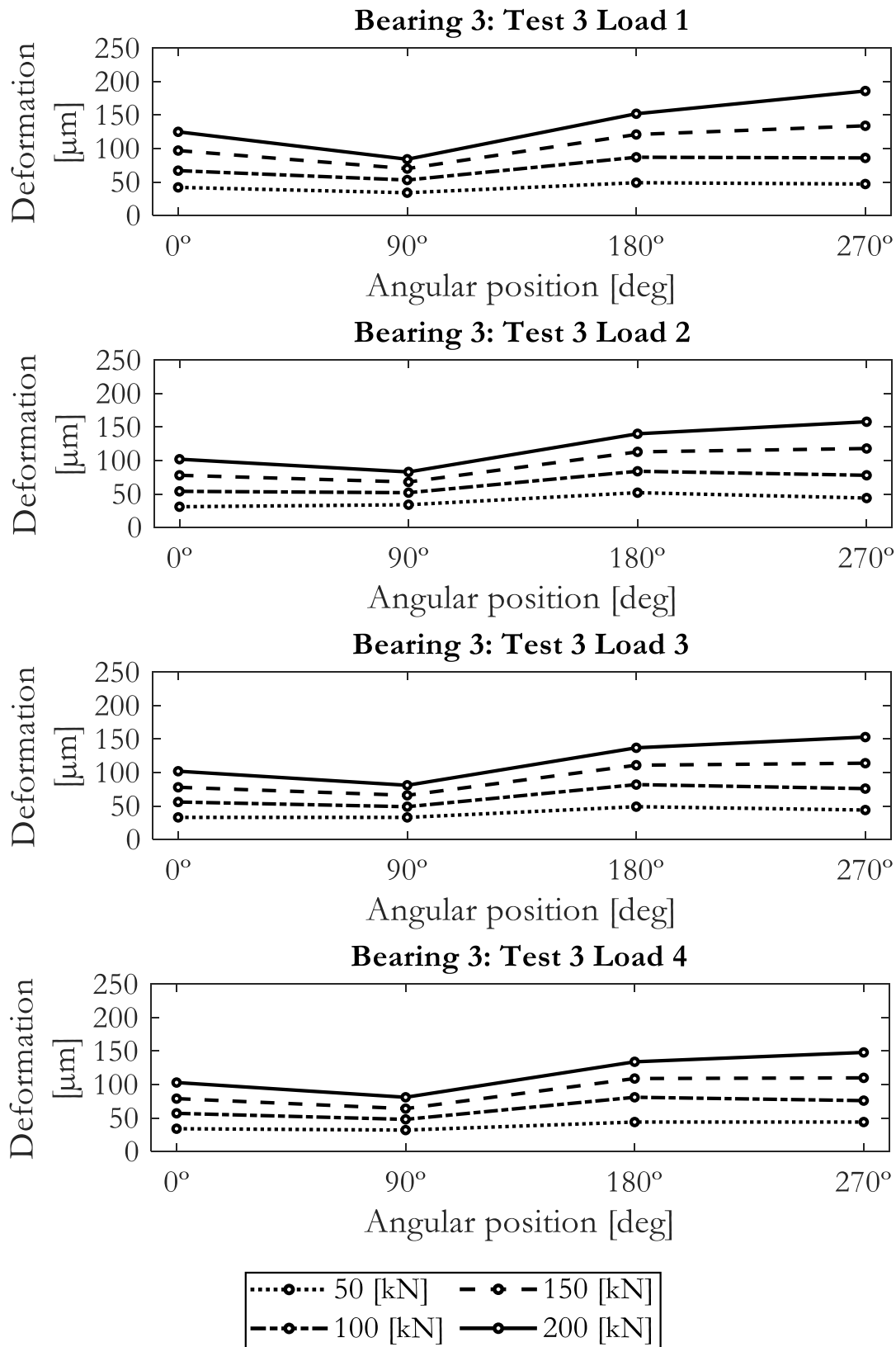
Figure B.21 Bearing 3: Bolt preload test 3.
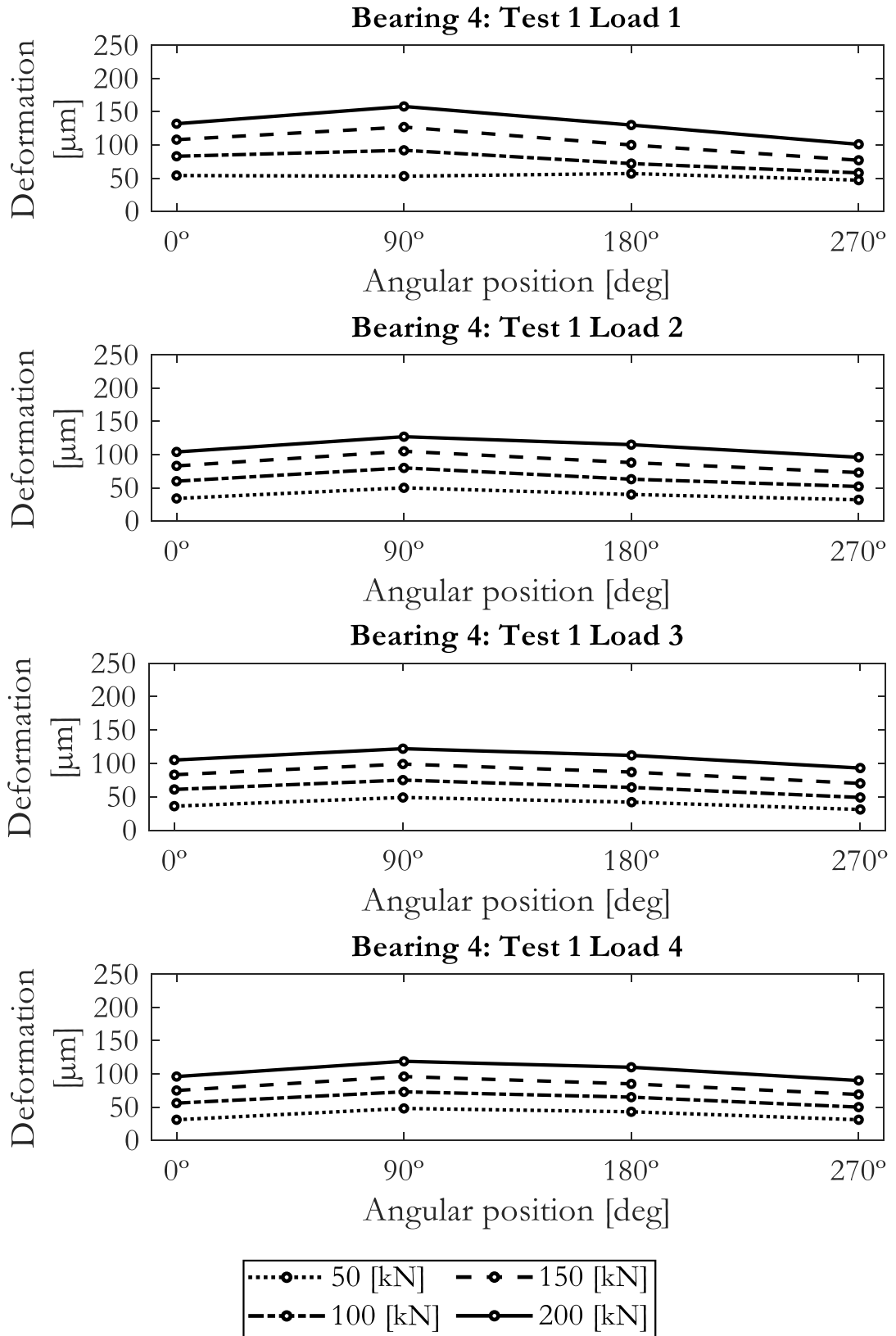
Figure B.22 Bearing 4: Bolt preload test 1.
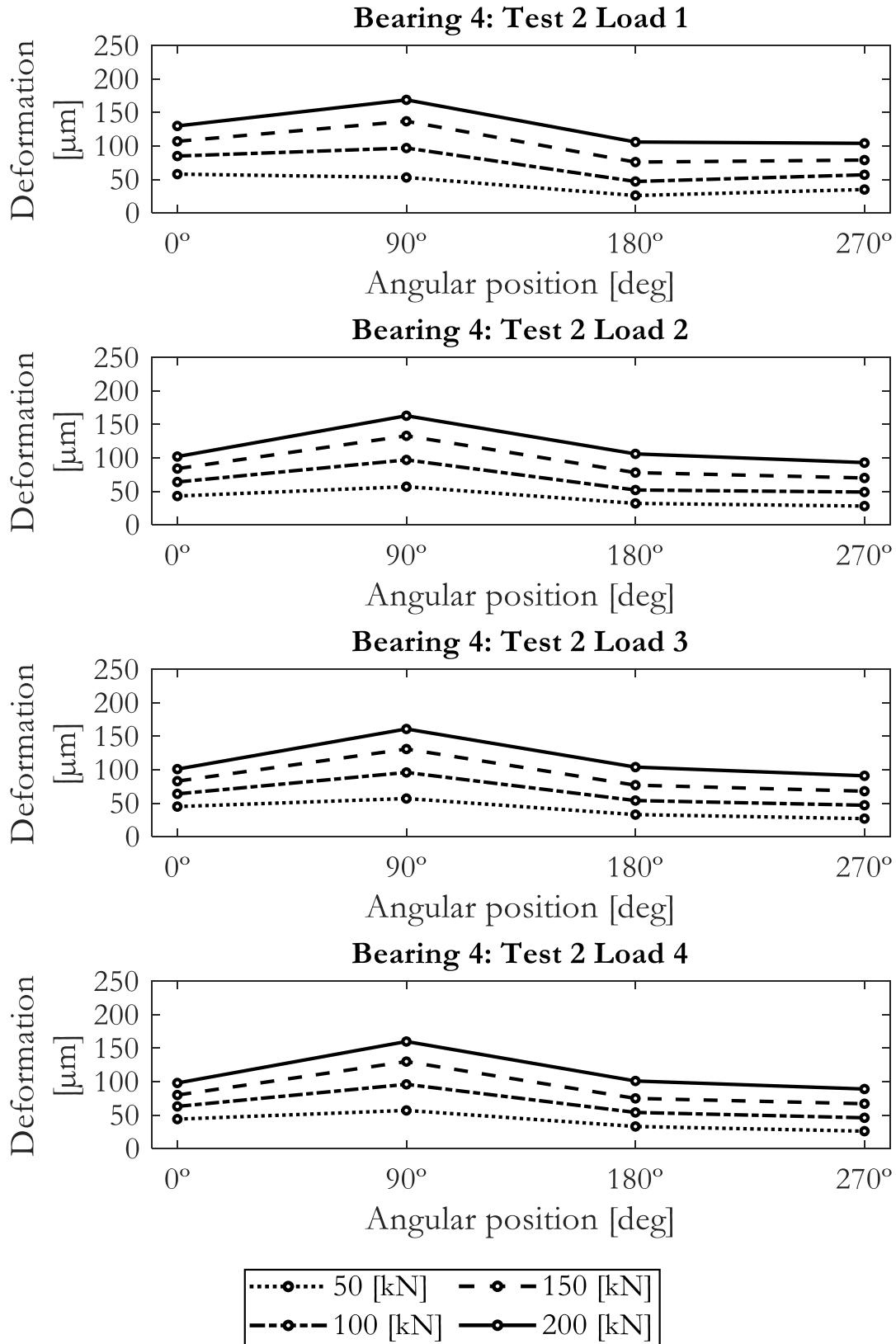
Figure B.23 Bearing 4: Bolt preload test 2.
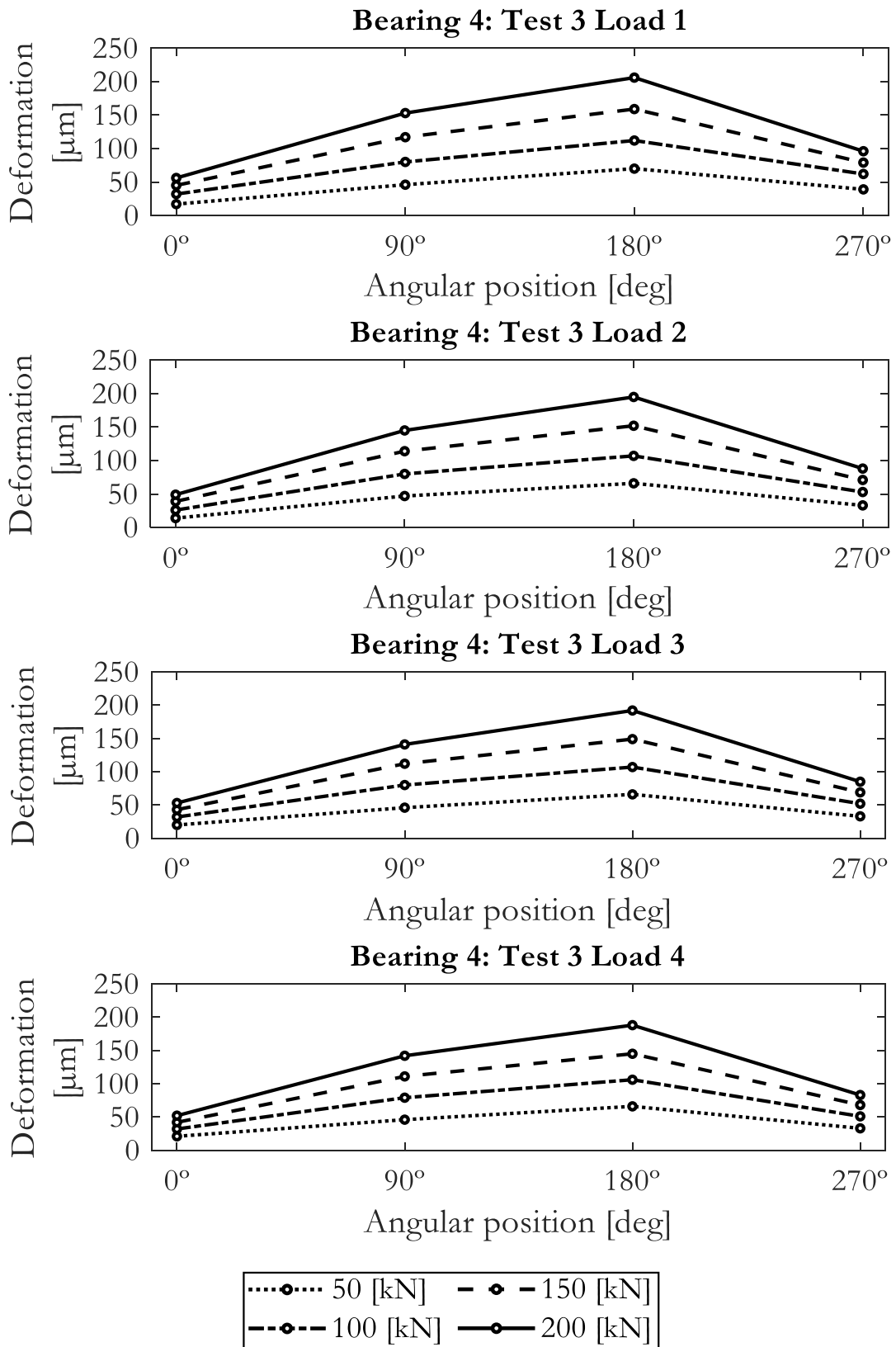
Figure B.24 Bearing 4: Bolt preload test 3.

Appendix C: Clamping tools drawings

In this appendix, the drawings of the clamping tools designed and manufactured for the experimental tests are presented. The object of these clamping tools is explained in Chapter 6.
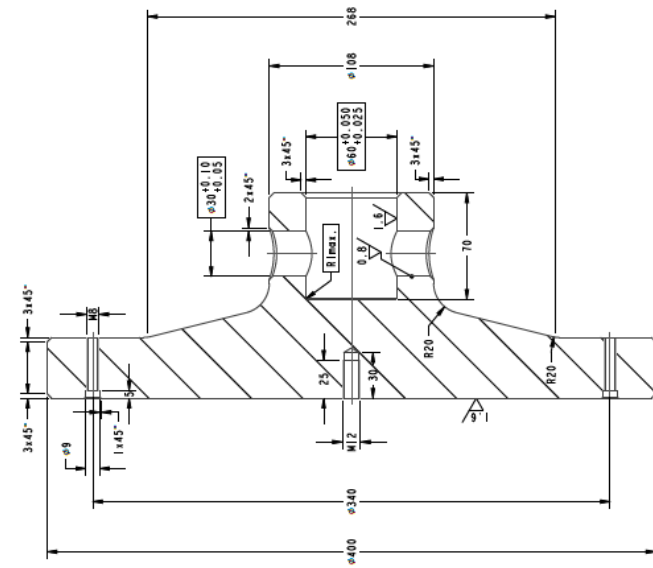
SECCIÓN A-A

SECCIÓN B-B

ADM

Description
Plato inferior para ensayos proyecto WIRE

Material
F1140 (PAVONADO)

Units in mm
General tolerances: ISO 2768-mK

Drawn by	Date	Scale	
IHERAS	12/04/2021		
		Sheet	

Drawing No.
PLANO_PLATO_INF_03

File Name
PLATO_INF.PRT

Appendix D: Certificates of inspection

In this appendix, the certificates of inspection of the dial indicators used for the experimental tests presented in Chapter 6 are included.
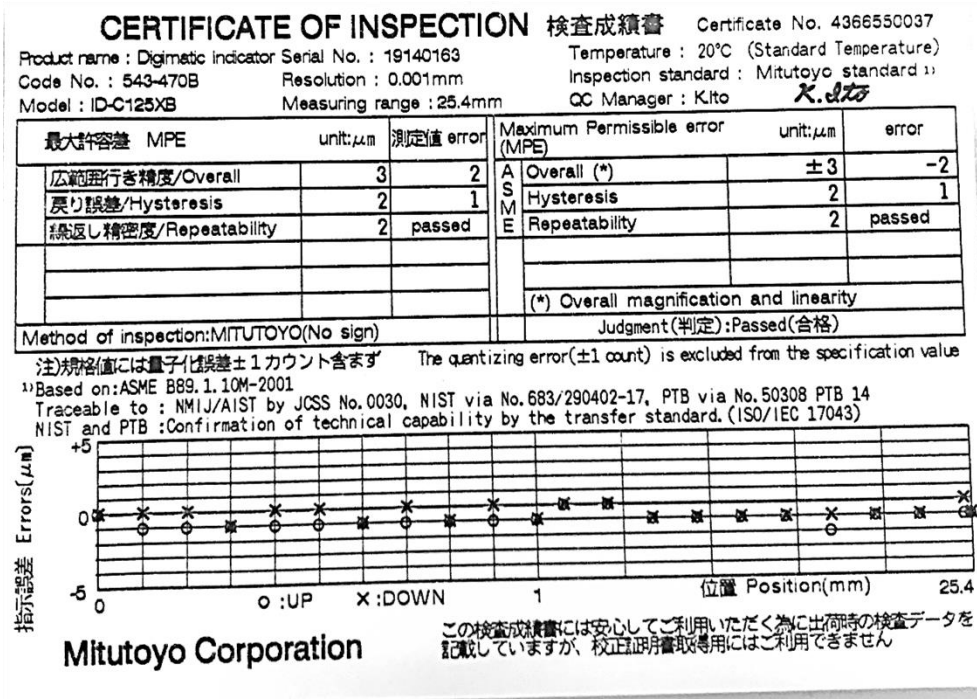
Figure D.1 Certificate of inspection of the dial indicator serial number 19140163.

Figure D.2 Certificate of inspection of the dial indicator serial number 20153892.
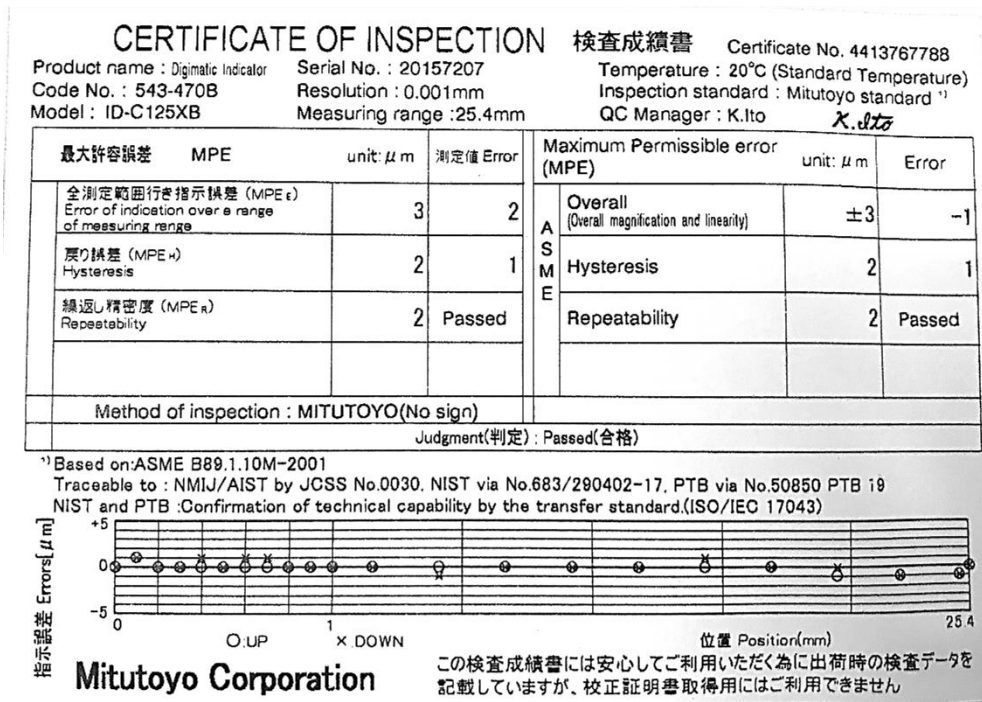
Figure D.3 Certificate of inspection of the dial indicator serial number 20157207.